Exploration of new sulfate-based cathode materials for lithium ion batteries

Laura Lander

Université Pierre et Marie Curie

ED 397 Chimie et physico-chimie des matériaux

Laboratoire de Chimie Solide et l'Energie

Exploration of new sulfate-based cathode materials for lithium ion batteries

by Laura LANDER

PhD thesis in chemistry

Directed by Gwenaëlle Rousse et Jean-Marie Tarascon

To be presented and defended in public on November 4th, 2016

In front of the jury:

Dr. Claire Villevieille	Group leader, PSI, Villingen	Referee
Dr. Olivier Mentré	Research director, ENSC, Lille	Referee
Prof. Christel Laberty	Professor, UPMC, Paris	Examiner
Dr. Jean-Noël Chotard	Associate professor, LRCS, Amiens	Examiner
Dr. Gwenaëlle Rousse	Associate professor, Collège de France, Paris	Director
Prof. Jean-Marie Tarascon	Professor, Collège de France, Paris	Director

Université Pierre et Marie Curie

ED 397 Chimie et physico-chimie des matériaux

Laboratoire de Chimie Solide et l'Energie

Exploration de nouveaux matériaux à base de sulfates pour des batteries lithium ion

Par Laura LANDER

Thèse de doctorat de chimie

Dirigée par Gwenaëlle Rousse et Jean-Marie Tarascon

Soutenance prévue le 4 novembre 2016

Devant un jury composé de :

Dr. Claire Villevieille	Group leader, PSI, Villingen	Rapporteur
Dr. Olivier Mentré	Directeur de recherche, CNRS, ENSC, Lille	Rapporteur
Prof. Christel Laberty	Professeur, UPMC, Paris	Examinateur
Dr. Jean-Noël Chotard	Maître de conférences, LRCS, Amiens	Examinateur
Dr. Gwenaëlle Rousse	Maître de conférences, Collège de France, Paris	Directrice
Prof. Jean-Marie Tarascon	Professeur, Collège de France, Paris	Directeur

À ma famille, à mes amis.

Alles Wissen und alle Vermehrung unseres Wissens endet nicht mit einem Schlusspunkt, sondern mit Fragezeichen.

Hermann Hesse

Acknowledgements

First of all, I want to thank my supervisor and director of the laboratory Jean-Marie Tarascon to give me the opportunity to do my PhD under his guidance. He was never too occupied to answer questions and he always took the time to discuss problems and results, which created a very dynamic ambiance and which I highly appreciated during my PhD. His integrity and his passion for science shall always serve as an example for my future path.

I want to thank Gwenaëlle Rousse, who was my supervisor and office neighbor for three years. Her positive attitude, encouragement and support always kept me going. It was a great pleasure to learn from Gwen and her curiosity to search for new compounds and her excitement for the beauty of a new structure were contagious and motivating. I will miss our fruitful discussions and the fun times in our common office and at the neutron reactor.

And it was of course also the lab colleagues that made these three years such a great experience. It was always a good atmosphere, which was productive but also relaxed and fun. And our Friday evening ritual definitely will always have a special place in my memory. ☺ I especially want to thank Chin and Eric, with whom we started this tradition. During the PhD I also made good friends and especially in Florent I have found a special one. We shared one office and spent probably 80 % of our time together for three years and a day when he was not in lab was a lonely day. I enjoyed every moment with him, especially those when we laughed and joked. He was always patient with me and was there for me when it got a little rough in lab or outside of work. He is a real friend and even though we are very different, I could not think of a better office mate! I truly hope that at one point we will share an office again! A special friend became also Florian, who I admire for his ease and work mentality. He always gave great advice – science related and life related – and was the motor of our social events (again Friday evenings ☺). Having him around meant having a great time and I really enjoyed our trip together to Phoenix!

At this point I want to thank all the collaborators - Moulay-Tahar Sougrati, Artem Abakumov, Dmitry Batuk, Robert Messinger, the group of Prof. Navrotsky at UC Davis, Christophe Bellin and Alain Polian, Benoît Baptiste, Nebil Katcho and Javier Carrasco. I also want to thank the LRCS group members in Amiens, which accommodated me for six months. Especially Marine Reynaud, with whom I closely worked together in the beginning and continued a collaboration

throughout the three years, made my first steps in the battery field a highly interesting experience, during which I learned important tools for my further research. She always kept being a role model for me.

Finally I want to thank my friends that I made throughout my studies. There is Tina, with whom I counted dead flies for genetic studies, did all-nighters for the exam the next morning and with whom I have been laughing now for over eight years and hopefully there are many more to come! And of course Leonard, who I met on the very first day and without his amazing humor our practical lab classes with Prof. Snape would not have been the same! The whole group – Niklas, Tina, Leonard, Kristina, Sara, Bruno, Mine – made the Zurich era one of the best times! Also in Paris I met wonderful friends, where I want to mention especially Dave, Franz and Victor. A special place keeps also Ji, who I admire for her personality, her strength, her open mind and life experience. She and Julian were an essential part of my Parisian times.

But my biggest thank you goes to my parents and family, who always supported me. It was my father, who taught me the fixity of purpose. But it was especially my mother, who encouraged me to go my own path and she was by my side in every adventure. She is a great inspiration and I am very grateful to her for showing me the world and passing on to me the curiosity to learn. It is thanks to her that I have been able to realize my dreams.

Abstract

Lithium-ion batteries (LIBs) have become the dominating electrical energy storage technology in the last two decades. However, depending on their applications, LIBs need to fulfill several requirements such as high energy density, low-cost, safety and sustainability. This calls for the development of new electrode materials. Focusing on the cathode side, we embarked on the synthesis of novel sulfate- and fluorosulfate-based polyanionic compounds. During the course of our study, we discovered a monoclinic $KFeSO_4F$ polymorph, whose structure was determined via combined X-ray and neutron powder diffraction. We could electrochemically extract K^+ and reinsert Li^+ into this new polymorphic "$FeSO_4F$" matrix at an average potential of 3.7 V *vs.* Li^+/Li^0. We then turned towards fluorine-free materials and synthesized a new orthorhombic $Li_2Fe(SO_4)_2$ phase, which presents appealing electrochemical properties in terms of working potential (3.73 and 3.85 V *vs.* Li^+/Li^0) and cycling stability. In a next step, we tested langbeinite $K_2Fe_2(SO_4)_3$ for its aptitude to intercalate Li^+ once K^+ is extracted, with however little success. Nevertheless, exploring other langbeinite $K_2M_2(SO_4)_3$ phases (*M*=3d transition metal), we discovered a new $K_2Cu_2(SO_4)_3$ compound, which crystallizes in an orthorhombic structure distinct from the langbeinite one. Finally, we investigated these compounds not only for their electrochemistry, but we were also able to demonstrate other interesting physical properties, namely magnetic features. Orthorhombic $Li_2Fe(SO_4)_2$ and monoclinic $KFeSO_4F$ both present a long-range antiferromagnetic spin ordering whose symmetry allows a magnetoelectric effect.

Résumé

Ces vingt dernières années, les batteries lithium-ion sont devenues dominantes parmi les technologies de stockage d'énergie électrique. Selon les applications, ces batteries (ou les matériaux qui la constituent) doivent présenter différentes spécificités: notamment une grande densité d'énergie, un bas coût, des contraintes de sécurité et de durabilité. Dans ce but, le développement de nouveaux matériaux d'électrode est indispensable. Nous nous sommes engagés, dans cette thèse, dans la synthèse des nouveaux composés polyanioniques à base de sulfates et fluorosulfates comme matériaux d'électrodes positives. Au cours de notre étude, nous avons synthétisé un nouveau polymorphe de $KFeSO_4F$, de symétrie monoclinique, dont nous avons déterminé la structure en combinant la diffraction des rayons X et des neutrons sur poudre. Il est possible d'extraire électrochimiquement K^+ de $KFeSO_4F$ et de réinsérer Li^+ dans cette nouvelle matrice «$FeSO_4F$» à un potentiel moyen de 3.7 V *vs.* Li^+/Li^0. Ensuite, nous nous sommes penchés vers des matériaux dépourvus de fluor et nous avons découvert une nouvelle phase $Li_2Fe(SO_4)_2$ orthorhombique, qui présente des propriétés électrochimiques intéressantes avec un potentiel de 3.73 et 3.85 V *vs.* Li^+/Li^0 et une bonne cyclabilité. Nous avons également étudié le composé langbeinite $K_2Fe_2(SO_4)_3$ pour son aptitude à intercaler Li^+ une fois le K^+ extrait, avec cependant peu de succès. Néanmoins, en examinant d'autres phases langbeinites $K_2M_2(SO_4)_3$ avec *M*=métaux de transition 3d, nous avons découvert un nouveau composé $K_2Cu_2(SO_4)_3$, qui cristallise dans une structure différente de celle des langbeinites. Enfin, nous n'avons pas seulement étudié ces nouveaux matériaux pour leurs propriétés électrochimiques mais nous avons été également capables de révéler d'autres caractéristiques physiques intéressantes, notamment magnétiques. Les composés $Li_2Fe(SO_4)_2$ orthorhombique et $KFeSO_4F$ monoclinique s'ordonnent antiferromagnétiquement à longue distance et leur structure magnétique autorise un couplage magnéto-électrique.

Table of Contents

General introduction **1**

Chapter I. State of the art **5**

I.1. Battery technologies **5**

I.1.1. The first rechargeable batteries 6

I.1.2. Lithium-based batteries 7

I.2. Cathode Materials for Li-ion batteries **9**

I.2.1. Layered oxide materials 9

I.2.2. Spinel structures ($LiMn_2O_4$ and $LiNi_{0.5}Mn_{1.5}O_4$) 12

I.2.3. Polyanionic cathode materials 14

I.3. Conclusion **28**

Chapter II. Fluorosulfate-based cathode materials **29**

II.1. Introduction **29**

II.2. Relationship between synthesis method and structural disorder **31**

II.3. Polymorphism in $KFeSO_4F$ **40**

II.4. Synthesis of a novel $KFeSO_4F$ polymorph **42**

II.5. Characterization of $KFeSO_4F$ **43**

II.5.1. Structure determination 43

II.5.2. Electrochemical performance and cation diffusion properties 48

II.6. Polymorph stability of orthorhombic and monoclinic $KFeSO_4F$ **53**

II.7. Magnetic properties of monoclinic $KFeSO_4F$ **56**

II.8. Conclusion **61**

Chapter III. Sulfate-based materials: Polymorphism in $Li_2M(SO_4)_2$ **65**

III.1. Introduction **65**

III.2. Synthesis of a novel $Li_2M(SO_4)_2$ polymorph **67**

III.3. Characterization of the $Li_2M(SO_4)_2$ polymorph **69**

III.3.1. Structure of orthorhombic $Li_2M(SO_4)_2$ 69

III.3.2. Electrochemistry of orthorhombic $Li_2Fe(SO_4)_2$ 77

III.4. Delithiation mechanisms of monoclinic and orthorhombic $Li_2Fe(SO_4)_2$ **81**

III.5. Polymorph stability 91

III.6. Magnetic properties of orthorhombic $Li_2M(SO_4)_2$ 98

III.7. Conclusions 110

Chapter IV. Langbeinite $K_2Fe_2(SO_4)_3$ and a new $K_2Cu_2(SO_4)_3$ phase 113

IV.1. Introduction 113

IV.2. Synthesis and diffusion properties of langbeinite $K_2Fe_2(SO_4)_3$ 114

IV.3. Synthesis of a novel $K_2Cu_2(SO_4)_3$ compound 118

IV.4. Characterization of $K_2Cu_2(SO_4)_3$ 119

IV.4.1. Structure determination of $K_2Cu_2(SO_4)_3$ 119

IV.4.2. Electrochemistry and cation diffusion of $K_2Cu_2(SO_4)_3$ 122

IV.5. Stability of $K_2Cu_2(SO_4)_3$ 125

IV.6. Synthesis of $K_2Cu_3O(SO_4)_3$ 128

IV.7. Conclusion 132

General conclusions 134

Annexe 138

1. Sample preparation 138

1.1. Spark Plasma Sintering (SPS) 138

1.2. Ball-milling 138

2. Structural characterization 139

2.1. Laboratory X-ray diffraction (XRD) 139

2.2. Synchrotron XRD 140

2.3. Neutron diffraction 141

2.4. Structure determination 141

2.5. Bond Valence Energy Landscape calculations 141

3. Electrochemical characterization 142

3.1. Electrochemical cells 142

3.2. Electrochemical cycling 143

4. Magnetic properties 144

4.1. Magnetic measurements 144

4.2. Magnetic structure determination 145

5. Additional characterization techniques 145

5.1. Electron microscopy and Energy-dispersive X-ray spectroscopy (EDX) 145
5.2. Mössbauer spectroscopy 145
5.3. ^{7}Li solid-state nuclear magnetic resonance (NMR) 147
5.4. Thermal analyses 147
5.5. Impedance spectroscopy 147
5.6. Raman measurements 149
5.7. High-pressure experiments 149

6. Tanabe-Sugano diagrams 150

7. Density Functional Theory calculations for $Li_2M(SO_4)_2$ 151

8. Calorimetric studies 152

References 154

General introduction

The most urgent challenges that our society has to face in the future are climate change, sustainable development and limited energy resources; all being intimately connected with fossil fuels such as oil, coal and natural gas. Not only will these resources, which deliver the major part of our used energy (Figure 0.1a)[1], fail at one point to meet our growing energy demand, but also their processing results in important emissions of green-house gases and CO_2, which have a significant influence on the atmosphere and on global warming (Figure 0.1b).[2]

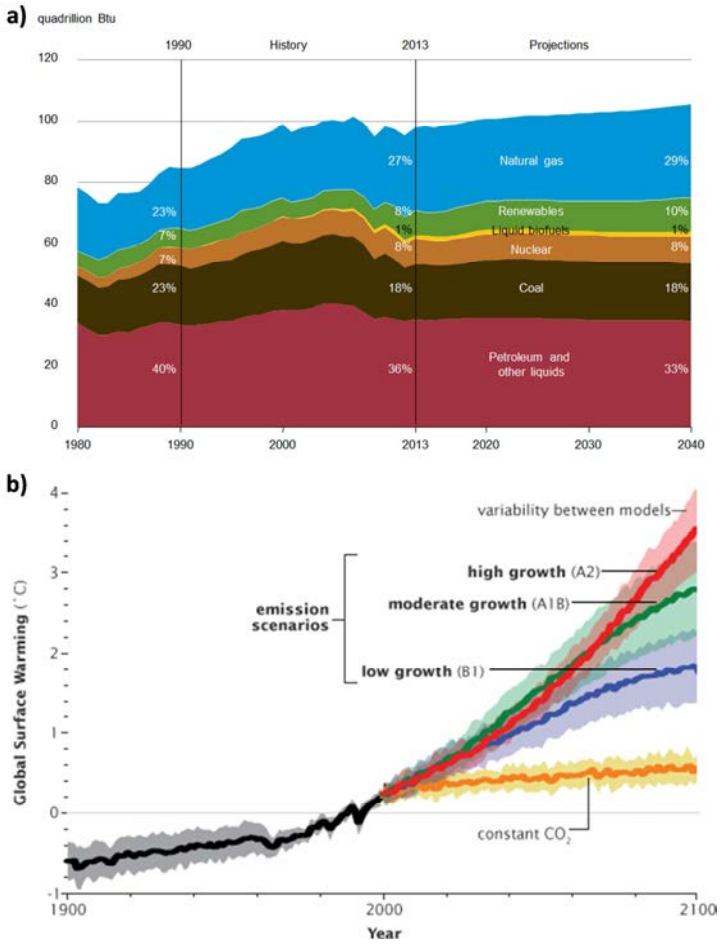

Figure 0.1: a) World energy consumption of different fuel types including an outlook until 2040.[1] b) Evolution of the global temperature increase depending on various CO_2 emission scenarios (high emission in red, medium in green, low in blue and constant CO_2 emission in yellow).[2]

It has been therefore an utmost concern for society, politics (e.g. COP21 in Paris 2015) and the scientific community to find solutions that address simultaneously the energy crisis as well as the energy-induced environmental pollution. In this quest, the focus turned towards renewable

energy resources such as solar energy and wind power, which are unlimited and environmentally benign. However, since these resources are intermittent, the produced energy needs to be stored and provided to the consumer on demand. This can be done by using large energy storage devices such as batteries for instance. Moreover, another interest in the battery technology is its applicability in electric vehicles, which would further significantly reduce the consumption of petroleum and fossil fuels and limit the emission of hazardous molecules. This is only true of course if the primary electricity is not coming from coal fire plants. Therefore, research groups all over the world embarked on the pursuit of a battery system that fulfills the criteria of sustainability, safety, low cost and high energy density. So far, the lithium-ion battery is the most promising technology on this sector and in the last decades, it quickly conquered the portable electronics market and is now penetrating the automobile industry.

Despite its huge success, lithium-ion batteries still need to be improved notably in terms of energy density to keep up with the rapid technological evolution. Even though the overall electrochemical performance of a battery depends on the favorable synergy of the anode, cathode and electrolyte, it is well-known that especially the cathode is essential for the achievement of high energy densities. In this context, we studied new possible cathode materials, where we focused on the exploration of new sulfate- and fluorosulfate-based polyanionic compounds. The obtained results are summarized and discussed in this thesis.

The manuscript is divided into the following parts:

Firstly, a brief overview is given over the functioning and history of the battery and the different battery technologies such as lead-acid and nickel-cadmium batteries until the emergence of the lithium-ion battery that out-passes all other technologies performance-wise. Hence, the focus of this thesis was directed towards Li-insertion positive electrodes. The various electrode materials will be reviewed in order to put our work in the context of recent developments.

The second chapter deals with the exploration of new "$FeSO_4F$" frameworks as Li^+/Na^+ intercalation compounds based on the previous work on $KTiOPO_5$-type $KFeSO_4F$ published by Recham *et al.* in 2012. In particular, a new monoclinic $KFeSO_4F$ polymorph is introduced and its synthesis conditions, structure and electrochemical performance are described in detail.

The third chapter focuses on a novel $Li_2M(SO_4)_2$ (*M* = Ni, Fe, Co, Zn) polymorph, which is stabilized via a mechanochemical synthesis approach. The Fe-based phase displays an average working potential of ~3.8 V *vs*. Li^+/Li^0 and its delithiation process was studied and further compared to its monoclinic counterpart. Besides electrochemical features, the magnetic properties of the orthorhombic $Li_2M(SO_4)_2$ phases were explored revealing a long-range antiferromagnetic ordering.

The last chapter addresses the stabilization of a novel Cu-based sulfate compound – $K_2Cu_2(SO_4)_3$. This material was inspired by the previous work on alluaudite $Na_2Fe_2(SO_4)_3$ and the mineral family of langbeinites $K_2M_2(SO_4)_3$. Synthesis, structure and electrochemical as well as cation diffusion properties of $K_2Cu_2(SO_4)_3$ are described in this chapter. Moreover, its chemical and structural relation to the oxysulfate $K_2Cu_3O(SO_4)_3$, also known as the mineral fedotovite, is discussed.

The general conclusion at the end of this report briefly summarizes the results obtained during the course of this thesis and discusses their impact and contribution to the materials science research community.

Chapter I. State of the art

I.1. Battery technologies

The general principle of an electrochemical cell is to transform chemical energy into electrical energy and *vice versa*. It consists of two electrodes, a positive (cathode) and a negative (anode), separated by an electrolyte, which allows the transport of the mobile ion species (in the case of Li-ion batteries this would be Li^+) (Figure I.1a).[3–6] During discharge the cations migrate from the anode to the cathode, whereas during charge the reverse process is triggered. The electrons that are formed during the electrochemical processes move through an external circuit and thus generate electricity. The overall cell potential (also open circuit voltage V_{OC}) is determined by the energy difference of the electrochemical potential of the anode (μ_A) and the cathode (μ_C) (Figure I.1b).[7,8] Commonly, the term "battery" is used to name a package of several such electrochemical cells connected in series or in parallel; however, for purists it should only be used when referring to a single electrochemical cell. We distinguish between non-rechargeable primary batteries and rechargeable secondary batteries.

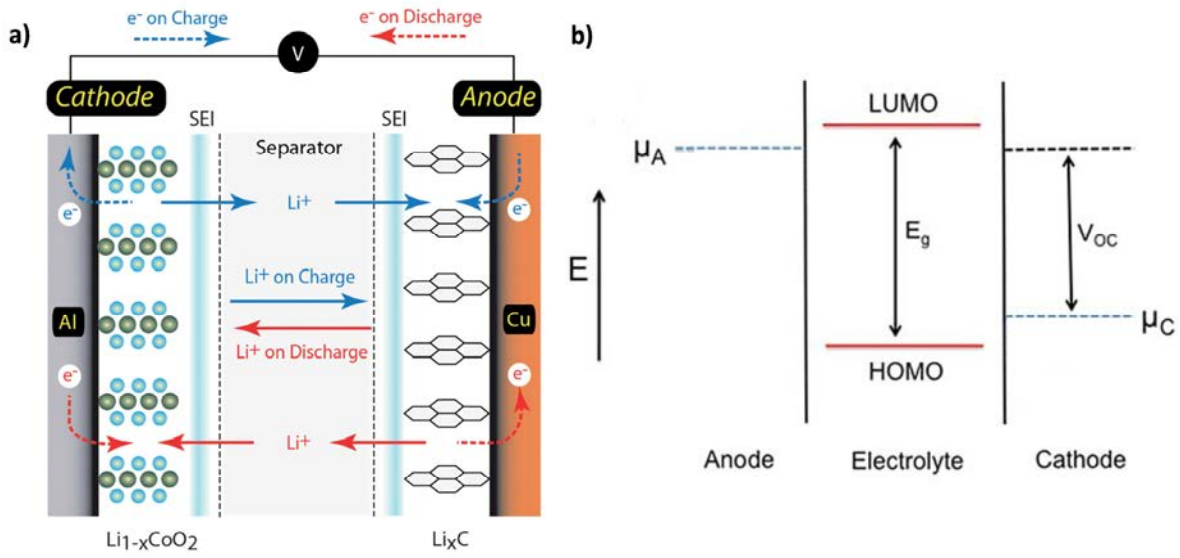

Figure I.1: a) Schematic principle of a lithium-ion battery in charge (blue arrows) and discharge (red arrows) with graphite as anode material, $LiCoO_2$ as an insertion cathode material and a liquid electrolyte.[6] b) Energy diagram of a lithium-ion battery showing the electrochemical potentials of the anode (μA) and cathode (μC) with respect to the energy gap of the electrolyte (E_g) and the resulting open circuit voltage (V_{OC}).[8]

The first primary battery was developed by Alessandro Volta in the beginning of the 19th century. It contained copper and zinc electrodes, a separator made out of cloth and an electrolyte: Volta's pile was born.[9] Even though this pile was far from being flawless, it laid the

groundwork for many more inventions related to electricity (*e.g.* water electrolysis) and was a major step towards the development of rechargeable batteries as we know them today.

I.1.1. The first rechargeable batteries

The major drawback of Volta's pile was that once discharged it could not be recharged. This setback was finally overcome by the French physicist Gaston Planté, who developed in the middle of the 19th century the lead-acid battery, the first ever rechargeable battery.[10] The electrochemical reaction between the Pb anode, the PbO_2 cathode and the H_2SO_4 electrolyte becomes reversible by passing a reverse current through the battery, thus recharging it. This low-cost system, even though it dates over 150 years, is still one of the most commercialized batteries nowadays and is used especially in the automobile industry and for stand-by applications.

Several decades after the commercialization of the lead-acid battery, the nickel-cadmium (NiCd) battery reached the market using a NiO(OH) cathode combined with a Cd anode. Compared to the lead-acid battery, the NiCd system displayed a higher energy density and was attractive especially for the portable electronics market owing to its power-rate. However, the use of cadmium raised toxicity concerns and it was soon after replaced by the nickel-metal-hydride (Ni-MH) battery, which was similar in functioning, but contained a hydrogen-absorbing alloy instead of cadmium as anode. This made the Ni-MH battery more environmentally benign and also significantly increased its volumetric energy (Figure I.2). However, the inevitable use of aqueous electrolytes limited the cell potential and the overall energy density of this system.

The quest for batteries with a high energy density soon directed the research focus towards the implementation of a lithium metal anode. Not only is lithium the most electropositive element in the periodic table (-3.04 V *vs*. SHE (Standard Hydrogen Electrode)), but it is also the lightest metal, which makes it an attractive candidate for portable electronics and electric vehicles. A brief overview of the various Li-based battery technologies is given in the next paragraphs.

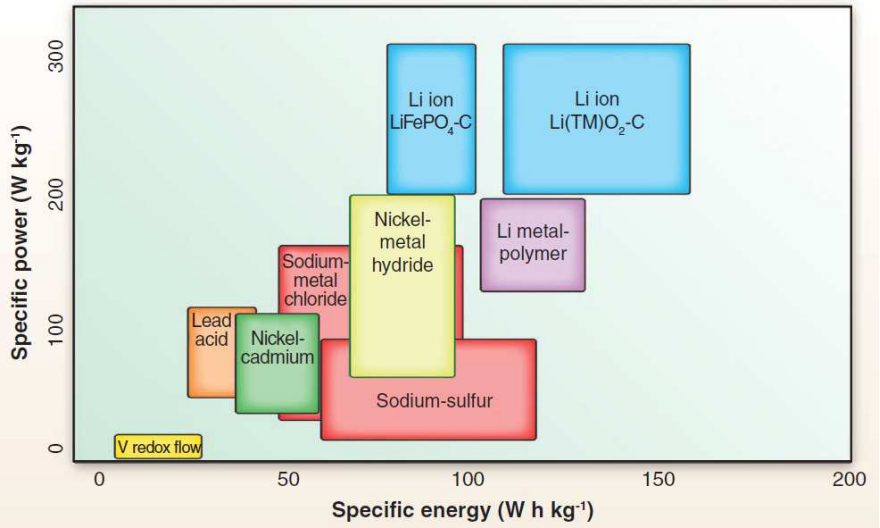

Figure I.2: Specific power *vs.* specific energy for different rechargeable battery technologies.[5]

I.1.2. Lithium-based batteries

The first important step towards a rechargeable Li-based battery was achieved with the discovery of TiS_2 as a reversible lithium intercalation material by Whittingham and co-workers (Exxon) in the 1970s.[11] In consequence, other chalcogenides were explored as potential cathode materials (e.g. $NbSe_3$) and finally, in the mid-1980s, Moli Energy commercialized the first Li-based battery using a MoS_2 cathode and a lithium metal anode. However, due to safety issues caused by lithium dendrites, this battery system had to be withdrawn from the market soon after. Nevertheless, thanks to the big advantages of this first Li-based battery in terms of energy density, huge research efforts have been undertaken ever since to further improve their safety and performances.

To avoid the use of lithium metal, the possibility of an insertion anode was investigated. First tests were performed with lithium alloys such as LiAl, but the large volume expansion of these materials upon lithium insertion made them rather unfavorable as anode materials.[3,4,12–14] Finally, graphite showed highly promising performances and was successfully implemented, which led to the concept of the Li-ion or also called “rocking-chair” battery as we know it today (Figure I.1a).[15–17] However, the use of graphite instead of lithium metal led to an overall decrease in energy density owing to the higher potential and lower capacity of graphite. To compensate for this loss, the focus turned towards oxide-based cathode materials such as MoO_3, V_2O_5 and $LiCoO_2$, which showed increased redox potentials as compared to

chalcogenides.[3,4] Especially $LiCoO_2$ introduced by Goodenough *et al.* brought the big breakthrough. In 1991, Sony commercialized the first Li-ion battery (Figure I.3a), which uses a carbon anode and a $LiCoO_2$ cathode resulting in an overall working potential of 3.6 V *vs*. Li^+/Li^0 and energy densities up to 150 $Wh \cdot kg^{-1}$.[18,19] This system is still, 25 years later, the mostly applied Li-ion battery and can be found in many of our portable electronic devices.

Another approach to circumvent the safety issues raised by the use of a lithium metal anode is to change the electrolyte in order to prevent dendrite formation. Therefore, common organic liquid electrolytes were replaced by dry polymer electrolytes, which consist of a solid solution of a lithium salt in polyethylene oxide. This system, developed by Armand and co-workers, is also known as lithium metal polymer batteries.[20,21] Another solution were hybrid polymer electrolytes (HPE), which used a solid polymer and additionally a liquid solvent.[4,22] However, while the lithium metal polymer batteries functioned only at temperatures around 80 °C, the HPE batteries presented difficulties in the synthesis procedure and dendrite formation. Nevertheless, Bellcore successfully developed a plastified polymer electrolyte that was easy to synthesize and that showed attractive ionic conductivity even at room temperature.[23] This finding enabled the commercialization of the plastic Li-ion (PLiON) battery in 2000, with a $LiMn_2O_4$ cathode and a graphite anode (no metal anode used) (Figure I.3b).[23] The PLiON battery exhibits excellent cycling performances and safety features as well as a large shape flexibility making it attractive for a variety of applications.

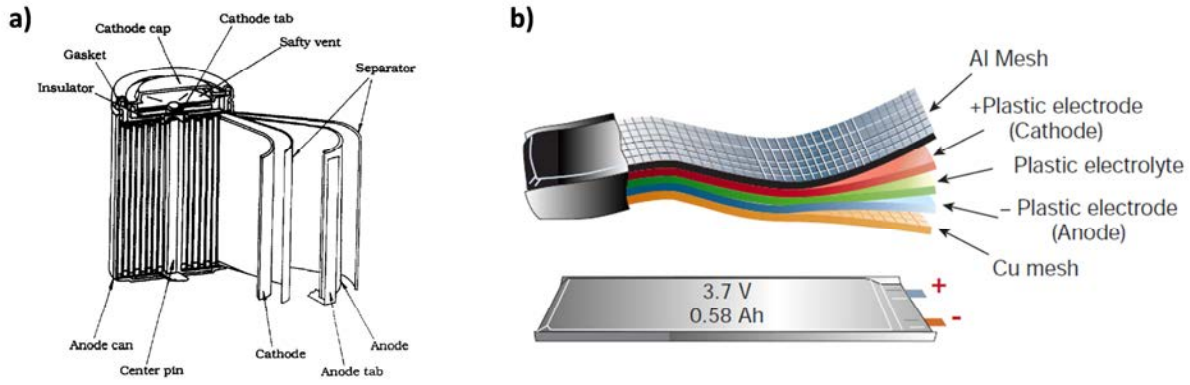

Figure I.3: a) Cell construction of the original lithium-ion rechargeable battery commercialized by Sony in 1991. $LiCoO_2$ and carbon were used as cathode material and anode material, respectively.[18] b) Construction principle of PLiON cell.[4]

I.2. Cathode Materials for Li-ion batteries

Since the emergence of the Li-ion technology, the scientific community has tried to identify innovative cathode materials that present attractive properties especially in terms of high capacity and voltage. Further they should display high electronic and ionic conductivity as well as chemical stability towards the electrolyte and structural stability towards lithium insertion/extraction (Figure I.4a). The amount of required features drastically limits the number of potentially interesting cathode materials. The main groups of cathode compounds that have been explored in the last few decades are layered oxides ($LiMO_2$), spinel-type phases ($LiMn_2O_4$) and polyanionic materials mostly known through olivine $LiFePO_4$ (Figure I.4b). The next paragraphs will give an overview of the various cathode materials pointing out their main properties, advantages and drawbacks.

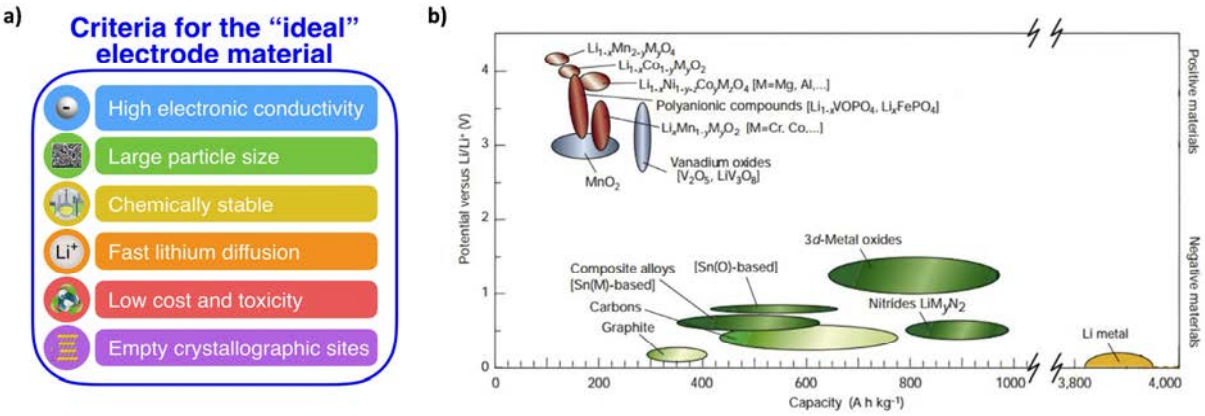

Figure I.4: a) Criteria for a cathode material. b) Voltage vs. capacity of different cathode and anode materials.[4]

I.2.1. Layered oxide materials

Soon after Whittingham *et al.* demonstrated with TiS_2 the feasibility of intercalation electrodes, other layered insertion materials were explored. The focus shifted quickly from sulfides to oxides, which present higher working potentials owing to the increased electronegativity of oxygen as compared to sulfur. In 1980, Goodenough *et al.* successfully introduced $LiCoO_2$ as an intercalation compound for lithium-based batteries.[24,25] $LiCoO_2$ crystallizes in the *R*-3*m* space group adopting a layered structure isostructural to α-$NaFeO_2$ (Figure I.5a).[24–28] It is built out of a cubic close-packed oxygen array with alternate lithium and cobalt planes. Its attractive electrochemical properties such as a high operating voltage between 3.5 and 4.2 V *vs*. Li^+/Li^0 and low polarization (Figure I.5b) led to the commercialization by Sony in 1991.[18,25,29] The setback of

this compound is however that for $Li_{0.5}CoO_2$ (> 4.2 V *vs*. Li^+/Li^0), the hexagonal structure experiences a distortion into a monoclinic structure with gliding of CoO_2 planes.[29–31] These severe structural changes result in a drastic increase of polarization and a large irreversible capacity upon discharge, which limit the useful capacity of $LiCoO_2$-based batteries to 150 $mAh \cdot g^{-1}$ (theoretical capacity: 275 $mAh \cdot g^{-1}$). That in addition to the high cost of cobalt was an impetus for researchers to look for alternative layered oxides as potential cathode materials.

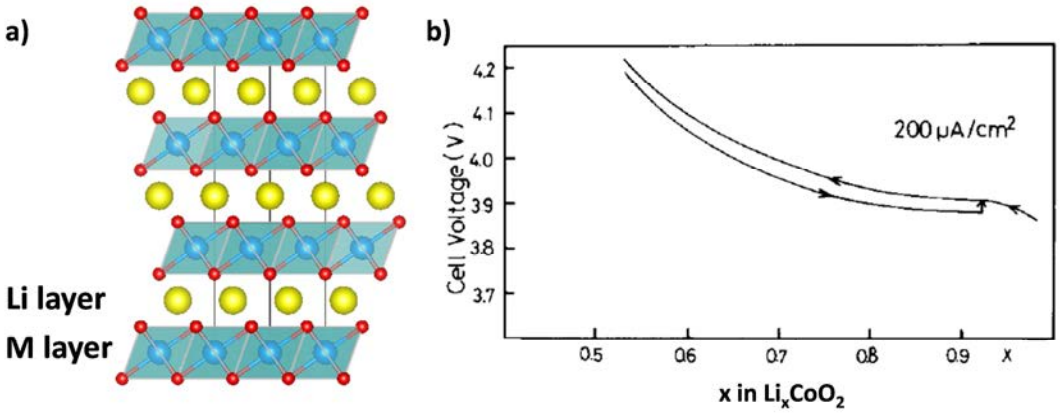

Figure I.5: a) Structure of LiMO_2 (*M* = Ni, Co, Mn) based on layers of MO_6 octahedra (blue) with oxygen atoms shown in red. Lithium located between the layers is illustrated as yellow balls. b) Voltage-composition trace of $LiCoO_2$ at a current of 200 µA/cm^2.[25,32]

The interest shifted towards $LiNiO_2$ being isostructural to $LiCoO_2$. This compound not only presents an advantage in terms of cost and availability of the transition metal, but also its electrochemical properties were rather promising with a reversible capacity of more than 150 $mAh \cdot g^{-1}$ at a potential above 3.5 V *vs*. Li^+/Li^0 and a long cycling life.[33–36] However, commercialization of this compound was never realized due to difficulties in the synthesis, thermal instability as well as nickel and lithium displacements in the structure upon cycling, which hampered the full electrochemical exploitation.[37,38] Furthermore, it was shown that the low stability of the delithiated phase might induce thermal runaway reactions when combined with organic electrolytes.[32,39]

At the same time, also $LiMnO_2$ was studied owing to its beneficial properties in terms of cost and toxicity. Even though layered $LiMnO_2$ has been synthesized, it turned out to be structurally and electrochemically unstable and it preferably crystallized in an orthorhombic unit cell (*Pmnm*) different from the α-$NaFeO_2$ structure of $LiCoO_2$ and $LiNiO_2$.[39–41] Electrochemical tests

on $LiMnO_2$ revealed that at higher voltages it irreversibly transformed into the spinel $LiMn_2O_4$, which is discussed in more detail in the next paragraph.[39,42–44]

To circumvent the capacity loss caused by structural instabilities in the above-described layered oxides, partial substitutions of the transition metal were performed, where either electrochemically inactive cations (e.g. Al, Ga, Mg) or other transition metals such as Ni, Co and Mn were inserted into the structure.[45–52] These substitutions were supposed to improve the cycling stability by avoiding structural transformations and atom displacements. The most promising and best studied of the so obtained materials is certainly $LiNi_{1/3}Mn_{1/3}Co_{1/3}O_2$, better known under the abbreviation NMC.[53–55] This material attracted a lot of attention owing to its reversible capacity of up to 200 $mAh{\cdot}g^{-1}$ when charged up to 4.6 V *vs*. Li^+/Li^0.[32,56] The Co- and Ni-content in these compounds helps to increase the structural stability.

In order to further improve the performance of layered oxide cathode materials, two research directions were pursued: 1) Layered oxide particles with a concentration gradient, which increases their chemical and electrochemical stability.[32,57] 2) Li-rich layered oxides based on the $LiMO_2$ framework, where M^+ is partially substituted by Li^+ in the transition metal layer (Figure I.6a) leading to the general composition $Li[Li_x^+M_{1-3x}^{3+}M_x^{4+}]O_2$.[32]

One of the most studied Li-rich layered oxides is $Li[Li_{1/3}Mn_{2/3}]O_2$ or alternatively written Li_2MnO_3.[32] Li_2MnO_3 however is electrochemically inert since Mn is in the oxidation state +IV and can neither be oxidized nor reduced since all the octahedral sites, in which lithium is located, are occupied. Nevertheless, Li_2MnO_3 can be activated either chemically by an acid leaching step, during which Li_2O is extracted from Li_2MnO_3, or at elevated voltages (> 4.4 V *vs*. Li^+/Li^0) so as to use the anionic redox activity of the O^{2-} in the structural framework.[40] Further research on these Li-rich layered oxides led to a variety of new materials, where Li-rich NMC ($Li[Li_xNi_yCo_zMn_{1-x-y-z}]O_2$) is certainly the most famous one presenting superior electrochemical features (capacities more than 250 $mAh{\cdot}g^{-1}$).[28,32,40,58,59] The extra capacity of these compounds was later shown to stem from the contribution of a reversible anionic redox processes ($O^{2-} \rightarrow O_2^{n-}$ with 3>n>1) in addition to the cationic redox.[60–64] Nevertheless, there are still some major performance issues such as the voltage decay upon cycling (Figure I.6b).[32,59,65,66] Thorough studies on the model compound $Li_2Ru_{1-x}M_xO_3$ (M = Sn, Ti) revealed that the voltage decay is related to cation

migrations and metal trapping.[32,67] These results mark an important step towards the improvement of the performance and commercialization of Li-rich NMC materials.

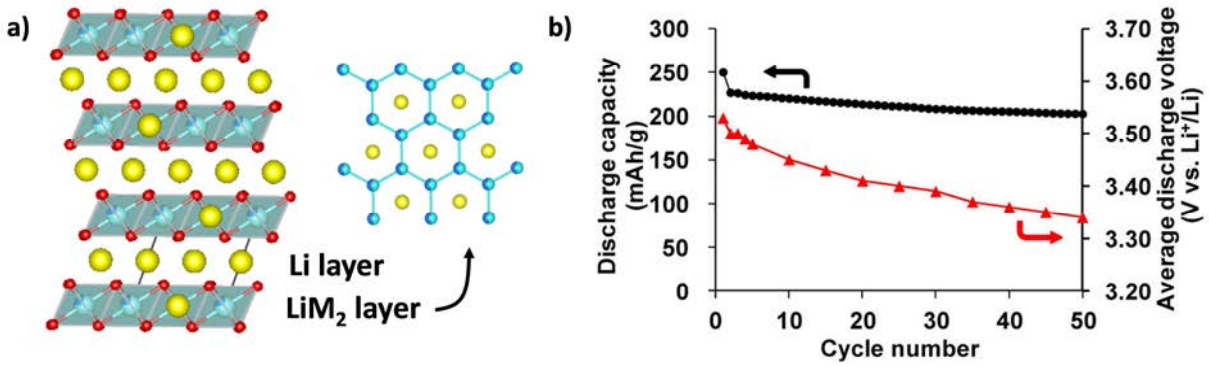

Figure I.6: a) Crystal structure of a Li-rich layered oxide Li_2MO_3 (*M* = Ni, Co, Mn) showing the Li-layer and the transition metal (LiM_2) layer. The lithium atoms (yellow balls) in excess are located in the LiM_2 layer.[32] b) Evolution of the average discharge voltage (red) and discharge capacity (black) vs. the cycle number in a $Li//Li_{1.20}Mn_{0.54}Co_{0.13}Ni_{0.13}O_2$.[65]

The extensive research on layered oxides was not only limited to Li-based materials, but was soon after extended to materials appropriate for Na-ion batteries (NIB). In terms of abundancy of Na and cost efficiency, NIBs seem preferable towards Li-based batteries. However, one large drawback of NIBs is the lower energy density caused by the lower redox potential of Na^+/Na^0 *vs.* SHE (-2.71 V *vs.* -3.04 V *vs.* NHE for the Li^+/Li^0 redox couple). Nevertheless, for grid scale applications, Na-based batteries could be the technology of choice and researchers focus on improving their performances. Among the studied compounds are Na_xMO_2 ($0.6 < x < 1.0$)with *M* = Mn, Fe, Co, Ni as well as binary and ternary layered oxides ($NaM'M''O_2$ and $NaM'M''M'''O_2$), which have been first introduced in the early 1980s and which experience a strong comeback nowadays.[68–72] Promising performances were observed for $NaFe_{0.5}Mn_{0.5}O_2$ and the Na-rich layered oxide $Na_{0.95}Li_{0.15}(Ni_{0.15}Mn_{0.55}Co_{0.1})O_2$.[73,74] The latter, which is prepared by electrochemical insertion of sodium into the Li-rich analogue structure, displays a reversible capacity of 200 $mAh{\cdot}g^{-1}$ when cycled against Na solely.[70,75]

I.2.2. Spinel structures ($LiMn_2O_4$ and $LiNi_{0.5}Mn_{1.5}O_4$)

In parallel to the exploration of layered oxides, research efforts were undertaken on the manganese-oxide based spinel $LiMn_2O_4$.[76] The spinel-type structure consists of a cubic close-packed oxygen framework in the *Fd*-3*m* space group with Li and Mn occupying tetrahedral and octahedral sites, respectively (Figure I.7a).[3,76–79] The $LiMn_2O_4$ spinel displays three plateaus in

total: in reduction at 3.0 V (formation of Mn^{3+}-containing tetragonal $Li_2Mn_2O_4$) and in oxidation at 3.9 V and 4.1 V *vs*. Li^+/Li^0 (formation of λ-MnO_2). The capacity can reach up to 130 mAh·g^{-1} in charge (Figure I.7b).[80,81]

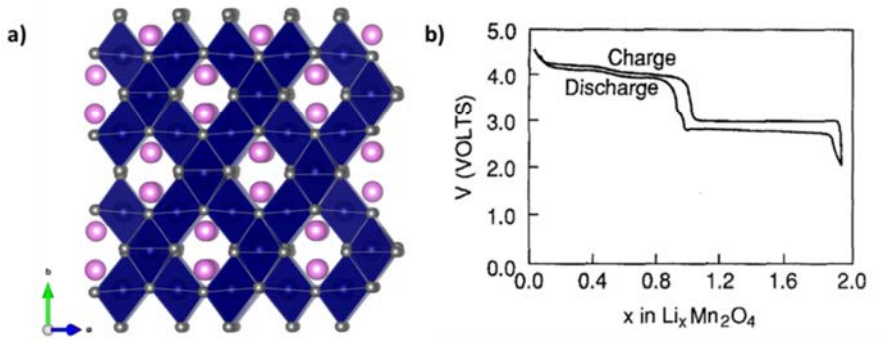

Figure I.7: a) Crystal structure of the $LiMn_2O_4$ spinel. The Mn-based polyhedra are shown in blue, lithium and oxygen are represented by pink and grey balls, respectively. b) Charge/discharge curve of the $LiMn_2O_4$ spinel.[79]

Despite the beneficial features in terms of low cost, safety and good rate capability of $LiMn_2O_4$, its commercialization was initially hampered due to its rapid capacity fading.[82] This phenomenon was ascribed to the Mn disproportionation/dissolution from the spinel structure provoked by HF formation from fluorine-based electrolytes.[65,82–84] The cycling performance was improved by two approaches: 1) Replacing the $LiPF_6$-based electrolyte by lithium bisoxalatoborate (LiBoB), which resulted in superior performance in terms of thermal stability and cycling stability.[82] 2) Synthesis of a non-stoichiometric spinel, where minute amounts of Mn on the octahedral sites were replaced by Li.[3,83,85] Moreover, partial substitutions with Al and F ($LiMn_{2-x}Al_xO_{4-y}F_y$) were explored with slight improvements of the overall performance.[82,86] Finally, the insertion of Ni into the spinel structure forming $LiNi_{0.5}Mn_{1.5}O_4$ led to an increased operating potential of 4.7 V *vs*. Li^+/Li^0.[87,88] This compound crystallizes in an ordered or disordered configuration depending on the synthesis conditions, where the latter exhibits a more stable cycling performance owing to its better ionic and electronic conductivity.[65] Nevertheless, the high working potential raises concerns in terms of the electrolyte stability and demands for further research on this system. Promising results have been obtained with the combination of $LiNi_{0.5}Mn_{1.5}O_4$ with superconcentrated electrolytes.[89]

I.2.3. Polyanionic cathode materials

Even though oxide-based materials, either in form of layered oxides or spinels, experienced a huge commercial success, the difficulties they are facing in terms of capacity fading, toxicity, sustainability and safety, urged battery scientists to continue their quest for other possible cathode compounds. In this context, the discovery of olivine $LiFePO_4$ as a positive electrode material in the late 1990s by Padhi *et al*.[90] opened up the research path for polyanionic compounds that have been widely explored ever since. Polyanionic materials obtain their name from the $(XO_4)^{n-}$ polyanionic group. Even though the polyanion adds to the weight of the active material and therefore decreases the theoretical capacity as compared to oxide-based compounds, the attractiveness of these materials stems from: 1) large variety of possible crystal structures depending on the combination of cations and anions, 2) structural and thermal stability as well as stability towards the electrolyte thus increased safety and 3) possibility to tune the potential of the redox couple with respect to the Fermi level of lithium by changing the polyanionic group (Figure I.8a).[65,91] This effect has been introduced by Goodenough *et al.* as the so-called inductive effect.[92] By implementing strong electronegative polyanions such as sulfates for instance, the ionicity of the oxygen-metal bond increases, which leads to a decrease of the σ* orbital with respect to the Fermi level of the Li redox couple (Figure I.8b). In consequence, the redox potential is augmented.

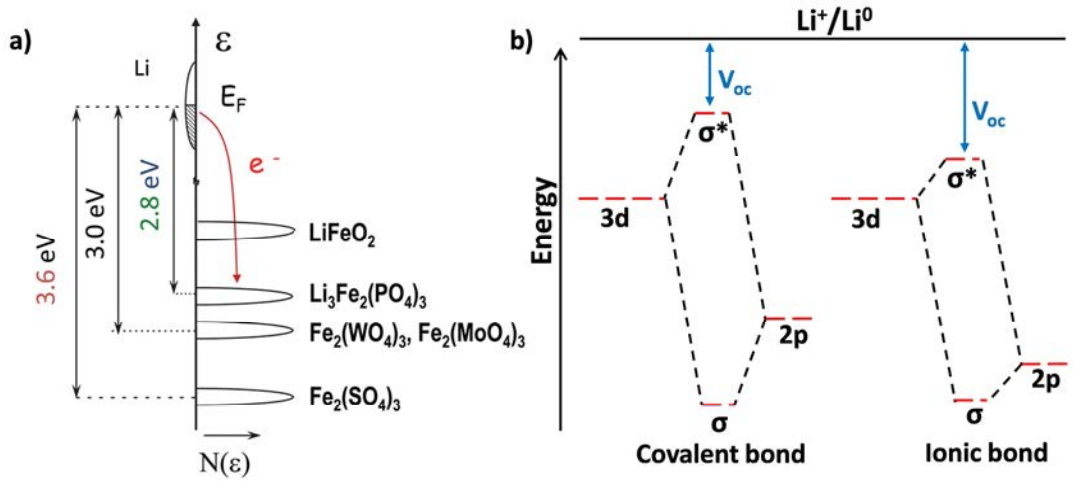

Figure I.8: a) Potential of the Fe^{3+}/Fe^{2+} redox couple vs. Li^+/Li^0 in $LiFeO_2$ and in different Nasicon-type structures $Li_yFe_2(XO_4)_3$ (X = P, Mo, W, S) illustrating the inductive effect.[91] b) Energy diagram of a covalent bond and an ionic bond and their respective potential V against lithium. The ionic bond results in a higher open circuit voltage (V_{OC}).

One of the first studied polyanion-based materials is the Nasicon-type structure $A_yMM'(XO_4)_3$ (e.g. $Fe_2(MoO_4)_3$, $Fe_2(WO_4)_3$ and $Fe_2(SO_4)_3$).[93–96] The Nasicon structure crystallizes in a rhombohedral unit cell and consist of MO_6 octahedra interconnected through XO_4 tetrahedra by the oxygen vertices forming the so-called lantern units (Figure I.9a). The large interstitial space makes these materials attractive compounds for intercalation reactions in Li-/Na-based batteries. $Li_yMM'(XO_4)_3$ can also adopt an anti-Nasicon configuration, which is however less favorable as an intercalation compound due to a denser structure (Figure I.9a).[91] The electrochemical performances of $Fe_2(SO_4)_3$ in its Nasicon and anti-Nasicon structure are illustrated in Figure I.9b) and c), where both exhibit the same potential (3.6 V *vs.* Li^+/Li^0) with a however higher capacity for the Nasicon structure. The above-described findings laid the groundwork for an intensive research on the field of polyanionic compounds, which led to the discovery of many new interesting cathode materials described in detail in the following paragraphs.

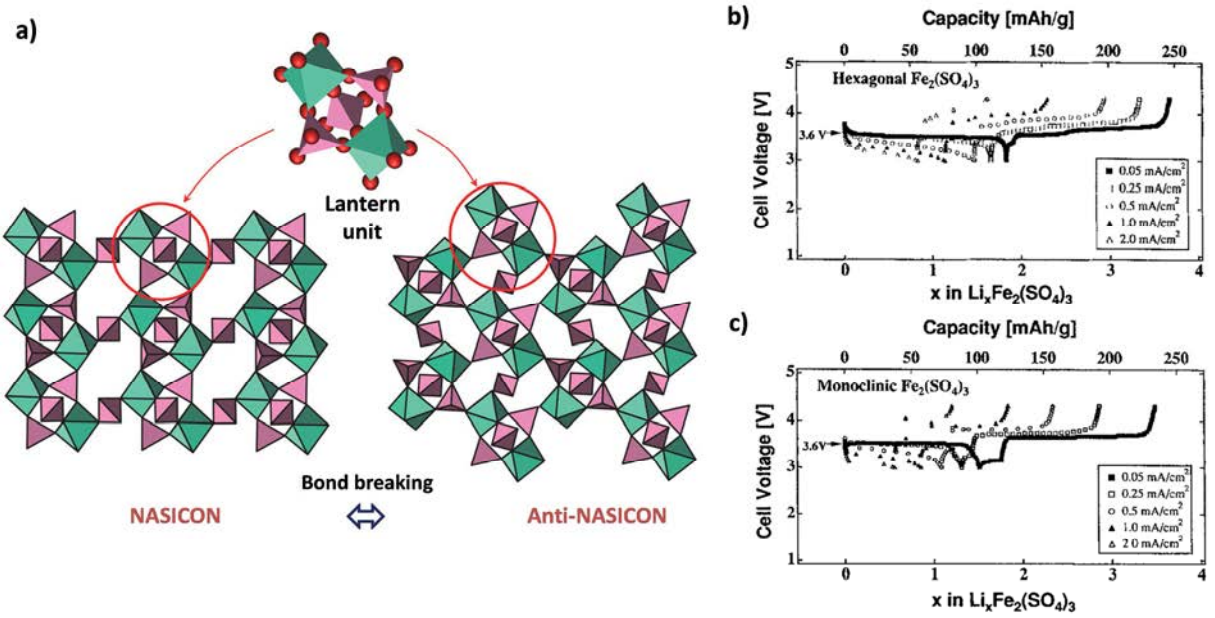

Figure I.9: a) Structure of Nasicon and anti-Nasicon built out of lantern units. MO_6 octahedra and SO_4 tetrahedra are shown in green and pink, respectively. Oxygen atoms are represented as red balls.[88] b) NASICON $Fe_2(SO_4)_3$ (rhombohedral or also hexagonal) and c) anti-Nasicon $Fe_2(SO_4)_3$ (monoclinic) exhibit both a potential of 3.6 V *vs.* Li^+/Li^0, however, the hexagonal structure (b) reveals a higher capacity than the monoclinic form (c).[91]

I.2.3.1. Phospho-olivines *AM*PO_4 (*A* = Li, Na; *M* = Fe, Mn, Co, Ni)

The unbeaten stellar in the sector of polyanionic cathode materials is still olivine $LiFePO_4$ (in the following referred to as LFP) first reported by Padhi *et al.*[90] Owing to its benefits in terms of

sustainability and cost-effectiveness as well as its appealing electrochemical performance with a potential of 3.45 V *vs.* Li^+/Li^0 (Figure I.10a) and a theoretical capacity of 170 $mAh \cdot g^{-1}$ (theoretical energy density of 580 $Wh \cdot kg^{-1}$), LFP is nowadays used as cathode materials for electric vehicles. This compound crystallizes in the orthorhombic *Pnma* space group with FeO_6 octahedra connected via their oxygen vertices forming zigzag chains along the *c*-axis. Further the octahedra share one edge and four corners with PO_4 tetrahedra (Figure I.10b). The so formed voids are occupied by lithium cations, which can diffuse along [010].[91,97]

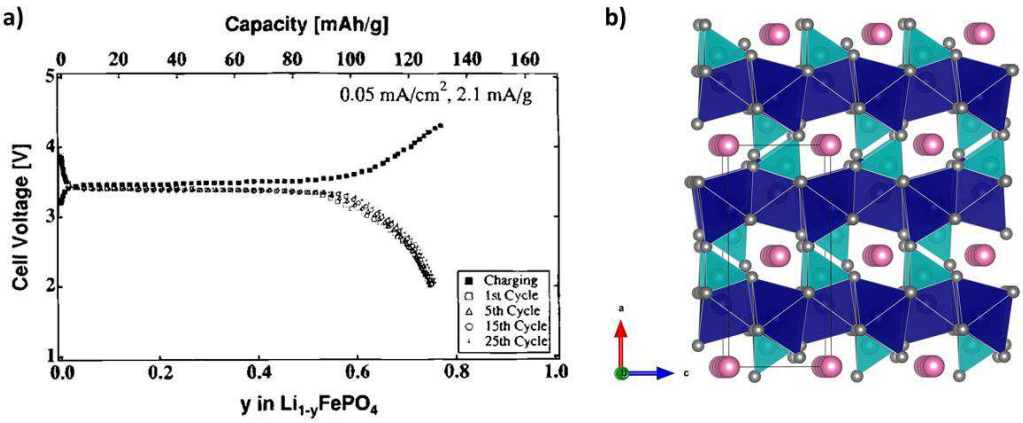

Figure I.10: a) Charge-discharge curve of olivine $LiFePO_4$ displaying a potential of ~3.45 V *vs.* Li^+/Li^0.[87] b) Crystal structure of $LiFePO_4$ illustrated along the b-axis based on FeO_6 octahedra and PO_4 tetrahedra, shown in blue and turquois, respectively. Lithium atoms are represented as pink balls, while oxygen atoms are grey.

Nevertheless, olivine LFP presents a poor intrinsic electronic and ionic conductivity urging researchers to optimize this material. One approach was to add a thin carbon coating, which was obtained either from a mixture of as-prepared LFP with a carbon precursor or directly during the synthesis procedure from carbon-containing additives.[91,97,98] Besides the coating, which plays on the electronic conductivity, it was also shown by numerous studies that the particle size has a significant influence on the electrochemical performance of LFP. Especially nano-sized particles display a higher capacity and better rate capability related to the reduced diffusion length of lithium.[99–101] An overview of the vast synthetic possibilities for LFP with different sizes and coatings (including glass-coatings) is given in Ref. 102 and Ref. 103.[102,103]

The structural analogue $LiMnPO_4$, which displays an elevated potential (4.12 V *vs.* Li^+/Li^0), was less aggressively developed due to low electrical conductivity and large structural distortions upon oxidation caused by the Jahn-Teller effect.[102] $LiCoPO_4$ and $LiNiPO_4$ being isostructural to $LiFePO_4$ exhibit redox potentials (4.8 V and 5.1 V *vs.* Li^+/Li^0, respectively) that surpass the

stability window of commonly used electrolytes. Furthermore, stability issues of delithiated $Li_{1-x}CoPO_4$ stopped their exploration at an early stage.[65,91,102,104]

Meanwhile, the Na-based olivine analogue was also studied for potential applications in Na-ion batteries. As the direct synthesis of $NaFePO_4$ was difficult due to the formation of the thermodynamically favored maricite polymorph, olivine $NaFePO_4$ was obtained by cation exchange from $LiFePO_4$.[105] The electrochemical curve shows two plateaus in oxidation at 2.8 V and 3.02 V *vs.* Na^+/Na^0 related to the formation of a distinct $Na_{0.7}FePO_4$ phase.[105,106] The capacity, however, decreases rapidly after only a few cycles, but can be significantly improved by carbon-coating for instance.[106,107]

I.2.3.2. Pyrophosphates $Li_2MP_2O_7$ (*M* = Mn, Fe, Co)

Another family of phosphate-based polyanionic compounds are pyrophosphates $Li_2MP_2O_7$ with *M* = Mn, Fe, Co. $Li_2FeP_2O_7$, described in the monoclinic space group $P2_1/c$, exhibits a complex structure with three distinct iron sites, where Fe1 is octahedrally coordinated (FeO_6) and Fe2 and Fe3, which present a Li/Fe site mixing,[108,109] form the center of distorted FeO_5 pyramids (Figure I.11a).[108] The Fe-based polyhedra are further interconnected via P_2O_7 units. The electrochemical plateau of $Li_2FeP_2O_7$ occurs at 3.5 V *vs.* Li^+/Li^0 (Figure I.11b), which is slightly above the 3.45 V *vs.* Li^+/Li^0 observed for $LiFePO_4$.[108] The rather weak rate capability (inset Figure I.11b) and low capacity retention of $Li_2FeP_2O_7$ can be further improved by carbon coatings and particle down-sizing.[109,110] Note that after the initial charge, $Li_2FeP_2O_7$ shows a minor voltage drop ascribed to irreversible structural rearrangements that might be related to the structural disorder.[110] However, partial substitution of Fe by Mn to form the solid-solution $Li_2(Fe_{1-x}Mn_x)P_2O_7$ prevented the voltage drop and further resulted in an increased Fe^{3+}/Fe^{2+} redox potential up to 3.9 V *vs.* Li^+/Li^0 for x = 0.5.[111,112] Nevertheless, the insertion of Mn into the structure led to a significant reduction of the capacity (~50 $mAh{\cdot}g^{-1}$ for $Li_2(Mn_{0.5}Fe_{0.5})P_2O_7$).

Isostructural $Li_2MnP_2O_7$ and $Li_2CoP_2O_7$ display electrochemical plateaus at an average voltage of 4.1 V *vs.* Li^+/Li^0 and 4.9 V *vs.* Li^+/Li^0, respectively, but low capacity and stability issues of the electrolyte slowed down their further exploration.[113–115]

Padhi *et al.* also reported on a different pyrophosphate with the composition $LiFeP_2O_7$.[116] The structure differs strongly from the one of $Li_2FeP_2O_7$ and consists of FeO_6 octahedra bridged by

diphosphate groups crystallizing in the monoclinic unit cell $P2_1$. On discharge, 0.5 Li^+ could be intercalated at a potential of 2.9 V *vs.* Li^+/Li^0, which is well below the redox potential of $LiFePO_4$. This can be related to differences in the structural arrangement and bonding.[116]

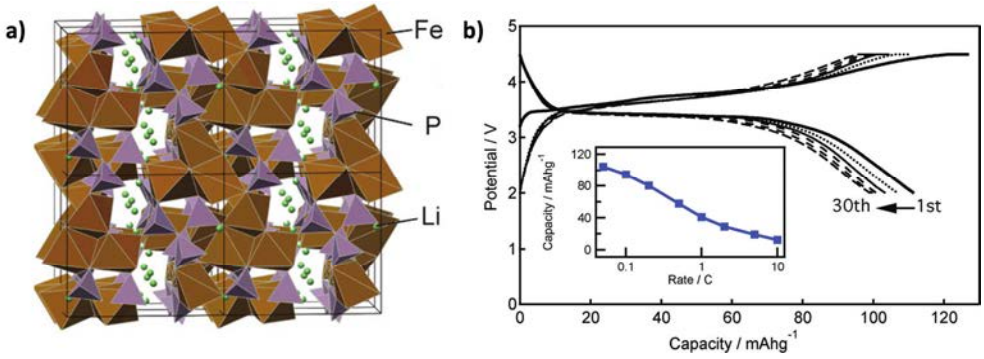

Figure I.11: The structure of $Li_2FeP_2O_7$ (a) is based on FeO_6 octahedra and distorted FeO_5 pyramids, both shown as brown polyhedra. The Fe-based polyhedra are connected by PO_4 tetrahedra (purple). Lithium atoms are represented as green balls. $Li_2FeP_2O_7$ displays a electrochemical potential of 3.5 V *vs.* Li^+/Li^0 (b). The rate capability is shown in the inset of Figure b).[106]

I.2.3.3. Hydroxy- and Fluorophosphates

Even though $LiFePO_4$ shows attractive electrochemical performance, its potential of 3.45 V *vs.* Li^+/Li^0 stands back compared to oxide-based materials for instance. Therefore, staying in the logic of the inductive effect, researchers tried to further increase the redox potential of the transition metal while avoiding the weight penalty. This was an impetus to explore compounds such as fluoro- and hyrdoxyphosphates, where the inductive effect of the PO_4^{3-} polyanion is enforced by the electronegativity of the relatively light fluorine atom and hydroxyl group. $LiFePO_4OH$ is a natural mineral occurring in the tavorite form. It is described in the triclinic space group *P*-1 and forms a three-dimensional framework with chains of corner-sharing FeO_6 octahedra running along the *b*-axis (Figure I.12a).[117] These chains are interconnected by PO_4 tetrahedra. Figure I.12b shows in detail the connectivity of the H-atom to oxygen.

The electrochemical response of $LiFePO_4OH$ is observed at an average potential of 2.6 V *vs.* Li^+/Li^0 and a reversible capacity of ~90 mAh·g^{-1} (Figure I.13a),[117] while isostructural $LiFePO_4F$ displays a redox potential close to 3 V *vs.* Li^+/Li^0 with a reversible capacity close to 150 mAh·g^{-1} (Figure I.13b).[118] Note that in coherence with the inductive effect, $LiFePO_4F$ exhibits a higher working potential than $LiFePO_4OH$ owing to the higher electronegativity of F^- in comparison to OH^-. To the same family of tavorite phosphates belongs also $LiVPO_4F$, which exhibits potentials

of 1.8 V *vs.* Li^+/Li^0 and 4.2 V *vs.* Li^+/Li^0 for the V^{2+}/V^{3+} and V^{3+}/V^{4+} redox couple, respectively (Figure I.13c).[91,119–121]

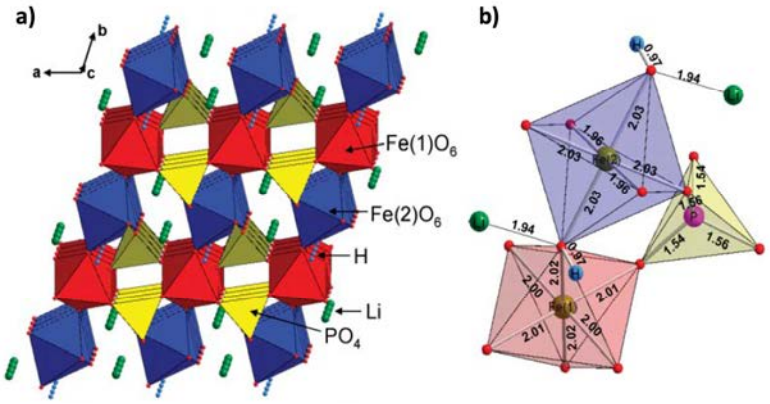

Figure I.12: a) Crystal structure of $LiFePO_4OH$ showing the PO_4 tetrahedra in yellow, and the two distinct FeO_6 octahedra in red and blue. Lithium atoms are illustrated as green balls. The hydrogen atoms (blue spheres) are linked to the axial oxygen atoms (red spheres) (b).[114] $LiFePO_4F$ and $LiVPO_4F$ are isostructural to $LiFePO_4OH$ structure.

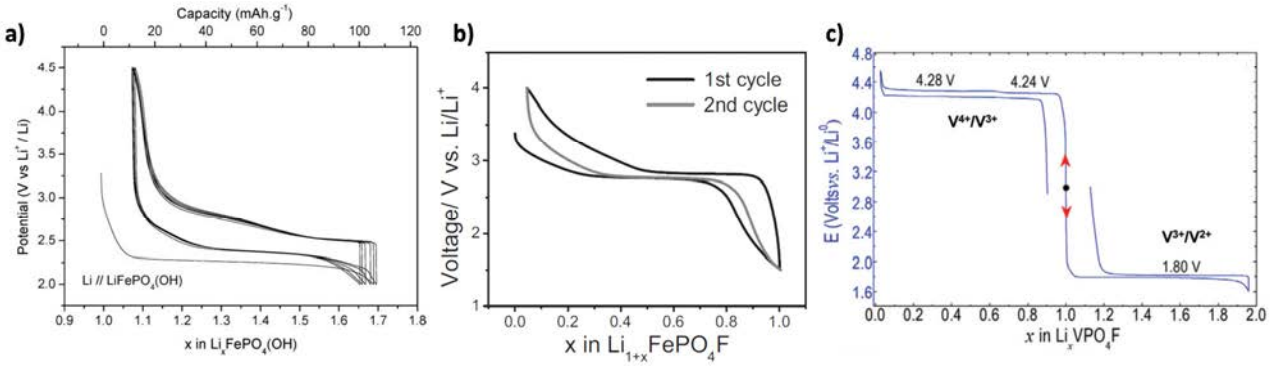

Figure I.13: Voltage-composition curves of a) $LiFePO_4OH$[114], b) $LiFePO_4F$[115] and c) $LiVPO_4F$[122]. The observed potentials of the respective compounds are at a) 2.6 V *vs.* Li^+/Li^0, b) 3 V *vs.* Li^+/Li^0 and c) 1.8 V *vs.* Li^+/Li^0 on discharge and ~4.25 V *vs.* Li^+/Li^0 on charge.

Fluorophosphates have been also exhaustively studied as cathode materials for Na-ion batteries, where especially $Na_3V_2(PO_4)_2F_3$ (NVPF) displayed highly interesting electrochemical properties with two main voltage plateaus at 3.7 and 4.2 V *vs.* Na^+/Na^0 and a reversible capacity of 110 $mAh{\cdot}g^{-1}$ (Figure I.14a).[69,123–125] More recently, a new fluorophosphate "$Na_{3+x}V_2(PO_4)_2F_3$" was reported synthesized by a ball-milling NVPF with metallic Na or Na_3P (Figure I.14b).[126,127] For x=0.5, the electrochemical performance displayed a more stable capacity retention than NVPF owing to the additional Na, which serves for the SEI formation (Figure I.14).

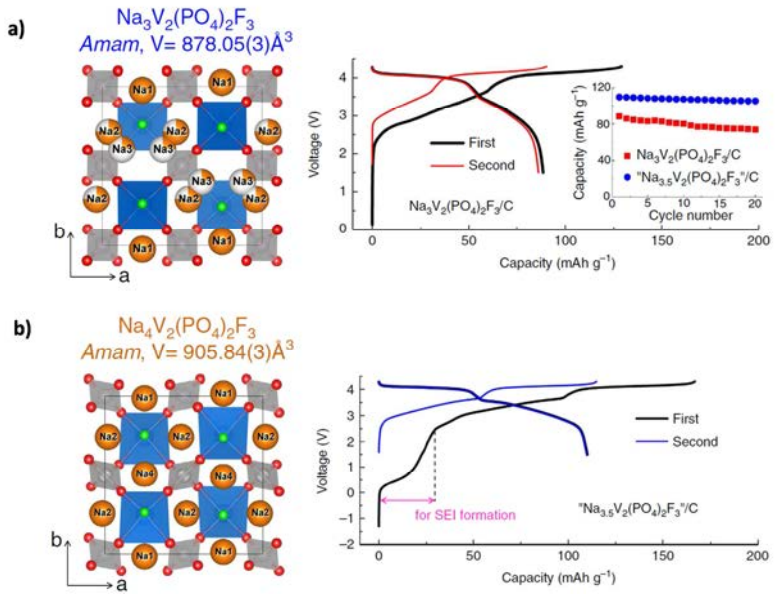

Figure I.14: Structure and electrochemical curve of two compounds of the NVPF family. The comparison of the capacity retention between the two compounds is shown in the inset in Figure a).[126]

I.2.3.4. Silicates Li_2MSiO_4 (*M* = Mn, Fe, Co)

Despite the beneficial properties of polyanionic materials in terms of sustainability and safety, their major setback is the lower gravimetric capacity inherent to the relatively heavy polyanions. One approach to overcome this shortcoming was to search for materials that allow the exchange of two electrons per transition metal. In this context, Li_2FeSiO_4, which is also lighter than pyrophosphates for instance, was vastly explored as a possible cathode material.[91] The structural resolution of this compound turned out to be rather complex since Li_2FeSiO_4 crystallizes in various polymorphic configurations depending on the synthesis conditions (Figure I.15).[128–131] The Li_2FeSiO_4 polymorphs are all derived from the β- and γ-Li_3PO_4 structures and are built out of FeO_4 and SiO_4 tetrahedra that differ only in their connectivity (Figure I.15).

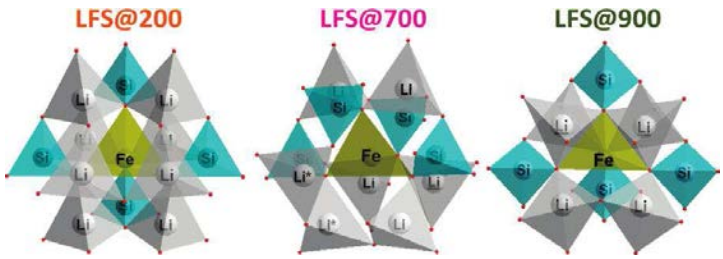

Figure I.15: Local structure in the *Pmn*2_1, *P*2_1/*n* and *Pmnb* Li_2FeSiO_4 polymorphs, synthesized at 200 °C, 700 °C and 900 °c respectively. The Fe-, Si- and Li-based polyhedra are shown in green, blue and grey.[128]

The electrochemical performance of Li_2FeSiO_4 is as complex as its polymorphism since it depends strongly on the synthesis conditions and the structure (Figure I.16a).[131,132] Moreover, the charge plateau at 3.1 V *vs.* Li^+/Li^0 observed in the first charge shifts to 2.8 V *vs.* Li^+/Li^0 in the subsequent cycles (Figure I.16b), which is attributed to irreversible structural rearrangements during cycling.[65,130,131,133] The extraction of the second lithium, which is achieved only at potentials around 4.9 V *vs.* Li^+/Li^0, is irreversible and leads to structural decomposition.[91,134] Furthermore, similar as for $LiFePO_4$, Li_2FeSiO_4 exhibits a low electronic conductivity, which was addressed through carbon coating and nano-sizing. However, this led only to marginal improvements of the electrochemical performance.[65,134]

Li_2MSiO_4 with *M* = Mn and Co were shown to present the same polymorphic configurations as Li_2FeSiO_4, but with limited electrochemical activities. Li_2MnSiO_4 exhibits a potential of 3.7 V *vs.* Li^+/Li^0 and a capacity of up to 200 $mAh \cdot g^{-1}$ in the first cycle. The high capacity is however rapidly fading after only a few cycles due to structural instabilities.[128,135,136]

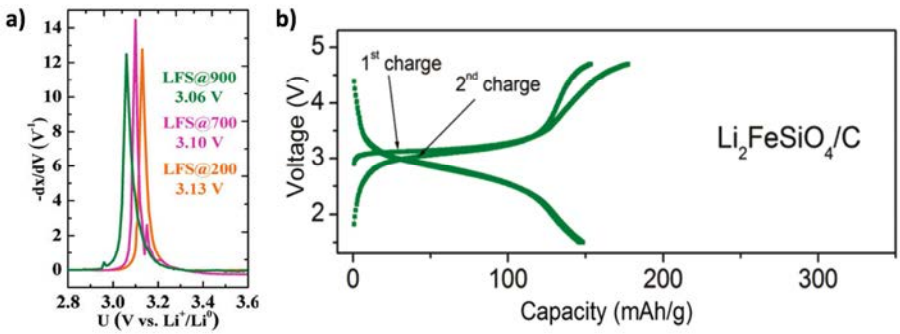

Figure I.16: a) Derivative curve of the potential of the first charge for the three polymorphs of Li_2FeSiO_4 shown in Figure 15.[128] b) First and second electrochemical cycles of nanocomposite Li_2FeSiO_4 showing the voltage drop in charge after the first cycle.[131]

I.2.3.5. Borates Li*M*BO_3

Another approach to overcome the low gravimetric energy density of polyanionic materials is to insert polyanions with a low molecular weight such as borates BO_3^{3-} (M_W =59 $g \cdot mol^{-1}$ *vs.* 95 $g \cdot mol^{-1}$ for PO_4^{3-} for instance). Li*M*BO_3 with *M* = Co, Fe, Mn crystallizes in the monoclinic *C*2/*c* space group (Figure I.17a), while $LiMnBO_3$ can be also stabilized in a hexagonal unit cell (*P*-6) (Figure I.17b).[137] The former consists of M_2O_8 trigonal bipyramids connected via planar BO_3 groups, while the latter is constructed out of square pyramids.

The electrochemical response for the Fe-based compound occurs at 3.0 V *vs.* Li^+/Li^0 and while first electrochemical tests showed only limited reversible capacity, later studies revealed a reversible capacity of 190 $mAh \cdot g^{-1}$ corresponding to an energy density of 570 $Wh \cdot kg^{-1}$ (Figure I.17c)[138,139] coming close to the one of $LiFePO_4$ (580 $Wh \cdot kg^{-1}$). This significant improvement of the performance relies strongly on the preparation method of the electrode sample (avoiding air/moisture exposure) and on the particle size, where nanoparticles are preferential.[138,139]

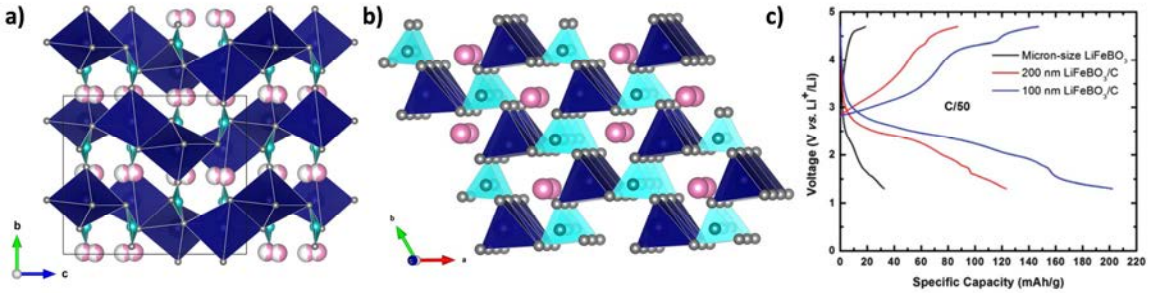

Figure I.17: Structures of monoclinic (a) and hexagonal (b) $LiMnBO_3$. The Mn- and B-based polyhedra are shown in blue and turquois, respectively. The Lithium atoms are represented as pink balls (half-coloured in the monoclinic structure). c) Electrochemical behaviour of $LiFeBO_3$ illustrating the dependence of the performance on the particle size.[138]

Mn-based Li*M*BO_3 displays an operating potential of 3.7 V *vs.* Li^+/Li^0 for the monoclinic structure and 4.1 V *vs.* Li^+/Li^0 for the hexagonal one.[91,140] Nevertheless, the high polarization caused by its low intrinsic conductivity renders this family of materials rather unattractive for practical applications. Further studies need to be conducted including the exploration of pyroborate ($B_2O_5^{4-}$)-based materials, which show an increased working potential.[141]

I.2.3.6. Sulfate-based polyanions

The motivation behind the investigation of sulfate-based compounds is to further increase the redox potential of the transition metal through a stronger inductive effect of SO_4^{2-} compared to PO_4^{3-}, while still maintaining the benefits of $LiFePO_4$.[142] The inductive effect can be further increased by the joint effect of the polyanion and the electronegativity of F^-, OH^- or O^{2-}, which led to the development of fluoro-, hydroxy- and oxysulfates.[142]

I.2.3.7. Sulfates

Inspired by minerals such as bloedite ($Na_2M(SO_4)_2.4H_2O$ (*M* = Mg, Zn)) and kröhnkite ($Na_2M(SO_4)_2.2H_2O$ (*M* = Cu, Cd, Mn)), Reynaud *et al.* investigated the family of $A_xM_y(SO_4)_z.nH_2O$ (*A* = alkaline, *M* = 3d transition metal, n > 0) phases, which led to the discovery of marinite $Li_2M(SO_4)_2$ (*M* = Mn, Co, Fe, Zn).[143–146] These phases, which are obtained via a classic solid-state synthesis approach, are described in the monoclinic $P2_1/c$ space group with isolated FeO_6 octahedra that share oxygen vertices with SO_4 tetrahedra (Figure I.18a). The electrochemical performance of the Fe-based phase, which is the only electrochemical active phase of this family, shows highly interesting performances with a working potential of 3.83 V *vs.* Li^+/Li^0, where almost an entire Li is extracted resulting in a capacity of around 100 $mAh{\cdot}g^{-1}$ (Figure I.18b). The sloping contribution at the beginning of the charge process, which was initially not understood, turned out to be caused by minor impurities of an amorphous secondary phase; namely the presence of an orthorhombic $Li_2Fe(SO_4)_2$ polymorph, which will be the topic of Chapter III.[147]

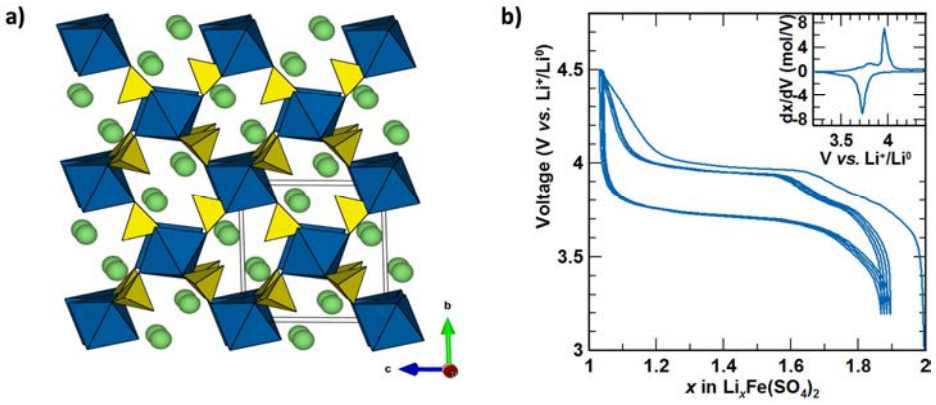

Figure I.18: a) Crystal structure of monoclinic $Li_2Fe(SO_4)_2$ displayed along the a-axis with the FeO_6 octahedra and SO_4 tetrahedra shown in blue and yellow, respectively. Lithium is represented by green balls. b) Voltage-composition trace of $Li_2Fe(SO_4)_2$ exhibiting a potential of 3.83 V *vs.* Li^+/Li^0. The inset shows the respective derivative curve.[143]

Monoclinic $Li_2Fe(SO_4)_2$ cycled in a sodium cell displays a potential of 3.40 V *vs.* Na^+/Na^0 with, however, a relatively large polarization.[143] The interesting properties towards Na inspired the exploration of other Na-based materials such as $Na_2Fe(SO_4)_2{\cdot}4H_2O$, $Na_2Fe(SO_4)_2{\cdot}2H_2O$ and anhydrous $Na_2Fe(SO_4)_2$ with potentials around 3.3 V *vs.* Na^+/Na^0, 3.25 V *vs.* Na^+/Na^0 and 3.4 V *vs.* Na^+/Na^0, respectively.[145,146] An advance on the field of sulfate-based cathode compounds for

Na-ion batteries was achieved with the discovery of the alluaudite-type material $Na_2Fe_2(SO_4)_3$ with an increased potential of 3.8 V *vs.* Na^+/Na^0.[148]

I.2.3.8. Hydroxy-, Oxy- and Fluorosulfates

With the aim to further increase the ionicity of the M-O bond, the influence of hydroxy-, oxy- and fluorosulfates moieties on the redox potential in polyanionic materials was investigated, which resulted in the successful preparation $LiFeSO_4OH$, $Fe_2O(SO_4)_2$ and $LiFeSO_4F$.

$LiFeSO_4OH$ can be stabilized in two different polymorphic configurations: layered $LiFeSO_4OH$, which is synthesized via high-energy ball-milling and displays an operating potential of 3.6 V *vs.* Li^+/Li^0 (Figure I.19a and b), and tavorite $LiFeSO_4OH$ stabilized by an electrochemical insertion of lithium into $FeSO_4OH$ at a potential of 3.2 V *vs.* Li^+/Li^0 (Figure I.19c and d).[149,150] The former crystallizes in the monoclinic $P2_1/c$ space group with edge-sharing $FeO_4(OH)_2$ octahedra forming zigzag-chains along the *b*-axis. These chains are interconnected via the oxygen vertices of the $FeO_4(OH)_2$ octahedra and further linked to SO_4 tetrahedra (Figure I.19a). The lithium atoms are located between the layers. The tavorite structure (space group: $P2_1/c$) forms a 3D-network out of corner-sharing $FeO_4(OH)_2$ octahedra and SO_4 tetrahedra leaving voids that are occupied by lithium (Figure I.19b).

Oxysulfates were introduced for the first time as promising cathode materials with $Fe_2O(SO_4)_2$ (Figure I.20a,b) and later with the Cu-based compound $Li_2Cu_2O(SO_4)_2$, which shows an increased redox potential of the Cu^{3+}/Cu^{2+} redox couple of 4.7 V *vs.* Li^+/Li^0 (Figure I.20c,d).[151,152] $Fe_2O(SO_4)_2$, on the other hand, exhibits a complex electrochemical behaviour, but is nevertheless interesting for pratical applications owing to its stability towards moisture.[151,153]

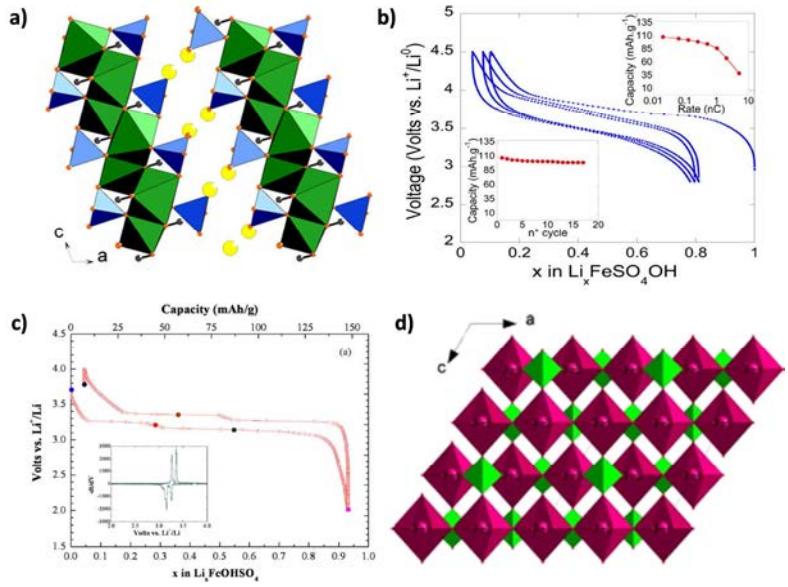

Figure I.19: a) Layered $LiFeSO_4OH$ with FeO_6 octahedra shown in green and SO_4 tetrahedra in blue. Lithium, oxygen and hydrogen are illustrated as yellow, red and black spheres, respectively. b) Electrochemical curve of layered $LiFeSO_4OH$ exhibiting a potential of 3.6 V *vs.* Li^+/Li^0. Insets: Capacity retention (bottom left) and rate capability (top right).[149] c) Voltage-composition curve of tavorite $LiFeSO_4OH$ starting in discharge. d) Crystal structure of tavorite $LiFeSO_4OH$ built of FeO_6 octahedra (pink) and SO_4 tetrahedra (green).[150]

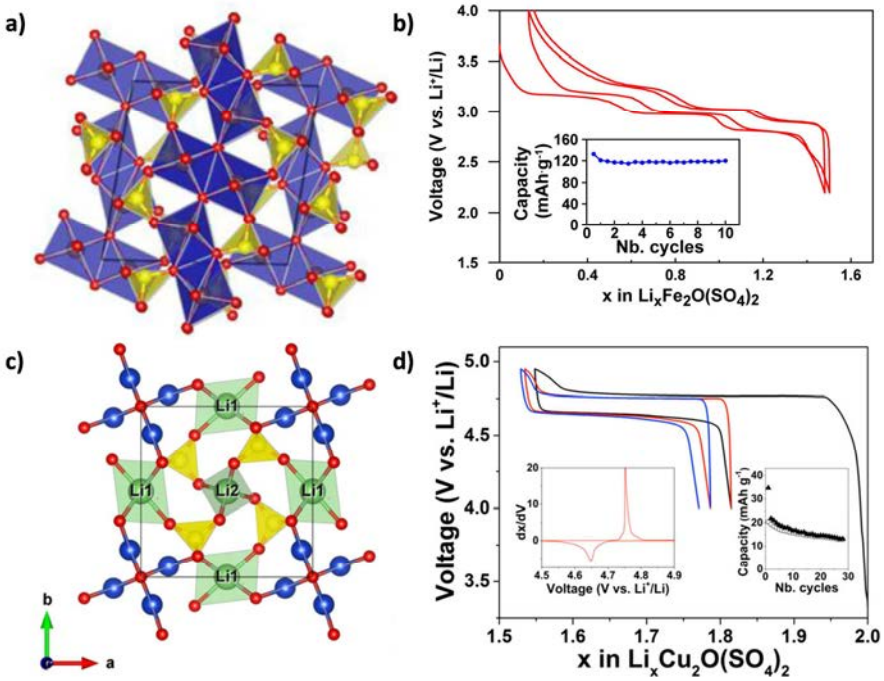

Figure I.20: a) Structure of $Fe_2O(SO_4)_2$ with FeO_6 octahedra and SO_4 tetrahedra shown in blue and yellow respectively. b) Electrochemical curve of $Fe_2O(SO_4)_2$ with the capacity retention shown in the inset.[151] c) Crystal structure of $Li_2Cu_2O(SO_4)_2$ with Cu (blue), Li (green), O (red) and S (yellow) atoms. d) Voltage-composition curve of $Li_2Cu_2O(SO_4)_2$.[152]

Even though oxy- and hydroxy-sulfates present interesting features, the most promising cathode candidate is still $LiFeSO_4F$. It crystallizes in the tavorite or triplite forms showing electrochemical potentials of 3.6 V *vs.* Li^+/Li^0 and 3.9 V *vs.* Li^+/Li^0, respectively (Figure I.21).[154–156] Tavorite $LiFeSO_4F$ is synthesized through an ionothermal approach via a topotactic reaction mechanism from $FeSO_4{\cdot}H_2O$ and crystallizes in the triclinic *P*-1 space group. The structure is based on FeO_4F_2 octahedra that share a fluorine atom and that are further bridged by SO_4 tetrahedra. The Co- and Ni-based compounds are isostructural to tavorite $LiFeSO_4F$, while $LiZnSO_4F$ crystallizes in a sillimanite structure (Figure I.21).[142,157] The triplite form is described in the monoclinic *C*2/*c* space group with edge-sharing $(Li,Fe)O_4F_2$ octahedra connected to SO_4 tetrahedra.[155] Besides the fluorine positions being in *trans*-configuration for tavorite and *cis*-configuration for triplite, the major difference between the two polymorphs is the Li/Fe site mixing in the latter, where Li and Fe occupy the same octahedral site (Figure I.21).[142] This structural disorder is often held responsible for the fact that the theoretical capacity of 150 $mAh{\cdot}g^{-1}$ has never been fully exploited for triplite $LiFeSO_4F$. The triplite polymorph can be synthesized by various methods including ball-milling, spark plasma sintering (SPS), rapid microwave synthesis and a classic solid-state approach.[142,156,158,159] The triplite structure can also be obtained for $LiMnSO_4F$ or as a solid-solution of $LiFe_{1-x}Mn_xSO_4F$, but has never been observed for $LiCoSO_4F$ or $LiNiSO_4F$.[142,155]

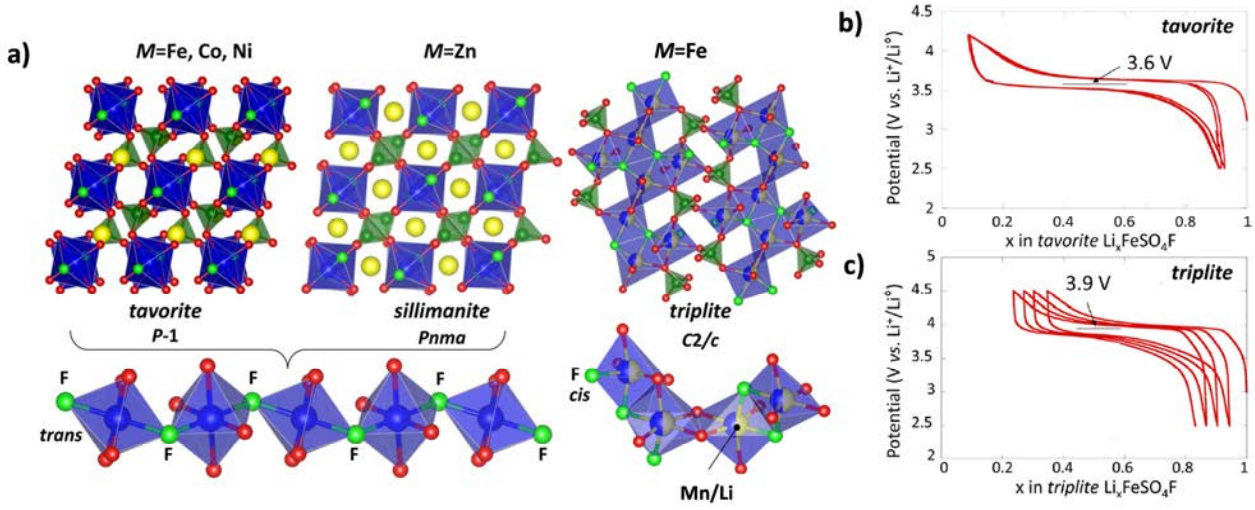

Figure I.21: a) Different crystal structures of the Li*M*SO_4F phases with *M* = Fe, Co, Ni and Zn crystallizing tavorite, sillimanite and triplite structure depending on the transition metal. MO_6 octahedra, SO_4 tetrahedra and oxygen atoms are shown in blue, green and red, respectively. Lithium is represented as yellow balls. Electrochemical curves for b) tavorite $LiFeSO_4F$ and c) triplite $LiFeSO_4F$.[142]

Fluorosulfates exist also as Na-based compounds Na*M*SO_4F (*M* = Mn, Fe, Co, Ni, Cu, Zn). These phases crystallize in the maxwellite structure (*C*2/*c*) (Figure I.22a).[160,161] However, no convincing electrochemical properties were observed as was neither for the bihydrated analogue $NaFeSO_4F{\cdot}2H_2O$.[161–163]

It was shown that by replacing Li by Na new interesting crystal structures are formed, but only few reports can be found dealing with potassium-based compounds. In 2012 however, Recham *et al.* reported on an orthorhombic $KFeSO_4F$ phase, which crystallizes in a structure related to $KTiOPO_4$ (KTP) (Figure I.22a) and from which K^+ can be extracted stabilizing a novel "$FeSO_4F$" polymorph. This new "$FeSO_4F$" framework, which is not structurally related to triplite nor to tavorite, can reversibly insert Li^+ and Na^+ at elevated potentials (Figure I.22b).[142,164] This capability makes it an interesting compound for both Li- and Na-ion batteries. Further research on $KFeSO_4F$ revealed a polymorphism described in detail in the second half of the next chapter.[165]

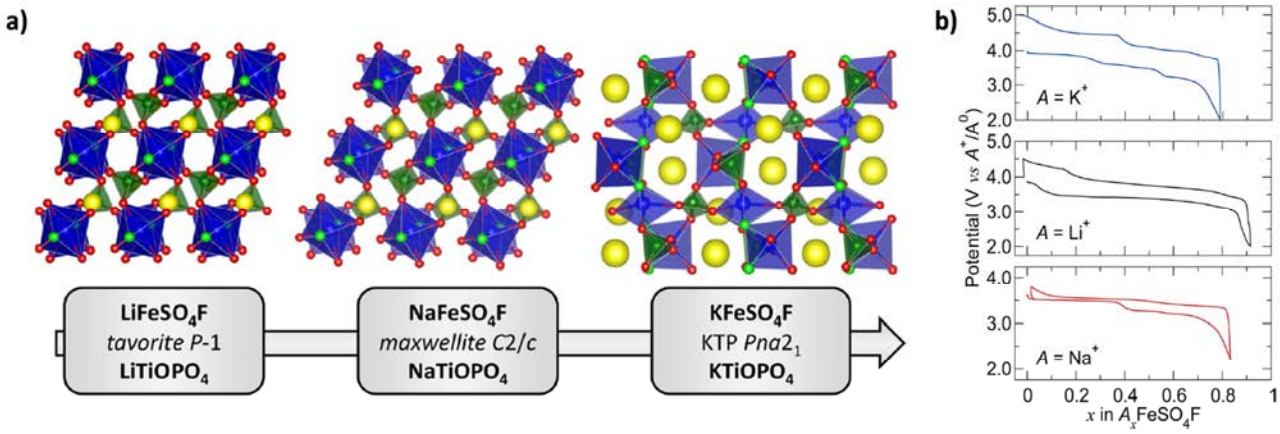

Figure I.22: a) The different crystal structures of *A*$FeSO_4F$ with *A* = Li, Na and K. MO_6 octahedra, SO_4 tetrahedra and oxygen atoms are shown in blue, green and red, respectively. The alkali cation (Li, Na, K) is represented as yellow balls.[142] b) Voltage *vs.* composition of the KTP-like "$FeSO_4F$" framework cycled against K, Li and Na.[164]

I.3. Conclusion

This chapter focused solely on lithium-based batteries and emphasized the importance of this invention for the progress of other technologies that are part of our every-day life. This explains the huge research efforts put into Li-ion batteries to constantly improve their performance. Of course simultaneously battery systems that go beyond the Li technology were explored. They enlist Na-ion batteries, multivalent ion batteries based on Mg, Ca and Al for instance, Li-air and sulfur-based batteries. Describing these technologies is beyond the scope of this chapter, but a large number of detailed review papers on these topics are available.[69,166–174]

Generally speaking, there are two main research directions for cathode materials. On one side, we have layered oxide-based materials, which evolved from $LiCoO_2$ to the nowadays exhaustively studied Li-rich NMC materials. On the other side, there are the polyanionic materials with its most famous representative olivine $LiFePO_4$. As described in this chapter, since the discovery of $LiFePO_4$ many other polyanionic materials have been explored with the aim to increase the potential and the capacity of the battery system.

The large number of studies published on polyanionic cathode materials illustrates their rich crystal chemistry and interesting electrochemical and physical properties (magnetoelectric effect, optical properties *etc.*). However, it also points out the myriad of possible compounds that might be worth exploring as potential cathode materials, which seems an almost impossible task. It is therefore important to identify indicators that allow us to narrow down these theoretically possible compounds to the most interesting ones in terms of electrochemical performances. The logic of the inductive effect is a first hint into this direction, but also other chemical/physical parameters such as bond lengths, structural density, thermodynamic stability *etc.* need to be taken into account to predict the redox potential of a compound. [142,175,176] We therefore aimed to study sulfate- and fluorosulfate-based materials in more depth with a special interest in polymorphism in order to identify structural and physical features that might help us for the targeted synthesis of high-performance polyanionic cathode materials.

Chapter II. Fluorosulfate-based cathode materials

II.1. Introduction

After the discovery of $LiFePO_4$, which presents a redox potential of 3.45 V *vs*. Li^+/Li^0 while showing appealing features in terms of sustainability and cost, polyanionic materials received a lot of attention from the battery community.[92,103,177] Researchers were especially interested in further increasing the potential of the Fe^{3+}/Fe^{2+} redox couple by taking advantage of the inductive effect, which predicts higher redox potentials for an elevated ionicity of the M-O bond (c.f. Chapter I.2.3.). This effect has been observed for example in Nasicon-type structures, where a substitution of PO_4^{3-} by SO_4^{2-} increased the redox potential about 0.8 eV.[178] Following this observation, the exploration of other sulfate-based compounds as cathode materials seemed worthwhile. Moreover, there was a growing interest in fluorosulfate-based materials to explore the joint effect of the SO_4^{2-} group and the highly electronegative fluorine atom on the redox potential. Fluorosulfates have been barely studied in the past and the first stabilized fluorosulfate was $LiMgSO_4F$ reported in 2002[179], followed a few years later by the successful synthesis of its Fe-based homologue $LiFeSO_4F$.[180,181] The latter is prepared via an ionothermal synthesis approach starting from $FeSO_4{\cdot}H_2O$ and LiF. It is described in a triclinic *P*-1 tavorite structure and displays a flat plateau at 3.6 V *vs*. Li^+/Li^0 with a reversible capacity of 140 $mAh{\cdot}g^{-1}$ (Figure II.1a). During the attempt to prepare further $LiMSO_4F$ homologues with different 3d transition metals (Mn, Co, Ni, Zn), it was observed that $LiMnSO_4F$ does not adopt the tavorite structure but is isostructural to the mineral triplite $(Mn,Fe,Mg,Ca)_2(PO_4)(F,OH)$.[182–184] Triplite $LiMnSO_4F$ crystallizes in the monoclinic unit cell *C*2/*c* and consists of $(Li,Mn)O_4F_2$ octahedra that are connected to SO_4 tetrahedra (Figure II.1b). The triplite structure shows some prominent differences compared to the tavorite one: 1) Triplite presents a random distribution of Mn and Li on two crystallographic sites. 2) The MO_4F_2 octahedra (M=Li, Mn) are edge-shared in triplite, while the FeO_4F_2 octahedra are corner-shared in tavorite. 3) The F-atoms are in *cis*-configuration for the former and in *trans*-configuration for the latter. 3) In terms of electrochemistry, triplite $LiMnSO_4F$ showed no activity.[182] Interestingly, substituting Mn^{2+} with only 5 % Fe^{2+} led to an Fe^{3+}/Fe^{2+} redox potential of 3.9 V *vs*. Li^+/Li^0, rendering this compound a highly interesting cathode material. Further studies on the triplite phase showed that also the pure Fe-based end phase $LiFeSO_4F$ could be stabilized in the same triplite configuration. The Rietveld refinement

and the corresponding structural parameters of triplite $LiFeSO_4F$ are presented in Figure II.2 and Table II.1.[185]

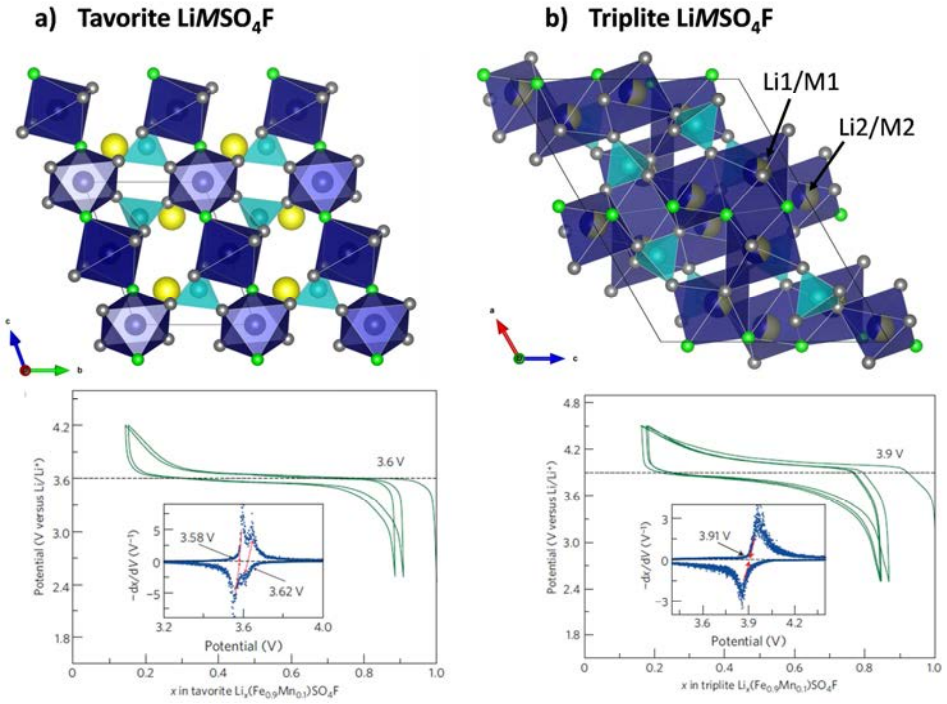

Figure II.1: Top: Structure of tavorite and triplite $LiMSO_4F$. Bottom: Voltage-composition curve of tavorite and triplite $Li(Fe_{0.9}Mn_{0.1})SO_4F$. The FeO_6 and SO_4 polyhedra are shown in blue and turquoise respectively. Lithium, oxygen and fluorine atoms are represented as yellow, grey and green balls. Note the Li/Fe site mixing in the triplite structure.[182]

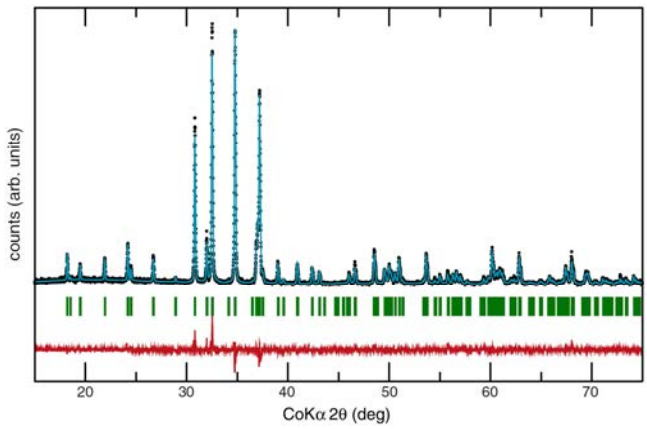

Figure II.2: Rietveld refinement of triplite $LiFeSO_4F$. The black points show the experimental XRD pattern (recorded with a Bruker D8 diffractometer), the blue and red lines show the calculated pattern and the difference pattern. Bragg positions are shown as green bars.[186]

Table II.1: Crystallographic data and atomic positions of triplite $LiFeSO_4F$ based on the Rietveld refinement shown in Figure 2.[186]

Triplite $LiFeSO_4F$

*C*2/*c*			R_{Bragg} = 6.48 %;	χ^2 = 1.48	
a=13.0238(6) Å	*b*=3.3957(3) Å		*c*=9.8341(5) Å	β=119.68(5)°	
Atom	Wyckoff site	*x*	*y*	*z*	B_{iso}(Å^2)
Li1/Fe1	8*f*	0.6472(2)	0.1064(4)	0.3488(3)	2.49(9)
Li2/Fe2	8*f*	0.5493(3)	0.2527(5)	0.9989(4)	2.97(11)
S	8*f*	0.8300(3)	0.0885(1)	0.1950(3)	0.23(7)
O1	8*f*	0.9188(5)	0.0323(7)	0.3531(5)	0.01(7)
O2	8*f*	0.7206(5)	0.1408(7)	0.1913(5)	0.01(7)
O3	8*f*	0.8614(4)	0.2810(8)	0.1440(5)	0.01(7)
O4	8*f*	0.7006(4)	0.4191(8)	0.4171(5)	0.01(7)
F	8*f*	0.5117(3)	0.0925(6)	0.3920(4)	0.01(7)

Even though triplite $LiFeSO_4F$ presents a higher redox potential compared to other polyanionic materials, the major drawbacks of this phase are the rather slow diffusion kinetics and the difficulty to obtain the full theoretical capacity (151 mAh·g^{-1}). This observation is often related to the Li/Fe site mixing, which might be detrimental to the free ionic diffusion in this compound and thus prevent the full extraction of lithium.[159,182,187–189] Nevertheless, this compound is highly interesting as it could out-pass the so far unrivalled $LiFePO_4$ in terms of energy density. Therefore, a large number of studies have been conducted describing various synthesis approaches such as solvothermal and solid-state as well as optimization methods of the active material (*e.g*. PEDOT coating).[153,159,185–187,189–192] Due to the industrial interest in this phase, we targeted an economically and ecologically optimized synthesis approach, which guarantees a high reproducibility. Further we aimed at controlling the structural disorder to study its influence on the electrochemical behaviour.

II.2. Relationship between synthesis method and structural disorder

The first triplite $LiMnSO_4F$ was synthesized from $MnSO_4{\cdot}H_2O$ and LiF precursors via an ionothermal approach at 295 °C using the ionic liquid EMI-TFSI as reaction medium or via a solid state approach in an autoclave for 24 h.[182] These synthesis methods were further transferred to the preparation of the Fe-based homologue. Another way to stabilize triplite $LiFeSO_4F$ is through a ceramic route where stoichiometric amounts of $FeSO_4{\cdot}H_2O$ and LiF are ball-milled for around 10 min, pressed to a pellet and heated in an under argon closed autoclave to 320 °C for 48 h.[186] Crucial in this synthesis approach is a quick heating ramp, where usually a value around

10°C/min was chosen. Deviations from this protocol often led to contaminated samples. Further reports describe the preparation of $LiFeSO_4F$ by reactive ball milling using a Spex 8000 miller or via spark plasma sintering (SPS; see Annexe for details).[185] For the former, stoichiometric amounts of LiF and anhydrous $FeSO_4$ were ball milled for 3 h with a ball-to-powder weight ratio of 40. The latter requires an intimate mixture of $FeSO_4$ and LiF (ball milling for 1 h), which was pressed to a pellet and heated at 320 °C for 15 min with a ramp of 75 °C/min and a pressure of 50 MPa in a HPD 10 FCT SPS machine. Moreover, it is also possible to obtain triplite from a transformation of the tavorite phase through a second annealing step at temperatures between 320-350 °C.[185,190]

Even though the triplite and tavorite $LiFeSO_4F$ phases are very close in energy from a thermodynamical point of view,[188,193–195] the formation of the two polymorphs can be synthetically controlled. Tavorite being the kinetically stabilized phase is preferentially formed with a $FeSO_4{\cdot}H_2O$ precursor, lower reaction temperatures and slow heating steps. It forms via an exchange reaction mechanism, which preserves the $FeSO_4{\cdot}H_2O$ structure. The water molecule in $FeSO_4{\cdot}H_2O$ is replaced by fluorine with a concomitant Li insertion.[185,187] Based on solution calorimetry measurements performed at U.C. Davis, it has been stated that triplite is the thermodynamically favored phase owing to its increased entropy.[194] Therefore, it is stabilized by methods that are prone to introduce disorder such as ball-milling.[194] Also rapid heating ramps favour the formation of triplite over tavorite.[185]

Compared to the other triplite synthesis methods, SPS is especially attractive owing to its short reaction times (15 min instead of several days), hence the interest of the method for an industrial scale synthesis. To find the optimal reaction conditions, we embarked into a survey of various experimental parameters starting from the previously reported SPS synthesis protocol (320 °C, ramp of 75 °C/min, 15 min, 50 MPa pressure)[185]. Table II.2 summarizes the tested synthesis conditions. All reactions were performed starting from a mixture of LiF and $FeSO_4$ ball milled for 45 min (except for sample F) using a slight excess of LiF as indicated in Table II.2. The mixture was further pressed into a pellet using the same amount of precursor and the same pressure resulting in the same thickness.

Table II.2: Different Spark Plasma Sintering (SPS) synthesis conditions varying reaction time, temperature, pressure and LiF excess.

Sample	Pressure (MPa)	Temperature (°C)	Time (min)	LiF excess (%)
A	50	320	15	5 and 11
B1	30	320	15	11
B2	75	320	15	11
C1	50	290	15	11
C2	50	350	15	11
D1	50	320	5	11
D2	50	320	40	11
E	50	350	40	11
F (1h BM)	50	350	15	11
G	50	350	60	7

Sample A is the reproduction of the previously reported synthesis conditions, where we additionally prepared a sample with 11 % LiF in excess.[185] For samples B and C, we varied the reaction pressure and temperature, respectively. Samples D were prepared at different reaction times and for samples E, F and G we merged the best parameters from the previous reactions to obtain phase-pure triplite. Aside from providing an optimized synthesis protocol, this study was conducted with the intention to find a way to control the Li/Fe disorder and to further establish a structure-electrochemistry correlation. So overall we focus on three major aspects: 1) purity of the sample and reproducibility 2) Li/Fe site occupation on the two M1 and M2 crystallographic sites and 3) electrochemical performance.

From the outcome of the various reaction conditions, it can be deduced that samples heated at temperatures around 320 °C or lower show the highest percentage of precursor residues, mainly $FeSO_4$ (Table II.3). For example, sample C1 heated at 290 °C has almost not reacted at all (76 % $FeSO_4$). Annealing at 350 °C on the other hand significantly reduces the remained precursor (e.g. 7 % $FeSO_4$ for sample C2). A similar trend is observed for the reaction time, where for instance 5 min (sample D1) seems not sufficient to lead to a complete reaction. Moreover, adding a higher excess of LiF further reduces the $FeSO_4$ amount in the sample as observed in previous studies.[192] Finally, single-phased triplite $LiFeSO_4F$ samples were obtained for the synthesis conditions E and G with temperatures at 350 °C and reaction times around 40-60 min. The Rietveld refinements for samples E and G are shown in Figure II.3. Their refined cell parameters for the various synthesis conditions (Table II.3) are in good agreement with the ones reported in literature.[186]

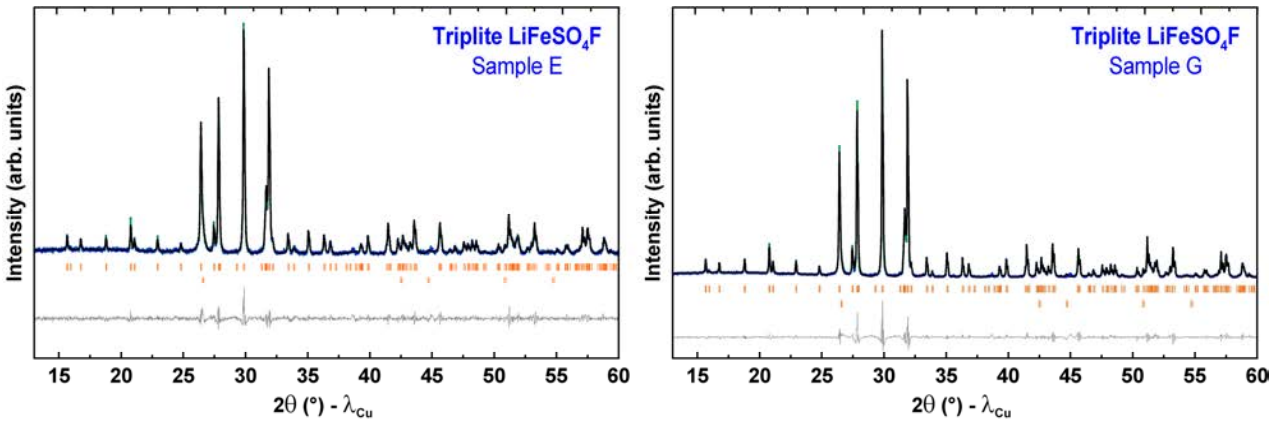

Figure II.3: Rietveld refinements of the XRD patterns of triplite $LiFeSO_4F$ – samples E and G. The blue line represents the experimental pattern, the black and grey lines show the refinement and the difference pattern. The orange bars represent the Bragg positions, where the first phase belongs to $LiFeSO_4F$ and the second one takes into account possible residues of the carbon foil that has been used during the SPS synthesis.

Table II.3: Cell parameters of $LiFeSO_4F$ samples A-G prepared via SPS. The cell parameters were obtained from Rietveld refinements of the respective XRD patterns.

Sample	a (Å)	b (Å)	c (Å)	β (°)	V (Å^3)	Impurities (in wt%)	
						$FeSO_4$	LiF
A5%	13.0436(3)	6.38675(15)	9.8538(3)	119.8147(11)	712.228(33)	11	0.7
A11%	13.0432(3)	6.38732(15)	9.8533(3)	119.8062(10)	712.291(32)	5	0.4
B1	13.0444(2)	6.38809(11)	9.8556(2)	119.8172(9)	712.536(25)	11	4
B2	13.0403(3)	6.38572(14)	9.8517(3)	119.8156(9)	711.777(30)	11	4
C1	13.0340(19)	6.3832(7)	9.847(3)	119.817(11)	710.832(13)	76	15
C2	13.0443(3)	6.38578(16)	9.8556(3)	119.8262(10)	712.205(35)	7	4
D1	13.0416(4)	6.38576(19)	9.8536(4)	119.8239(11)	711.932(40)	14	5
D2	13.0440(3)	6.38642(14)	9.8552(3)	119.8235(8)	712.254(31)	10	3
E	13.0428(3)	6.38546(16)	9.8547(3)	119.8136(10)	712.115(34)	0.6	1
F	13.0433(4)	6.39143(17)	9.8517(3)	119.7933(11)	712.736(35)	2	1
G	13.0411(2)	6.38611(11)	9.85311(19)	119.8217(7)	711.924(22)	0	4
Ref. 187	13.0238(6)	6.3957(3)	9.8341(5)	119.68(5)	711.64(1)	-	-

To access the Li/Fe site mixing, we performed simulations of the XRD patterns for various Li and Fe occupation ratios on the crystallographic sites M1 and M2 (Figure II.4a). The major differences in the simulated patterns can be seen in the low angle region and between 27° and 32°, where the relative peak intensity changes with the occupation ratio of the sites.

Comparing the simulated patterns to the experimental ones for the SPS samples A-G (Figure II.4b), it can be stated that the Li/Fe occupation ratio is probably in the range of 50:50 for M1 and M2. Based on this observation, we freely refined the site occupation with the results being summarized in Table II.4. Independent of the SPS synthesis conditions, the occupation ratios are

always in the same range of around 40:60 for Li1:Fe1 and 60:40 for Li2:Fe2. These values and the minor preference of Li for the M2 site has been previously observed.[182,187]

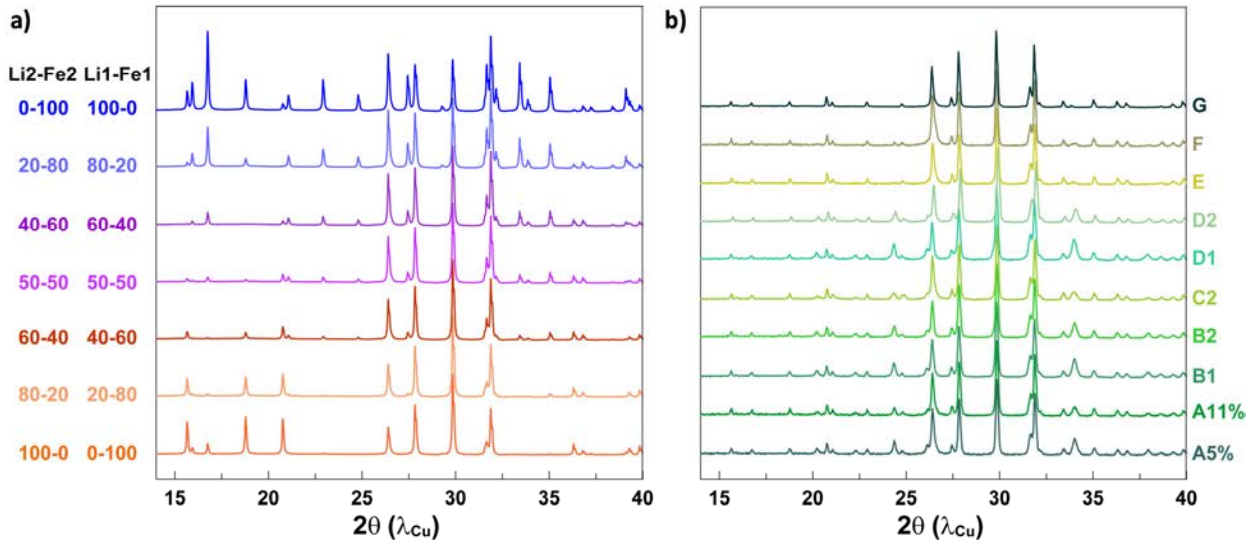

Figure II.4: a) Simulated XRD patterns of different possible Li/Fe occupation ratios of M1 and M2. b) XRD patterns of $LiFeSO_4F$ samples A-G obtained by SPS synthesis.

Table II.4: Summary of the Li/Fe site occupations for SPS $LiFeSO_4F$ samples A-G based on the Rietveld refinements of the respective XRD patterns.

	Li1	Fe1	Li2	Fe2
A5%	0.42(3)	0.58(3)	0.58(3)	0.42(3)
A11%	0.42(4)	0.58(4)	0.58(4)	0.42(4)
B1	0.41(1)	0.59(1)	0.59(1)	0.41(1)
B2	0.42(3)	0.58(3)	0.58(3)	0.42(3)
C2	0.43(5)	0.57(5)	0.57(5)	0.43(5)
D1	0.42(1)	0.58(1)	0.58(1)	0.42(1)
D2	0.42(2)	0.58(2)	0.58(2)	0.42(2)
E	0.42(2)	0.58(2)	0.58(2)	0.42(2)
F	0.42(4)	0.58(4)	0.58(4)	0.42(4)
G	0.42(3)	0.58(3)	0.58(3)	0.42(3)

We can state that the different SPS synthesis conditions (time, temperature, pressure and precursor) did not affect the Li/Fe site mixing. Nevertheless, we achieved an improved purity and reproducibility of the SPS approach. Next we explored the electrochemical performance of the various samples. Even though all the samples were tested for their electrochemistry, for reasons of length and conciseness we present only sample G. This sample was ball-milled for 20 min with 20 wt% Carbon Super P (Csp) and the powder was then loaded into a Swagelok-type

cell (loading: 7-10 mg·cm^{-2}) with LP30 as electrolyte and a lithium metal anode. The galvanostatic cycling was performed at a rate of C/20. A typical galvanostatic cycle is shown in Figure 5a. We observe a potential plateau at 3.9 V *vs*. Li^+/Li^0 characteristic of the triplite phase. In total 0.7 Li^+ are extracted with 0.5 Li^+ being reinserted, which corresponds to a reversible capacity of ~78 mAh·g^{-1}. Our SPS triplite samples present similar electrochemical features as the one reported by Ati *et al.*[185] (Figure II.5) but with a lower capacity as compared to the triplite solid solution $Li(Fe_{0.9}Mn_{0.1})SO_4F$ shown in Figure II.1b. Hence, the need for alternative synthesis methods that might improve the electrochemical performance.

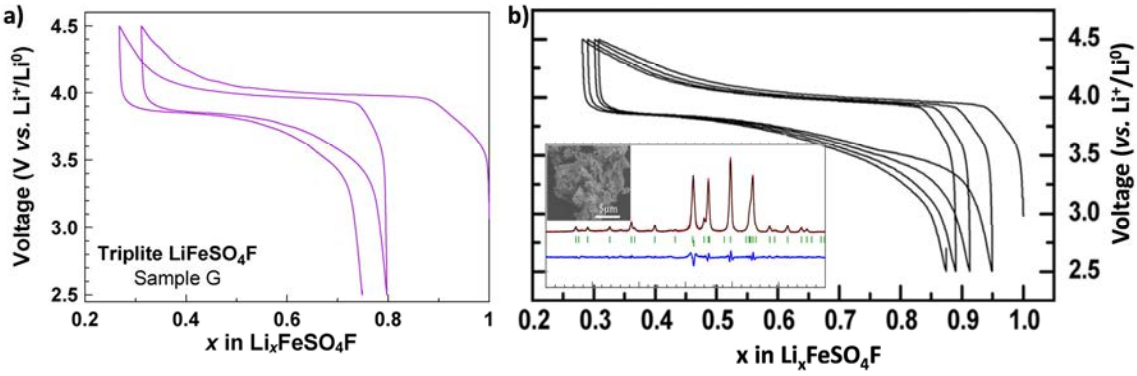

Figure II.5: Electrochemical curve of triplite $LiFeSO_4F$ sample G cycled at C/20 (a) and SPS prepared triplite $LiFeSO_4F$ reported by Ati *et al.* (b).[185] Both present the same cycling behaviour. The inset in (b) shows the respective XRD pattern.

Screening through literature, we noticed a recent report by Kim *et al.*[159] on the synthesis of triplite $LiFeSO_4F$ through ball-milling of $FeSO_4·H_2O$ or $FeSO_4$ with LiF for 48 h in acetone followed by an annealing step at 400 °C for 1 h under argon. The obtained material reaches almost the full capacity on cycling (Figure II.6c).[159] This prompted us to get a deeper insight into the structural features provided by this new solid state synthesis method.

In a first trial, we could only extract 0.6 Li^+ and were therefore far from the reported capacity. We therefore modified the synthesis procedure and ball milled $FeSO_4$ or $FeSO_4·H_2O$ with LiF (excess of 11 %) for 1 h with a ball-to-powder ratio of 40 using a Spex 8000 miller in analogy to reports by Liu *et al.*[192] The obtained mixture was pressed into a pellet and heated at 380 °C for 30 min with a ramp of 5 °C/min. Rietveld refinements of the resulting XRD pattern (Figure II.6a, shown for the $FeSO_4$ precursor) gave the same M1 and M2 occupation ratios as for the SPS samples. Also under these conditions we failed in removing more than 0.6 Li^+ from the triplite structure (Figure II.6b) for both precursors ($FeSO_4$ or $FeSO_4·H_2O$).

Kim *et al.* explained their results with the formation of a corner-sharing structure of triplite in contrast to the edge-sharing one.[159] However, caution need to be exercised since no prove has been delivered. We hypothesized that the difference between ours and Kim's results could be related to differences in powder morphology and particle size. Indeed, SEM experiments (insets Figure II.6a, c) showed that the particle size is similar (~250 nm) but that the morphology is different, with namely the presence of agglomerates of particles in our samples as compared to single particles in Kim's sample. To test the effect of morphology on the electrochemical performances, we explored other synthesis approaches.

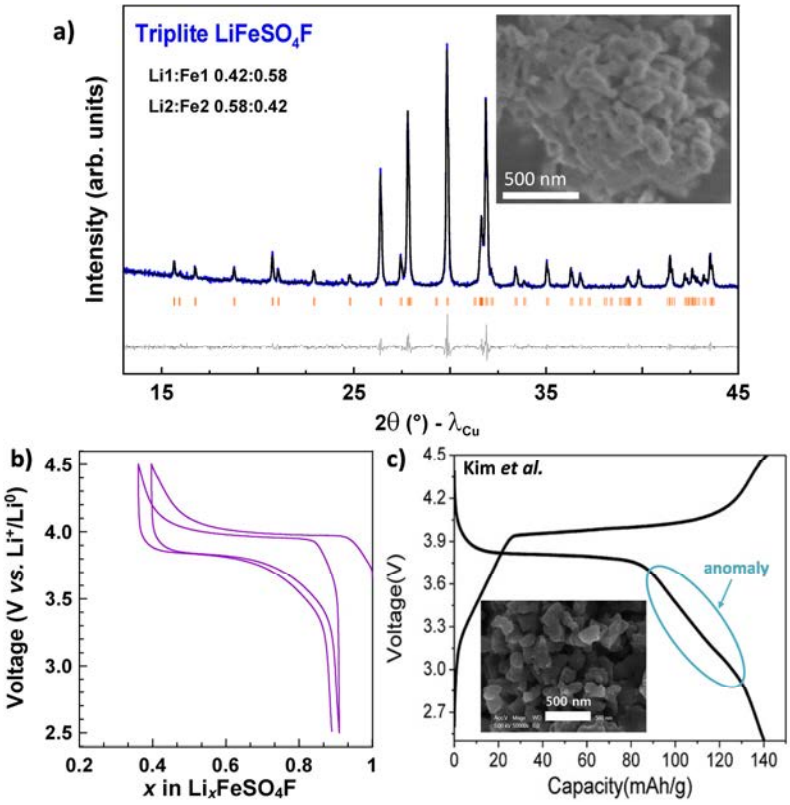

Figure II.6: a) Rietveld refinement of triplite $LiFeSO_4F$ prepared at 380 °C for 30 min. The blue, black and grey lines show the experimental XRD pattern, the calculated pattern and the difference between the two. The Bragg positions are shown as orange bars. The inset shows an SEM image of this triplite sample. b) Voltage-composition trace of triplite $LiFeSO_4F$ cycled at C/20 with 20 wt% Csp. c) Electrochemical performance of $LiFeSO_4F$ as reported by Kim *et al*.[159]

We turned towards microwave-assisted syntheses (in the following referred to as MW). Within this context we should recall the report by Tripathi *et al.* on the MW solvothermal synthesis of tavorite, which was then transformed into triplite in a second annealing step at 350 °C for 1h.[187,190] Inspired by this approach, we directly synthesized the triplite phase by a MW approach, short-circuiting the tavorite intermediate. To do so, LiF and $FeSO_4$ were ball milled for 2h and the obtained mixture was heated in ethylene glycol at 290 °C for 15 min under constant

stirring in an Anton Paar 300 microwave. Rietveld refinements of the respective XRD patterns result in a similar site occupation as the solid state approaches and is also in agreement with what has been reported by Tripathi and co-workers for their triplite phase (Li1:Li2 - 43:57).[190] SEM shows that the morphology of the MW-prepared phase is alike to that of the ceramic route (particle agglomerates), but deviate drastically from the morphology reported in literature (Figure II.7a).[190] The reversible capacity of our MW sample amounts ~100 $mAh{\cdot}g^{-1}$ (Figure II.7b), which is slightly higher than the capacity of the ceramic samples (78 $mAh{\cdot}g^{-1}$), but still lower than the reported value[190] of ~120 $mAh{\cdot}g^{-1}$. It is worth mentioning at this point that even though the electrochemical performance seemed to have improved, the direct synthesis of triplite $LiFeSO_4F$ by a MW-assisted solvothermal approach is rather problematic due to a low reproducibility of the synthesis, where often unreacted precursors or tavorite impurities were detected.

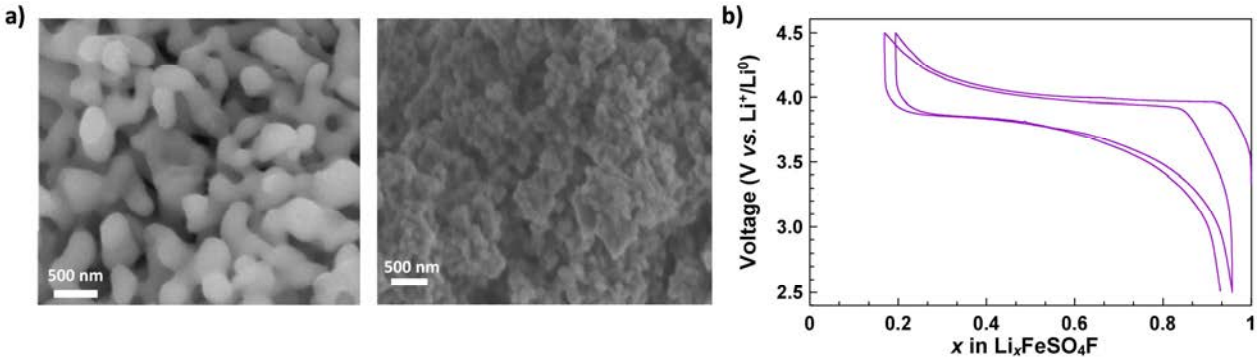

Figure II.7: a) SEM pictures of triplite prepared via microwave-assisted approach as reported by Tripathi *et al.* (left) compared to our microwave-prepared triplite (right). b) Voltage-composition trace of our triplite $LiFeSO_4F$ prepared via microwave-assisted synthesis.

Even though the reason for the increase in capacity of the MW sample has not been clarified so far, these experiments are rich of conclusions. First, whatever the synthesis approach used, the particle sizes and the Li/Fe site distributions remain the same. We systematically obtained a statistical distribution of Li and Fe on the M1 and M2 sites, with a minor preference of Li for the M2 site in agreement with what has been reported by several groups.[182,186,188,190,195] However, the electrochemical result shows slightly better performances for the MW sample compared to the ceramic route samples suggesting that the site mixing does not have a direct effect on the capacity of the triplite phase. Moreover, since the particle morphology between the MW

sample and the solid state one is alike but the electrochemical performance better for the former one, morphology does not seem to be a relevant parameter either.

It has been demonstrated in the past that a way to decrease the structural disorder in $LiFe_{1-x}Mn_xSO_4F$ triplite is to increase the Fe content (Figure II.8), where the end phases $LiMnSO_4F$ and $LiFeSO_4F$ present a site mixing of 50:50 and 60:40, respectively. However, this seems to be the most ordered phase we are able to achieve for the Fe-based samples. The only fully ordered triplite phase observed so far was obtained by completely replacing Fe^{2+} by Cu^{2+} forming triplite $LiCuSO_4F$, where the M1 site is 100 % occupied by Cu and M2 by Li. Note that $LiCuSO_4F$ shows a strong distortion of the Cu^{2+}-based polyhedra.[196]

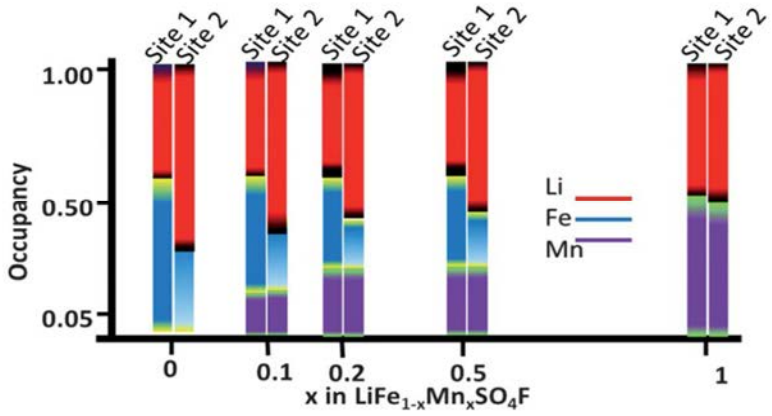

Figure II.8: Distribution of Li and M (Fe,Mn) on the metal sites M1 and M2 for various $LiFe_{1-x}Mn_xSO_4F$ compositions.[187]

Although the Fe/Li site mixing is often held responsible for the limited capacity of triplite $LiFeSO_4F$, where the Fe atoms block the Li diffusion and thus hinder a full delithiation, our above-described results could indicate that the site distribution might not be the key factor for the triplite electrochemical behaviour. Other structural parameters should be considered such as the stability of the triplite $FeSO_4F$ framework upon delithiation. Indeed, Ati *et al.* reported on major structural changes during oxidation, where the MO_4F_2 octahedra are transforming into square pyramidal MO_3F_2 polyhedra.[186] Furthermore, Lee *et al*. pointed out that the delithiation of the octahedral site in which Li is located in triplite leads to a strong destabilization of the structure due to Fe^{3+}-Fe^{3+} repulsions around the vacancy.[188] In the tavorite structure, where Li is coordinated by one fluorine and two oxygen atoms[197], this repulsion is less pronounced. Another reason for the hampered electrochemical performance of triplite might also be related to the edge-sharing configuration of the $(Li,Fe)O_4F_2$ octahedra, which might restrict the Li-

diffusion.[188] Interestingly, this edge-sharing (Li,Fe)O_4F_2 framework was also proposed to account for the increased redox potential of triplite compared to tavorite since the increased Fe^{3+}-Fe^{3+} repulsion in the former leads to a destabilization of the delithiated structure.[193]

In short, despite the early excitement that the 3.9 V triplite phase generated, we are still unable today to master its full electrochemical performance due to the complexity in establishing the synthesis-structure-electrochemical properties relationship. Nevertheless, this study had the merit to stress the richness of polymorphism within the sulfate family. This was an impetus to pursue further research in this direction to investigate polymorphism in the delithiated $FeSO_4F$ phases.

II.3. Polymorphism in $KFeSO_4F$

Since the discovery of triplite $LiFeSO_4F$, further studies on fluorosulfate-based phases were conducted leading to various $AFeSO_4F$ (A being an alkali cation) compounds with different structures.[160,161,164] The motivation behind the exploration of these alkali-based compounds was to stabilize new "$FeSO_4F$" frameworks that could be used as cathode materials in Li- and Na-ion batteries. In 2012, Recham *et al.* stabilized a new phase with the composition $KFeSO_4F$.[164] This new compound was prepared via a classic solid-state synthesis approach, where KF and $FeSO_4$ were first thoroughly mixed by ball-milling and then heated as a pellet in an evacuated sealed quartz tube at 380 °C for four days. We later optimized the synthesis conditions and were able to stabilize single-phased $KFeSO_4F$ by a heating step at 370-380 °C for only one hour in a tubular furnace under Ar-atmosphere.

$KFeSO_4F$ is isostructural to the previously reported $KTiOPO_4$ phase[198] (in the following referred to as KTP) crystallizing in the orthorhombic *Pna*2_1 space group (Figure II.9a). By having a non-centrosymmetric space group the compound can be of interest for non-linear optical properties. The structure is based on chains of FeO_4F_2 octahedra that are connected via their fluorine vertices (Figure II.9b). The FeO_4F_2 octahedra are further interconnected by SO_4 tetrahedra through their oxygen vertices. The so formed 3D network presents large voids, in which the potassium atoms are located. Electrochemically tests revealed that after extraction of K^+, the newly formed $FeSO_4F$ polymorph with its open structure can reversibly intercalate various alkali cations such as Li^+, Na^+ and K^+ (Figure II.9c).

The analogous phases $KCoSO_4F$ and $KNiSO_4F$ were stabilized following the same protocol with the annealing step being conducted at temperatures around 290 °C for approximately 45h. The electrochemical performance of these compounds however is hampered by the stability of the electrolyte and therefore could not be exploited in depth.

During the exploration of various experimental conditions for the synthesis of orthorhombic $KFeSO_4F$, the presence of a secondary unknown crystalline phase was observed at temperatures around 300 °C (Figure II.10). Different synthesis approaches were tested to prepare this unknown phase as a pure single-phased compound.[165]

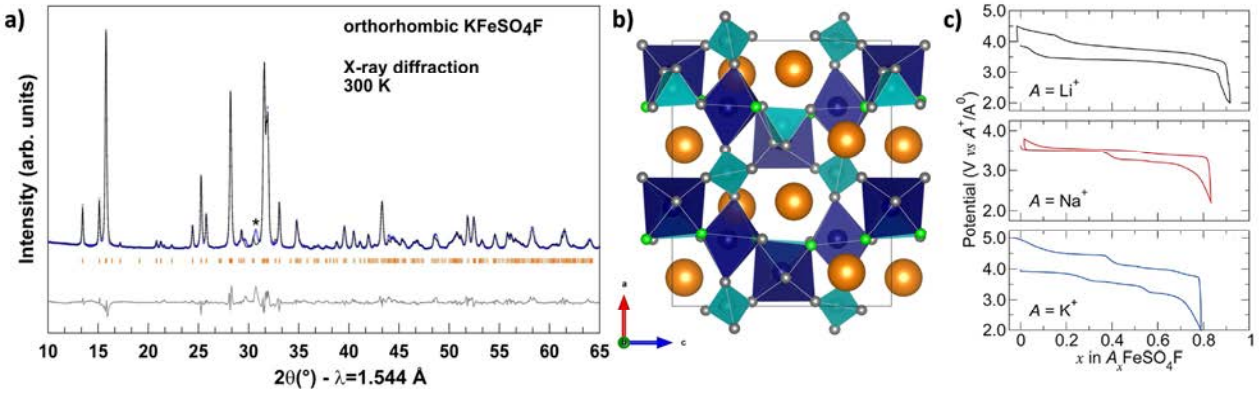

Figure II.9: a) Rietveld refinement of orthorhombic KTP-like $KFeSO_4F$. The peak marked with the star is attributed to a K_2SO_4 impurity. b) Structure of KTP-like $KFeSO_4F$. The FeO_6 octahedra are shown in blue, SO_4 tetrahedra in turquoise. K, O and F atoms are represented as orange, grey and green balls. c) Electrochemical curves of the $FeSO_4F$ framework cycled against Li, Na and K.[164]

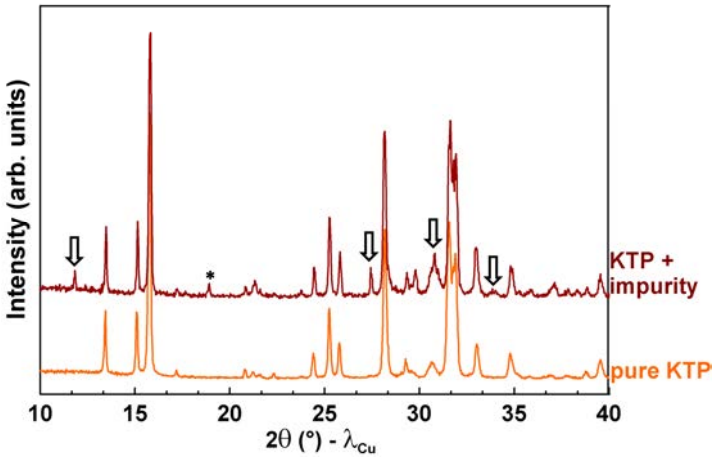

Figure II.10: XRD patterns of pure KTP-like $KFeSO_4F$ (orange pattern) and KTP-like $KFeSO_4F$ with a slight impurity marked by arrows (red pattern).

II.4. Synthesis of a novel $KFeSO_4F$ polymorph

A survey of several synthesis approaches enlisting solid state, microwave, ionothermal and ball-milling and using a variety of used precursors and temperatures was undertaken. The final optimized synthesis protocol consists of three steps, where 1) $FeSO_4 \cdot 7H_2O$ was purified in water with minute amounts of ascorbic acid in order to reduce all the Fe^{3+} residues to Fe^{2+}, washed with ethanol and dehydrated in an ionic liquid (EMI-TFSI) at 120 °C to form $FeSO_4 \cdot H_2O$.[199] The obtained monohydrate was further dehydrated through a heat treatment at 270 °C under Ar/H_2 atmosphere for 20h. 2) Anhydrous $FeSO_4$ was then ball milled for 20 minutes with a slight excess (3%) of KF (dried at 70 °C overnight under vacuum), in an Ar-filled ball-mill jar using a Spex 8000 vibratory miller and a ball-to-powder ratio of around 20. 3) The obtained mixture was pressed into a pellet and annealed in an evacuated sealed quartz tube at temperatures between 270 °C and 310 °C for three days to produce a single-phased product. Deviations from the milling conditions (longer milling durations or higher ball-to-powder ratio) can lead to the formation of traces of orthorhombic $KFeSO_4F$. It is therefore of importance to regularly control the purity of the precursors after the initial ball-milling step to avoid contaminations of orthorhombic $KFeSO_4F$ in the final sample.

The new phase was also obtained by microwave-assisted and ionothermal synthesis approaches. For the former, the mixed precursors were heated in ethylene glycol for 30-45 min at temperatures around 280 °C, while for the latter several days of heating at 280 °C in EMI-TFSI were necessary. Again here, the right ball-milling conditions of the precursors were crucial for the reproducibility of the synthesis and to avoid the formation of KTP-like $KFeSO_4F$.

A similar synthesis protocol was used to stabilize the homologous Mn-based phase, where the ball milled precursors ($MnSO_4$ + KF) were heated at 280 °C for 2 days. However, even though monoclinic $KMnSO_4F$ was stabilized, we could never obtain a phase-pure sample due to the presence of $K_2Mn_2(SO_4)_3$ as a secondary phase. For the synthesis of the Cu-based compound, $CuSO_4$ and KF were ball-milled for two hours and annealed at 400 °C for 2 days. Deviations from these conditions can lead to the formation of $K_2Cu_3O(SO_4)_3$. Moreover, our attempts to stabilize the Co- and Ni-based analogues failed whatever the applied synthesis routes and all samples were heavily contaminated by the KTP-like phase.

II.5. Characterization of $KFeSO_4F$

II.5.1. Structure determination

The chemical composition of the new compound was identified by EDX measurements using a Hitachi S-3400N SEM (Table II.5). This confirms that we indeed synthesized a new $KFeSO_4F$ polymorph. Its structure was resolved from synchrotron XRD (SXRD) data recorded at 300 K in transmission mode (λ=0.4138 Å) at the 11BM beam line at Argonne National Lab combined with neutron powder diffraction (NPD) data (λ=1.495 Å, high intensity mode, 300K) measured at the HRPT neutron diffractometer at SINQ-PSI (Villigen, Switzerland).

Table II.5: Result of EDX measurements averaged over five different zones of a monoclinic $KFeSO_4F$ sample.

Element	**K**	**Fe**	**S**	**O**	**F**
at%	13.4(2)	11.8(1)	13.6(1)	51.9(3)	9.0(1)

The observed SXRD peaks can be indexed in a monoclinic C-centered unit cell with lattice parameters *a*=14.977(1) Å, *b*=4.284(1) Å, *c*=6.905(1) Å and β=91.44(1)° and a volume of V=442.9 $Å^3$ with four $KFeSO_4F$ formula units (Figure II.11). We attempted to resolve the structure by *ab initio* structural determination using the FOX program and direct methods with the EXPO software. We obtained possible structural models in the *C*2/*m* space group and in its subgroups *C*2 and *Cm.* However, there are several tiny peaks in the SXRD pattern that could not be indexed within these space groups and that could neither be ascribed to impurities. Also, when tested against the neutron diffraction pattern, these structural models resulted in high discrepancy between the collected pattern and the calculated one. Moreover, all obtained structural models presented either strongly distorted FeO_4F_2 octahedra or unusually short O-O distances (~1.5 Å).

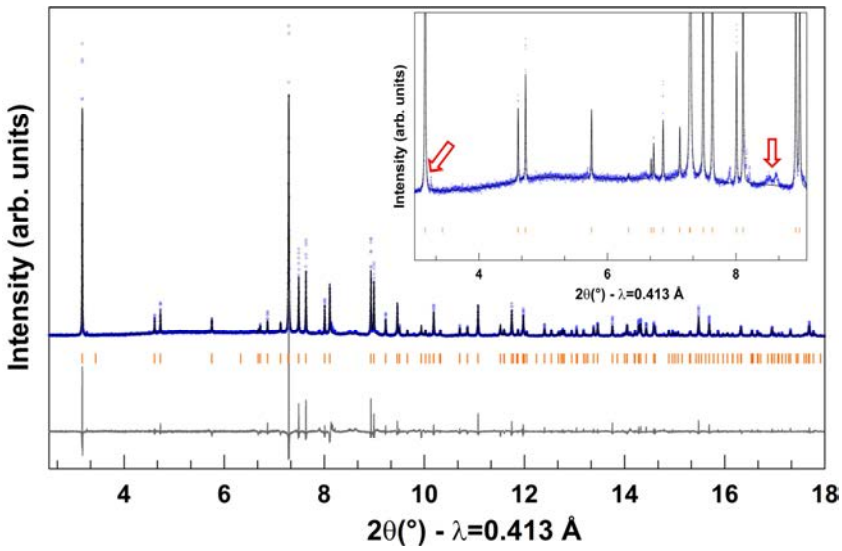

Figure II.11: Synchrotron XRD data of low-temperature $KFeSO_4F$ refined in a *C*2/*m* space group. The inset zooms in on the low angle region to highlight the additional peaks in the recorded pattern that have not been indexed by this structural model.

At this point, to get more information about the possible structure, we decided to perform TEM analysis in collaboration with A. Abakumov at EMAT, Belgium. To do so, the sample was prepared in an Ar-filled glove box by crushing the grainy powder in a mortar in anhydrous hexane and depositing drops of suspension onto holey carbon grids. The sample was transported to the microscope column completely excluding contact with air. The measurements were performed on a Tecnai G2 electron microscope operated at 200 kV. All bright reflections can be indexed with the monoclinic unit cell with *a*~15 Å, *b*~4.3 Å, *c*~6.9 Å, with the only *hkl*: *h*+*k*=2*n* reflection condition suggesting a C-centered unit cell in agreement with the from SXRD obtained results (Figure II.12). However, we can also notice weak *h*, *k*/2, *l*/2 reflections in the [011] ED pattern, which formally require a unit cell with doubled *b* and *c* parameters.

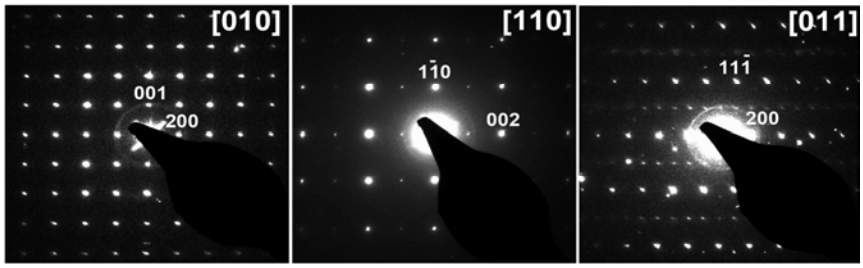

Figure II.12: Electron diffraction patterns; weak *h*, *k*/2, *l*/2 reflections in the [011] ED pattern indicate that the quadruple unit cell should be used for solving the structure.

Indeed, this new determined unit cell, which accommodates 16 $KFeSO_4F$ formula units, turns out to perfectly index all peaks observed in the SXRD and NPD patterns (Figure II.13). In the end, the structure was solved in the *C*2/*c* space group with the lattice parameters *a*=13.81021(3) Å, *b*=8.568480(17) Å, *c*=14.97753(4) Å and *β*=91.43387(15)° (*V*=1771.774(7) Å^3). The atomic positions were obtained by global optimization methods with rigid SO_4 tetrahedra as well as direct methods on SXRD and NPD patterns. Table II.6 summarizes the refined atomic positons and structural parameters deduced from the refinement of the neutron and synchrotron data. There are 18 independent atomic positions; all of them in the general Wyckoff position 8*f* except two of the three iron positions, which sit in 4*e*. There are two independent K and F positions and three different Fe sites.

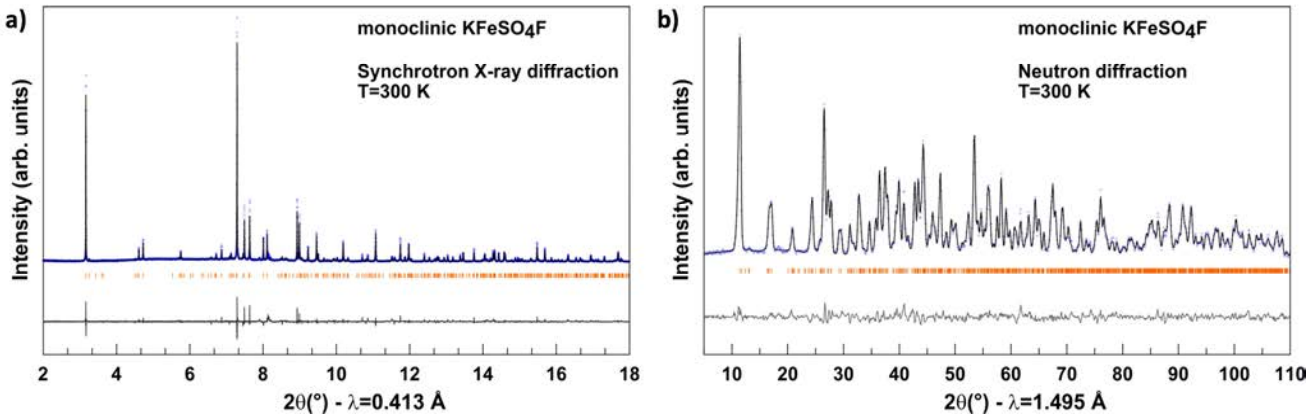

Figure II.13: Rietveld refinement of synchrotron (a), and neutron (b) diffraction patterns of $KFeSO_4F$ (T=300 K). The blue crosses, black continuous line and bottom grey line represent the observed, calculated and difference patterns, respectively. Vertical orange bars mark the reflection positions.

Table II.6: Structural parameters for $KFeSO_4F$ deduced from the Rietveld refinement of the neutron diffraction pattern recorded at 300 K. Results of bond valence sum (BVS) analysis are also indicated.

Monoclinic $KFeSO_4F$

*C*2/*c*			R_{Bragg} = 3.28 %			χ^2 = 3.97	
a = 13.81021(3) Å	*b* = 8.568480(17) Å		*c* = 14.97753(4) Å	β=91.43387(15)°		*V* = 1771.774(7) Å^3	
Atom	Wyckoff position	Occupancy	*x*/*a*	*y*/*b*	*z*/*c*	B_{iso} (Å^2)	BVS
K1	8*f*	1	0.1295(11)	0.366(3)	0.4449(10)	2.198(3)	0.895(29)
K2	8*f*	1	0.3745(10)	0.377(3)	0.0787(10)	1.753(3)	1.116(27)
Fe1	8*f*	1	0.2507(5)	0.1331(12)	0.2508(4)	0.657(8)	1.847(31)
Fe2	4*e*	1	0	0.1694(8)	¼	0.639(15)	1.987(27)
Fe3	4*e*	1	0	0.5823(12)	¼	1.698(20)	2.120(32)
F1	8*f*	1	0.1313(8)	0.1574(12)	0.3176(7)	1.317(20)	1.043(22)
F2	8*f*	1	0.3730(9)	0.0866(13)	0.1870(7)	1.805(2)	1.010(22)
S1	8*f*	1	0.1333(11)	0.372(3)	0.1157(10)	0.832(2)	5.954(173)
O1	8*f*	1	0.1968(11)	0.2354(16)	0.1344(9)	2.493(3)	1.986(105)
O2	8*f*	1	0.3027(9)	0.0168(13)	0.3744(8)	1.693(2)	1.723(90)
O3	8*f*	1	0.0969(7)	0.3643(17)	0.0256(6)	1.927(16)	2.194(83)
O4	8*f*	1	0.0555(5)	0.3727(15)	0.1808(5)	1.106(12)	2.090(71)
S2	8*f*	1	0.3938(12)	0.374(3)	0.3548(10)	0.962(2)	6.053(195)
O5	8*f*	1	0.0452(10)	0.0144(14)	0.1496(9)	1.813(2)	2.025(109)
O6	8*f*	1	0.5494(11)	0.2388(16)	0.1534(9)	2.095(2)	2.301(133)
O7	8*f*	1	0.1541(7)	0.1219(18)	0.5542(6)	2.335(17)	1.738(65)
O8	8*f*	1	0.3147(6)	0.3785(19)	0.2859(6)	1.686(16)	1.809(71)

Monoclinic $KFeSO_4F$ adopts a layered-type structure, where each layer is constructed of corner and edge-shared FeO_4F_2 octahedra that are further connected via SO_4 tetrahedra (Figure II.14). The "$FeSO_4F$" layers are stacked along [001] with the potassium atoms located between them. The three Fe1, Fe2 and Fe3 sites are all in octahedral coordination with the two fluorine atoms in *trans*-configuration. Fe1 is linked to another $Fe(1)O_4F_2$ octahedra through an oxygen atom and to Fe2 and Fe3 via its two fluorine corners. The Fe2 and Fe3 octahedra share an O-O edge. The K1 and K2 positions are nine-fold and eight-fold coordinated, respectively; both with two F atoms and oxygen atoms at distances ranging between 2.6 and 3.2 Å. Bond valence sum (BVS) analysis (Table II.6) indicates that all atoms present the expected formal charge.

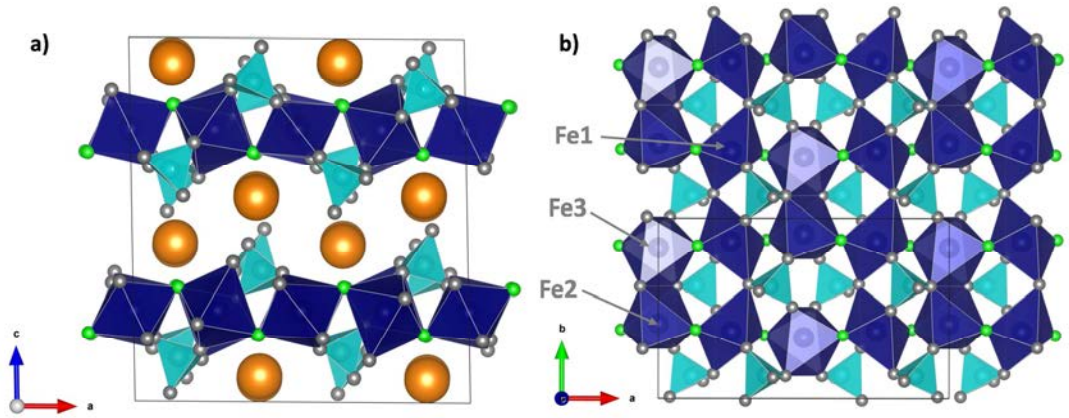

Figure II.14: Structure of $KFeSO_4F$ seen along a) [010] and b) [100] directions. K is orange, Fe is blue, F is green, O is grey. SO_4 tetrahedral groups are shown in light blue. FeO_4F_2 octahedra are linked either via edges or vertices and are further connected to each other through SO_4 groups.

To get more insight into the environment of the Fe-sites, ^{57}Fe Mössbauer measurements were conducted in collaboration with M.-T. Sougrati (ICGM, Montpellier; see Annexe for details). The spectrum (Figure II.15a) confirms the oxidation state of Fe^{2+}. Further, it can be fitted using three doublets with similar isomer shifts of 1.28, 1.29 and 1.28 mm/s, respectively, thus confirming the structure with its three crystallographically distinct Fe sites. Their relative absorption area ratio of approximately 50:25:25 is in perfect agreement with the multiplicity of Fe1, Fe2 and Fe3. It is worth mentioning that the quadrupole splitting of the Fe1 site (2.68 mm/s) is larger than the one for the Fe2 and Fe3 sites (2.17 mm/s and 2.55 mm/s respectively), which is consistent with the fact that the Fe1 atom sits in a more distorted octahedral environment than Fe2 and Fe3 (Figure II.15b).

The volume change of monoclinic $KMSO_4F$ (*M* = Mn, Cu) is in agreement with the respective ionic radius of the 3d transition metal, where the Cu-based phase shows a smaller and the Ni-based phase a higher volume compared to their Fe-based analogue (Figure II.16). Note that the unit cell volume for the monoclinic phases is systematically lower than those of the corresponding orthorhombic KTP-like polymorphs.

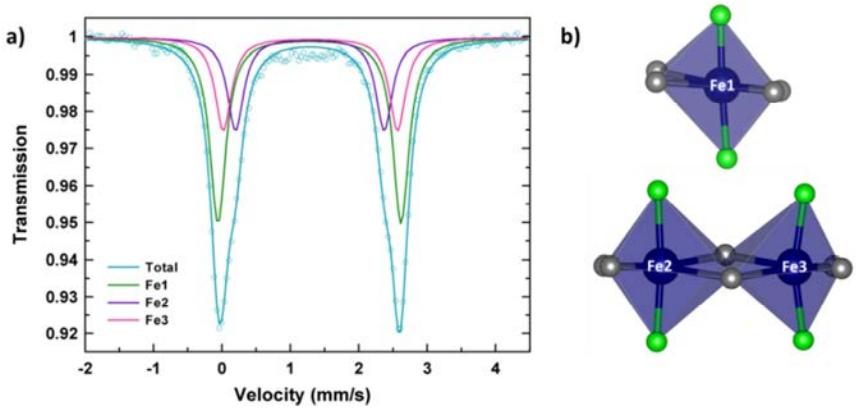

Figure II.15: a) Room temperature ^{57}Fe Mössbauer spectrum of monoclinic $KFeSO_4F$ showing the three distinct Fe^{2+} sites. b) Coordinational environment of the three Fe-sites with O and F atoms in grey and green.

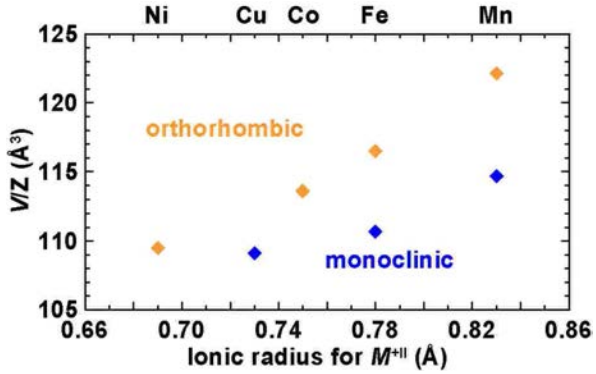

Figure II.16: Evolution of the volume per formula unit as a function of the ionic radii of the 3d transition metal cations M^{+II} in the $KMSO_4F$ series with *M*= Ni, Cu, Co, Fe, Mn. Blue and orange points represent the monoclinic and orthorhombic polymorphs, respectively.

II.5.2. Electrochemical performance and cation diffusion properties

Swagelok-type cells using lamellar $KFeSO_4F$ ball-milled with 20 wt% Csp for 15 min as the cathode, lithium metal as the anode and LP30 as electrolyte were assembled. If not otherwise specified, cells were cycled at C/50 (1C means uptake or removal of 1 Li^+ in 1h).

During the first charge, a well pronounced potential plateau at 3.8 V *vs*. Li^+/Li^0 and a pseudo-plateau at 4.4 V *vs*. Li^+/Li^0 can be identified, which are also visualized in the derivative curve (dx/dV) (Figure II.17). Of the 0.8 K^+ that are extracted upon oxidation, around 0.5 Li^+ can be reinserted during discharge, which corresponds to a reversible capacity of 78 $mAh{\cdot}g^{-1}$. EDX experiments were conducted on the discharged sample to confirm that Li^+ was inserted upon reduction and not K^+. The following cycles display an S-shaped voltage-composition trace centered at 3.7 V *vs*. Li^+/Li^0. Note the voltage drop between the first and the second charge.

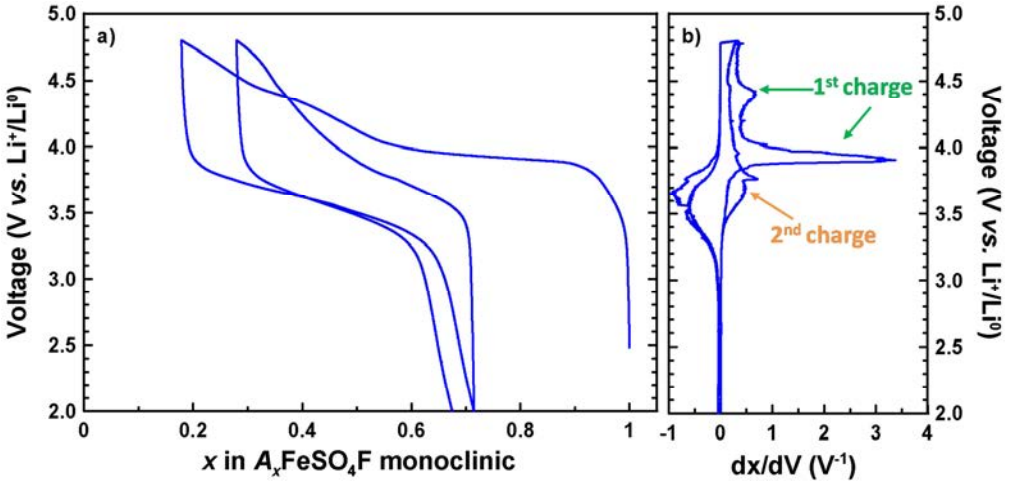

Figure II.17: The Voltage-composition trace (a) and its derivative (b) of the monoclinic $KFeSO_4F$ show two plateaus in the initial charge and an S-shaped curve upon following cycling. The high polarization indicates sluggish kinetics. *A* in $AFeSO_4F$ corresponds to K in the first charge and Li onwards.

To check the possible origin of this voltage decay, electrochemical *in situ* XRD measurements were performed (Figure II.18a). The main changes can be observed at low angles, where during charge a peak grows around 11.3° to the expense of the high intensity peak at 11.8°. The process is reversible upon discharge. However, the low crystallinity of the ball-milled electrode material did not allow us to extract any structural information about the newly formed phase. We therefore performed a chemical oxidation of $KFeSO_4F$ using 0.5 mol or 1.2 mol equivalent of NO_2BF_4 as oxidizing agent in acetonitrile to obtain $K_{0.5}FeSO_4F$ and K_0FeSO_4F, respectively (Figure II.18b). In both cases, the formation of KBF_4 confirms the chemical extraction of K^+ from the structure. However, a complete K^+ extraction was not possible even after several days of chemical treatment as Mössbauer measurements indirectly revealed a composition of ~$K_{0.3}FeSO_4F$ for a treatment with 1.2 mol NO_2BF_4. In agreement with the *in situ* XRD experiments, upon oxidation, a peak grows around 11.3°, while the (002) peak at 11.8° attributed to pristine $KFeSO_4F$ decreases (Figure II.18). The new peak can be indexed in the same space group as the pristine phase (*C*2/*c*) with the following lattice parameters *a*=13.52(2) Å, *b*=8.32(4) Å, *c*=15.5(5) Å and β=88.75(3)°. This evolution of the lattice parameters is coherent with the layered structure of $KFeSO_4F$. Upon K^+ extraction, the electrostatic repulsion of the "$FeSO_4F$" layers lead to an increase of *c* by 0.67 Å. The contraction of *a* and *b* in-plane distances is associated to the reduction in size of Fe^{2+} when oxidized to Fe^{3+}. The volume change amounts only 2 % compared to the 11 % observed for the KTP-like phase. To test the structural reversibility of the process, chemically prepared $K_{0.3}FeSO_4F$ was loaded in a Swagelok-type cell

and cycled against lithium. As can be seen in Figure II.18b, the peaks of the oxidized phase decrease, while the pristine peak regains in intensity. Note that the (002) peak is slightly shifted towards higher angles, which indicates a lower *c*-parameter as compared to the pristine $KFeSO_4F$ phase (14.85 Å vs. 14.97 Å). This is in agreement with the insertion of the smaller Li^+ (0.69 Å vs. 1.21 Å for K^+). The voltage decay might therefore be related to local structural changes during the first cycle. During the following cycles, the structure as well as the redox potential remain stable supporting this correlation.

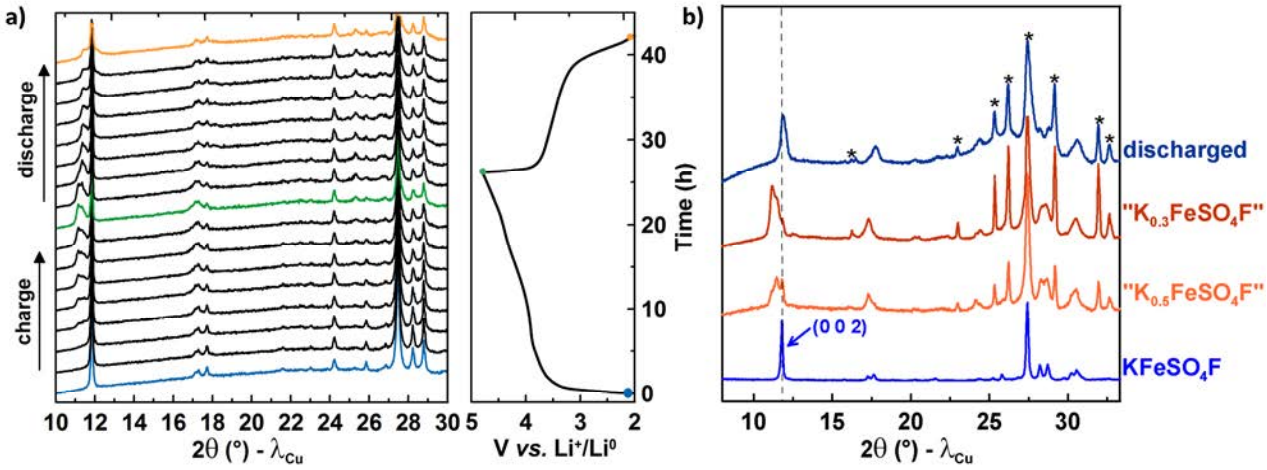

Figure II.18: a) *In situ* XRD patterns of the pristine monoclinic $KFeSO_4F$ during charge (K extracted) and subsequent discharge (Li inserted) indicative of a reversible biphasic process. b) XRD patterns of chemically oxidized samples K_xFeSO_4F with x=0.5 and x~0.3. The pristine phase $KFeSO_4F$ is shown for comparison as well as the sample prepared by electrochemical reinsertion of lithium into $K_{0.3}FeSO_4F$. The dashed line marks the position of the (002) peak of the pristine phase, which intensity decreases at the expense of a new peak appearing at lower angle during oxidation. * mark the peaks attributed to KBF_4.

The Mössbauer measurements performed on the chemically oxidized sample $K_{0.3}FeSO_4F$ revealed an oxidation of 47 % of the Fe1 site and solely 7 % of each of the Fe2 and Fe3 sites, respectively. Based on the obtained voltage-composition trace, the first plateau at 3.8 V *vs*. Li^+/Li^0 with an amplitude of 0.5 K^+ might correspond to the oxidation of Fe1 bearing in mind that there is 50 % of Fe1 in the structure. The removal of K^+ beyond x=0.5 corresponds to the partial oxidation of both Fe2 and Fe3 sites. Such a simultaneous depopulation could be at the origin of the pseudo-plateau. Note that the oxidation of the edge-sharing octahedral (Fe2 and Fe3) is energetically unfavorable due to strong Fe^{3+}-Fe^{3+} repulsions. This certainly explained our inability to fully oxidize these Fe^{2+} to Fe^{3+} and therefore to fully remove K^+. Furthermore, the K^+ residue might be necessary to prevent a collapse of the layered structure.

Going back to the electrochemical curve of monoclinic $KFeSO_4F$, we can see that it presents a large irreversible capacity and a considerable polarization indicating sluggish diffusion kinetics. This could be due to the remaining K^+ that is detrimental to the Li^+ insertion and diffusion. To get more insight into the diffusion properties of both $KFeSO_4F$ polymorphs, Bond Valence Energy Landscapes (BVEL) calculations and impedance measurements were performed (see Annexe for details). The BVEL approach allows visualizing conduction pathways in the structure while giving hints to possible conduction mechanisms. Figure II.19 shows the calculated BVEL for K^+ diffusion pathways in the two $KFeSO_4F$ polymorphs. These calculations reveal that percolation energies of 2.83 eV and 0.40 eV for the monoclinic and the orthorhombic phases are necessary to get an infinitely connected network in at least one dimension. This indirectly translates into the expectation of a much higher conductivity for the orthorhombic than for the monoclinic $KFeSO_4F$ polymorph. Moreover, the monoclinic phase presents 2D conduction pathways along the [100] and [010] directions, whereas the orthorhombic structure generates a 3D conduction network. It is worth mentioning at this point, that the K2 site of the KTP-like phase is slightly lower in energy than the K1 site, which suggests the preferential depopulation of the latter. This is in perfect agreement with previously reported DFT calculations showing that the preferential depopulation of the K1 site is related to a selective oxidation of $Fe^{2+,}$ which sits in the center of an FeO_4F_2 octahedra with the F atoms in *trans*-configuration.[200] Only after the K1 site has been completely emptied, the K2 cations are removed, which results in the oxidation of Fe^{2+} being the center of an FeO_4F_2 octahedra with F in *cis*-configuration. The removal of more than 0.5 K^+ leads to a phase transition from $Pna2_1$ to *Pnna* to minimize the electrostatic repulsion between the oxidized Fe^{3+}-Fe^{3+} metal centers and by the same reduce the distortion of the FeO_4F_2 octahedra. BVEL and calculations of KTP-like $KFeSO_4F$ reflect well the experimental observations by Recham *et al.*, which showed that the Fe sites with fluorine in *trans*-configuration are preferentially oxidized.[164]

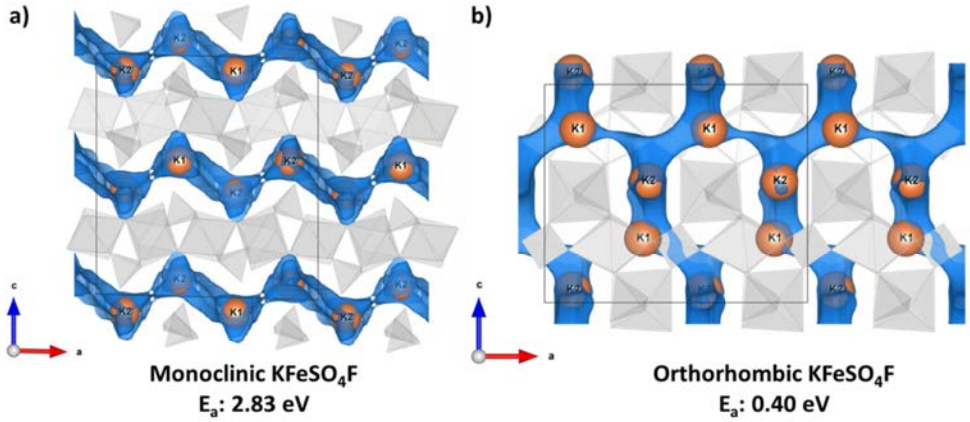

Figure II.19: Bond valence energy landscape (BVEL) of a) monoclinic and b) orthorhombic $KFeSO_4F$. The energy values chosen for the plots lay 0.2 eV and 0.96 eV above the activation energies for the monoclinic and orthorhombic polymorph, respectively. The BVEL reveals that monoclinic $KFeSO_4F$ is a 2D conductor, whereas the orthorhombic phase is a 3D conductor.

To rationalize such a finding we explored the conduction properties of $KFeSO_4F$ by performing a.c. conductivity measurements using a BioLogic MTZ-35 setup with platinum electrodes equipped with an HTF-1100 furnace. Sintered pellets (10 mm diameter, relative densities of ~70%, sputtered with gold) of monoclinic and orthorhombic $KFeSO_4F$ were measured from 35 MHz to 1Hz in the temperature range of 50 °C to 450 °C under argon flow. Figure II.20a shows the evolution of the temperature-dependent a.c. conductivity for the two polymorphs, where the orthorhombic phase (orange curve) displays a three orders of magnitude higher conductivity than its monoclinic counterpart (blue curve). The experimental data was fitted using the Arrhenius equation $\sigma(T) = \sigma_0 \cdot \exp(-E_a/k_B T)$, where σ is the conductivity at the temperature T, σ_0 is a pre-exponential factor, E_a the apparent activation energy for K^+ migration, and k_B the Boltzmann constant. Activation energies of 0.94 eV for monoclinic $KFeSO_4F$ and 0.60 eV for the orthorhombic polymorph were obtained and room temperature a.c. conductivities of $8 \cdot 10^{-14}$ S/cm for the former and $8.5 \cdot 10^{-8}$ S/cm for the latter were extrapolated. These experimental conductivity results are therefore in good agreement with the BVEL calculations, which predict a better conductivity for the orthorhombic phase. Note that upon heating of the monoclinic phase, a sudden increase of the conductivity occurs at ~390 °C, which is indicative of a possible phase transformation (Figure II.20b). XRD showed that the sample transformed into the KTP-like phase during the impedance measurements. In light of this finding, we decided to focus on the stabilities of the two polymorphs with respect to each other.

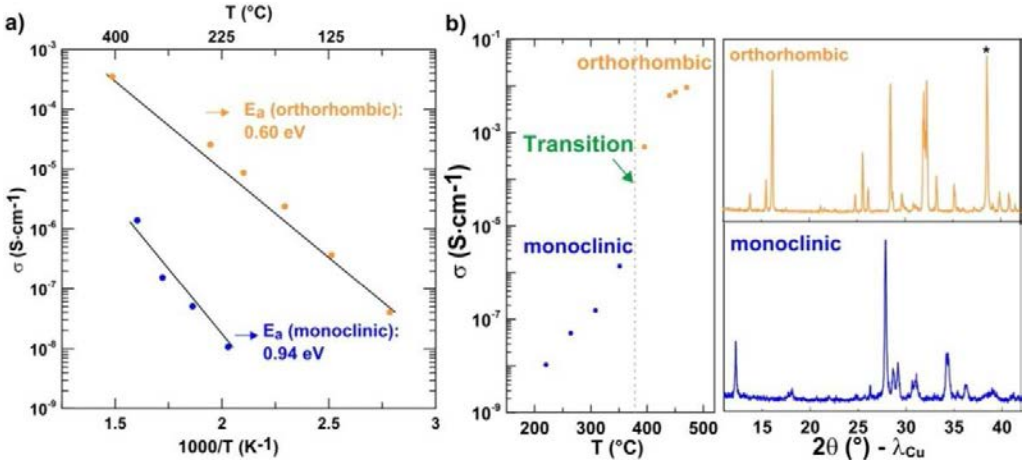

Figure II.20: a) Temperature dependence of the a.c. conductivity of the orthorhombic (orange) and monoclinic (blue) $KFeSO_4F$ polymorphs. b) Monoclinic-orthorhombic phase transition measured by a.c. conductivity with their respective XRD patterns. * marks a peak due to the gold sputter.

II.6. Polymorph stability of orthorhombic and monoclinic $KFeSO_4F$

The thermal evolution of monoclinic $KFeSO_4F$ was explored through Differential Scanning Calorimetry (DSC) measurements coupled with thermogravimetric analysis measurements (TGA, Figure II.21, green line) with a ramp of 1 °C/min under argon. The DSC trace shows an endothermic peak at 430 °C with an enthalpy of approximately 4.35(5) kJ/mol, which corresponds to the monoclinic to orthorhombic $KFeSO_4F$ phase transition as confirmed by XRD. The peak associated to this phase transition is better seen with a faster heating rate of 5 °C/min (Figure II.21, blue line), with however a significant shift in temperature. Since there is no structural similarity between the two polymorphs, we believe that this phase transition is reconstructive.

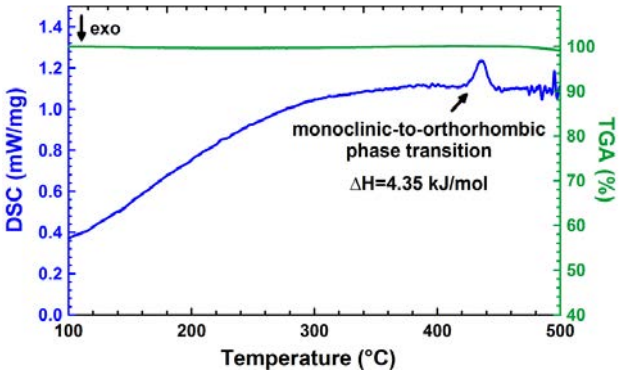

Figure II.21: DSC measurement (blue) of the monoclinic $KFeSO_4F$ heated to 500 °C with a ramp of 5 °C/min under argon atmosphere. The green line corresponds to a coupled TGA measurement.

Besides the temperature induced phase transformation, a legitimate question was regarding the feasibility to induce a phase transition through other methods. Indeed, we were able to transform the monoclinic phase into its orthorhombic counterpart by ball-milling the former for 15 min using a ball-to-powder ratio of ~40 and a Spex 8000 miller (Figure II.22), even though the transition is not complete and competes with a global amorphisation process. Note, that the stabilization of the less dense orthorhombic $KFeSO_4F$ polymorph from the denser monoclinic one (2.99 g/cm^3 vs. 3.15 g/cm^3) by ball-milling is counter intuitive since ball-milling usually favors the formation of the densest phase. It contrasts with previously observed trends for $LiFeSO_4F$, $LiFeSO_4OH$ and $Li_2Fe(SO_4)_2$,[147,149,176,185,201] where for each case the formation of the denser polymorph was favored by mechanical milling. The formation of KTP-like $KFeSO_4F$ can be explained by a local heating during the ball-milling process. This observation prompted us to get more information about the thermodynamic stabilities of the two $KFeSO_4F$ polymorphs. Therefore calorimetric experiments were conducted on both phases in collaboration Prof. Navrotsky at University of California, Davis. Experimental details are given in the Annexe.

Figure II.22: Scheme of the monoclinic-to-KTP phase transition induced either by heating or by ball-milling.

The formation enthalpies of monoclinic and orthorhombic $KFeSO_4F$ calculated from the Born-Haber cycle from KF and $FeSO_4$ (Table II.7) are negative for both polymorphs indicating that these phases are thermodynamically stable at room temperature (Table II.8). Room temperature and high temperature calorimetry gave similar results. The formation enthalpy of the monoclinic phase is about 10 kJ/mol lower than that of the orthorhombic phase indicating that monoclinic $KFeSO_4F$ is the more stable polymorph at room temperature. Further $KMnSO_4F$ was found to have larger exothermic formation enthalpy than both the polymorphs of $KFeSO_4F$.

Table II.7: Thermochemical cycle used for the calculation of heats of formation of K*M*SO_4F using data from room temperature acid solution calorimetry (T=25 °C) and high temperature oxide melt solution calorimetry (T=700 °C). sln = solution; cr = crystal.

Equation (*M* = Fe and Mn)	Enthalpy
$KMSO_4F_{(cr,\ 25\ °C)} \rightarrow KF_{(sln,\ T)} + MSO_{4(sln,\ T)}$	H_{sol1}
$KF_{(cr,\ 25\ °C)} \rightarrow KF_{(sln,\ T)}$	H_{sol2}
$MSO_{4(cr,\ 25\ °C)} \rightarrow MSO_{4(sln,\ T)}$	H_{sol3}
$MSO_{4(cr,\ 25\ °C)} + KF_{(cr,\ 25\ °C)} \rightarrow KMSO_4F_{(cr,\ 25\ °C)}$	ΔH_f
With $\Delta H_f = -H_{sol1} + H_{sol2} + H_{sol3}$	

Table II.8: Thermochemical data for orthorhombic and monoclinic $KFeSO_4F$ as well as orthorhombic $KMnSO_4F$ obtained from acid solution calorimetry (T=25°C) and high temperature oxide melt solution (T=700°C) calorimetry. [a]Uncertainty is two standard deviations of the mean, number in parentheses is number of experiments performed; * irreproducible values due to incomplete dissolution of sample

Enthalpy (kJ/mol)	**T=25°C**	**T=700°C**
$H_{sol}1$ (monoclinic $KFeSO_4F$)	10.90 ± 0.60 (6)[a]	52.62 ± 0.25 (8)
$H_{sol}1$ (orthorhombic $KFeSO_4F$)	0.17 ± 0.32 (6)	36.50 ± 0.78 (8)
$H_{sol}1$ (orthorhombic $KMnSO_4F$)	-*	161.54 ± 1.8 (8)
$H_{sol}2$ (KF)	-11.86 ± 0.50 (6)	34.13 ± 0.92 (8)
$H_{sol}3$ ($FeSO_4$)	-35.44 ± 0.42 (5)	-39.16 ± 1.12 (8)
$H_{sol}3$ ($MnSO_4$)	-20.68 ± 0.04 (4)	66.65 ± 1.42 (8)
ΔH_f (monoclinic $KFeSO_4F$)	**-58.20 ± 0.79**	**-57.60 ±1.52**
ΔH_f (orthorhombic $KFeSO_4F$)	**-47.48 ± 0.60**	**-40.52 ±1.69**
ΔH_f (orthorhombic $KMnSO_4F$)	**-**	**-60.75 ±2.1**

It was thus only by chance that the first discovered $KFeSO_4F$ was the metastable orthorhombic KTP-like phase. This might be related to the initial ball-milling step of the precursors, where the orthorhombic phase already started to form. KTP-like $KFeSO_4F$ shows neither structural disorder nor an elevated density, which could have explained its preferential formation upon milling. Thus a plausible reason might be rooted in a rapid local temperature increase that favours the nucleation/growth of the high-temperature orthorhombic phase. This explains also why even slight deviations from the optimized milling conditions (20 min, ball-to-powder ratio: 20) lead to orthorhombic $KFeSO_4F$ contaminations in monoclinic $KFeSO_4F$ samples. The formation of

orthorhombic $KFeSO_4F$ might therefore be governed by kinetic factors, while monoclinic $KFeSO_4F$ is thermodynamically favored. This is further supported by the fact that we can stabilize orthorhombic $KFeSO_4F$ directly via ball-milling KF and $FeSO_4$ for 30 min with a ball-to-powder ratio of ~40 and a Spex 8000 miller.

II.7. Magnetic properties of monoclinic $KFeSO_4F$

Besides its electrochemistry, we also examined monoclinic $KFeSO_4F$ for its physical properties, namely its magnetic features. The temperature dependence of the molar susceptibility was measured using a SQUID (XL, Quantum Design) in both ZFC (zero-field cooling) and FC (field-cooling) conditions under 1 kOe between 2 K and 400 K. The magnetic susceptibility χ of monoclinic $KFeSO_4F$ shows an antiferromagnetic ordering of the Fe^{2+} magnetic moments occurring at the Néel temperature T_N = ~ 22(3) K (Figure II.23a). The high-temperature region (50–400 K) of the susceptibility curve was fitted with the modified Curie-Weiss equation $\chi = C/(T - \theta_{CW}) + \chi_0$, which includes a temperature independent term to account for a possible diamagnetic contribution. An effective magnetic moment of 5.91 μ_B per Fe and θ_{CW} = –101 K are deduced. The effective moment is in the range expected for a high spin Fe^{2+} ion (5.48 μ_B) with an unquenched orbital moment that is fully decoupled from the spin contribution as calculated using the equation $\mu_{S+L} = (4S(S + 1) + L(L + 1))^{1/2}$ (Figure II.23b). The negative Curie-Weiss temperature θ_{CW} confirms strong antiferromagnetic correlations, while the overall linear dependence of the magnetization on the applied field (Figure II.23c) indicates the absence of a ferromagnetic component.

To get more insight into the magnetic structure, high intensity neutron powder diffraction (D20, ILL) experiments were conducted at low temperature down to 1.6 K with a wavelength of 2.42 Å (Figure II.23d). Upon cooling below the Néel temperature (22(1) K) additional magnetic peaks appear, which indicate the onset of a long-range ordering of the magnetic moments carried by the Fe^{2+} atoms. The temperature of the magnetic ordering is in perfect agreement with the Néel Temperature (T_N=22(3) K) deduced from the susceptibility measurements. Further, the Bragg peaks belonging to the nuclear structure show no changes indicating that the structure remains intact upon the magnetic ordering.

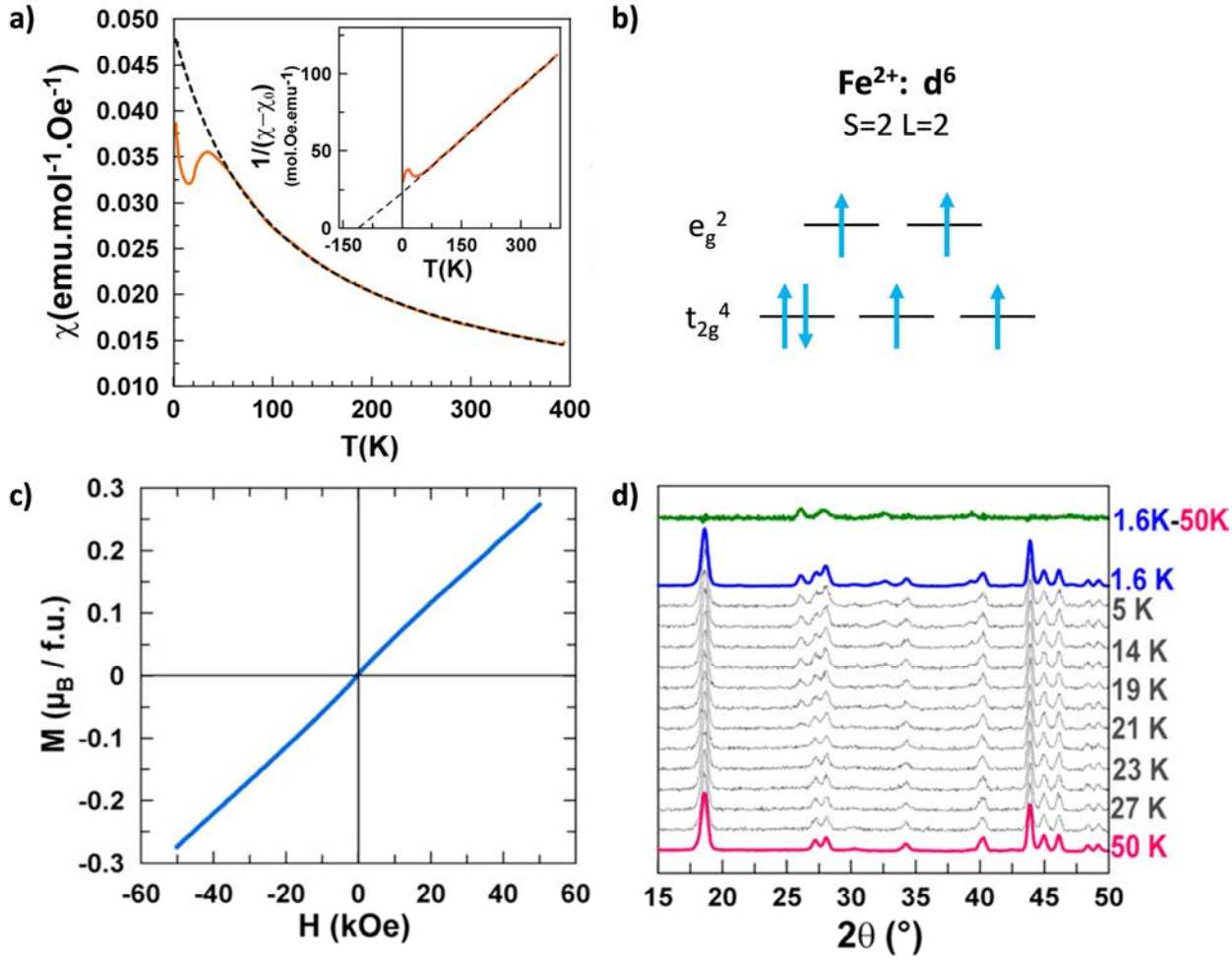

Figure II.23: a) Temperature dependence of the magnetic susceptibility (χ) of $KFeSO_4F$, measured under field-cooling conditions with a field of 1 kOe between 400 K and 2 K. The fit of the Curie-Weiss law is indicated by the black dotted line. The inset shows the inverse magnetic susceptibility ($1/(\chi - \chi_0)$) in function of temperature as well as the Curie-Weiss fit. b) Electronic configuration of Fe^{2+} being a d^6 system. The spin contribution S=2 and the orbital contribution L=2 are decoupled as described in the text. c) $KFeSO_4F$ magnetization curve as a function of the applied field measured at 2 K. d) Evolution of the neutron powder patterns of $KFeSO_4F$ between 1.6 K and 50 K. The green pattern shows the difference between the patterns recorded at 1.6 K and 50 K, thus representing the magnetic contribution only.

The determination of the propagation vector for the additional magnetic peaks resulted in **k** = (1, 0, 0) indicating that the magnetic unit cell is located within the nuclear unit cell. In a next step, we performed a symmetry analysis for the three iron sites using Bertaut's method[202] with the program BasIreps as implemented in the FullProf suite[203]. This symmetry analysis allows determining all of the possible spin configurations that are compatible with the crystal symmetry of $KFeSO_4F$. We found four irreducible representations associated with the 8*f* and 4*e* Wyckoff sites occupied by iron atoms:

$\Gamma_{mag}(8f) = 3\,\Gamma_1 \oplus 3\,\Gamma_2 \oplus 3\,\Gamma_3 \oplus 3\,\Gamma_4$

$\Gamma_{mag}(4e) = \Gamma_1 \oplus \Gamma_2 \oplus 2\,\Gamma_3 \oplus 2\,\Gamma_4$

The results are described in detail in Table II.9, where we also provide the Shubnikov group (magnetic space group). For the 8*f* site (Fe1), each representation is composed of three basis vectors Ψ_i (i=1, 2, 3) which correspond to moments oriented along the *a*, *b* or *c* unit-cell directions. For Fe2 and Fe3 atoms (4*f* Wyckoff site), symmetry analysis imposes magnetic moments along [010] for representations Γ_1 and Γ_2, and perpendicular to [010] for Γ_3 and Γ_4.

Table II.9: Results of the symmetry analysis of the *C*2/*c* unit cell for the propagation vector **k** = (1, 0, 0). The characters (χ) of the representations and the basis vectors Ψ_i (*i* = 1, 2, 3), as well as the Fourier coefficients (S_k = m, magnetic moments) of the positions generated for the 8*f* (*x*, *y*, *z*) and 4*e* (0, y, ¼) Wyckoff sites are given for each irreducible representation Γ_n ($1 \le j \le 4$). Note that atoms linked to the (½, ½, 0)+ centering have opposite magnetic moments to those of the (0, 0, 0)+ lattice.

k = (1, 0, 0)							
		Fe1 in 8*f*				**Fe2 and Fe3 in 4*e***	
		Fe1(1)	**Fe1(2)**	**Fe1(3)**	**Fe1(4)**	**Fe2,3(1)**	**Fe2,3(2)**
		x, y, z	***-x, y, -z+½***	***-x, -y, -z***	***x, -y, z+½***	***0, y, ¼***	***0, -y, ¾***
Γ_1 *C*2/*c*	χ	1	1	1	1	1	1
	Ψ_1	1, 0, 0	$\bar{1}$, 0, 0	1, 0, 0	$\bar{1}$, 0, 0	0, 1, 0	0, 1, 0
	Ψ_2	0, 1, 0	0, 1, 0	0, 1, 0	0, 1, 0		
	Ψ_3	0, 0, 1	0, 0, $\bar{1}$	0, 0, 1	0, 0, $\bar{1}$		
	S_k	***M_x, M_y, M_z***	***-M_x, M_y, -M_z***	***M_x, M_y, M_z***	***-M_x, M_y, -M_z***	***0, M_y, 0***	***0, M_y, 0***
Γ_2 *C*2/*c'*	χ	1	1	-1	-1	1	-1
	Ψ_1	1, 0, 0	$\bar{1}$, 0, 0	$\bar{1}$, 0, 0	1, 0, 0	0, 1, 0	0, $\bar{1}$, 0
	Ψ_2	0, 1, 0	0, 1, 0	0, $\bar{1}$, 0	0, $\bar{1}$, 0		
	Ψ_3	0, 0, 1	0, 0, $\bar{1}$	0, 0, $\bar{1}$	0, 0, 1		
	S_k	***M_x, M_y, M_z***	***-M_x, M_y, -M_z***	***-M_x, -M_y, -M_z***	***M_x, -M_y, M_z***	***0, M_y, 0***	***0, -M_y, 0***
Γ_3 *C*2′/*c'*	χ	1	-1	1	-1	1	1
	Ψ_1	1, 0, 0	1, 0, 0	1, 0, 0	1, 0, 0	1, 0, 0	1, 0, 0
	Ψ_2	0, 1, 0	0, $\bar{1}$, 0	0, 1, 0	0, $\bar{1}$, 0	0, 0, 1	0, 0, 1
	Ψ_3	0, 0, 1	0, 0, 1	0, 0, 1	0, 0, 1		
	S_k	***M_x, M_y, M_z***	***M_x, -M_y, M_z***	***M_x, M_y, M_z***	***M_x, -M_y, M_z***	***M_x, 0, M_z***	***M_x, 0, M_z***
Γ_4 *C*2′/*c*	χ	1	-1	-1	1	1	-1
	Ψ_1	1, 0, 0	1, 0, 0	$\bar{1}$, 0, 0	$\bar{1}$, 0, 0	1, 0, 0	$\bar{1}$, 0, 0
	Ψ_2	0, 1, 0	0, $\bar{1}$, 0	0, $\bar{1}$, 0	0, 1, 0	0, 0, 1	0, 0, $\bar{1}$
	Ψ_3	0, 0, 1	0, 0, 1	0, 0, $\bar{1}$	0, 0, $\bar{1}$		
	S_k	***M_x, M_y, M_z***	***M_x, -M_y, M_z***	***-M_x, -M_y, -M_z***	***-M_x, M_y, -M_z***	***M_x, 0, M_z***	***-M_x, 0, -M_z***

All the possible representations given by this symmetry analysis were tested against the NPD pattern recorded at 1.6 K. To do so, we refined the coefficients that multiply the three basic vectors and compared the goodness of the fit for each combination of the four representations Γ_i (i=1,4). The best results were obtained for the two magnetic structures following Γ_3 and Γ_4 with moments projected along basis vectors Ψ_1 and Ψ_3. The two refinements in Γ_3 and Γ_4 are

shown in Figure II.24. As the two proposed models (corresponding to Shubnikov groups *C*2'/*c*' and *C*2'/*c*) show only slight differences in the 2θ region (33-35°) it is difficult to determine the final model based on powder diffraction data. The two possible magnetic structures are summarized in Table II.10. The refined value of the magnetic moment is M=2.85(3) μ_B, a value slightly lower than what expected for Fe^{2+} (d^6, g·S = 4 μ_B), which might be due to not fully saturated magnetic moments.

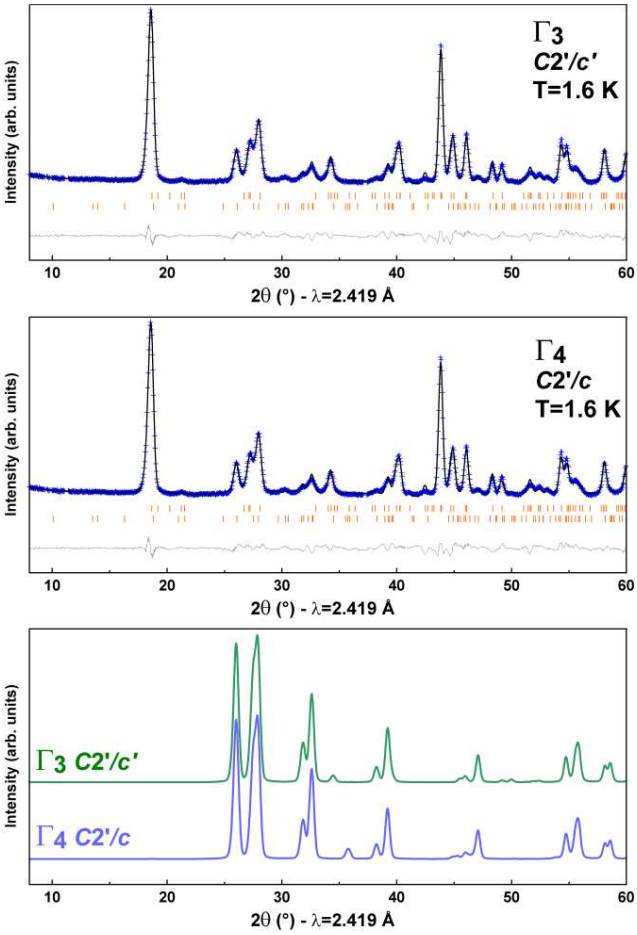

Figure II.24: Results of the refinement of the nuclear and magnetic parts of the neutron powder diffraction pattern measured at 1.6 K, with the Γ_3 (top) and Γ_4 (middle) representations. The blue crosses and the black line represent the experimental and the calculated patterns, respectively. The grey line is the difference curve of these two patterns. The first line of orange bars corresponds to the Bragg positions of the nuclear part while the second line of orange bars shows the position of the expected magnetic reflections. The bottom figure shows the comparison between the two models.

Table II.10: The two possible magnetic structures for $KFeSO_4F$, corresponding to the Γ3 and Γ4 representations deduced from the symmetry analysis (space group *C*2/*c*; propagation vector k = (1, 0, 0)). Magnetic moments (μB) at 1.6 K, the components (in μB) are given along the a, b, c axes (M_X, M_Y, M_Z) and spherical components (M, θ, φ) with respect to a Cartesian system in which x is parallel to a, y is in the ab-plane and z is along c*. Therefore, φ=0 corresponds to moments in the (a, c) plane. Atoms whose label is preceded with a C correspond to those linked with the (½, ½, 0)+ lattice centering.

Refined magnetic moment	Magnetic moments (μ_B) along the **a**, **b**, **c** axes **M_x=−1.15(9)** **M_Y=0** **M_z=2.58(4)**			Spherical coordinates **M=2.85(3)** μ_B **θ= −25(2)°** **φ=0°**			
Representation Γ$_3$ Shubnikov group *C*2'/*c*'							
Fe1(1) *x*, *y*, *z* +M	**Fe1(2)** *-x*, *y*, *-z+½* +M	**Fe1(3)** *-x*, *-y*, *-z* +M	**Fe1(4)** *x*, *-y*, *z+½* +M	**C-Fe1(1)** *x+½*, *y+½*, *z* −M	**C-Fe1(2)** *-x+½*, *y+½*, *-z+½* −M	**C-Fe1(3)** *-x+½*, *-y+½*, *-z* −M	**C-Fe1(4)** *x+½*, *-y+½*, *z+½* −M
Fe2(1) 0, *y*, ¼ +M	**Fe2(2)** 0, *-y*, ¼ +M	**C-Fe2(1)** *½*, *y+½*, ¼ −M	**C-Fe2(2)** *½*, *-y+½*, ¼ −M	**Fe3(1)** 0, *y*, ¼ −M	**Fe3(2)** 0, *-y*, ¼ −M	**C-Fe3(1)** *½*, *y+½*, ¼ +M	**C-Fe3(2)** *½*, *-y+½*, ¼ +M
Representation Γ$_4$ Shubnikov group *C*2'/*c*							
Fe1(1) *x*, *y*, *z* +M	**Fe1(2)** *-x*, *y*, *-z+½* +M	**Fe1(3)** *-x*, *-y*, *-z* −M	**Fe1(4)** *x*, *-y*, *z+½* −M	**C-Fe1(1)** *x+½*, *y+½*, *z* −M	**C-Fe1(2)** *-x+½*, *y+½*, *-z+½* −M	**C-Fe1(3)** *-x+½*, *-y+½*, *-z* +M	**C-Fe1(4)** *x+½*, *-y+½*, *z+½* +M
Fe2(1) 0, *y*, ¼ +M	**Fe2(2)** 0, *-y*, ¼ −M	**C-Fe2(1)** *½*, *y+½*, ¼ −M	**C-Fe2(2)** *½*, *-y+½*, ¼ +M	**Fe3(1)** 0, *y*, ¼ −M	**Fe3(2)** 0, *-y*, ¼ +M	**C-Fe3(1)** *½*, *y+½*, ¼ +M	**C-Fe3(2)** *½*, *-y+½*, ¼ −M

Both models show an antiferromagnetic arrangement in the layers with collinear moments, where adjacent magnetic moments are antiparallel (Figure II.25). The structural difference between Γ_3 (*C*2'/*c*') and Γ_4 (*C*2'/*c*) is the way the layers are stacked, which corresponds to the way magnetic moments are transformed by the inversion operator. For the former, Fe^{2+} magnetic moments linked through inversion are maintained parallel, while they are antiparallel for the latter. At this stage, the interesting feature of this magnetic structure *C*2'/*c* (representation Γ_4) is that the character of the inversion center ($\chi_2(g) = \chi_2(\bar{1}) = -1$) is negative, so the spatial inversion is associated with time reversal (the operator $\bar{1}'$ belongs to *C*2'/*c*). This allows the linear magnetoelectric effect to be active below the Néel temperature. Therefore, if the magnetic structure follows Γ_4 (*C*2'/*c*), an applied electric field may induce a magnetization or *vice versa*. However, single crystals are needed to fully clarify this point.

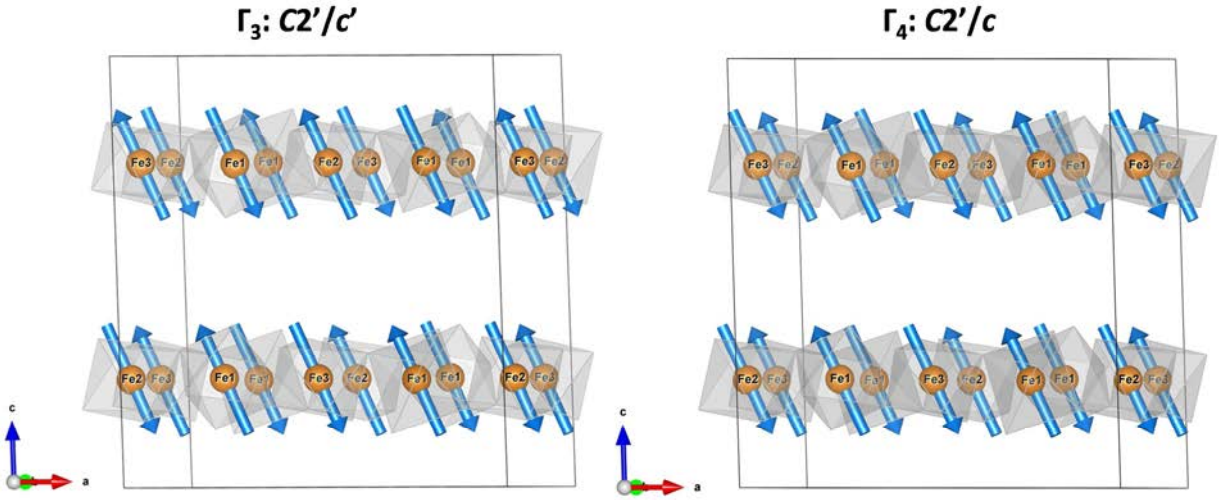

Figure II.25: Two magnetic structures corresponding to Γ_3 (left) and Γ_4 (right), respectively. Arrows represent the magnetic moments carried by iron atoms (orange balls); for sake of clarity only Fe atoms are represented. Both of them have in common the antiferromagnetic arrangement within a layer, only the inter-layer orientation changes. Note that the Shubnikov group *C*2'/*c* associated with Γ_4 contains the time reversal symmetry, so that $KFeSO_4F$ may present magnetoelectric properties in its magnetically ordered phase, while it will not be the case if the magnetic structure is *C*2'/*c*' (Γ_3).

II.8. Conclusion

The first part of this chapter described the optimized synthesis conditions to prepare in a reproducible way pure triplite $LiFeSO_4F$ via an SPS synthesis approach (350 °C, 60 min, 75 MPa) or via a rapid solid state synthesis (380 °C for 30-60 min). Further studying the impact of the synthesis approach on the Li/Fe site mixing, we showed that whatever the synthesis methods (solid state, microwave, SPS) and conditions, the structural disorder stays identical (Li1:Fe1 40:60 and Li2:Fe2 60:40). In light of our results and of those reported in literature, we believe that neither the Li/Fe site mixing nor the particle morphology have a direct influence on the electrochemical performance; the reason why the complex electrochemical behaviour of the triplite phase still remains to be fully unveiled.

Further pursuing our interest for polymorphism, we reported on the successful synthesis of a novel low-temperature $KFeSO_4F$ phase, which crystallizes in a monoclinic layered-like structure. K^+ can be extracted and Li^+ reversibly inserted at an average potential of 3.7 V *vs.* Li^+/Li^0. Through BVEL calculations and experimental impedance measurements we revealed lower diffusion kinetics for monoclinic $KFeSO_4F$ as compared to its orthorhombic counterpart. This was

explained by the higher density of the former resulting in higher activation energy and limited geometrical diffusion pathways.

Besides the tavorite, triplite and KTP-like $FeSO_4F$ frameworks, we prepared a new $FeSO_4F$ polymorph upon K^+ extraction from layered-like monoclinic $KFeSO_4F$. The four "$FeSO_4F$" phases are summarized in Figure II.26. Note the volume difference of the Li-based triplite and tavorite "$FeSO_4F$" frameworks (~90 $Å^3$) as compared to the K-based ones (~100-110 $Å^3$). Taking advantage of the open structure of the K-based phases, which allow the up-take of Li^+ and Na^+, we even tried to insert divalent cations such as Mg^{2+} into KTP-like "$FeSO_4F$", with however little success.

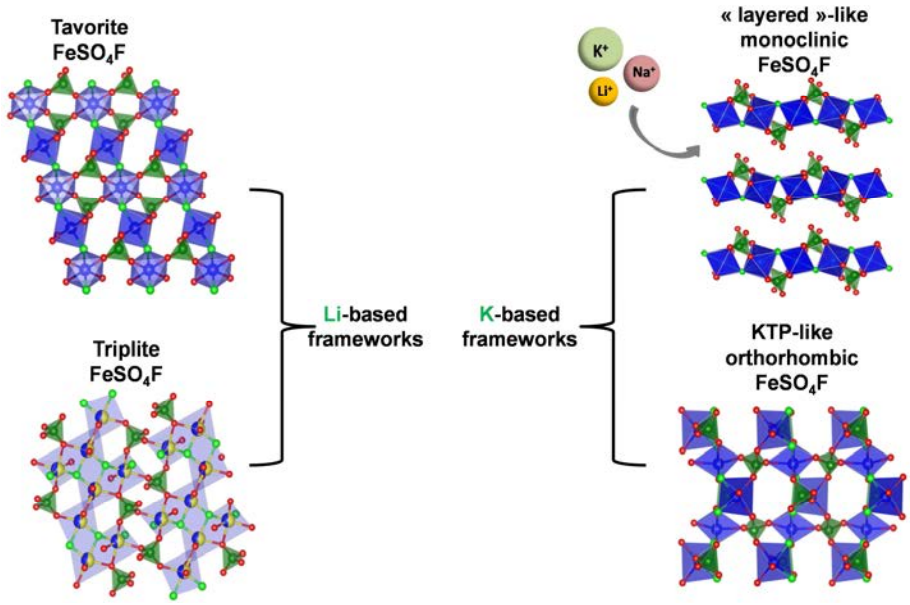

Figure II.26: Summary of Li- and K-based $FeSO_4F$ polymorphic frameworks with the possibility to insert several cations.

It is worth mentioning at this point that the structural differences between the tavorite and triplite $FeSO_4F$ frameworks have a direct influence on the electrochemical potential. As mentioned earlier, the increased potential of triplite compared to tavorite is often related to the edge-sharing structure of the latter. In analogy to this observation, Ling and co-workers predicted that an edge-sharing polymorph of the KTP-like $KFeSO_4F$ phase might also result in an increased redox potential.[200] With the isolation of monoclinic $KFeSO_4F$, we were able to stabilize this desired polymorph with (partially) edge-sharing FeO_4F_2 octahedra. However, electrochemical tests showed that the potential stays in the same range as the one for the KTP-

like phase when cycled against Li. This observation again underlined the fact that the prediction of the redox potential of a material is a complex task, which demands the consideration of many different parameters.

To conclude, even though the electrochemistry of this new monoclinic $KFeSO_4F$ polymorph stands back compared to other polyanionic materials such as $LiFePO_4$ (theoretical energy density of ~590 $Wh{\cdot}kg^{-1}$ for $LiFePO_4$ *vs.* ~550 $Wh{\cdot}kg^{-1}$ for $KFeSO_4F$), the studies on the $KFeSO_4F$ phases inspired research groups to explore other K-based compounds as means to prepare new cathode materials such as $KVPO_4F$[204] once the K^+ has been removed. Aside from electrochemistry the monoclinic $KFeSO_4F$ shows promises for exciting magnetic properties such as the possibility of a magneto-electric effect below the Néel temperature. Lastly, this study once again emphasized the richness of crystal chemistry of the sulfate-based phases with new phases waiting to be discovered as described in the next chapter.

Chapter III. Sulfate-based materials: Polymorphism in $Li_2M(SO_4)_2$

III.1. Introduction

We have seen in the previous chapters that polyanionic materials are of great interest owing to the ability to tune their redox potential by changing the ligand $(XO_4)^{n-}$. Even though it was shown that fluorosulfates display an increased Fe^{3+}/Fe^{2+} redox potential compared to other polyanionic compounds, the use of fluorine-containing cathodes in batteries is a possible source of safety concerns.[205] This was an impetus for us to explore fluorine-free sulfate-based cathode materials. Inspired by natural sulfate-based minerals containing alkali cations and 3d transition metal centers, Reynaud *et al.* reported on a variety of new interesting electrode materials.[144,206] Especially the bisulfate $Li_2Fe(SO_4)_2$ crystallizing in a monoclinic unit cell gained a lot of attention as it showed a potential of 3.83 V *vs*. Li^+/Li^0 (Figure III.1), which comes close to the 3.9 V *vs*. Li^+/Li^0 of triplite $LiFeSO_4F$ without the need of the hazardous fluorine atom.[207]

In this chapter, we present a novel $Li_2M(SO_4)_2$ (*M* = Fe, Co) polymorph, which we characterized for its structural, electrochemical and physical properties. To better put this finding in its context with respect to the polymorphism in $Li_2M(SO_4)_2$, we shortly recall herein the synthesis and characteristics of monoclinic $Li_2M(SO_4)_2$, which are described in depth in the PhD thesis of M. Reynaud.[144]

Monoclinic $Li_2Fe(SO_4)_2$ is synthesized via a classic ceramic synthesis approach, where stoichiometric ratios of $FeSO_4$ and Li_2SO_4 were thoroughly mixed and annealed at 310 °C for 48 hours in an evacuated sealed quartz tube to avoid oxidation of Fe^{2+} to Fe^{3+}. This phase is described in a monoclinic unit cell (space group $P2_1/c$) with the cell parameters a = 4.9886(2) Å, b = 8.2062(2) Å, c = 8.8293(2) Å and β = 121.7499(2)°. The structure consists of isolated FeO_6 octahedra that are interconnected by six SO_4 tetrahedra via their oxygen vertices (Figure III.1a). The so formed 3D network leaves channels running along [100], in which the lithium atoms are located. $Li_2M(SO_4)_2$ with *M* = Co, Mn, Zn and Mg are isostructural to $Li_2Fe(SO_4)_2$, while $Li_2Ni(SO_4)_2$ was shown to crystallize in an orthorhombic unit cell as described by Isasi *et al.*[208] Furthermore, $Li_2Zn(SO_4)_2$ can be stabilized either in the monoclinic or orthorhombic structure depending on the annealing temperature.

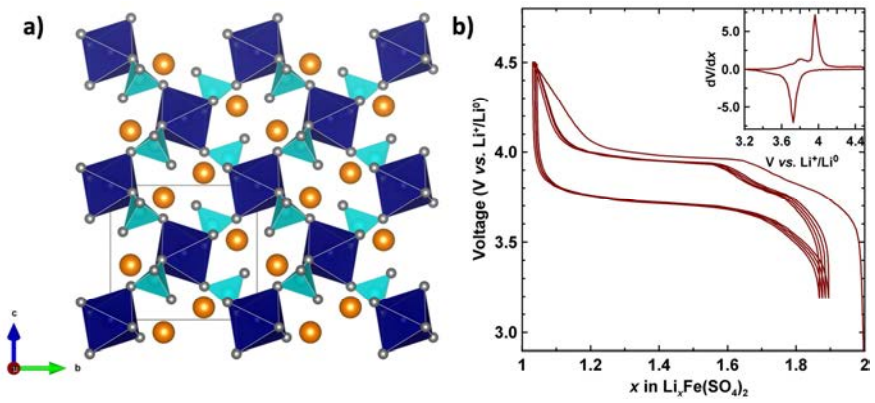

Figure III.1: a) Representation of the structure of monoclinic $Li_2Fe(SO_4)_2$. The SO_4 tetrahedra and FeO_6 octahedra are shown in turquois and blue, respectively. Oxygen and lithium atoms are illustrated by grey and orange balls. b) Respective galvanostatic curve. The inset shows the corresponding derivative curve dx/dV.[207]

Upon charge, close to 1 Li^+ can be extracted from monoclinic $Li_2Fe(SO_4)_2$, while 0.86 Li^+ are reinserted during discharge (Figure III.1b) resulting in a capacity of 88 $mAh{\cdot}g^{-1}$. Note the presence of a sloping contribution located at around 3.7 V *vs*. Li^+/Li^0 at the beginning of the charge process. However, XRD studies on the ball-milled electrode sample did not show any modification of the pristine material. To grasp full insight into this issue, combined ^7Li NMR and Mössbauer experiments were performed on the as-prepared material that was ball-milled up to 60 min.[144] It can be seen in Figure III.2b and 2c that a second phase (green line in Mössbauer and NMR spectra) gradually grows upon ball-milling. The broader line width of the growing Li peak in the ^7Li NMR spectra suggests that this Li atom is located in an amorphous phase. This would be coherent with the fact that no additional peaks were observed in the XRD pattern. Moreover, the growing secondary phase coincides with an increasing sloping contribution in the voltage-composition trace (Figure III.2a) suggesting a correlation between the two of them. Since sulfate-based materials present a rich crystal chemistry and are prone to polymorphism (*e.g*. $LiFeSO_4F$, $KFeSO_4F$, $LiFeSO_4OH$)[150,165,180,182,209,210] and bearing in mind that orthorhombic structures for $Li_2Ni(SO_4)_2$ and $Li_2Zn(SO_4)_2$ were reported, we decided to carefully revisit the synthesis of monoclinic $Li_2Fe(SO_4)_2$.[147,211]

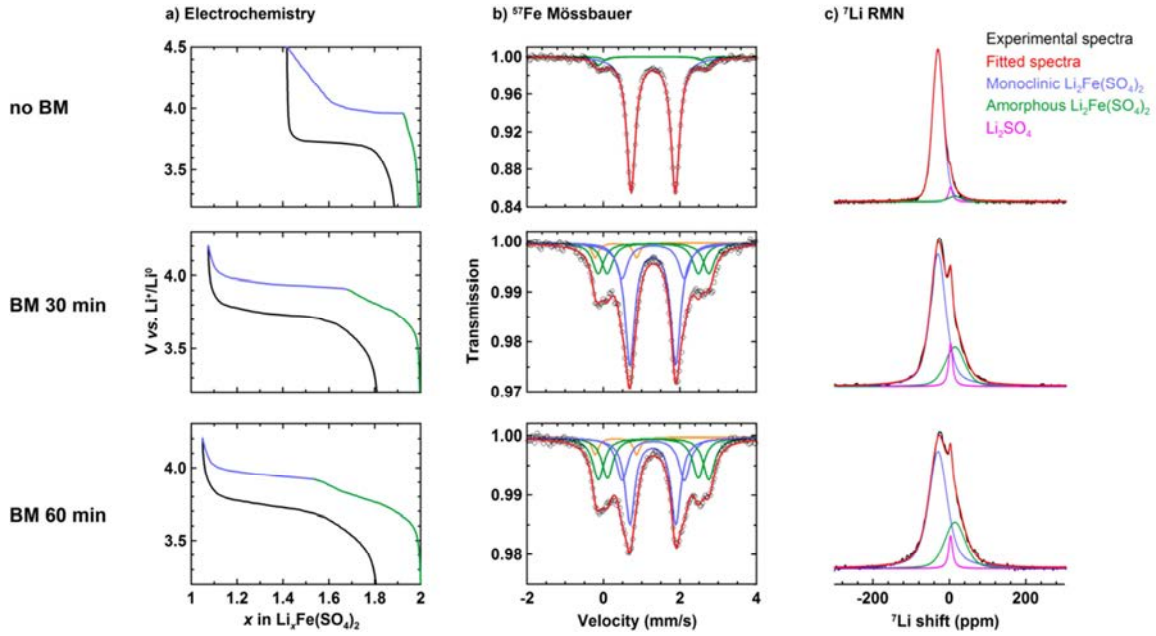

Figure III.2: a) Voltage-composition traces, b) ^{57}Fe Mössbauer spectra, and c) solid-state ^{7}Li NMR spectra (central band) obtained for different electrode materials made of the monoclinic $Li_2Fe(SO_4)_2$ active material mixed with carbon SP. Increasing the ball-milling (BM) time increases the sloping part (green) of the charge curve at the expense of the plateau (blue), which is correlated with the appearance of different iron and lithium environments (see legend) observed in the ^{57}Fe Mössbauer and solid-state ^{7}Li NMR spectra.[144,212]

III.2. Synthesis of a novel $Li_2M(SO_4)_2$ polymorph

Since this amorphous phase formed during ball-milling of monoclinic $Li_2Fe(SO_4)_2$, we attempted to isolate it by a mechano-chemical approach. We mixed stoichiometric amounts of Li_2SO_4 and anhydrous $FeSO_4$, which was prepared from commercial $FeSO_4.7H_2O$ through a two-step procedure in EMI-TFSI at 120 °C to form $FeSO_4.H_2O$ that was further dehydrated at 270 °C under Ar/H_2 atmosphere. The precursors were loaded into an under vacuum closed stainless-steel container and ball-milled using a Retsch PM100 planetary miller (500 rpm) and a ball-to-powder ratio of around 40. The milling time was separated into 30 min steps with 15 min pauses and a reverse milling direction between each step. Analyses of the 30 min ball-milled sample (Figure III.3) reveal the appearance of weak diffraction peaks, which grew in intensity with increased milling time. After 5 to 10 hours of milling we obtained a rather well-crystallized sample that contained no traces of the sulfate precursors implying the growth of a new compound with the composition $Li_2Fe(SO_4)_2$.

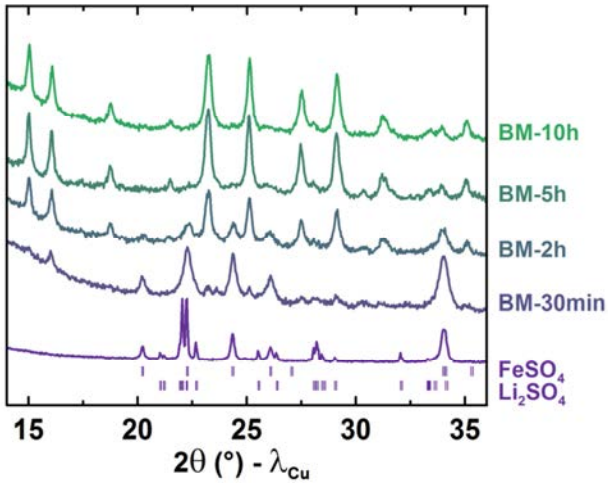

Figure III.3: Evolution of the XRD patterns of a stoichiometric mixture of Li_2SO_4 and $FeSO_4$ ball-milled (Retsch PM100 planetary miller) for different times, showing the progressive formation of a new $Li_2Fe(SO_4)_2$ phase.

A similar synthesis protocol was applied for the Co-, Ni-, Mn and Zn-based phases. $Li_2Co(SO_4)_2$, $Li_2Ni(SO_4)_2$ and $Li_2Zn(SO_4)_2$ were prepared through ball-milling the precursors for 1 h, 5 h and 7 h, respectively. Occasionally and when specified, the resulting ball-milled powders were pressed into a pellet and annealed at around 200°C to improve the crystallinity of the samples. For the case of magnesium, 18 hours of ball-milling resulted in a mixture of the targeted $Li_2Mg(SO_4)_2$ compound and the previously reported $Li_2Mg_2(SO_4)_3$ phase[213]. Curiously, all our attempts to stabilize an analogous manganese-based phase through mechanical milling remained unsuccessful and systematically led to the formation of the monoclinic phase.

Scanning electron microscopy (SEM) coupled with energy-dispersive X-ray diffraction (EDX) measurements of the new $Li_2Co(SO_4)_2$ phase revealed a Co:S ratio of 1:2 and hence confirmed the stoichiometry of the novel polymorph. Transmission electron microscopy (TEM) performed on the same phase showed the formation of particle aggregates with crystallite sizes in the sub-micrometer range (Figure III.4).

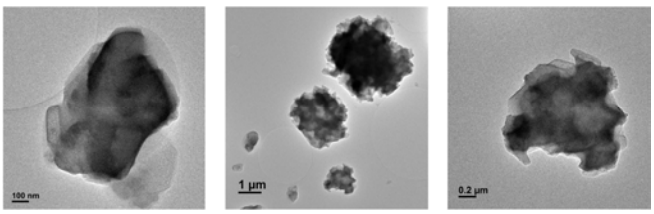

Figure III.4: TEM pictures of orthorhombic $Li_2Co(SO_4)_2$ showing crystalline particle aggregates in the micrometer range.

III.3. Characterization of the $Li_2M(SO_4)_2$ polymorph

III.3.1. Structure of orthorhombic $Li_2M(SO_4)_2$

The Rietveld refinement of the XRD pattern of $Li_2Fe(SO_4)_2$, which was recorded with a Panalytical X'Pert Pro MPD diffractometer equipped with a cobalt source ($\lambda_{Co\text{-}K\alpha1}$ = 1.78897 and $\lambda_{Co\text{-}K\alpha2}$ = 1.79285) and an X'Celerator detector, was performed starting with the structural model proposed by Isasi *et al.* for $Li_2Ni(SO_4)_2$ and using the Rietveld method as implemented in the FullProf program.[203,208,214] The final result is shown in Figure III.5a. Indeed, $Li_2Fe(SO_4)_2$ is isostructural to $Li_2Ni(SO_4)_2$ and crystallizes in the orthorhombic space group *Pbca*. To confirm the structure and to locate the Li ions in the unit cell, high-resolution neutron powder diffraction experiments were performed on the D20 diffractometer at the Institut Laue Langevin (ILL, Grenoble) with a wavelength λ= 1.544 Å at 30 K. The resulting Rietveld refinement on the NPD pattern, where we freely refined all atomic positions and B_{iso}, is shown in Figure III.5b. The lattice parameters as well as the structural data deduced from NPD experiments of the new orthorhombic $Li_2Fe(SO_4)_2$ phase are presented in Table III.1. All atoms are located in the general Wyckoff site *8c*. Note that there are two crystallographic Li sites. BVS analysis confirmed that all atoms present the expected formal charge.

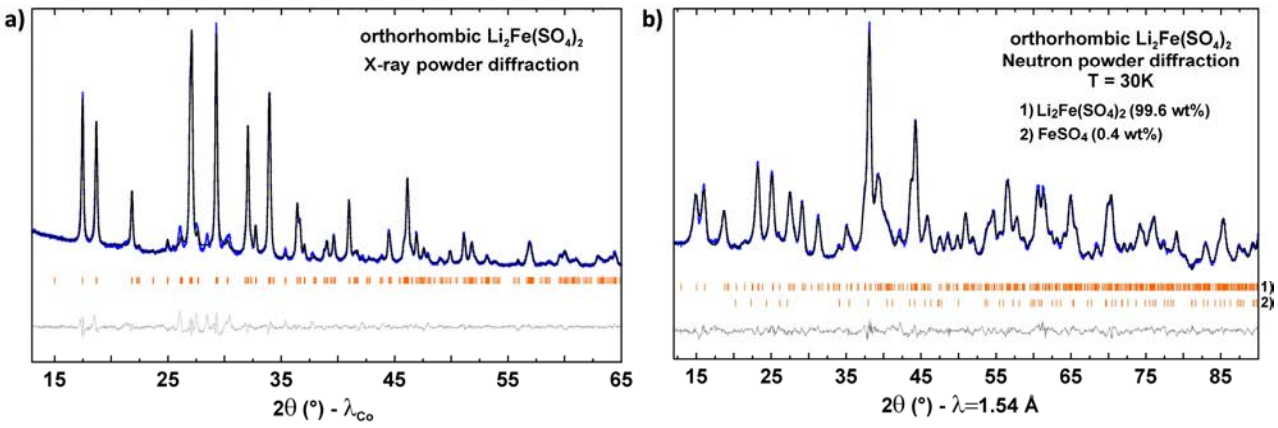

Figure III.5: Rietveld refinements of a) XRD pattern and b) NPD pattern orthorhombic $Li_2Fe(SO_4)_2$. Blue, black and grey lines represent the experimental, calculated and difference pattern, respectively. Bragg positions are shown as orange bars. Tiny impurities are due to residual precursors.

Table III.1: Crystallographic data and atomic positions of orthorhombic $Li_2Fe(SO_4)_2$ determined from Rietveld refinements of its NPD pattern recorded at 30 K. All atoms belonging to the same chemical species were considered to have the same B_{iso}. Results of bond valence sum (BVS) analysis are also indicated.

Orthorhombic $Li_2Fe(SO_4)_2$

P b c a			R_{Bragg} = 2.49 %			χ^2 = 5.68	
a = 9.2798(9) Å		*b* = 9.2089(11) Å	*c* = 13.6765(14) Å			*V* = 1168.8(3) Å^3	
Atom	Wyckoff position	Occupancy	*x*/*a*	*y*/*b*	*z*/*c*	B_{iso} (Å^2)	BVS
Li1	8*c*	1	0.489(7)	0.712(7)	0.355(5)	1.3(2)	0.91(8)
Li2	8*c*	1	0.747(6)	0.560(5)	0.624(5)	1.3(2)	1.20(9)
Fe	8*c*	1	0.8635(12)	0.6024(14)	0.3763(10)	0.62(4)	2.06(5)
S1	8*c*	1	0.6600(14)	0.8129(13)	0.5109(10)	1.20(11)	5.67(14)
S2	8*c*	1	0.5777(15)	0.4250(15)	0.2734(10)	1.20(11)	5.70(15)
O1	8*c*	1	0.5010(13)	0.8005(19)	0.5198(12)	0.84(2)	1.90(8)
O2	8*c*	1	0.7107(17)	0.9667(13)	0.4997(12)	0.84(2)	1.95(8)
O3	8*c*	1	0.687(2)	0.7288(16)	0.4193(10)	0.84(2)	2.00(8)
O4	8*c*	1	0.7455(17)	0.7411(18)	0.5904(11)	0.84(2)	1.90(10)
O5	8*c*	1	0.4847(16)	0.500(2)	0.3470(11)	0.84(2)	1.80(10)
O6	8*c*	1	0.533(2)	0.4643(17)	0.1720(9)	0.84(2)	2.01(8)
O7	8*c*	1	0.5684(19)	0.2633(12)	0.2786(14)	0.84(2)	2.06(9)
O8	8*c*	1	0.7294(15)	0.478(3)	0.2780(13)	0.84(2)	1.91(9)

The Rietveld refinements and structural data of orthorhombic $Li_2Ni(SO_4)_2$, $Li_2Co(SO_4)_2$ and $Li_2Zn(SO_4)_2$ (prepared via ceramic route or ball-milling) deduced from XRD patterns recorded using either a Bruker D8 Advance diffractometer ($\lambda_{Cu\text{-}K\alpha1}$ = 1.54056 Å, $\lambda_{Cu\text{-}K\alpha2}$ = 1.54439) or a Panalytical X'Pert Pro MPD diffractometer ($\lambda_{Co\text{-}K\alpha1}$ = 1.78897 Å, $\lambda_{Co\text{-}K\alpha2}$ = 1.79285 Å) are shown in Figure III.6 and Table III.2 -Table III.4.

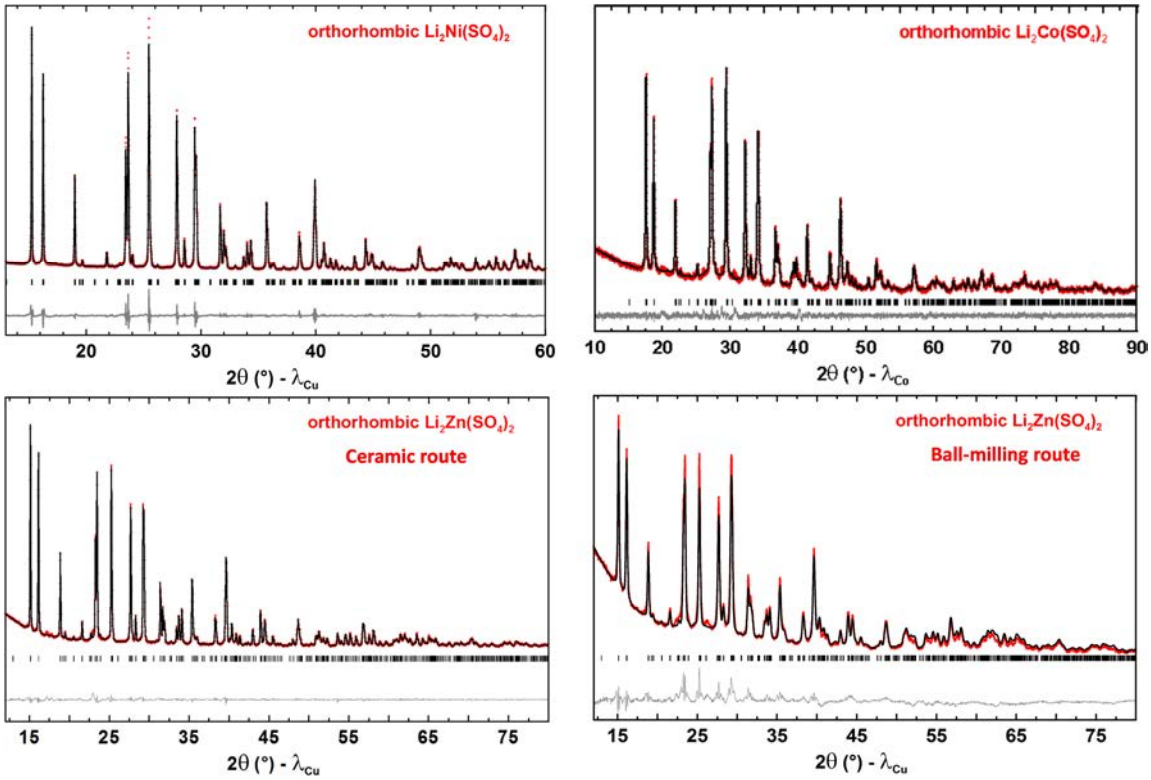

Figure III.6: Results of the Rietveld refinements of the XRD pattern of the orthorhombic $Li_2Ni(SO_4)_2$ (ceramic route), $Li_2Co(SO_4)_2$ (ball-milling route) and $Li_2Zn(SO_4)_2$ (prepared via ceramic and ball-milling route). Red crosses, black and grey line represent the observed, calculated and difference patterns, respectively. The positions of the Bragg reflections are shown as vertical black bars.

Table III.2: Crystallographic data and atomic positions of the orthorhombic $Li_2Ni(SO_4)_2$ prepared via ceramic route determined from the Rietveld refinement of its XRD pattern. All atoms belonging to the same chemical species were considered to have the same B_{iso}. Results of bond valence sum (BVS) analysis are also indicated.

Orthorhombic $Li_2Ni(SO_4)_2$

P b c a			R_{Bragg} = 2.44 %			χ^2 = 7.4	
a = 9.13999 (12) Å	*b* = 9.02400 (12) Å		*c* = 13.59113 (18) Å			*V* = 1120.99 (3) Å^3	
Atom	Wyckoff position	Occupancy	*x/a*	*y/b*	*z/c*	B_{iso} (Å^2)	BVS
Li1	8*c*	1	0.466 (4)	0.718 (4)	0.362 (4)	1.5 (0)	1.04 (5)
Li2	8*c*	1	0.719 (4)	0.538 (4)	0.635 (4)	1.5 (0)	0.97 (6)
Ni	8*c*	1	0.8617 (4)	0.6030 (4)	0.3778 (3)	0.13 (17)	1.90 (3)
S1	8*c*	1	0.6603 (8)	0.8131 (7)	0.5089 (5)	0.1 (3)	5.94 (12)
S2	8*c*	1	0.5755 (7)	0.4303 (7)	0.2735 (5)	0.1 (3)	5.87 (12)
O1	8*c*	1	0.5003 (13)	0.7967 (13)	0.5236 (11)	0.3 (3)	1.90 (6)
O2	8*c*	1	0.7050 (12)	0.9707 (15)	0.4963 (12)	0.3 (3)	1.92 (7)
O3	8*c*	1	0.6886 (14)	0.7281 (14)	0.4187 (9)	0.3 (3)	2.04 (6)
O4	8*c*	1	0.7422 (10)	0.7561 (14)	0.5939 (13)	0.3 (3)	1.88 (7)
O5	8*c*	1	0.4804 (14)	0.4993 (12)	0.3505 (10)	0.3 (3)	2.01 (7)
O6	8*c*	1	0.5230 (13)	0.4617 (12)	0.1720 (9)	0.3 (3)	1.90 (6)
O7	8*c*	1	0.5725 (13)	0.2656 (15)	0.2752 (11)	0.3 (3)	2.01 (7)
O8	8*c*	1	0.7246 (16)	0.4883 (15)	0.2750 (11)	0.3 (3)	2.07 (7)

Table III.3: Crystallographic data and atomic positions of the orthorhombic $Li_2Co(SO_4)_2$ prepared via ball-milling route determined from the Rietveld refinement of its XRD pattern. All atoms belonging to the same chemical species were considered to have the same B_{iso}. Results of bond valence sum (BVS) analysis are also indicated.

Orthorhombic $Li_2Co(SO_4)_2$

P b c a			R_{Bragg} = 1.99 %			χ^2 = 1.63	
a = 9.20688 (9) Å		*b* = 9.10175(9) Å	*b* = 13.71190(16) Å			*V* = 1149.039(2) Å^3	
Atom	Wyckoff position	Occupancy	*x/a*	*y/b*	*z/c*	B_{iso} (Å^2)	BVS
Li1	8*c*	1	0.48303(2)	0.72126(3)	0.35835(3)	1.500(0)	0.97(38)
Li2	8*c*	1	0.72349(3)	0.53352(3)	0.62806(3)	1.500(0)	1.01(43)
Co	8*c*	1	0.86178(3)	0.60185(3)	0.37681(2)	1.427(10)	2.08(24)
S1	8*c*	1	0.66120(7)	0.81462(5)	0.50953(4)	1.360(11)	5.87(98)
S2	8*c*	1	0.57515(5)	0.43129(6)	0.27050(3)	1.360(11)	5.52(83)
O1	8*c*	1	0.49807(10)	0.80082(10)	0.52608(8)	1.093(12)	1.78(42)
O2	8*c*	1	0.71029(9)	0.96712(13)	0.49606(9)	1.093(12)	2.04(58)
O3	8*c*	1	0.68838(9)	0.73419(11)	0.41870(7)	1.093(12)	2.08(48)
O4	8*c*	1	0.74203(7)	0.75467(11)	0.59307(11)	1.093(12)	1.85(59)
O5	8*c*	1	0.48154(10)	0.50184(10)	0.34816(7)	1.093(12)	1.87(49)
O6	8*c*	1	0.52322(10)	0.46143(9)	0.17067(7)	1.093(12)	2.07(45)
O7	8*c*	1	0.57732(9)	0.26572(11)	0.27880(8)	1.093(12)	1.94(50)
O8	8*c*	1	0.73039(12)	0.48742(11)	0.27686(7)	1.093(12)	1.83(48)

Table III.4: Crystallographic data and atomic positions of the orthorhombic $Li_2Zn(SO_4)_2$ prepared via ceramic route determined from the Rietveld refinement of its XRD pattern. All atoms belonging to the same chemical species were considered to have the same B_{iso}. Results of bond valence sum (BVS) analysis are also indicated.

Orthorhombic $Li_2Zn(SO_4)_2$

P b c a			R_{Bragg} = 2.26 %			χ^2 = 5.0	
a = 9.21805(9) Å		*b* = 9.10553(8) Å	*c* = 13.66601(14) Å			*V* = 1147.060(19) Å^3	
Atom	Wyckoff position	Occupancy	*x/a*	*y/b*	*z/c*	B_{iso} (Å^2)	BVS
Li1	8*c*	1	0.46626(3)	0.73490(3)	0.36438(3)	1.500 (0)	0.98(4)
Li2	8*c*	1	0.72366(3)	0.54908(3)	0.63386(2)	1.500 (0)	1.02(2)
Zn	8*c*	1	0.86158(2)	0.60404(2)	0.37746(16)	0.882(6)	2.08(22)
S1	8*c*	1	0.66328(6)	0.81300(5)	0.50916(3)	0.896(9)	5.91(86)
S2	8*c*	1	0.57522(5)	0.43205(5)	0.27194(3)	0.896(9)	5.81(84)
O1	8*c*	1	0.50422(9)	0.79791(9)	0.52200(8)	0.809(9)	1.92(43)
O2	8*c*	1	0.70861(9)	0.96902(10)	0.49707(8)	0.809(9)	1.92(43)
O3	8*c*	1	0.68960(9)	0.72844(9)	0.41760(7)	0.809(9)	2.00(44)
O4	8*c*	1	0.74289(7)	0.75266(9)	0.59204(9)	0.809(9)	2.00(56)
O5	8*c*	1	0.48067(1)	0.50253(8)	0.34832(7)	0.809(9)	1.81(45)
O6	8*c*	1	0.51764(10)	0.46368(8)	0.17148(7)	0.809(9)	2.04(43)
O7	8*c*	1	0.57028(10)	0.26973(10)	0.27812(7)	0.809(9)	2.03(49)
O8	8*c*	1	0.72345(12)	0.48911(10)	0.27401(7)	0.809(9)	2.07(53)

The structure of the orthorhombic $Li_2M(SO_4)_2$ phases is based on isolated MO_6 octahedra linked though SO_4 tetrahedra via the oxygen atoms (Figure III.7). Each octahedron is linked to six SO_4 tetrahedra, whereas each SO_4 group is only bound to three MO_6 octahedra, with the unshared fourth corner of the tetrahedral pointing into open channels where the lithium ions reside. The lithium cations occupy distorted octahedral sites in these tunnels, thus forming zig-zag chains of edge-sharing LiO_6 octahedra running along the *b*-axis. The structures of the orthorhombic and monoclinic polymorphs (Figure III.8a and Figure III.8b) differ solely in the connectivity of the SO_4 tetrahedra and the MO_6 octahedra. Moreover, we state that the M-M distances are shorter for the orthorhombic phase, which leads to a higher density compared to its monoclinic counterpart (ρ_{ortho} ~ 2.97-3.14 g/cm^3 *vs.* ρ_{mono} ~ 2.55-2.99 g/cm^3) (Figure III.8c).

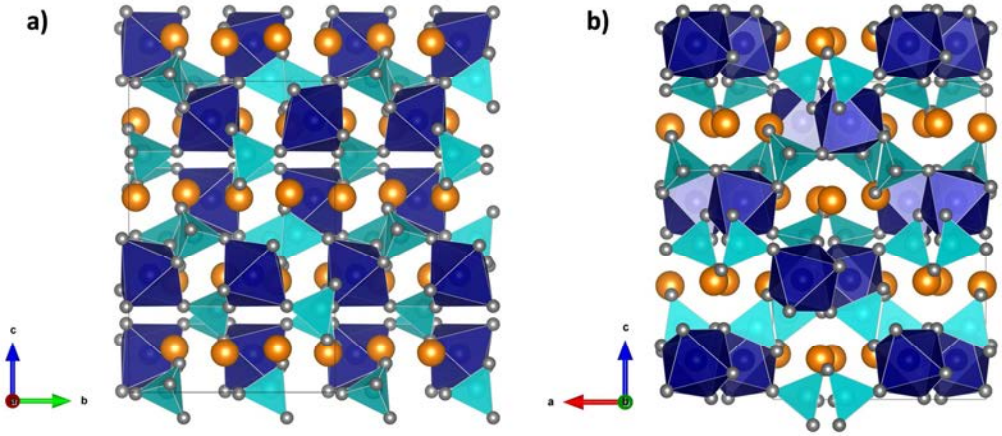

Figure III.7: Representation of the orthorhombic $Li_2M(SO_4)_2$ structure viewed along a) [100] and b) [010]. MO_6 octahedra and SO_4 tetrahedra are blue and turquois, respectively. Lithium cations are shown as orange spheres, O atoms as grey balls.

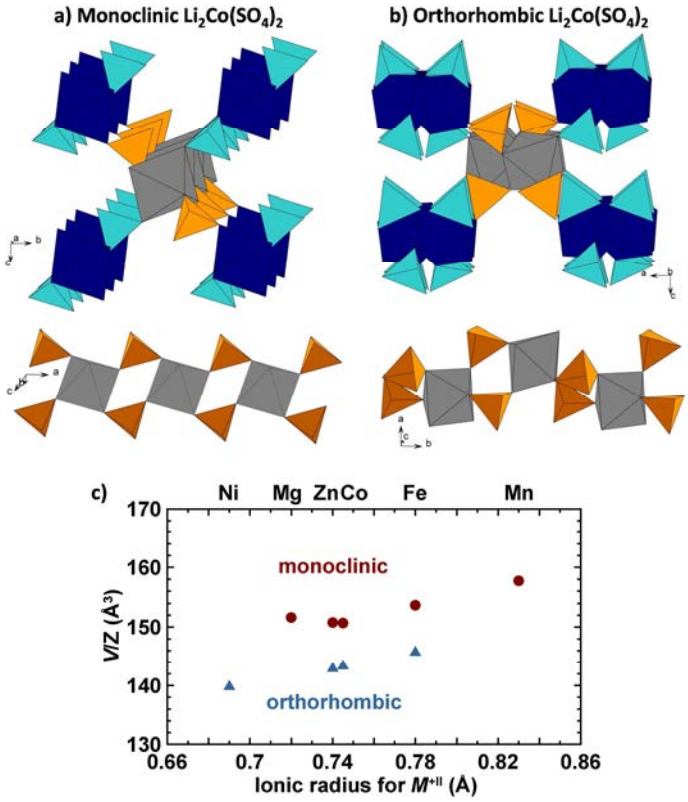

Figure III.8: Comparison of the MO_6 and SO_4 connectivity in the 3D frameworks of the a) monoclinic and b) orthorhombic structures. In both structures, the MO_6 octahedra (blue and grey) are isolated from each other and are only linked through six corner-sharing SO_4 tetrahedra (turquois and orange). The main structural differences between the two polymorphs are associated with the position of the bridging SO_4 groups (orange) around the MO_6 octahedra within the chains running along the *a*-axis in the monoclinic structure and the *b*-axis in the orthorhombic structure. c) Evolution of the volume per formula unit as a function of the ionic radii of the divalent cations M^{II+} in the $Li_2M(SO_4)_2$ series (*M* = Ni, Mg, Zn, Co, Fe, Mn). Blue and red points represent the orthorhombic and monoclinic polymorphs, respectively.

The ^{57}Fe Mössbauer spectrum of orthorhombic $Li_2Fe(SO_4)_2$ (performed in collaboration with M. Tahar-Sougrati, ICGM Montpellier; see Annexe for details) presents a Fe^{2+} doublet with an isomer shift of 1.27(1) mm/s and a quadrupole splitting of 3.05(1) mms/s (Table III.5). The close quadrupole splitting (QS) of the crystallized orthorhombic $Li_2Fe(SO_4)_2$ phase and the amorphous phase observed in monoclinic $Li_2Fe(SO_4)_2$ subjected to extended ball-milling suggest that we have similar Fe-environments in both samples (Table III.5). Mössbauer studies therefore confirm that the novel orthorhombic phase is indeed identical to the amorphous phase observed in the monoclinic sample upon ball-milling. ^{7}Li NMR studies (Figure III.9) conducted by R. Messinger (CEMHTI, Orléans; see Annexe for details) led to the same conclusion since the spectra of orthorhombic $Li_2Fe(SO_4)_2$ corresponds to the one for the amorphous phase observed in

monoclinic $Li_2Fe(SO_4)_2$ (Figure III.2c). The fact that this amorphous orthorhombic phase displays an electrochemical contribution to the galvanostatic cycling of its monoclinic counterpart motivated us to study in detail the electrochemical performance of crystallized orthorhombic $Li_2Fe(SO_4)_2$.

Table III.5: ^{57}Fe Mössbauer parameters of the orthorhombic $Li_2Fe(SO_4)_2$. For comparison, ^{57}Fe Mössbauer parameters of as-prepared monoclinic $Li_2Fe(SO_4)_2$ and the secondary amorphous phase that was observed in monoclinic $Li_2Fe(SO_4)_2$ after 20 min ball-malling are indicated. IS represents the isomer shift relative to metallic iron standard at room temperature, while QS and LW are the quadrupole splitting and the line width, respectively.

	Attribution	IS (mm/s)	QS (mm/s)	LW (mm/s)
monoclinic $Li_2Fe(SO_4)_2$	crystallized phase	1.30(1)	1.16(1)	0.27(1)
Secondary phase in ball milled monocl. $Li_2Fe(SO_4)_2$	amorphous phase	1.30(1)	2.44(10)	0.34(4)
orthorhombic $Li_2Fe(SO_4)_2$	well crystallized phase	1.27(1)	3.05(1)	0.24(1)

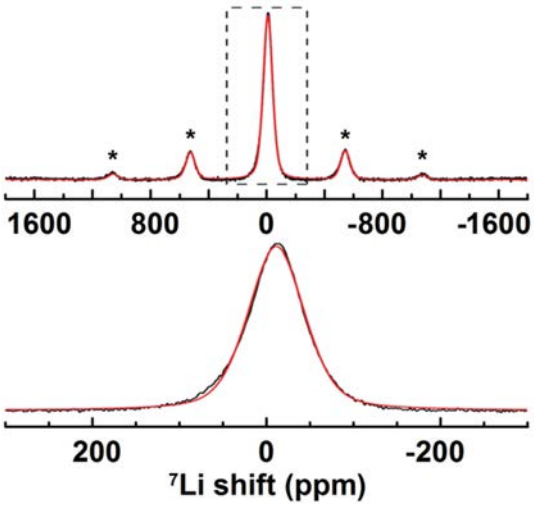

Figure III.9: Solid-state ^{7}Li NMR spectrum (top, entire spectrum; bottom, central band) of orthorhombic $Li_2Fe(SO_4)_2$ obtained after 10 hours of planetary ball-milling.

Table III.6: Solid-state ^{7}Li solid-state NMR parameters of both the monoclinic and the orthorhombic polymorphs of $Li_2Fe(SO_4)_2$, acquired at 7.05 T and 62.5 kHz MAS under ambient conditions. (PSA=paramagnetic shift anisotropy)

	Isotropic ^{7}Li shift (ppm)	Gaussian/ Lorentzian ratio	Full-width-half-maximum (ppm)	δPSA (ppm)	ηPSA
monoclinic $Li_2Fe(SO_4)_2$	32	0.72	34	1110	0.4
orthorhombic $Li_2Fe(SO_4)_2$	-12	0.64	77	725	0.9

III.3.2. Electrochemistry of orthorhombic $Li_2Fe(SO_4)_2$

$Li_2Fe(SO_4)_2$ was ball milled for 20 min with carbon SP (20 wt%) and loaded into a Swagelok-type cell against a lithium metal anode. The cycling properties were tested using $LiClO_4$ 1M in PC as well as LP30 as electrolyte. $LiClO_4$ was used since in previous studies a slight reactivity of monoclinic $Li_2Fe(SO_4)_2$ towards LP30 and especially HF was observed.[207]

A typical voltage-composition trace obtained for the orthorhombic $Li_2Fe(SO_4)_2$ cycled at a rate of C/20 is shown in Figure III.10a. It reveals the presence of two successive potential plateaus centred at 3.73 V and 3.85 V *vs.* Li^+/Li^0 also shown by the corresponding d*x*/dV derivative curve and GITT (Galvanostatic Intermittent Titration Technique) experiments (Figure III.10c). During the first charge up to 4.5 V *vs.* Li^+/Li^0, about 0.95 Li^+ are removed from $Li_2Fe(SO_4)_2$, while 0.85 Li^+ are reinserted upon the subsequent discharge, resulting in a reversible capacity of around 91 $mAh \cdot g^{-1}$ (theoretical specific capacity: 102 $mAh \cdot g^{-1}$) and a good capacity retention over more than 10 cycles (Figure III.10b).

Orthorhombic $Li_2M(SO_4)_2$ with *M* = Co, Zn, Mg and Ni showed no electrochemical response. This can be explained by the fact that Zn and Mg are electrochemically inactive. Further, the expected potentials of the Co^{3+}/Co^{2+} and Ni^{3+}/Ni^{2+} redox couples are higher than the Fe^{3+}/Fe^{2+} couple and therefore probably outside of the stability window of commonly used electrolytes.

To follow the structural changes during the electrochemical cycling, we performed *in situ* XRD experiments on charge and discharge (Figure III.11a). Upon charge, we observe two successive biphasic processes, where the Bragg peaks of the pristine phase disappear while new peaks shifted to higher angles and gained in intensity until the formation of "$Li_{1.0}Fe(SO_4)_2$" at the end of charge (Figure III.11b). Between the two potential plateaus, presumably an intermediate "$Li_{1.5}Fe(SO_4)_2$" phase forms. The redox process is reversible since the pattern recorded at the end of discharge superimposes well with the XRD pattern of pristine orthorhombic $Li_2Fe(SO_4)_2$ (Figure III.11c).

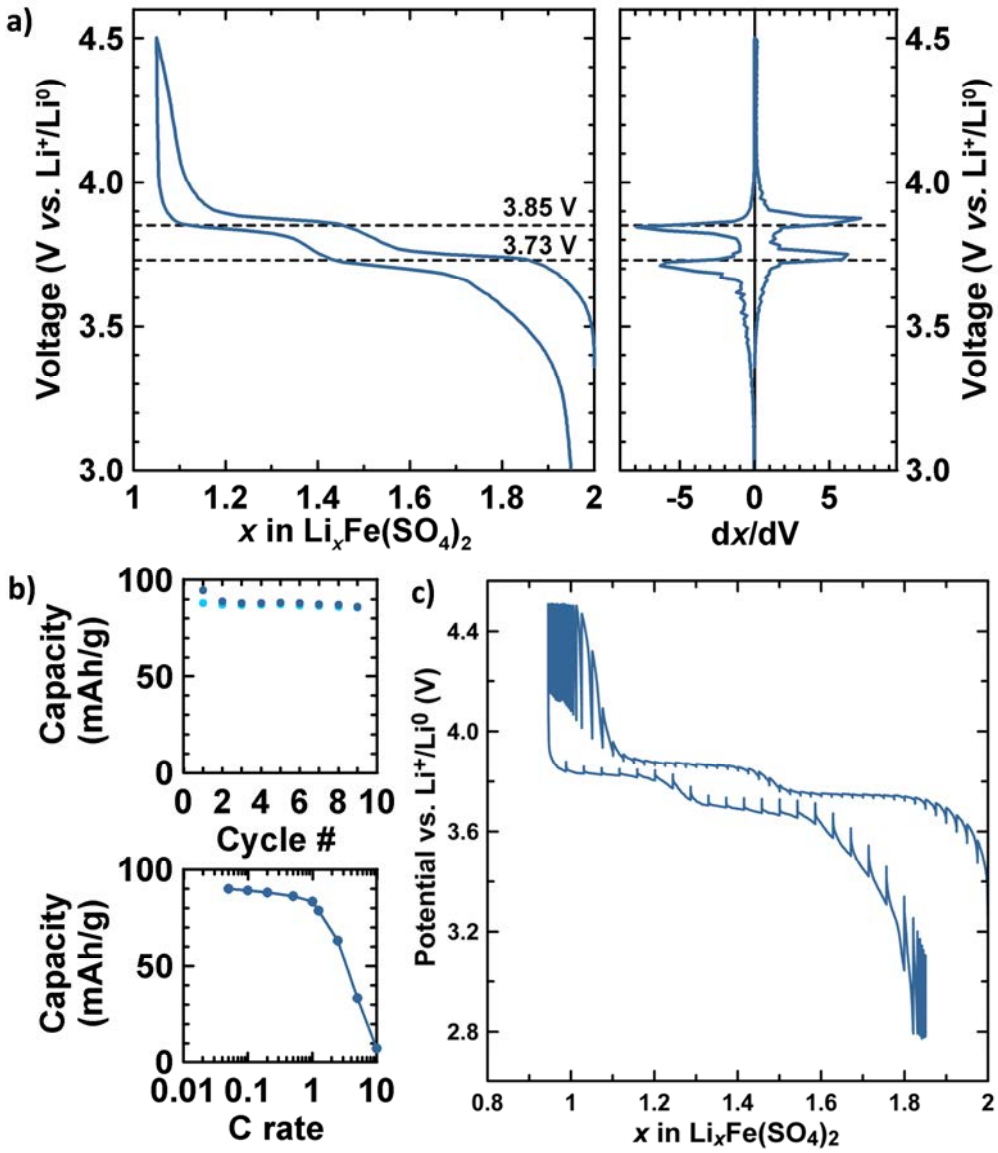

Figure III.10: a) Galvanostatic curve and its derivative of orthorhombic $Li_2Fe(SO_4)_2$ show two potential plateaus at 3.73 V and 3.85 V. The low polarization (a), the capacity retention after 10 charge-discharge cycles and the capacity retention (b) indicate good insertion kinetics for the orthorhombic polymorph. c) Typical GITT curve obtained for orthorhombic $Li_2Fe(SO_4)_2$ compound. For this experiment, the cell was charged and discharged using a current equivalent to C/20 for steps of 30 minutes, alternated with open circuit stages of 5 hours.

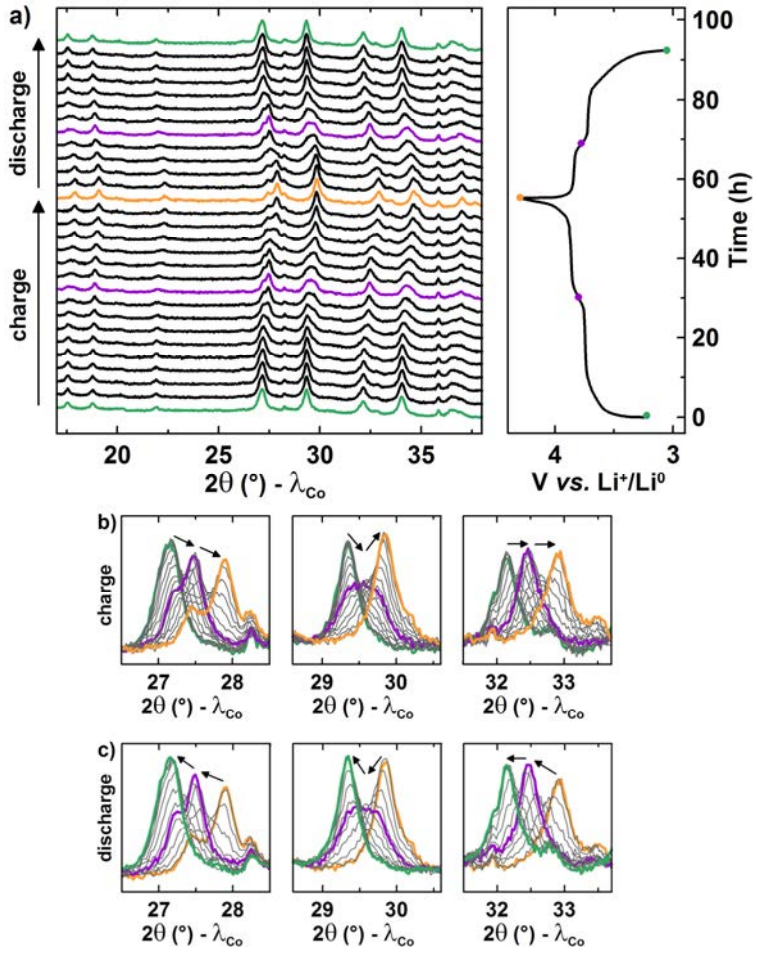

Figure III.11: *In situ* XRD measurement of the orthorhombic $Li_2Fe(SO_4)_2$ active material, acquired during the first charge/discharge cycle. (a) Evolution of the XRD patterns along the electrochemical curve. The green, violet and orange patterns are assigned to the pristine $Li_2Fe(SO_4)_2$ compound, the half-delithiated intermediate phase "$Li_{1.5}Fe(SO_4)_2$", and the delithiated phase "$Li_{1.0}Fe(SO_4)_2$", respectively. The bottom panels display zoomed-in areas of relevant peaks, which show the two subsequent bi-phasic mechanisms that occur during (b) charge and (c) discharge.

The delithiated phase $Li_{1.0}Fe(SO_4)_2$ was also prepared by chemically oxidizing orthorhombic $Li_2Fe(SO_4)_2$ using an excess of NO_2BF_4 dissolved in acetonitrile. The XRD pattern obtained for this chemically delithiated phase is in very good agreement with the XRD pattern recorded at the end of charge during the *in situ* XRD experiment. The Bragg reflections observed for $Li_{1.0}Fe(SO_4)_2$ could be indexed in the same orthorhombic space group *Pbca* with the lattice parameters a = 9.1652(4) Å, b = 8.9304(4) Å, c = 13.4532(8) Å and V = 1101.12(9) Å^3 resulting in a volume reduction of about 6 %. The Rietveld refinement on XRD pattern of this phase is shown in Figure III.12a. The evolution of the lattice parameters is uniformly distributed along *a*, *b* and *c*-directions and can be explained by the size-reduction of the FeO_6 octahedra due to the

oxidation of Fe^{2+} to Fe^{3+}.

^{57}Fe Mössbauer spectroscopy performed on the delithiated orthorhombic $Li_{1.0}Fe(SO_4)_2$ confirmed the complete oxidation of Fe^{2+} to Fe^{3+}. Next, a solid-state ^{7}Li NMR spectrum was acquired on the chemically oxidized orthorhombic $Li_{1.0}Fe(SO_4)_2$ phase to characterize the local lithium environments (Figure III.12b). The spectrum shows an intense ^{7}Li signal at 28 ppm with a broad spinning-side-band manifold associated with lithium within well-crystallized $Li_{1.0}Fe(SO_4)_2$ domains. The different isotropic ^{7}Li shift in this structure compared to pristine orthorhombic $Li_2Fe(SO_4)_2$ (-12 ppm) indicates that the lithium atoms experience different average local environments after chemical oxidation, consistent with the slight structural distortions and volume changes discussed above. The narrower line width (full-width-half-maximum = 14 ppm) compared to the pristine phase (77 ppm) is likely due to enhanced lithium mobility within the crystal structure upon partial lithium removal, where faster lithium motions partially average the electron-nuclear interactions that broaden the ^{7}Li NMR linewidths. The small peak at 52 ppm is due to a slight impurity in the chemically oxidized sample.

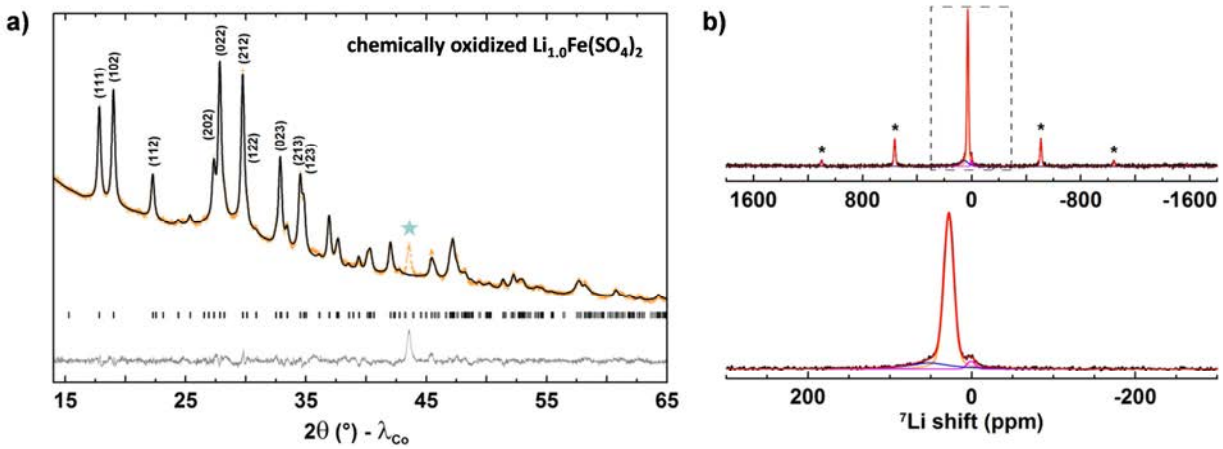

Figure III.12: a) Rietveld refinement of the XRD pattern of chemically oxidized orthorhombic $Li_{1.0}Fe(SO_4)_2$. The orange crosses, black line, and grey line represent the measured, calculated, and difference patterns, respectively. The positions of the Bragg reflections are shown as black bars. The blue star indicates a peak assigned to a homemade anoxic chamber. b) Solid-state ^{7}Li NMR spectrum (top, entire spectrum; bottom, central band) of oxidized orthorhombic $Li_1Fe(SO_4)_2$.

If we compare the electrochemical behaviour of both $Li_2Fe(SO_4)_2$ polymorphs, we can see that the polarization of the orthorhombic phase is lower than the one of its monoclinic counterpart. This suggests better diffusion properties for the former. Moreover, the rate capability plots show that at higher C-rates (*e.g.* 1 C), the orthorhombic phase (Figure III.13, blue line) maintains

90 % of the initial capacity as opposed to only 80 % for the monoclinic polymorph (Figure III.13, red line). This prompted us to investigate in depth the transport properties and redox mechanisms of both $Li_2Fe(SO_4)_2$ polymorphs.

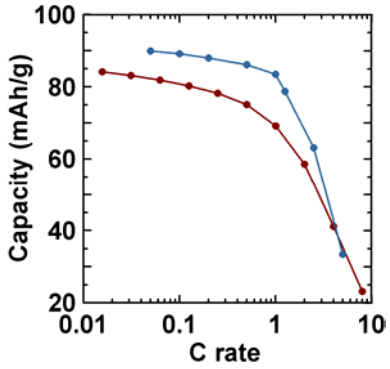

Figure III.13: Capacity retention plots of both monoclinic (red) and orthorhombic (blue) $Li_2Fe(SO_4)_2$ polymorphs.

III.4. Delithiation mechanisms of monoclinic and orthorhombic $Li_2Fe(SO_4)_2$

To shed some light into the delithiation of orthorhombic $Li_2Fe(SO_4)_2$ and the origin of the two redox plateaus, we started with the determination of the lithium positions in the delithiated phases $Li_{1.5}Fe(SO_4)_2$ and $Li_{1.0}Fe(SO_4)_2$. To do so, we performed neutron powder diffraction experiments (NPD) using the D20 diffractometer (ILL, Grenoble) with a high-resolution configuration and a wavelength of λ = 1.544 Å on the delithiated phases (prepared by chemical oxidation with the respective molar amount of NO_2BF_4 in acetonitrile). The Rietveld refinements of the delithiated phases were started from the structural model of the pristine mother phase (space group *Pbca*).

Further, to clarify the lithium distribution on the two crystallographic sites Li1 and Li2, we created Fourier difference maps based on the refinements of the NPD patterns of $Li_2Fe(SO_4)_2$, $Li_{1.5}Fe(SO_4)_2$ and $Li_{1.0}Fe(SO_4)_2$, where solely the $Fe(SO_4)_2$ framework was taken into account. A cross-section of these Fourier maps at z=0.62 is shown in Figure III.14. These maps are plotted so that the largest negative peaks are in blue, while intensities greater than zero are in yellow. The Fourier difference maps present negative domains that correspond to the coherent scattering length of Li (b_{Li}= -1.90 fm). For the pristine $Li_2Fe(SO_4)_2$ compound, the two crystallographically distinct Li1 and Li2 sites can be easily spotted. On delithiation, the Li1 site remains fully occupied, while the density of the Li2 atom gets weaker for the partially

delithiated $Li_{1.5}Fe(SO_4)_2$ sample and finally vanishes for $Li_{1.0}Fe(SO_4)_2$.

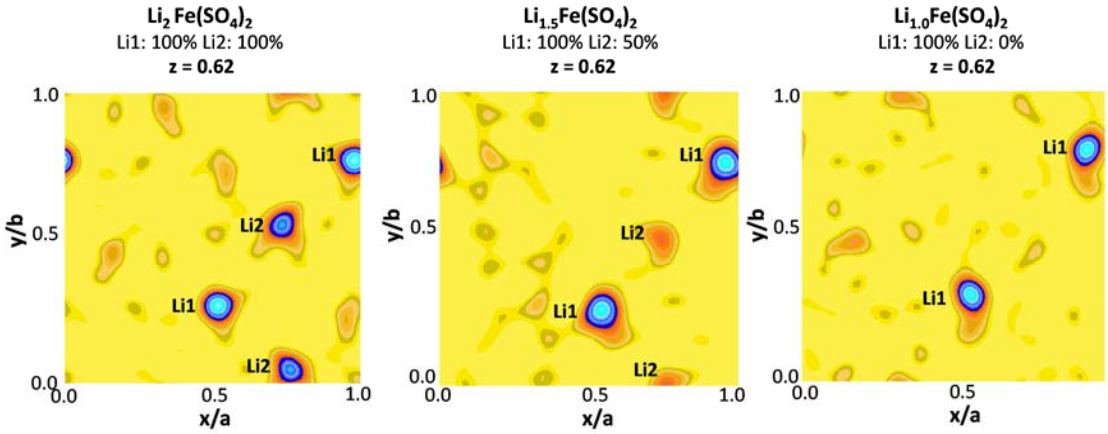

Figure III.14: Difference Fourier maps plotted for z = 0.62, obtained from the refinement of the NPD patterns of the orthorhombic phases $Li_2Fe(SO_4)_2$, $Li_{1.5}Fe(SO_4)_2$ and $Li_{1.0}Fe(SO_4)_2$ by taking into account solely the $Fe(SO_4)_2$ framework. The light blue ellipsoids refer to a negative value and correspond to the positions of the missing lithium cations.

Moreover, we simulated NPD patterns with different occupation ratios for orthorhombic $Li_{1.0}Fe(SO_4)_2$ (Figure III.15). The main impact of the lithium occupation can be spotted in the low angle region, where the intensities of the first three peaks change depending on the site distribution. An empty Li1 site (orange pattern) leads to the highest intensity for the (102) peak (2θ = 16.3°) and the lowest intensity for the (112) and (200) peaks (2θ = 19.2°), while a delithiated Li2 site (green pattern) shows the reverse trend. The best match between the simulated and experimental patterns is obtained for a fully occupied Li1 site and a completely delithiated Li2 site (green pattern) in agreement with our observations in the difference Fourier maps.

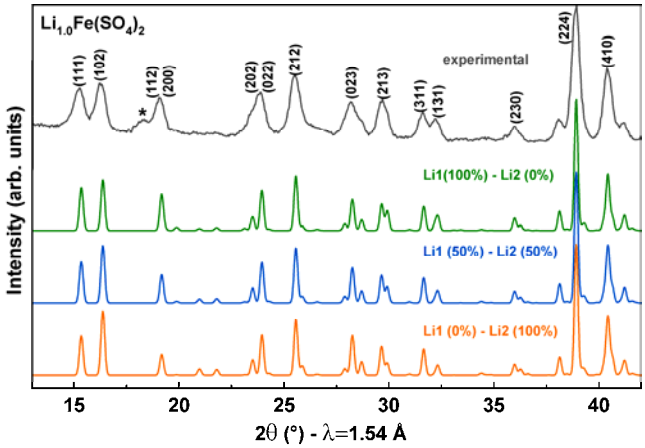

Figure III.15: Simulation of patterns for $Li_{1.0}Fe(SO_4)_2$ with either an unoccupied Li1 site (orange pattern), an unoccupied Li2 site (green pattern) or equally occupied Li1/Li2 sites (blue pattern) and the experimental NPD pattern of $Li_{1.0}Fe(SO_4)_2$ (grey pattern). The star marks a peak attributed to an $FeSO_4 \cdot H_2O$ impurity.

We further tested the various occupation possibilities for Li1 and Li2 during the refinements by fixing the occupation of the two sites. Three scenarios were considered: occupied, half-occupied or empty. The best result was obtained for a fully occupied Li1 site and a half delithiated ($Li_{1.5}Fe(SO_4)_2$) and fully delithiated ($Li_{1.0}Fe(SO_4)_2$) Li2 site. For the final Rietveld refinements of the $Li_{1.5}Fe(SO_4)_2$ and $Li_{1.0}Fe(SO_4)_2$ NPD patterns (Figure III.16) we used soft constraints for the S-O distances and angles, while the Li and Fe atomic positions were freely refined. The obtained structural data for both delithiated phases is given in Table III.7 and Table III.8. The resulting structures are shown in Figure III.17.

Upon Li extraction, the general structural framework composed of FeO_6 octahedra and SO_4 tetrahedra is preserved and only a slight contraction of the structure is observed. The refined cell parameters vary from *a*=9.2798(8) Å , *b*=9.2089(11) Å and *c*=13.6765(14) Å for $Li_2Fe(SO_4)_2$ to *a*=9.1776(3) Å, *b*=9.045(3) Å and to *c*=13.612(4) Å for $Li_{1.5}Fe(SO_4)_2$ and *a*=9.1576(5) Å, *b*=8.9162(5) Å and *c*=13.3978(8) Å for $Li_{1.0}Fe(SO_4)_2$. This corresponds to an isotropic volume change of merely ΔV/V=7%. The from NPD data obtained lattice parameters and volume change for $Li_{1.0}Fe(SO_4)_2$ are in good agreement with the above-described values obtained from XRD experiments.

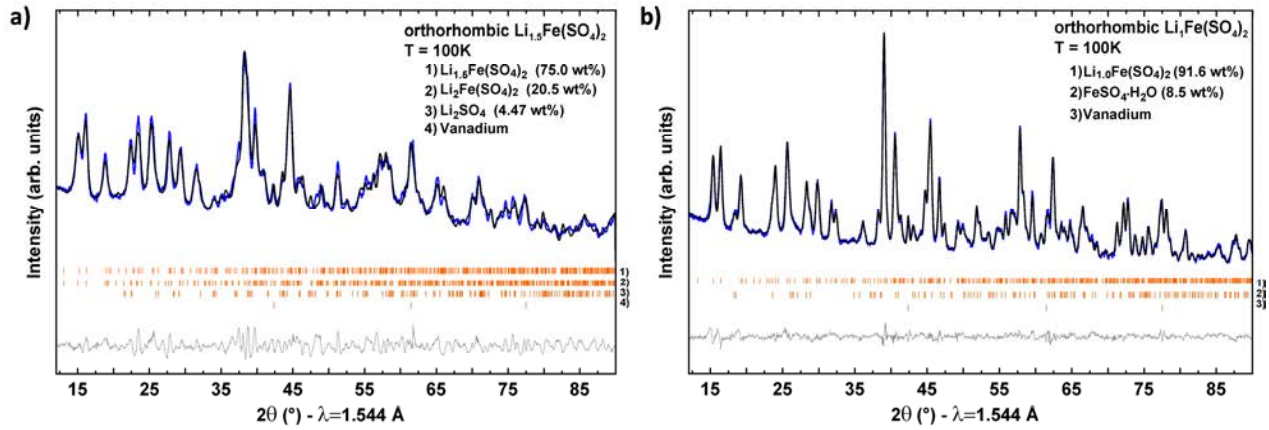

Figure III.16: Rietveld refinements of NPD patterns of orthorhombic a) $Li_{1.5}Fe(SO_4)_2$ and b) $Li_{1.0}Fe(SO_4)_2$ recorded on D20 at ILL using a wavelength of λ = 1.544 Å. The additional vanadium peaks stem from the sample container. Blue, black and grey lines represent the experimental, calculated and difference pattern, respectively. Bragg positions are shown as orange bars.

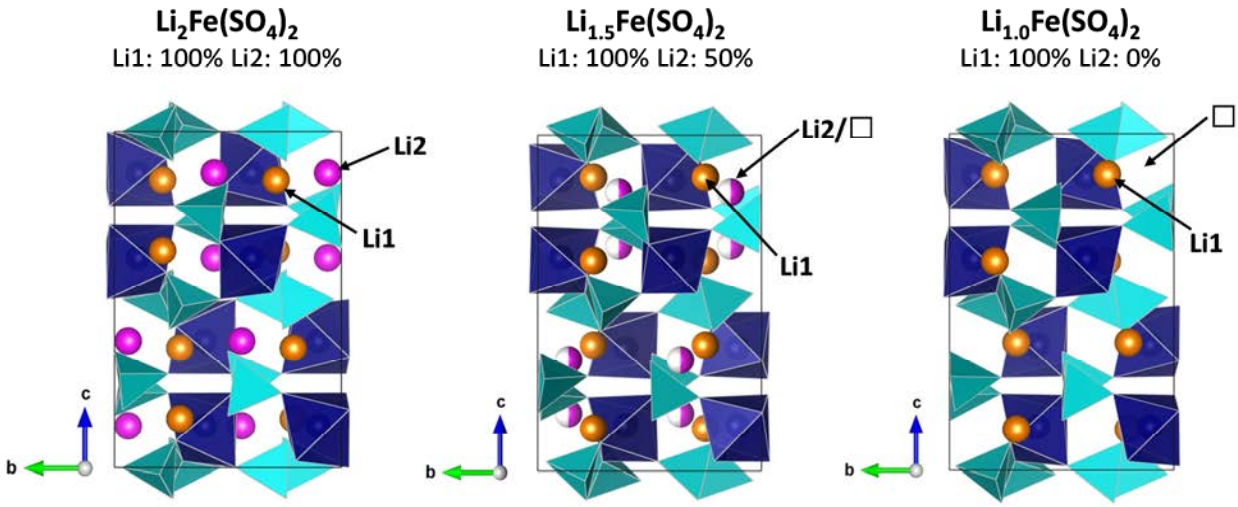

Figure III.17: Comparison of the structures $Li_2Fe(SO_4)_2$, $Li_{1.5}Fe(SO_4)_2$ and $Li_{1.0}Fe(SO_4)_2$. The FeO_6 octahedra and SO_4 tetrahedra are displayed in blue and turquois, respectively. Lithium atoms in the Li1 site are illustrated as orange balls and in Li2 sites as pink balls. In $Li_{1.5}Fe(SO_4)_2$ the half delithiated Li2 site is represented through half-colored white-yellow balls. The square marks the emptied Li2 site.

Table III.7: Crystallographic data and atomic positions of the orthorhombic $Li_{1.5}Fe(SO_4)_2$ determined from Rietveld refinements of its NPD pattern recorded at 100 K. All atoms belonging to the same chemical species were considered to have the same B_{iso}. Results of bond valence sum (BVS) analysis are also indicated.

Orthorhombic $Li_{1.5}Fe(SO_4)_2$

P b c a		R_{Bragg} = 3.76 %		χ^2 = 42.1
a = 9.1776(3) Å	*b* = 9.049(3) Å	*c* = 13.612(4) Å		*V* = 1130.4(6) Å^3

Atom	Wyckoff position	Occupancy	*x/a*	*y/b*	*z/c*	B_{iso} (Å^2)	BVS
Li1	8*c*	1	0.464(16)	0.750(19)	0.374(14)	0.3(2)	1.17(3)
Li2	8*c*	0.5	0.69(3)	0.64(3)	0.670(2)	0.3(2)	1.1(5)
Fe	8*c*	1	0.846(4)	0.606(4)	0.3650(3)	1.08(16)	2.69(18)
S1	8*c*	1	0.6265(14)	0.8080(14)	0.5102(10)	0.8(3)	5.59(3)
S2	8*c*	1	0.5905(14)	0.4411(16)	0.2683(10)	0.8(3)	5.63(3)
O1	8*c*	1	0.4667(2)	0.789(6)	0.528(5)	1.33(7)	1.99(15)
O2	8*c*	1	0.646(6)	0.9629(3)	0.473(4)	1.33(7)	1.94(15)
O3	8*c*	1	0.637(19)	0.719(5)	0.4175(2)	1.33(7)	2.13(3)
O4	8*c*	1	0.74267(4)	0.782(6)	0.586(3)	1.33(7)	1.76(25)
O5	8*c*	1	0.493(4)	0.489(6)	0.3507(3)	1.33(7)	1.59(30)
O6	8*c*	1	0.527(5)	0.496(6)	0.1738(2)	1.33(7)	1.99(17)
O7	8*c*	1	0.587(5)	0.2768(18)	0.282(4)	1.33(7)	2.04(14)
O8	8*c*	1	0.7506(2)	0.471(6)	0.273(5)	1.33(7)	2.16(2)

Table III.8: Crystallographic data and atomic positions of the orthorhombic $Li_{1.0}Fe(SO_4)_2$ determined from Rietveld refinements of its NPD pattern recorded at 100 K. All atoms belonging to the same chemical species were considered to have the same B_{iso}. Results of bond valence sum (BVS) analysis are also indicated.

Orthorhombic $Li_{1.0}Fe(SO_4)_2$

P b c a			R_{Bragg} = 2.69 %			χ^2 = 4.77	
a = 9.1576(5) Å	*b* =8.9162(5) Å		*c* = 13.3978(8) Å			*V* = 1093.95(11) Å^3	
Atom	Wyckoff position	Occupancy	*x*/*a*	*y*/*b*	*z*/*c*	B_{iso} (Å^2)	BVS
Li1	8*c*	1	0.442(5)	0.702(5)	0.379(3)	0.34(19)	1.06(6)
Li2	8*c*	0	-	-	-	-	-
Fe	8*c*	1	0.8591(10)	0.6076(10)	0.3719(7)	0.54(4)	3.08(6)
S1	8*c*	1	0.652(3)	0.813(3)	0.5062(19)	0.41(6)	6.0(3)
S2	8*c*	1	0.581(3)	0.436(3)	0.274(2)	0.41(6)	6.0(3)
O1	8*c*	1	0.4973(15)	0.7929(13)	0.5265(9)	0.511(15)	2.17(14)
O2	8*c*	1	0.6880(12)	0.9740(14)	0.4881(10)	0.511(15)	2.13(10)
O3	8*c*	1	0.6895(15)	0.7271(15)	0.4173(9)	0.511(15)	2.22(12)
O4	8*c*	1	0.7403(13)	0.7663(16)	0.5956(10)	0.511(15)	2.07(12)
O5	8*c*	1	0.4882(15)	0.4977(15)	0.3530(10)	0.511(15)	1.95(13)
O6	8*c*	1	0.5199(14)	0.4773(14)	0.1760(8)	0.511(15)	2.20(13)
O7	8*c*	1	0.5854(13)	0.2701(13)	0.2742(10)	0.511(15)	2.14(12)
O8	8*c*	1	0.7301(14)	0.4964(16)	0.2775(10)	0.511(15)	2.23(13)

To rationalize these NPD findings, DFT calculations were undertaken in collaboration with J. Carrasco and N.A. Katcho (CIC Energigune, Spain; see Annexe for details). It was shown that the structure having the full occupation of the Li1 site and a complete delithiation of the Li2 site in $Li_{1.0}Fe(SO_4)_2$ is indeed the most stable structure energetically-wise. The opposite configuration with all of the Li2 sites occupied possesses a significantly higher energy. Analog results have been obtained for $Li_{1.5}Fe(SO_4)_2$, where a fully occupied Li1 site and a half-occupied Li2 site is energetically favored.

From combined NPD-DFT studies we could confirm the stabilization of an intermediate $Li_{1.5}Fe(SO_4)_2$ phase upon oxidation of orthorhombic $Li_2Fe(SO_4)_2$ prior to the stabilization of the delithiated phase $Li_{1.0}Fe(SO_4)_2$ (as suggested by previous *in situ* XRD experiments) and the preferential removal of Li from the Li2 site during the oxidation process. The formation of an intermediate phase might act as a buffer to compensate for a possible minor structural elasticity of the orthorhombic phase. This would be coherent with the low volume change of this polymorph compared to its monoclinic counterpart.

Note that the preferential delithiation of the Li2 site was also confirmed by Bond Valence Energy Landscape (BVEL) calculations[203,214,215] (described in the Annexe), which show that in

orthorhombic $Li_2Fe(SO_4)_2$, the Li1 site is slightly lower in energy than the Li2 site. Moreover, these calculations reveal the existence of 3D conduction pathways for both $Li_2Fe(SO_4)_2$ polymorphs (Figure III.18) with a threshold energy of nearly 1.1 eV. To further experimentally qualify the diffusion kinetics of the two polymorphs, we performed impedance measurements. To do so, pellets of orthorhombic and monoclinic $Li_2Co(SO_4)_2$ (1-2 mm thick, compacity of 85 % after sintering at 200 °C overnight) were heated from 200 to 400 °C under air flow using a Solartron Analytical Modulab unit and ionically blocking gold electrodes. Further experimental details are given in the Annexe. The temperature dependence of the a.c. conductivity (Figure III.19) shows clearly a higher conductivity for the orthorhombic phase. Fitting the obtained data with the Arrhenius equation $\sigma_T = \sigma_0 \cdot \exp(-E_a/k_B T)$, where σ_T is the conductivity at the temperature T, σ_0 is a pre-exponential factor, E_a the apparent activation energy for Li^+ migration, and k_B the Boltzmann constant, gives an activation energy of 1.54 eV for the monoclinic $Li_2Co(SO_4)_2$ and 1.19 eV for its orthorhombic counterpart. Conductivity values of $2.6 \cdot 10^{-18}$ S/cm for the former and $2.2 \cdot 10^{-14}$ S/cm for the latter are obtained by an extrapolation of the linear fit to room temperature. These results are consistent with the lower polarization and better rate capability for the orthorhombic phase compared to the monoclinic one. Note the sudden drop of conductivity upon heating at around 370 °C (inset Figure III.19), which is indicative of a possible phase transition. This will be discussed in detail in the next section of this chapter.

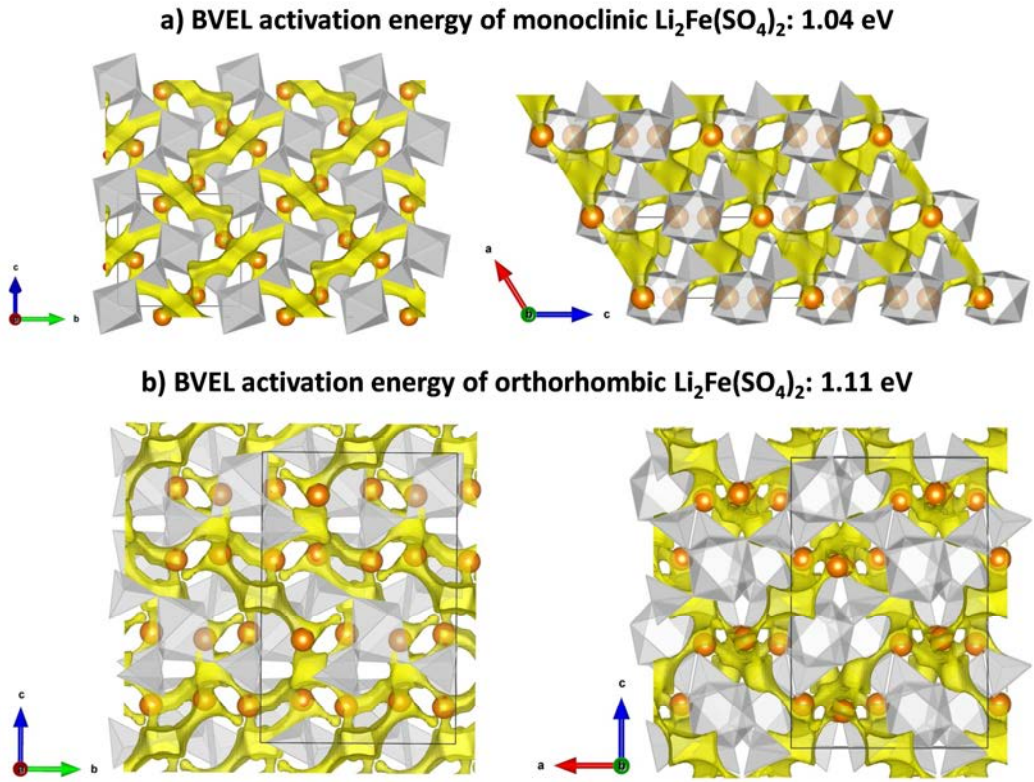

Figure III.18: BVEL maps of monoclinic (top) and orthorhombic (bottom) $Li_2Fe(SO_4)_2$. Grey polyhedra represent the SO_4 tetrahedra and FeO_6 octahedra of the main frameworks of the structures, orange balls indicate the position of the Li atoms as found experimentally, yellow volumes represent the volume of stability of a Li atom for the given energy cut-off (indicated in the figure). For the plots shown here the chosen cut-off values lie 0.5 eV above the activation energies (1.04 eV for monoclinic $Li_2Fe(SO_4)_2$ and 1.11 eV for orthorhombic $Li_2Fe(SO_4)_2$).

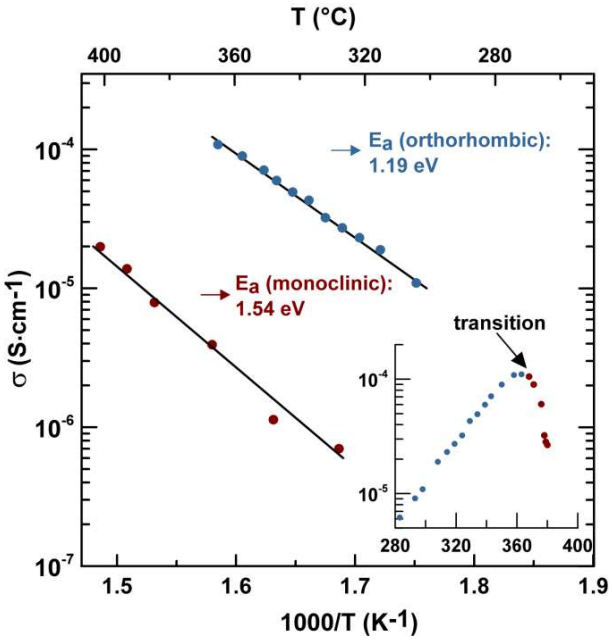

Figure III.19: Temperature dependence of the a.c. conductivity of the orthorhombic (blue) and monoclinic (red) polymorphs of $Li_2Co(SO_4)_2$. The inset shows the abrupt decrease of the a.c. conductivity that occurs when heating the orthorhombic phase at temperatures higher than 360 °C.

Electrode kinetics depend on both ionic and electronic conductivities, hence our desire to compare the electronic conductivity for both polymorphs while being aware that such electronic conductivities can be measured by d.c. experiments as well as with the optical band gap via UV/Vis spectroscopy. Such band gaps, besides accounting for the color of a material, also give qualitative information about the electronic behavior.

UV/Vis spectroscopy was performed on the orthorhombic and monoclinic polymorphs of the $Li_2M(SO_4)_2$ series with *M*= Mn, Fe, Co, Ni, Zn with a Perkin Elmer Lambda 1050 spectrometer equipped with an integration sphere. The UV/Vis spectra were recorded between 180 and 2500 nm with a 1 nm step. The baseline was measured with a spectralon reference. The obtained spectra are shown in Figure III.20 for the two polymorphs with the absorbance plotted against the energy. In the visible region between 3.10 and 1.55 eV (400 and 800 nm) we can see the absorption peaks that are responsible for the colour of the samples. The peaks can be attributed to the corresponding d-d transitions with help of the Tanabe-Sugano diagrams for the respective d-systems (see Annexe).[216]

The pink colour of the Co-based compounds is attributed to a $^4T_1$ to $^4T_{1g}$ transition around 2.28 eV for the orthorhombic and 2.29 eV for the monoclinic polymorph. The slight difference in the absorption energies is also conveyed in the colour difference between these two polymorphs, where the orthorhombic phase has a slight blue touch due to the absorption at lower energy (higher wavelength) compared to the monoclinic phase. $Li_2Ni(SO_4)_2$ absorbs at higher energy (2.95 eV) compared to the Co-based phases and appears therefore yellow. Further, the orthorhombic and monoclinic $Li_2Fe(SO_4)_2$ samples show a weak absorption over the entire visible range, which explains the light beige/brown colour of the Fe-based polymorphs, whereas the absorption of the Mn- and Zn-based samples is close to 0 so that they are nearly white. The absence of absorption peaks for $Li_2Zn(SO_4)_2$ and $Li_2Mn(SO_4)_2$ does not come as a surprise since Zn is a filled d^{10} system and no d-d transition is possible and Mn is a half-filled d^5 system, which is energetically stable and hence no transition is observed in the visible region. The observed d-d transitions are summarized in Figure III.20 (right) for the case of the orthorhombic $Li_2Co(SO_4)_2$.

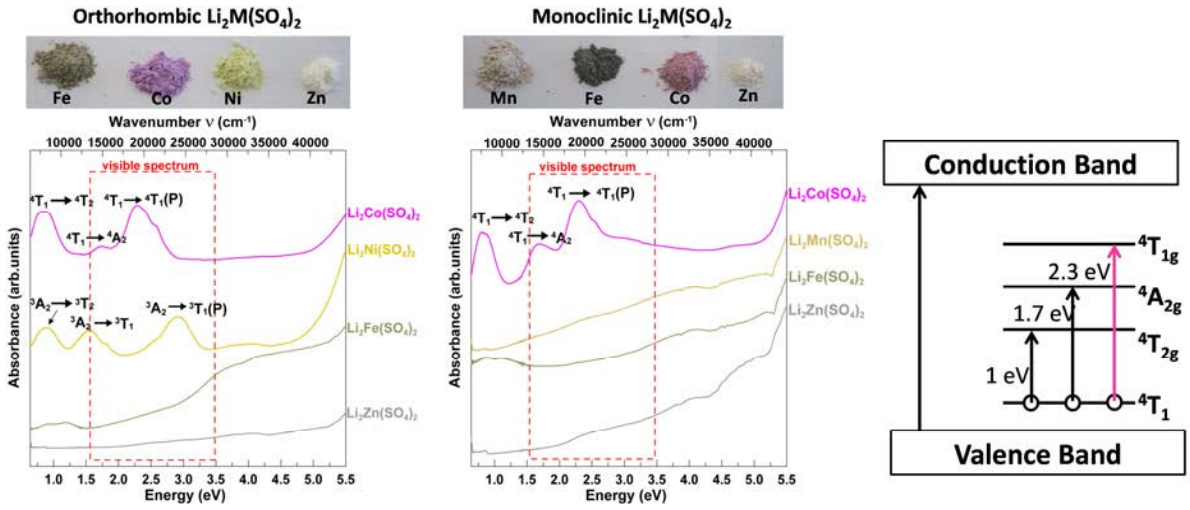

Figure III.20: On the top, pictures of the powder samples of the orthorhombic and monoclinic $Li_2M(SO_4)_2$ (*M* = Mn, Fe, Co, Ni, Zn) compounds illustrating the different colors depending on the 3d transition metal. On the bottom, UV/Vis spectra of the orthorhombic and monoclinic $Li_2M(SO_4)_2$ series. The various d-d transitions for $Li_2Co(SO_4)_2$ are summarized in the right scheme.

The gap between the valence and the conduction bands was calculated by treating the UV/Vis data with the Kubelka-Munk function $f(R) = (1-R)^2/2R = K/s$, where R is the reflectance, K the absorption coefficient and s the scattering coefficient.[217] This specific equation of the Kubelka-Munk theory is usually applied to highly light scattering and optical dense materials. Plotting $(f(R)\cdot h\nu)^n$ with n=1/2 or n=2 against the energy, is commonly used to determine the energy of the gap E_g (indirect or direct) between the conduction and the valence bands.[218] For the calculation of E_g for the different $Li_2M(SO_4)_2$ (*M*=Co,Fe) compounds, both formulas gave similar results as previously observed in literature.[218] For the following, a direct transition was assumed by using the equation $(f(R)\cdot h\nu)^2$. Figure III.21 illustrates the Kubelka-Munk plot for the orthorhombic and monoclinic $Li_2Co(SO_4)_2$ and $Li_2Fe(SO_4)_2$ phases.

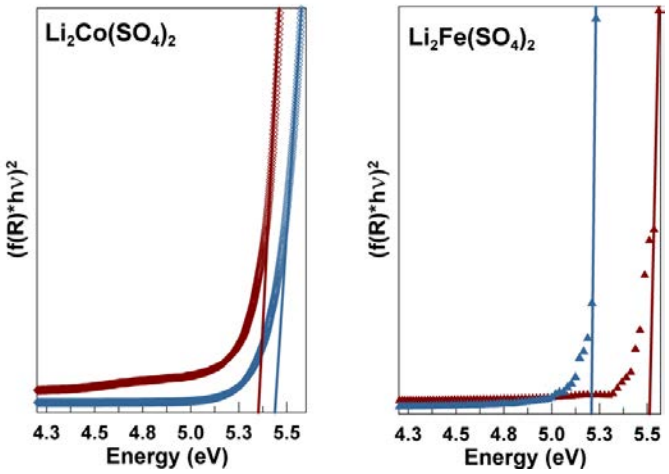

Figure III.21: Kubelka-Munk functions for $Li_2Co(SO_4)_2$ (left) and $Li_2Fe(SO_4)_2$ (right). The blue symbols refer to the orthorhombic polymorph and the red ones to the monoclinic phases.

The band gap energies for the different compounds are all in the range between 5.2 and 5.5 eV (Table III.9) and hence show no difference between the two polymorphs in terms of band gap energy. Note that the here obtained band gap energies are higher than what has been reported for other polyanionic materials such as $LiFePO_4$ (3.7 eV), Li_2FeSiO_4 (3.7 eV) and $LiFeSO_4F$ (2.8-3.6 eV, depending on the polymorph and the calculation method).[219–224]

In short, neither structural bottlenecks (BVEL energy values) nor electronic conductivity properties (band gap energies) could account for the polarization difference between the two polymorphs. This might suggest an important role of defects and/or grain boundaries in these polymorphs that could influence their conducting performances. At this point, we should recall our difficulties in achieving a pure monoclinic phase due to the remaining presence of minute amounts of amorphous orthorhombic material as shown by Mössbauer spectroscopy of pristine monoclinic $Li_2Fe(SO_4)_2$.[144] It is possible that such developed grain boundaries could be responsible for the lower conductivity of the monoclinic polymorph.

Table III.9: Band gap energies E_g for both $Li_2M(SO_4)_2$ polymorphs obtained with the Kubelka-Munk formalism from UV/Vis spectroscopy.

Band Gap E_g	**$Li_2Mn(SO_4)_2$**	**$Li_2Fe(SO_4)_2$**	**$Li_2Co(SO_4)_2$**	**$Li_2Ni(SO_4)_2$**	**$Li_2Zn(SO_4)_2$**
Monoclinic	5.3(1) eV	5.5(3) eV	5.3(3) eV	–	5.3(2) eV
Orthorhombic	–	5.2(5) eV	5.4(1) eV	5.5(1) eV	5.3(2) eV

III.5. Polymorph stability

The above-described impedance experiments have suggested the presence of an orthorhombic-to-monoclinic phase transition upon heating (Figure III.19). In the light of these observations we decided to further study the respective thermodynamic stabilities of the two polymorphs and to explore in detail the phase transformations with various synthesis approaches.

The alteration of monoclinic $Li_2Fe(SO_4)_2$ by ball-milling prompted us to try a complete transformation of the monoclinic phase to its orthorhombic counterpart. To do so we ball-milled as prepared monoclinic $Li_2Co(SO_4)_2$ in a Retsch PM100 planetary ball miller (500 rpm) for various durations under argon atmosphere. Following the reaction progress via XRD we could clearly see the stepwise monoclinic-to-orthorhombic phase transition (Figure III.22). We observed the same phase transition for the $Li_2Fe(SO_4)_2$ and $Li_2Zn(SO_4)_2$ phases, while interestingly the Mn-based monoclinic phase showed no sign of transformation to the orthorhombic polymorph even after several hours of high-energy ball-milling. This is consistent with our failure to stabilize orthorhombic $Li_2Mn(SO_4)_2$ through a mechano-chemical synthesis approach.

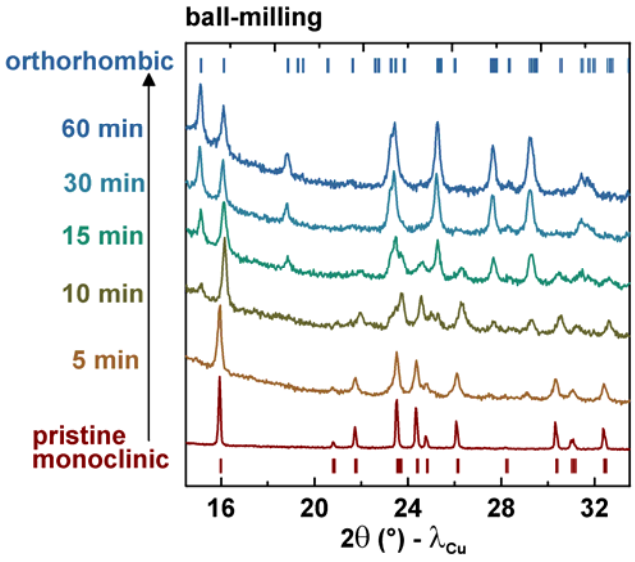

Figure III.22: XRD measurements of a $Li_2Co(SO_4)_2$ sample, which follows the monoclinic-to-orthorhombic phase transition that occurs upon mechanical milling.

To further test the thermal stability of the orthorhombic phase, we performed DSC measurements coupled with TGA (experimental details in the Annexe) by heating orthorhombic $Li_2Co(SO_4)_2$ up to 500 °C with a ramp of 10 K/min (Figure III.23a). The peak in the temperature range from 100-200 °C can be attributed to the evaporation of surface water (sulfates are highly water-sensitive and prone to hydratation[153]). The exothermic peak at 420 °C is assigned to an orthorhombic-to-monoclinic transformation as confirmed by XRD measurements after cooling down. This phase transition is irreversible and the formed monoclinic phase (red line) remains stable as has been shown by a second heating cycle. From the DSC curve, we can deduce the enthalpy ΔH of the phase transformation as being approximately -2.36 kJ/mole for $Li_2Fe(SO_4)_2$ and -1.06 kJ/mole for $Li_2Co(SO_4)_2$.

To monitor this phase transition upon heating we performed *in situ* XRD experiments on orthorhombic $Li_2Co(SO_4)_2$ using a Panalytical X'Pert Pro MPD diffractometer supplied with a cobalt source ($\lambda_{Co\text{-}K\alpha1}$ = 1.78897 Å, $\lambda_{Co\text{-}K\alpha2}$ = 1.79285 Å) and an X'Celerator detector coupled with an Anton Paar furnace (Figure III.23b). Up to 320 °C, the orthorhombic phase (blue) did not show any changes except for an improved crystallinity. Between 340 °C and 360 °C, the peaks of the monoclinic phase began to grow at the expense of the peaks of the pristine orthorhombic phase (pink). Pure monoclinic $Li_2Co(SO_4)_2$ (red) was obtained at 380 °C and remained stable till the end of the measurement at 480 °C (light blue pattern). The results are in good agreement with the DSC measurements to the exception of a difference in the transition temperature that is a result of different heating rates and durations (10 K/min for DSC, 2-hours steps for each temperature for XRD). Similar results were observed for the iron and zinc systems, with the transition temperature being around 360 °C and 480 °C, respectively.

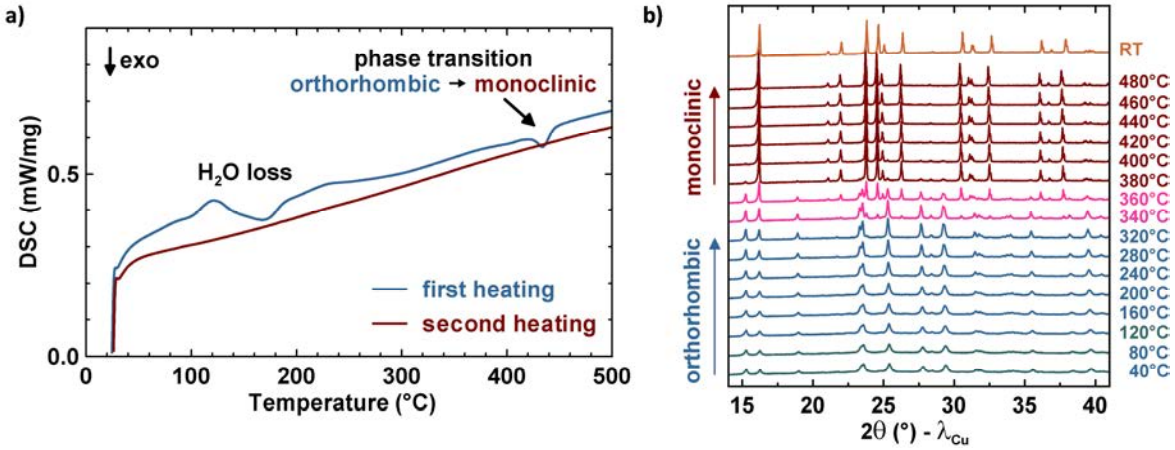

Figure III.23: a) DSC measurement of the orthorhombic $Li_2Co(SO_4)_2$ heated from room temperature up to 500 °C with a ramp of 10 K/min. The blue line corresponds to the first heating cycle of pristine orthorhombic $Li_2Co(SO_4)_2$; the red line corresponds to a subsequent heating cycle of the product. The exothermic peak at 420°C is assigned to the orthorhombic-to-monoclinic phase transition. b) *In situ* high-temperature XRD measurements of $Li_2Co(SO_4)_2$ upon heating, which follows the orthorhombic-to-monoclinic phase transition. The blue, pink, and red patterns correspond to the orthorhombic polymorph, the co-existence of the orthorhombic and monoclinic phases, and the monoclinic polymorph. The light red pattern (top) was recorded after cooling the sample to room temperature, showing that the monoclinic structure is preserved.

In Figure III.24a, we summarize the formation conditions for the monoclinic and orthorhombic phases with various 3d transition metals depending on the synthesis approach. The transformation conditions from one polymorph to the other upon heating or ball-milling is shown in Figure III.24b. While ball-milling and ceramic processes usually lead to the orthorhombic and monoclinic polymorphs, respectively, there are a few exceptions worthy of comments. For example, the orthorhombic polymorph of $Li_2Mn(SO_4)_2$ could not be stabilized despite many attempts, nor could the monoclinic phase of the nickel-based compound. It is quite likely that such an effect is linked to the size of the transition metals, where the denser orthorhombic phase is favored by smaller transition metal cations (Ni^{2+}) and the less dense monoclinic phases by larger cations (Mn^{2+}).

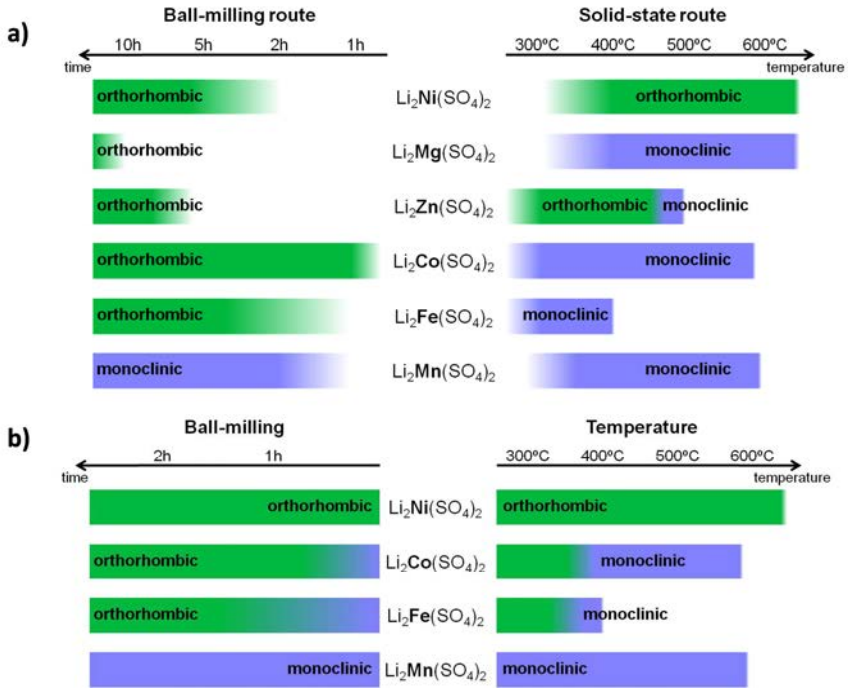

Figure III.24: a) Diagram summarizing the nature of the $Li_2M(SO_4)_2$ polymorph (orthorhombic in green *vs.* monoclinic in blue) using different synthesis conditions (mechanical milling *vs.* solid-state route) for the six metals *M* = Ni, Mg, Zn, Co, Fe, Mn. b) Diagram summarizing the stability of the orthorhombic (green) polymorph upon heating and the monoclinic (blue) polymorph upon mechanical milling of $Li_2M(SO_4)_2$ for the four metals *M* = Ni, Co, Fe, Mn.

This hypothesis prompted us to use pressure as a mean to induce a monoclinic-to-orthorhombic phase transition for $Li_2Mn(SO_4)_2$. High-pressure experiments in a Diamond anvil cell (DAC) were performed in close collaboration with A. Polian and C. Bellin (IMPMC, UPMC, Paris) and are described in detail in the Annexe. We started the high-pressure experiments on monoclinic $Li_2Co(SO_4)_2$ to obtain a first feeling for the transition conditions and the Raman signals for the monoclinic and orthorhombic phases. The reference Raman spectra for both $Li_2Co(SO_4)_2$ polymorphs and monoclinic $Li_2Mn(SO_4)_2$ are shown in Figure III.25a with the different SO_4 modes corresponding to stretching modes (ν_1 and ν_3) and bending modes (ν_2 and ν_4). After loading monoclinic $Li_2Co(SO_4)_2$ into the DAC (Figure III.25b (left): DAC - as made), we gradually increased the pressure. The evolution of the Raman spectra upon pressure illustrated in Figure III.25b (left) shows the growing of new peaks until 3.65 GPa and onwards. The spectrum at 5.65 GPa resembles the reference spectra of orthorhombic $Li_2Co(SO_4)_2$ implying its structural transformation. The same experiment was performed with a DAC loaded with monoclinic $Li_2Mn(SO_4)_2$. Figure III.25b (right) shows that from 3 GPa onwards, the Raman spectra evolve

with increasing pressure in a similar way as the cobalt system suggesting the feasibility to transform the Mn-based polymorph as well. However, caution has to be exercised here as we obviously do not have the Raman spectra for the Mn-based orthorhombic polymorph. In order to confirm the phase transitions observed by Raman spectroscopy, we also performed *in situ* XRD measurements in the DAC (in collaboration with Benoît Baptiste, IMPMC, UPMC, Paris). Even though we observed a change of the Bragg peaks with increasing pressure, the poor resolution of the XRD patterns did not allow us to unambiguously identify the stabilized phase. Additional *in situ* synchrotron experiments are needed to get better insights into the pressure-driven monoclinic-orthorhombic structural changes.

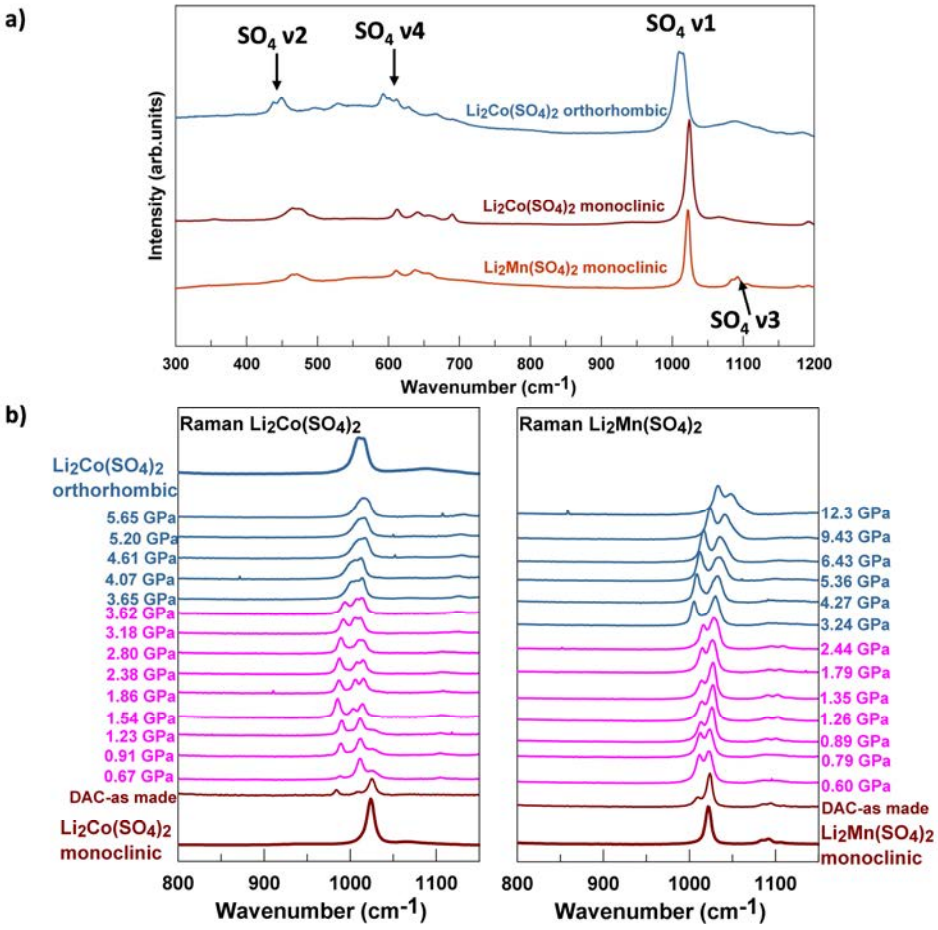

Figure III.25: a) Raman spectra of orthorhombic and monoclinic $Li_2Co(SO_4)_2$ and monoclinic $Li_2Mn(SO_4)_2$. The different Raman active modes of the SO_4 groups as described in the main manuscript are indicated. The spectra were recorded outside of the DAC. b) Evolution of the Raman spectra of $Li_2Co(SO_4)_2$ (left) and $Li_2Mn(SO_4)_2$ (right) loaded in a Diamond Anvil cell as a function of the increasing pressure.

To finally settle for good the relative thermodynamic stability issues and the driving forces behind the phase transformations of the two polymorphs, acid solution calorimetric

measurements were undertaken in collaboration with Prof. Navrotsky and co-workers (UC Davis).[201] Experimental details are given in the Annexe. The Born-Haber cycle used for the calculation of the formation enthalpies of the $Li_2M(SO_4)_2$ phases from the precursors (Li_2SO_4 and MSO_4) is given in Table III.10. The solution enthalpies and formation enthalpies for both polymorphs are summarized in Table III.11. Overall, the solution enthalpies of the monoclinic phases are less exothermic than orthorhombic $Li_2Fe(SO_4)_2$ and $Li_2Co(SO_4)_2$ (Figure III.26a), which suggests that the monoclinic phases are more stable than their orthorhombic counterparts. This is further supported by the lower formation enthalpies of monoclinic $Li_2M(SO_4)_2$ compared to their orthorhombic counterparts (Figure III.26b).

Table III.10: Thermochemical cycles for adsorbed water correction ($\Delta H_{sol\text{-}corr\text{-}H2O}$) and enthalpy of formation ($\Delta H_{formation}$) of monoclinic and orthorhombic $Li_2M(SO_4)_2$ (M = Mn, Fe Co and Ni).

I - Reaction Scheme: Correction for adsorbed water ($\Delta H_{sol\text{-}corr\text{-}H2O}$)	Enthalpy Measurement
$Li_2M(SO_4)_2{\cdot}nH_2O_{(s,\ 25\ ºC)} + 4HCl_{(l,\ 25\ ºC)} \rightarrow 2LiCl_{(sln,\ 25ºC)} + MCl_{2\ (sln,\ 25ºC)} + 2H_2SO_{4(sln,\ 25ºC)} + nH_2O_{(sln,\ 25ºC)}$	$\Delta H_1 = \Delta H_{solun}(Li_2M(SO_4)_2{\cdot}nH_2O)$
$H_2O_{\ (l,\ 25ºC)} \rightarrow H_2O_{\ (sln,\ 25ºC)}$	ΔH_2 = -0.4 kJ/mol
$Li_2M(SO_4)_{2\ (s,\ 25\ ºC)} + 4HCl \rightarrow 2LiCl_{(sln,\ 25ºC)} + MCl_{2\ (sln,\ 25ºC)} + 2H_2SO_{4(sln,\ 25ºC)}$	$\Delta H_3 = \Delta H_{sol\text{-}corr\text{-}H2O}(Li_2M(SO_4)_2) = \Delta H_1 - n\ \Delta H_2$
II - Reaction Scheme: Enthalpy of formation ($\Delta H_{formation}$)	
$Li_2M(SO_4)_{2\ (s,\ 25\ ºC)} + 4HCl \rightarrow 2LiCl_{(sln,\ 25ºC)} + MCl_{2\ (sln,\ 25ºC)} + 2H_2SO_{4(sln,\ 25ºC)}$	$\Delta H_3 = \Delta H_{sol\text{-}corr\text{-}H2O}(Li_2M(SO_4)_2)$
$Li_2SO_{4(s,\ 25ºC)} + 2HCl \rightarrow 2LiCl_{(sln,\ 25ºC)} + H_2SO_{4\ (sln,\ 25ºC)}$	$\Delta H_4 = \Delta H_{solun}(Li_2SO_4)$
$MSO_{4\ (s,\ 25ºC)} + 2HCl \rightarrow MCl_{2\ (sln,\ 25ºC)} + H_2SO_{4(sln,\ 25ºC)}$	$\Delta H_5 = \Delta H_{solun}(MSO_4)$
$Li_2SO_{4(s,\ 25ºC)} + MSO_{4\ (s,\ 25ºC)} \rightarrow Li_2M(SO_4)_{2\ (s,\ 25\ ºC)}$	$\Delta H_6 = \Delta H_{formation}(Li_2M(SO_4)_2) = -\Delta H_3 + \Delta H_4 + \Delta H_5$

Even though the formation enthalpies of both polymorphic phases are positive, their Gibbs free energies of formation from the binary sulfates must be negative since these materials can be synthesized from the binary sulfates under various conditions. This implies the existence of a significant entropy contribution to the Gibbs free energy (Equation 1).

$$\Delta G = \Delta H - T\Delta S \quad \textbf{(1)}$$

The impact of entropy has previously been observed for the triplite Li*M*SO_4F (*M* = Fe, Mn) polymorph owing to its Li/metal site mixing. However, neither positional disorder nor possible rotations of the SO_4 tetrahedra ("paddle-wheel effect") in sulfate-based materials as proposed by Lundén *et al.*[225], which could have explained the entropy contribution, were confirmed by NPD experiments. So we are left with defect formations to account for such a large entropy term. This would at least be consistent with the observation that the orthorhombic polymorph can be stabilized by a mechano-chemical synthesis approach, which is prone to introduce defects. Along that line, the reverse monoclinic-to-orthorhombic transformation upon ball-milling might be explained by the introduction of energetically unfavorable defects into the monoclinic structure, which would make a transition into the orthorhombic phase energetically more attractive.

Table III.11: The water content and calorimetric data of $Li_2M(SO_4)_2$ (*M* = Co, Fe and Mn) samples.

Composition	H_2O (n) (mol)	ΔH_{solun} (kJ/mol)	$\Delta H_{solun\text{-}corrected}$ (kJ/mol)	$\Delta H_{formation}$ (kJ/mol)	M^{2+} ionic radius (Å)
Monoclinic samples					
$Li_2Mn(SO_4)_2$	0.029	-18.58 ± 0.34 (7)	-18.57 ± 0.34	0.78 ± 0.74	0.83
$Li_2Fe(SO_4)_2$	0.058	-31.69 ± 0.44 (7)	-33.01 ± 0.45	0.99 ± 0.61	0.78
$Li_2Co(SO_4)_2$	0.00	-37.54 ± 0.2 (6)	-37.54 ± 0.2	3.51 ± 0.24	0.745
Orthorhombic samples					
$Li_2Fe(SO_4)_2$	0.117	-40.80 ± 0.40 (9)	-40.75 ± 0.40	8.73 ± 0.34	0.78
$Li_2Co(SO_4)_2$	0.099	-48.58 ± 0.28 (8)	-48.54 ± 0.28	14.51± 0.31	0.745
$Li_2Ni(SO_4)_2$	0.01	-49.00 ± 0.30 (8)	-49.00 ± 0.30	2.34 ± 0.58	0.69

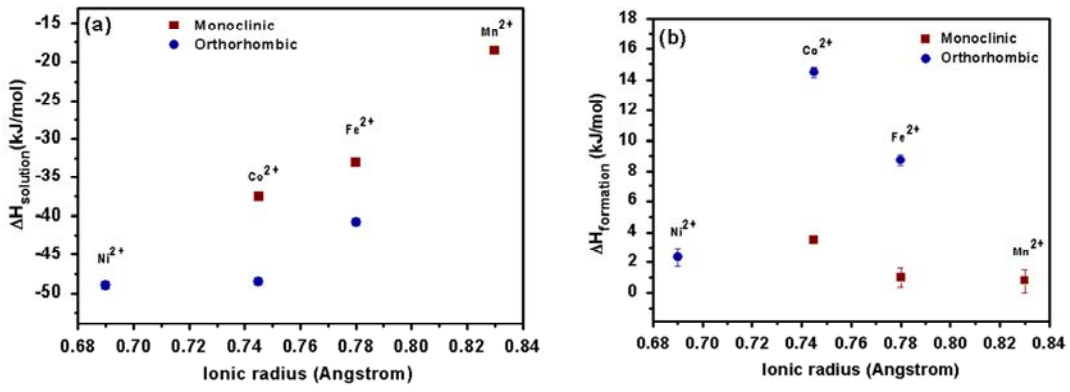

Figure III.26: Enthalpies of (a) dissolution in 5M HCl in 25 °C and (b) formation from Li_2SO_4 and MSO_4 at 25 °C of $Li_2M(SO_4)_2$ (*M* = Mn, Fe, Co, and Ni) samples as a function of the M^{2+} ionic radius (Å).

III.6. Magnetic properties of orthorhombic $Li_2M(SO_4)_2$

Since electrochemical as well as magnetic properties are both somewhat governed by the iono-covalency of the metal-oxygen bond, a multitude of electrode materials have been tested for their magnetic features such as borates, phosphates and fluorosulfates.[189,197,226–230] More recently, studies on the monoclinic $Li_2M(SO_4)_2$ (*M* = Mn, Fe, Co) and orthorhombic $Li_2Ni(SO_4)_2$ phases revealed a long-range antiferromagnetic interaction of the transition metal centers via M-O-O-M super-super-exchange pathways (Figure III.27), which are imposed by the isolated MO_6 octahedra.[231,232] Moreover, $Li_2Ni(SO_4)_2$ presents a magnetic structure allowing a magnetoelectric effect. In light of such previous findings we studied the magnetic properties of the recently described orthorhombic $Li_2Co(SO_4)_2$ and $Li_2Fe(SO_4)_2$ compounds as well as of the oxidized phases $Li_{1.5}Fe(SO_4)_2$ and $Li_1Fe(SO_4)_2$.

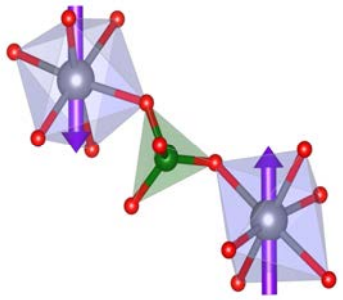

Figure III.27: Antiferromagnetic ordering of the magnetic moments (illustrated as arrows through the metal center) via a super-super-exchange interaction. The red and green spheres illustrate oxygen and sulfur atoms, respectively.

The temperature-dependence of the molar magnetic susceptibility was measured via Superconducting Quantum Interference Device (SQUID; Quantum design) experiments in zero field cooled (ZFC) and field cooled (FC) modes, under applied magnetic fields of 10 kOe between 350 K and 10 K (Annexe). The resulting χ=f(T) susceptibility curves are shown in Figure III.28. All four curves show characteristic cusps of an antiferromagnetic ordering at Néel temperatures of ~15 K and ~13 K for $Li_2Co(SO_4)_2$ and $Li_2Fe(SO_4)_2$, respectively. In the case of the oxidized phase $Li_1Fe(SO_4)_2$, the curve shows two cusps between ~30 K and ~40 K. We hypothesize the first ordering temperature (30 K) to correspond to the Néel temperature of $FeSO_4{\cdot}H_2O$, which was present as a minor impurity, as detected by XRD and NPD. This was confirmed by SQUID

measurements performed on single-phase $FeSO_4 \cdot H_2O$ as the same Néel temperature was obtained. The partially oxidized phase $Li_{1.5}Fe(SO_4)_2$ also displays two features in the susceptibility curve, at ~20 K and at ~35 K; the latter corresponds to T_N of $Li_{1.5}Fe(SO_4)_2$ as will be further demonstrated by NPD experiments, while the former one (smaller feature) remains still unknown. However, no magnetic ordering of a secondary phase was observed in the NPD patterns for $Li_{1.5}Fe(SO_4)_2$ recorded below the Néel temperature.

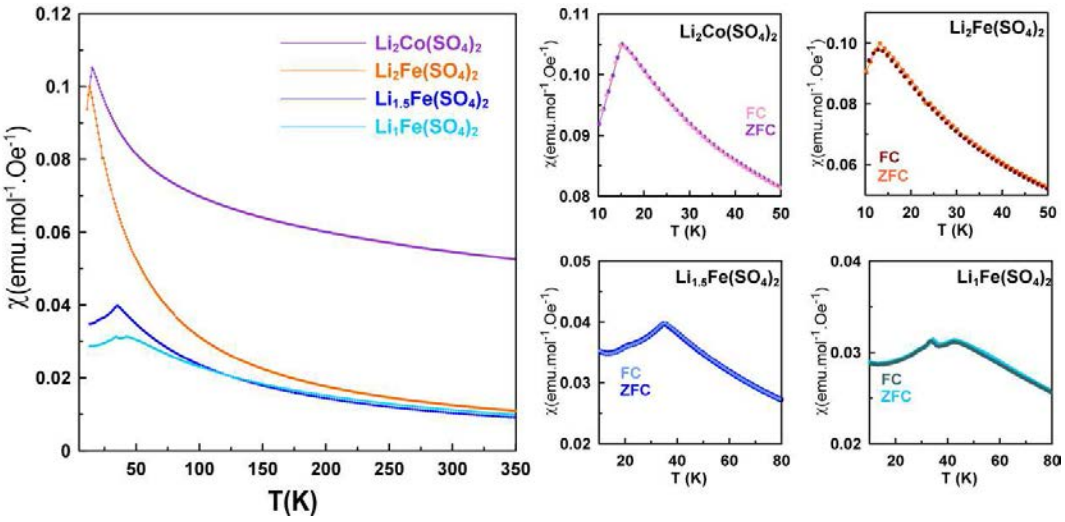

Figure III.28: Temperature dependence of the molar magnetic susceptibility of orthorhombic $Li_2Co(SO_4)_2$ (purple), $Li_2Fe(SO_4)_2$ (orange), $Li_{1.5}Fe(SO_4)_2$ (blue) and $Li_1Fe(SO_4)_2$ (light blue) recorded at 10 kOe in ZFC mode. Comparison of ZFC and FC curves recorded at 10 kOe for all four compounds is shown in the right panels.

The high-temperature region (above 100 K) of the inverse susceptibility was then fitted with the modified Curie-Weiss law $\chi = \chi_0 + C/(T-\theta_{CW})$ with χ_0 being the temperature-independent component arising from the sample holder and core diamagnetism of the compound, C the Curie constant and θ_{CW} the Curie-Weiss temperature (Figure III.29). The obtained θ_{CW} and C values and the diamagnetic contribution χ_0 are listed in Table III.12. χ_0 equals zero for the oxidized samples $Li_{1.5}Fe(SO_4)_2$ and $Li_1Fe(SO_4)_2$ indicating that they follow a perfect Curie-Weiss law; the χ_0 contribution for $Li_2Co(SO_4)_2$ is however rather large. The Curie-Weiss temperatures θ_{CW} show negative values pointing out antiferromagnetic correlations. Note that θ_{CW} decreases with increasing oxidation state of the Fe atom indicating a stronger coupling of the magnetic moments. This trend is further confirmed by the increasing Néel temperatures T_N when going from orthorhombic $Li_2Fe(SO_4)_2$ (Fe^{2+}; d^6 system) to $Li_{1.5}Fe(SO_4)_2$ and $Li_1Fe(SO_4)_2$ (Fe^{3+}; d^5 system), which is explained by a strengthening of the orbital overlap due to changing bond angles as well

as the depopulation of the t_{2g} orbitals upon oxidation. A similar increase of T_N upon oxidation of Fe^{2+} has been previously observed for $LiFeSO_4F$ and monoclinic $Li_2Fe(SO_4)_2$.[197,231] Turning to the evolution of T_N, we note a decrease in T_N from 28 K to 16 K and 12 K when going from Ni^{2+} (d^8) to Co^{2+} (d^7) and Fe^{2+} (d^6), respectively. Such a trend has been similarly noted for malonate-based $Na_2M(H_2C_3O_4)_2{\cdot}2H_2O$ phases,[233] but is exactly the opposite to what was observed for $LiFeSO_4F$ for instance.[197,227] This could come from the fact that we have M-O-O-M super-super-exchange interactions in contrast to the M-F-M super-exchange interactions in $LiFeSO_4F$. Further comparing the orthorhombic $Li_2M(SO_4)_2$ compounds to their monoclinic counterparts (T_N = 4-8 K for M^{2+}, 35 K for Fe^{3+}) we can state that the orthorhombic phases systematically show higher T_N and larger absolute θ_{CW} values suggesting stronger antiferromagnetic interactions. This does not come as a surprise given the structural differences of the two polymorphs, where the orthorhombic phases present shorter M-M distances and a higher density enhancing the super-super-exchange interactions.

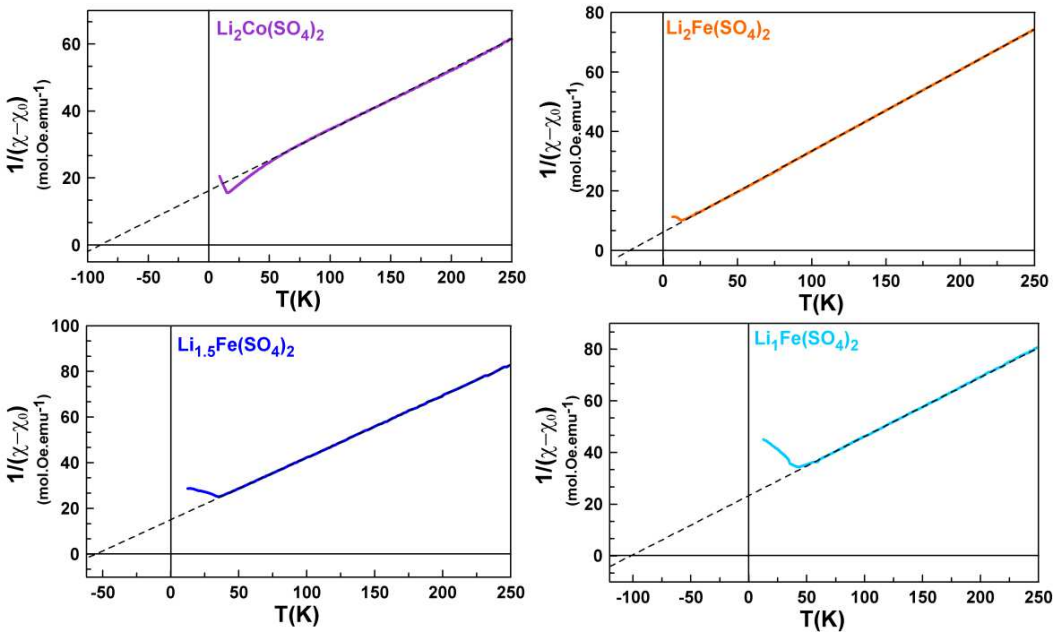

Figure III.29: Inverse susceptibility fitted with the modified Curie-Weiss law for $Li_2Co(SO_4)_2$ (purple), $Li_2Fe(SO_4)_2$ (orange), $Li_{1.5}Fe(SO_4)_2$ (blue) and $Li_1Fe(SO_4)_2$ (light blue).

The effective magnetic moment μ_{eff} of a cation can be calculated by various approaches. For a free ion the formula $\mu_{eff}(J) = g_J{\cdot}[J(J+1)]^{1/2}$ is used with g being the Landé gyromagnetic factor and J the total angular momentum (S + L). However, due to the crystal field splitting of the d-

orbitals in a coordinated cation, the effective moment is calculated either with the formula $\mu_{S+L}=[4S(S + 1) + L(L + 1)]^{1/2}$ or $\mu_S = 2\cdot[S(S + 1)]^{1/2}$. The former is valid if the orbital angular momentum L is decoupled from the spin angular momentum S, while the latter is used for a quenched orbital moment L with a spin-only effective moment. The experimental μ_{eff} values (Table III.12) obtained for $Li_2Fe(SO_4)_2$ and $Li_1Fe(SO_4)_2$ (5.4(1) μ_B and 5.9(3) μ_B per Fe atom, respectively) correspond well to what we expect for Fe^{2+} and Fe^{3+} in an octahedral environment with an orbital angular momentum uncoupled from the spin contribution (μ_{S+L}). For $Li_{1.5}Fe(SO_4)_2$ we obtain an effective magnetic moment of 5.4(3) μ_B. The large effective moment μ_{eff} for $Li_2Co(SO_4)_2$ (6.6(2) μ_B) can be explained by the strong spin-orbit coupling (L·S) often observed for high-spin Co^{2+} and a strong magnetic anisotropy related to the triplet ground state.[163,227,234]

Table III.12: Magnetic parameters of the orthorhombic $Li_xM(SO_4)_2$ phases deduced from magnetic measurements and neutron diffraction, and compared to the expected theoretical values.

	$Li_2Co^{II}(SO_4)_2$	$Li_2Fe^{II}(SO_4)_2$	$Li_{1.5}Fe^{II/III}(SO_4)_2$	$Li_1Fe^{III}(SO_4)_2$
Electronic configuration	$d^7 : t_{2g}^5 e_g^2$ S=3/2, L=3	$d^6 : t_{2g}^4 e_g^2$ S=2, L=2		$d^5 : t_{2g}^3 e_g^2$ S=5/2, L=0
Experimental values deduced from magnetic measurements (H = 10 kOe)				
Néel temperature T_N (K)	15(1) K	13(1) K	35(2) K	36(7) K
Curie Constant C (emu.K.mol^{-1})	5.5(2)	3.7(1)	3.7(1)	4.4(1)
Curie Weiss temperature θ_{CW} (K)	-89(2) K	-22(1) K	-55(1) K	-101(2) K
χ_0 (emu·mol^{-1}·Oe^{-1})	0.039(4)	0.001(1)	0	0
Effective moment μ_{eff}	6.6(3) μ_B	5.4(1) μ_B	5.4(2) μ_B	5.9(1) μ_B
Frustration parameter $\lvert\theta_{CW}/T_N\rvert$	5.9(4)	1.6(2)	1.6(1)	2.5(2)
Experimental values deduced from neutron diffraction				
Néel temperature T_N (K)	16(1) K	12(2) K	35(2) K	34(2) K
Magnetic moment at 2 K	3.11(5) μ_B	2.98(4) μ_B	4.82(10) μ_B	4.12(9) μ_B
Expected theoretical values				
Effective moment μ_{eff} $\mu_{eff} = g_J\cdot(J(J+1))^{1/2}$	6.6 μ_B	6.7 μ_B	-	5.9 μ_B
Effective moment μ_{eff} $\mu_{eff} = (4S(S+1)+L(L+1))^{1/2}$	5.2 μ_B	5.5 μ_B	-	5.9 μ_B
Effective moment μ_{eff} $\mu_{eff} = 2\cdot(S(S+1))^{1/2}$	3.9 μ_B	4.9 μ_B	-	5.9 μ_B
Magnetic moment m = g·S	3 μ_B	4 μ_B	-	5 μ_B

In addition, the linear response of the isothermal field-dependence of the magnetization M = f(H) was recorded at 2 K. The magnetization curves (Figure III.30) confirm the antiferromagnetic ordering for all samples with the exception of $Li_2Co(SO_4)_2$. The deviation from a perfect

antiferromagnetic behaviour might be related to a minute ferromagnetic impurity that was not detected by XRD.

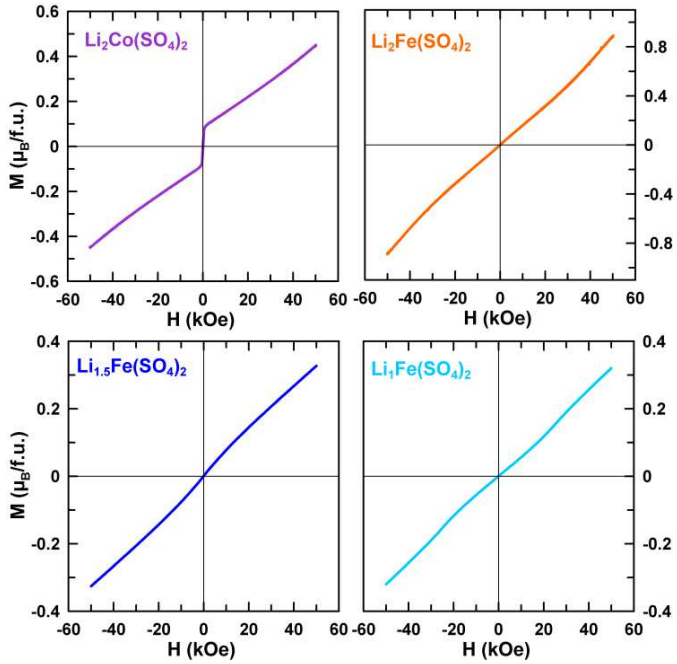

Figure III.30: Isothermal magnetization curves of $Li_2Co(SO_4)_2$ (purple), $Li_2Fe(SO_4)_2$ (orange), $Li_{1.5}Fe(SO_4)_2$ (blue) and $Li_1Fe(SO_4)_2$ (light blue) recorded at 2 K.

For a better understanding of the antiferromagnetic ground states we conducted NPD experiments at the wavelength λ = 2.419 Å on the D20 neutron diffractometer (ILL, Grenoble). Upon cooling we observe a gradual growing of additional peaks attributed to the ordering of the magnetic moments as shown in Figure III.31 for the four compounds. The difference patterns (green) between 30 K or 100 K (red) and 2 K (blue) illustrate well the new magnetic reflections with a preservation of the nuclear structure over the whole temperature range. The transition temperatures observed by NPD experiments are in good agreement with the Néel temperatures deduced from SQUID measurements (Table III.12). However, because the relative intensities of the magnetic peaks differ from one sample to another, one should expect differences in their magnetic structures.

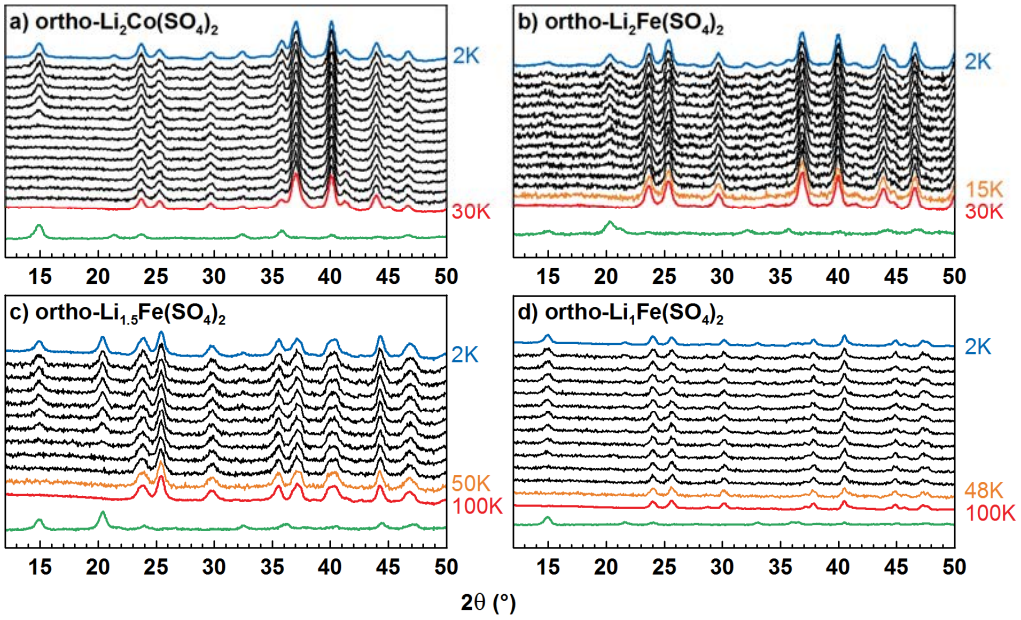

Figure III.31: Evolution of the NPD patterns of orthorhombic a) $Li_2Co(SO_4)_2$, b) $Li_2Fe(SO_4)_2$, c) $Li_{1.5}Fe(SO_4)_2$ and d) $Li_1Fe(SO_4)_2$ while cooling the sample to 2 K. Blue patterns are measured at 2 K, while red ones are measured at 30 K for a) and b) and at 100 K for b) and c). Green patterns correspond to the difference between the blue and the red patterns, i.e. solely the magnetic contribution. The patterns were recorded with a wavelength of λ = 2.419 Å.

The magnetic structures of the four orthorhombic phases was obtained through refinements on the NPD patterns recorded at 2 K at λ = 2.419 Å. Since for all compounds the magnetic peaks can be indexed in the crystallographic unit cell, the propagation vector is **k** = (0, 0, 0). We then performed a symmetry analysis using Bertaut's method as implemented in the BasIReps program of the FullProf suite in order to determine all spin configurations that are compatible with the orthorhombic unit cell *Pbca*.[202,203] The possible spin configurations and the corresponding Shubnikov space groups are given in Table III.13.

Table III.13: Results of the symmetry analysis of the *Pbca* unit cell for the propagation vector k = (0, 0, 0). The characters (χ) of the representations and the basis vectors Ψ_i (i = 1, 2, 3), as well as the Fourier coefficients (S_k = m, magnetic moments) of the eight general positions generated for the Wyckoff site 8*c* are given for each irreducible representation Γ_n ($1 \le j \le 8$) with the corresponding Shubnikov group (magnetic space group).

k = (0, 0, 0)									
		M(1)	**M(2)**	**M(3)**	**M(4)**	**M(5)**	**M(6)**	**M(7)**	**M(8)**
		x, y, z	***-x+½, -y, z+½***	***-x, y+½, -z+½***	***x+½, -y+½, -z***	***-x, -y, -z***	***x+½, y, -z+½***	***x, -y+½, z+½***	***-x+½, y+½, z***
Γ_1 ***Pbca***	χ	1	1	1	1	1	1	1	1
	Ψ_1	1, 0, 0	$\bar{1}$, 0, 0	$\bar{1}$, 0, 0	1, 0, 0	1, 0, 0	$\bar{1}$, 0, 0	$\bar{1}$, 0, 0	1, 0, 0
	Ψ_2	0, 1, 0	0, $\bar{1}$, 0	0, 1, 0	0, $\bar{1}$, 0	0, 1, 0	0, $\bar{1}$, 0	0, 1, 0	0, $\bar{1}$, 0
	Ψ_3	0, 0, 1	0, 0, 1	0, 0, $\bar{1}$	0, 0, $\bar{1}$	0, 0, 1	0, 0, 1	0, 0, $\bar{1}$	0, 0, $\bar{1}$
	S_k	***u, v, w***	***-u, -v, w***	***-u, v,-w***	***u, -v, -w***	***u, v, w***	***-u, -v, w***	***-u, v, -w***	***u, -v, -w***
Γ_2 ***Pb'c'a'***	χ	1	1	1	1	-1	-1	-1	-1
	Ψ_1	1, 0, 0	$\bar{1}$, 0, 0	$\bar{1}$, 0, 0	1, 0, 0	$\bar{1}$, 0, 0	1, 0, 0	1, 0, 0	$\bar{1}$, 0, 0
	Ψ_2	0, 1, 0	0, $\bar{1}$, 0	0, 1, 0	0, $\bar{1}$, 0	0, $\bar{1}$, 0	0, 1, 0	0, $\bar{1}$, 0	0, 1, 0
	Ψ_3	0, 0, 1	0, 0, 1	0, 0, $\bar{1}$	0, 0, $\bar{1}$	0, 0, $\bar{1}$	0, 0, $\bar{1}$	0, 0, 1	0, 0, 1
	S_k	***u, v, w***	***-u, -v, w***	***-u, v, -w***	***u, -v, -w***	***-u, -v, -w***	***u, v, -w***	***u, -v, w***	***-u, v, w***
Γ_3 ***Pb'c'a***	χ	1	1	-1	-1	1	1	-1	-1
	Ψ_1	1, 0, 0	$\bar{1}$, 0, 0	1, 0, 0	$\bar{1}$, 0, 0	1, 0, 0	$\bar{1}$, 0, 0	1, 0, 0	$\bar{1}$, 0, 0
	Ψ_2	0, 1, 0	0, $\bar{1}$, 0	0, $\bar{1}$, 0	0, 1, 0	0, 1, 0	0, $\bar{1}$, 0	0, $\bar{1}$, 0	0, 1, 0
	Ψ_3	0, 0, 1	0, 0, 1	0, 0, 1	0, 0, 1	0, 0, 1	0, 0, 1	0, 0, 1	0, 0, 1
	S_k	***u, v, w***	***-u, -v, w***	***u, -v, w***	***-u, v, w***	***u, v, w***	***-u, -v, w***	***u, -v, w***	***-u, v, w***
Γ_4 ***Pbca'***	χ	1	1	-1	-1	-1	-1	1	1
	Ψ_1	1, 0, 0	$\bar{1}$, 0, 0	1, 0, 0	$\bar{1}$, 0, 0	$\bar{1}$, 0, 0	1, 0, 0	$\bar{1}$, 0, 0	1, 0, 0
	Ψ_2	0, 1, 0	0, $\bar{1}$, 0	0, $\bar{1}$, 0	0, 1, 0	0, $\bar{1}$, 0	0, 1, 0	0, 1, 0	0, $\bar{1}$, 0
	Ψ_3	0, 0, 1	0, 0, 1	0, 0, 1	0, 0, 1	0, 0, $\bar{1}$	0, 0, $\bar{1}$	0, 0, $\bar{1}$	0, 0, $\bar{1}$
	S_k	***u, v, w***	***-u, -v, w***	***u, -v, w***	***-u, v, w***	***-u, -v, -w***	***u, v, -w***	***-u, v,-w***	***u, -v, -w***
Γ_5 ***Pb'ca'***	χ	1	-1	1	-1	1	-1	1	-1
	Ψ_1	1, 0, 0	1, 0, 0	$\bar{1}$, 0, 0	$\bar{1}$, 0, 0	1, 0, 0	1, 0, 0	$\bar{1}$, 0, 0	$\bar{1}$, 0, 0
	Ψ_2	0, 1, 0	0, 1, 0	0, 1, 0	0, 1, 0	0, 1, 0	0, 1, 0	0, 1, 0	0, 1, 0
	Ψ_3	0, 0, 1	0, 0, $\bar{1}$	0, 0, $\bar{1}$	0, 0, 1	0, 0, 1	0, 0, $\bar{1}$	0, 0, $\bar{1}$	0, 0, 1
	S_k	***u, v, w***	***u, v, -w***	***-u, v, -w***	***-u, v, w***	***u, v, w***	***u, v, -w***	***-u, v, -w***	***-u, v, w***
Γ_6 ***Pbc'a***	χ	1	-1	1	-1	-1	1	-1	1
	Ψ_1	1, 0, 0	1, 0, 0	$\bar{1}$, 0, 0	$\bar{1}$, 0, 0	$\bar{1}$, 0, 0	$\bar{1}$, 0, 0	1, 0, 0	1, 0, 0
	Ψ_2	0, 1, 0	0, 1, 0	0, 1, 0	0, 1, 0	0, $\bar{1}$, 0	0, $\bar{1}$, 0	0, $\bar{1}$, 0	0, $\bar{1}$, 0
	Ψ_3	0, 0, 1	0, 0, $\bar{1}$	0, 0, $\bar{1}$	0, 0, 1	0, 0, $\bar{1}$	0, 0, 1	0, 0, 1	0, 0, $\bar{1}$
	S_k	***u, v, w***	***u, v, -w***	***-u, v, -w***	***-u, v, w***	***-u,-v, -w***	***-u, -v, w***	***u, -v, w***	***u, -v, -w***
Γ_7 ***Pbc'a'***	χ	1	-1	-1	1	1	-1	-1	1
	Ψ_1	1, 0, 0	1, 0, 0	1, 0, 0	1, 0, 0	1, 0, 0	1, 0, 0	1, 0, 0	1, 0, 0
	Ψ_2	0, 1, 0	0, 1, 0	0, $\bar{1}$, 0	0, $\bar{1}$, 0	0, 1, 0	0, 1, 0	0, $\bar{1}$, 0	0, $\bar{1}$, 0
	Ψ_3	0, 0, 1	0, 0, $\bar{1}$	0, 0, 1	0, 0, $\bar{1}$	0, 0, 1	0, 0, $\bar{1}$	0, 0, 1	0, 0, $\bar{1}$
	S_k	***u, v, w***	***u, v, -w***	***u, -v, w***	***u,-v, -w***	***u, v, w***	***u, v, -w***	***u, -v, w***	***u, -v, -w***
Γ_8 ***Pb'ca***	χ	1	-1	-1	1	-1	1	1	-1
	Ψ_1	1, 0, 0	1, 0, 0	1, 0, 0	1, 0, 0	$\bar{1}$, 0, 0	$\bar{1}$, 0, 0	$\bar{1}$, 0, 0	$\bar{1}$, 0, 0
	Ψ_2	0, 1, 0	0, 1, 0	0, $\bar{1}$, 0	0, $\bar{1}$, 0	0, $\bar{1}$, 0	0, $\bar{1}$, 0	0, 1, 0	0, 1, 0
	Ψ_3	0, 0, 1	0, 0, $\bar{1}$	0, 0, 1	0, 0, $\bar{1}$	0, 0, $\bar{1}$	0, 0, 1	0, 0, $\bar{1}$	0, 0, 1
	S_k	***u, v, w***	***u, v, -w***	***u, -v, w***	***u, -v, -w***	***-u, -v, -w***	***-u, -v, w***	***-u, v, -w***	***-u, v, w***

The magnetic representation associated with the Wyckoff site 8*c* of the transition metal centers can be decomposed into eight irreducible representations (*irreps*):

Γ_{mag} (8c) = 3 $\Gamma_1 \oplus$ 3 $\Gamma_2 \oplus$ 3 $\Gamma_3 \oplus$ 3 $\Gamma_4 \oplus$ 3 $\Gamma_5 \oplus$ 3 $\Gamma_6 \oplus$ 3 $\Gamma_7 \oplus$ 3 Γ_8

Each of these *irreps* consists of three basis vectors Ψ_i (i=1, 2, 3) corresponding to the moments collinear to the *a*, *b* and *c* axes. The magnetic structures were solved by trial and error, where we tested all possibilities obtained by the symmetry analysis against the NPD patterns recorded at 2 K and compared the goodness of the fit for each representation. For $Li_2Co(SO_4)_2$ and $Li_1Fe(SO_4)_2$, the best fit was obtained with the irreproducible representation Γ_2, with moments along [001] (Ψ_3 basis vector) with the corresponding Shubnikov space group *Pb'c'a'*. Regarding $Li_2Fe(SO_4)_2$ and $Li_{1.5}Fe(SO_4)_2$ none of the eight representations could provide an accurate description of the intensities of the magnetic peaks. A moderate agreement was found with Γ_6 (Shubnikov group *Pbc'a*) with moments along *a* (Ψ_1) or Γ_8 (Shubnikov group *Pb'ca*) with moments along *b* (Ψ_2). The resulting patterns are compared to the experimental contribution (difference pattern 2 K – 30 K) in Figure III.32. Adding components along *b* and *c* (Ψ_2 and Ψ_3) for Γ_6, or along *a* and *c* (Ψ_1 and Ψ_3) for Γ_8 did not improve the quality of the fit. However, we obtain a very good agreement by mixing Γ_6 and Γ_8 representations, i.e. putting the magnetic moment as a linear combination of Ψ_1 (Γ_6) and Ψ_2 (Γ_8). For $Li_{1.5}Fe(SO_4)_2$ we directly refined the difference pattern 2 K – 100 K to circumvent the problem of impurities such as $Li_2Fe(SO_4)_2$ and Li_2SO_4 arising from the difficult preparation of that intermediate oxidized structure. The Shubnikov group corresponding to the mixing of $\Gamma_6 \oplus \Gamma_8$ is $P112_1'/a$, so the single set of 8 Fe atoms splits into two sets of four atoms resulting in two independent sites in the unit cell; however as we cannot see any structural distortion from our powder diffraction patterns, we have constrained to have the two sites the same magnitude of their magnetic moments. The general operators of $P112_1'/a$ are 1=(x, y, z), $2_1'$ =(–x+½, –y, z+½)', -1'= (–x, –y, –z)', a=(x+½, y, –z+½) and the representative atoms of the two Fe sites are: Fe(1)≈(0.85, 0.61, 0.37) and Fe(2)≈(0.15, 0.11, 0.13). The second site representative is generated by the operator (–x, y+½, –z+½)+[1,-1, 0] of the *Pbca* space group that is no more a symmetry operator in $P112_1'/a$. The magnetic moments of the atoms in the general position generated by the above operators are: (*u*, *v*, *w*), (*u*, *v*, -*w*), (-*u*, -*v*, -*w*), (-*u*, -*v*, *w*). The constraint we have applied is w=0 (collinear

structure) for all cases and that the magnetic moment of Fe(2) is opposite to the magnetic moment of Fe(1). The final Rietveld refinements of the magnetic structures of the four title compounds are gathered in Figure III.33 with the respective magnetic moments summarized in Table III.14. It is worth mentioning at this point that having a mixture of representations is rare feature, which has been reported for only 10 % of the magnetic structures such as $RbMnF_4$.[235]

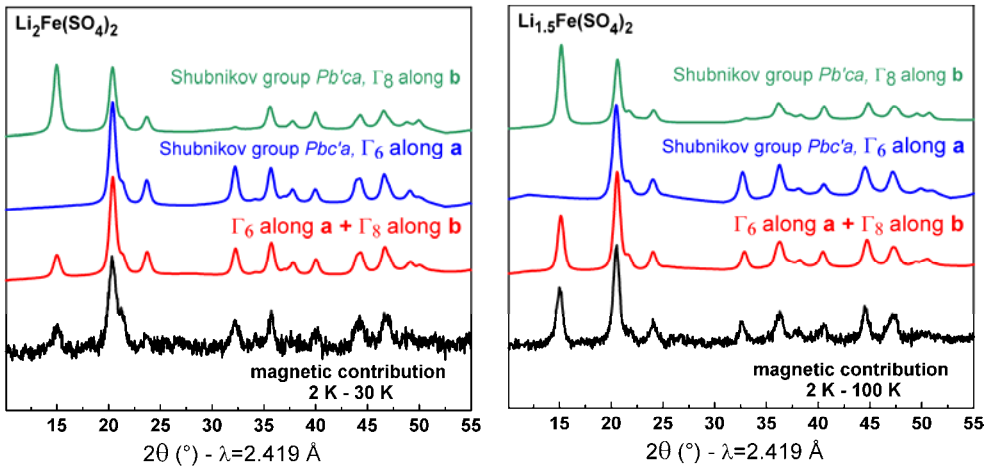

Figure III.32: Comparison between the neutron difference patterns (2 K - 30 K) of $Li_2Fe(SO_4)_2$ and (2 K - 100 K) $Li_{1.5}Fe(SO_4)_2$ (bottom black line), and the magnetic simulated pattern for the three models: Shubnikov group *Pb'ca*, Γ_8 with moments along b (top green pattern), Shubnikov group *Pbc'a*, Γ_6 with moments along a (blue pattern) and a mixture of the latter with Shubnikov group $P112_1'/a$ (red pattern).

Table III.14: Magnetic moments of orthorhombic $Li_xM(SO_4)_2$ deduced from Rietveld refinements of NPD pattern recorded at 2 K. Components of the magnetic moments are shown along x, y and z and the resulting total magnetic moments (M) are given for each compound. The eight magnetic atoms in the unit cell obtained by the symmetry operators (x, y, z), (–x+½, –y, z+½), (–x, y+½, –z+½), (x+½, –y+½, –z), (–x, –y, –z), (x+½, y, –z+½), (x, –y+½, z+½) and(–x+½, y+½, z) have their magnetic moments following (+ + – – – – + +).

Orthorhombic $Li_2M(SO_4)_2$ *M*=Co, Fe and $Li_xFe(SO_4)_2$ with x=1.5 and x=1

k = (0, 0, 0)					
Compound	**Representation**	**$M_x(\mu_B)$**	**$M_y(\mu_B)$**	**$M_z(\mu_B)$**	**$M(\mu_B)$**
$Li_2Co(SO_4)_2$	Γ_2	0	0	+3.11(5)	3.11(5)
$Li_2Fe(SO_4)_2$	$\Gamma_6 + \Gamma_8$	+2.70(5)	+1.27(8)	0	2.98(4)
$Li_{1.5}Fe(SO_4)_2$	$\Gamma_6 + \Gamma_8$	+3.49(12)	+3.32(9)	0	4.82(10)
$Li_1Fe(SO_4)_2$	Γ_2	0	0	+4.12(9)	4.12(9)

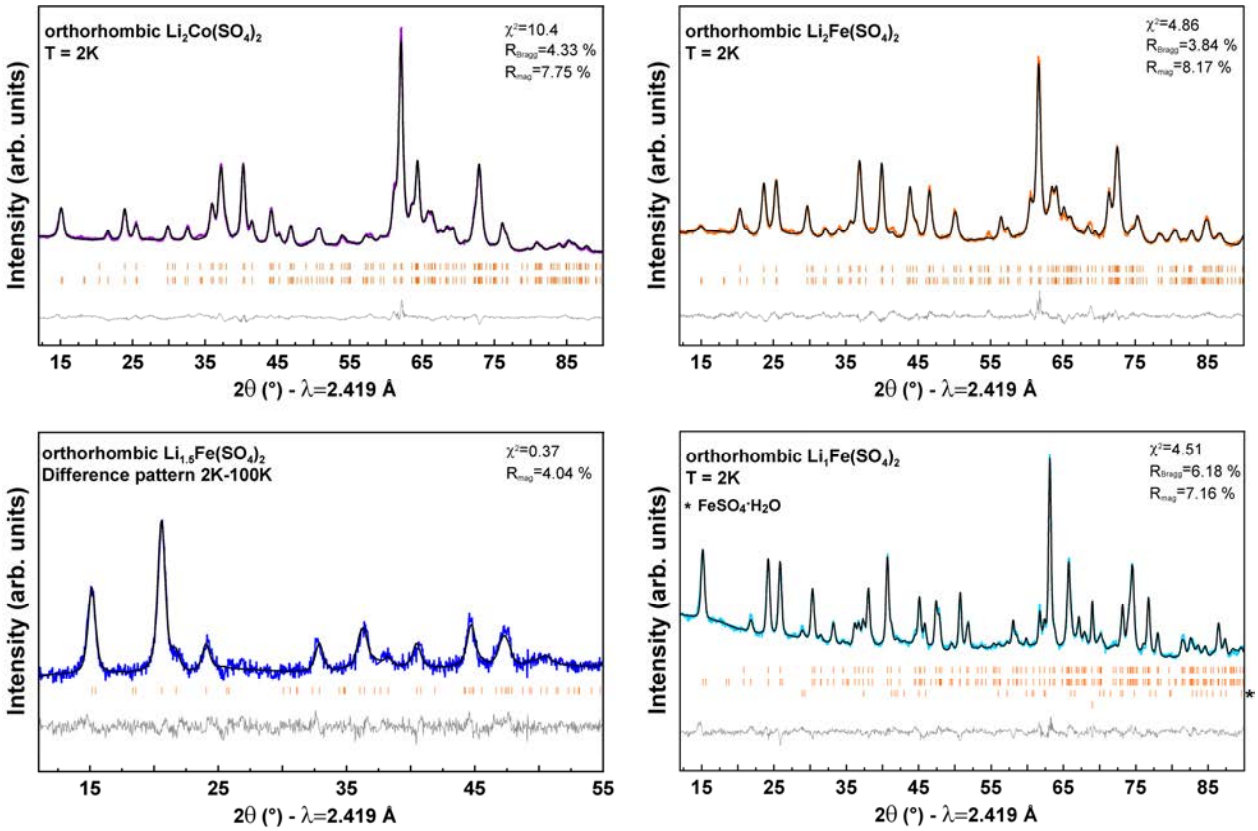

Figure III.33: Rietveld refinements of the nuclear and magnetic structures of orthorhombic $Li_2Co(SO_4)_2$, $Li_2Fe(SO_4)_2$, $Li_{1.5}Fe(SO_4)_2$ and $Li_1Fe(SO_4)_2$ phases. The coloured symbols correspond to the recorded patterns. The black and grey lines represent the calculated and difference pattern, respectively. The Bragg positions are shown as orange bars, where the upper phase corresponds to the nuclear structure and the bottom one to the magnetic structure. The phase marked with a star in $Li_1Fe(SO_4)_2$ is attributed to $FeSO_4{\cdot}H_2O$. Further, the vanadium peak of the sample container was included in this refinement. For $Li_{1.5}Fe(SO_4)_2$, the refinement was done on the difference pattern 2 K – 100 K that contains only the magnetic contribution.

The magnetic structures deduced from the refinements are shown in Figure III.34. We found a long-range antiferromagnetic alignment of the magnetic spins in agreement with the results of the susceptibility measurements. All magnetic structures the 8 magnetic moments in the cell present the sign sequence (+ + – – – – + +) where + and – signs represent the spin direction of the eight magnetic atoms taken in the same order as in the International Tables for Crystallography for position 8*c* in the *Pbca* space group. The four compounds present collinear magnetic structures, which can be also described as a ferromagnetic arrangement in the [110] direction with an antiferromagnetic stacking along [001]. However, as initially guessed from the relative intensities of the magnetic reflections, the orientation of the magnetic moments differs from one compound to the other. For both $Li_2Co(SO_4)_2$ and $Li_1Fe(SO_4)_2$ the magnetic moments

are found collinear to the *c*-axis. The same orientation of their magnetic moments is consistent with the similar relative intensities of the magnetic peaks in the NPD patterns (Figure III.31). For $Li_2Fe(SO_4)_2$ and $Li_{1.5}Fe(SO_4)_2$ the magnetic moments are orientated in the *ab*-plane with zero contribution of the z-component. The M-O-O-M super-super-exchange pathway is illustrated in Figure III.27.

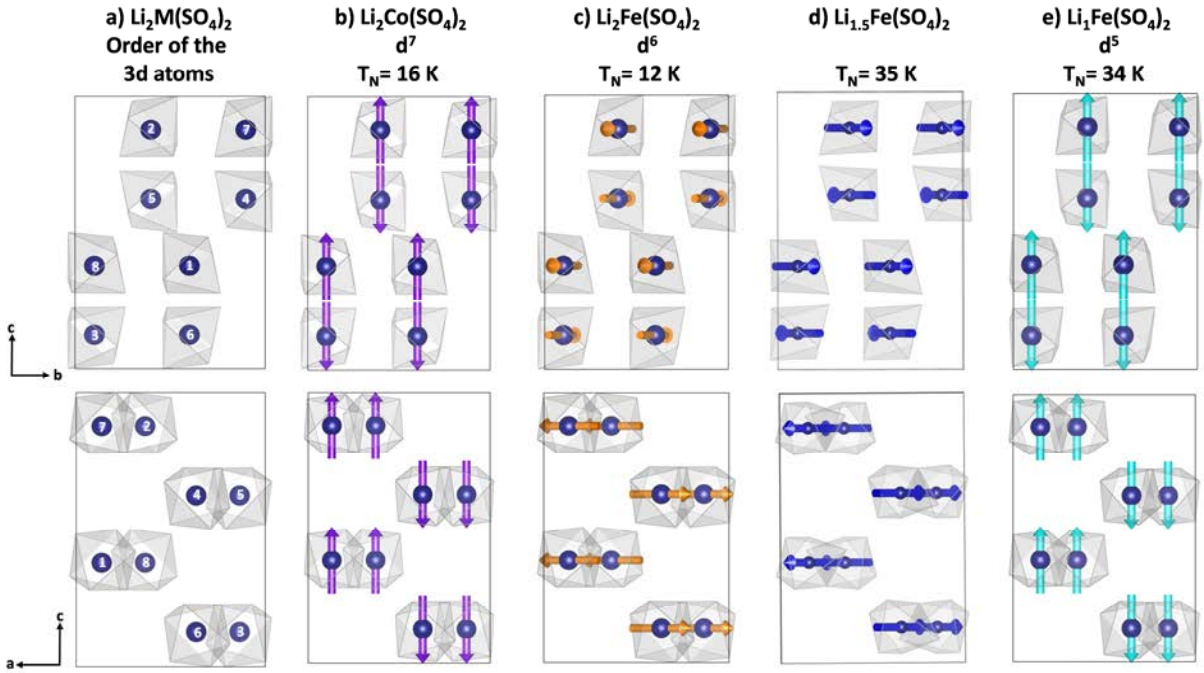

Figure III.34: a) The transition metal centers of the octahedra are numbered according to Table 12 defining the order of the magnetic moments. Magnetic structures of a) $Li_2Co(SO_4)_2$, b) $Li_2Fe(SO_4)_2$, c) $Li_{1.5}Fe(SO_4)_2$ and d) $Li_1Fe(SO_4)_2$. Magnetic moments are represented as arrows through the transition metal center shown as blue spheres. For the sake of clarity, Li, S and O atoms are omitted.

The obtained spin sequence (+ + – – – – + +) of the herein presented orthorhombic $Li_2M(SO_4)_2$ phases indicates that the magnetic moments is reverted (+M → –M) by the spatial inversion (x, y, z → –x, –y, –z). The Γ_2, Γ_6 and Γ_8 irreducible representations involved here show a negative character for the inversion center, so the spatial inversion is associated with time reversal. This characteristic enables the linear magnetoelectric effect to be active below T_N, which means that a magnetic field can induce an electrical polarization and *vice versa*. This feature is especially interesting in the data storage sector, where the magnetoelectric effect attracted a lot of attention for the development of multiferroics.[236] However, only few materials present this quality, such as Cr_2O_3 and the yttrium iron garnet (YIG).[237–239]

Since the described orthorhombic $Li_2M(SO_4)_2$ phases present the same spin sequence as the previously reported isostructural $Li_2Ni(SO_4)_2$ phase,[232] we can conclude that this possible magneto-electric effect is not linked to the Ni^{2+} transition metal center, but indeed more generally to the orthorhombic structural framework of these materials and the topology of the super-super-exchange interactions between transition metals inherent to this structure. This new insight into the relation between structure and magnetic properties might help to widen the rather small family of magnetoelectric compounds in the future by screening reported phases on their structural features.

III.7. Conclusions

In this chapter, we discussed a novel $Li_2M(SO_4)_2$ polymorph, which crystallizes in the orthorhombic space group *Pbca*. This new polymorph is synthesized via a mechano-chemical synthesis approach, in contrast to its monoclinic counterparts stabilized via a classic ceramic route. The Fe-based compound displays two redox plateaus at 3.73 and 3.85 V *vs.* Li^+/Li^0 with overall a better cycling performance and conductivity than monoclinic $Li_2Fe(SO_4)_2$ as shown by a.c. impedance measurements. Detailed studies combining NPD experiments, BVEL and DFT calculations revealed that the oxidation of orthorhombic $Li_2Fe(SO_4)_2$ takes place via a preferential delithiation of the Li2 site, while the Li1 site stays fully occupied during the whole redox process. Furthermore, we could identify the intermediate phase $Li_{1.5}Fe(SO_4)_2$, which forms prior to the complete oxidation of $Li_2Fe(SO_4)_2$ to $Li_1Fe(SO_4)_2$.

The transformation from one polymorph into the other can be achieved either by ball-milling (monoclinic-to-orthorhombic) or by annealing at temperatures between 300-400°C (orthorhombic-to-monoclinic). The fact that the monoclinic compounds are stabilized preferably at high temperatures does not come as a surprise given that it has been identified as the thermodynamically favored phase.

To conclude, this new orthorhombic $Li_2M(SO_4)_2$ family might not be the next contender for Li-ion batteries due to its restricted capacity and high water-sensibility, but nevertheless it emphasizes the richness of the structural, electrochemical and physical properties of Li-based 3d metal sulfates. From a magnetic point of view these $Li_2M(SO_4)_2$ phases, monoclinic or

orthorhombic, are highly interesting. Besides serving as model compounds for magnetic super-super exchange interactions owing to their particular structure, they are also of potential interest for data storage applications, namely orthorhombic $Li_2M(SO_4)_2$ (*M* = Fe, Co, Ni), which magnetic structure is compatible with a magnetoelectric effect.

These results motivated us to search deeper for unexplored sulfates that might present attractive properties. In this spirit, we came across a family of natural occurring bi-sulfates that has not been studied for their electrochemical properties. The next chapter will describe in detail the results of our investigation of this material.

Chapter IV. Langbeinite $K_2Fe_2(SO_4)_3$ and a new $K_2Cu_2(SO_4)_3$ phase

IV.1. Introduction

As described in the second chapter, the stabilization of new polyanionic frameworks, which allow the uptake of various alkali cations, led to discovery of new compounds such as KTP-like and monoclinic "$FeSO_4F$" and a novel "VPO_4F" polymorph.[165,204,240] In this context, we turned towards sulfate-based materials with the aim to prepare new host structures for the insertion of Li^+ and Na^+ and came across several $A_2Fe_2(SO_4)_3$ (A= Li, Na, K) phases, which all present polymorphic "$Fe_2(SO_4)_3$" structures (Figure IV.1).

1. $A_2Fe_2(SO_4)_3$ with A=Li[94,96] is prepared via electrochemical insertion of Li^+ into $Fe_2(SO_4)_3$ and displays a potential of 3.6 V *vs.* Li^+/Li^0. $Fe_2(SO_4)_3$ exists in the Nasicon and anti-Nasicon structures, where both $Fe_2(SO_4)_3$ configurations are built out of the so-called lantern-units consisting of two FeO_6 octahedra connected via three SO_4 tetrahedra (Figure IV.1a; see also Chapter I).

2. $A_2Fe_2(SO_4)_3$ with A=Na[148,241,242] crystallizes in an alluaudite-like structure (space group $P2_1/c$), where the $Fe_2(SO_4)_3$ framework consists of edge-sharing FeO_6 octahedra forming isolated Fe_2O_{10} dimers that are connected via SO_4 tetrahedra (Figure IV.1b). It presents an electrochemical potential of 3.8 V *vs.* Na^+/Na^0.

3. $A_2Fe_2(SO_4)_3$ with A=K[243,244] crystallizes in the cubic langbeinite structure (space group $P2_13$) with isolated FeO_6 octahedra that are connected via their six oxygen vertices to SO_4 tetrahedra (Figure IV.1c). K^+ is located in the large cavities of the formed 3D network.

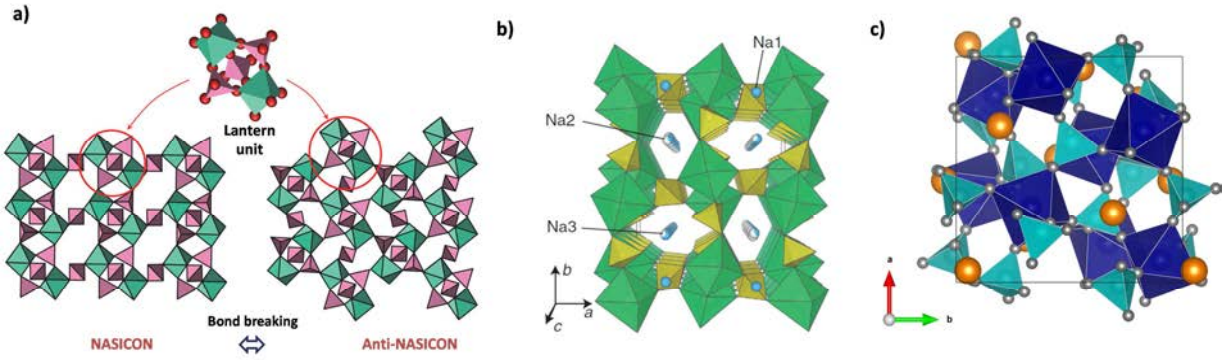

Figure IV.1: Structures of a) $Fe_2(SO_4)_3$ in its Nasicon and ani-Nasicon configuration, b) alluaudite-type $Na_2Fe_2(SO_4)_3$ and c) langbeinite $K_2Fe_2(SO_4)_3$.[91,148]

The langbeinite phases with the general composition $A_2M_2(SO_4)_3$ (A=K, NH_4, Rb, Tl and M = Mg, Mn, Ni, Zn, Ca, Fe, Cd and Co), which are derived from the mineral $K_2Mg_2(SO_4)_3$, have been vastly studied for their interesting physical features including antiferromagnetic spin-ordering, electro-optical effects, ferroelectric and ferroelastic properties.[243,245–251] Furthermore, they present complex phase-transitions upon cooling.[243,252,253] However, while $Li_2Fe_2(SO_4)_3$ and $Na_2Fe_2(SO_4)_3$ present attractive electrochemical performances, $K_2Fe_2(SO_4)_3$ has not been studied for its electrochemical properties yet. Thus our motivation to look into the redox properties of $K_2Fe_2(SO_4)_3$ as described in this chapter.

Furthermore, during the course of our exploration of the $A_2M_2(SO_4)_3$ phases, we were able to bring to light the so far unknown composition $K_2Cu_2(SO_4)_3$, which presents a different crystal structure than cubic $K_2Fe_2(SO_4)_3$. The synthesis, structure and electrochemical and physical properties of $K_2Cu_2(SO_4)_3$ are discussed in detail in the following.

IV.2. Synthesis and diffusion properties of langbeinite $K_2Fe_2(SO_4)_3$

Previously reported langbeinite $K_2Fe_2(SO_4)_3$ was prepared from an aqueous solution of K_2SO_4 and $FeSO_4$.[243] In our case however, we applied a straightforward solid-state approach, where stoichiometric amounts of $FeSO_4$ and K_2SO_4 were first ball-milled for 1 h under argon atmosphere using a Spex 8000 miller and then heated in a tubular furnace under argon atmosphere at 400 °C for 7h. The preparation of anhydrous $FeSO_4$ is described in detail in chapter II. The phase purity of the sample was verified via X-ray diffraction (XRD). The Rietveld refinement (Figure IV.2) was performed based on the previously reported cubic structure (space

group $P2_13$) of $K_2Mn_2(SO_4)_3$.[245] The resulting structural parameters are summarized in Table IV.1 and are in good agreement with the literature values.[244,245,248]

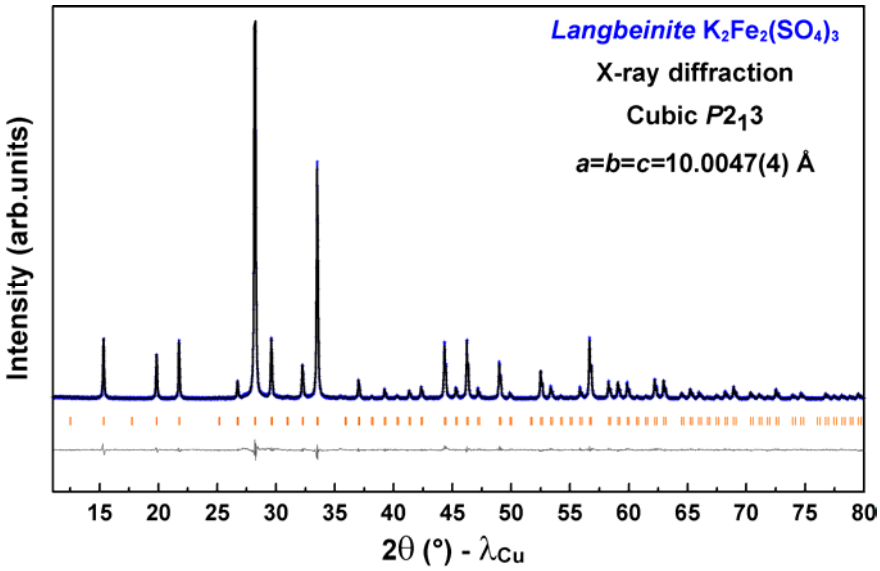

Figure IV.2: Rietveld refinement of langbeinite $K_2Fe_2(SO_4)_3$. Blue, black and grey lines represent the experimental, calculated and difference pattern, respectively. Bragg positions are shown as orange bars.

Table IV.1: Crystallographic data and atomic positions of langbeinite $K_2Fe_2(SO_4)_3$ as deduced from its Rietveld refinement. B_{iso} values were kept the same for the same elemental species.

Cubic $K_2Fe_2(SO_4)_3$

Space group $P2_13$			R_{Bragg} = 3.42 %			χ^2 = 1.50	
a = 10.00478(3) Å	b = 10.00478(3) Å		c = 10.00478(3) Å			V = 1001.433(6) Å^3	
Atom	Occupancy	Wyckoff position	x/a	y/b	z/c	B_{iso} (Å^2)	BVS
K1	1	4*a*	0.8135(3)	0.8135(3)	0.8135(3)	2.21(7)	1.145(8)
K2	1	4*a*	0.0502(3)	0.0502(3)	0.0502(3)	2.21(7)	1.006(8)
Fe1	1	4*a*	0.3350(2)	0.3350(2)	0.3350(2)	1.39(4)	2.193(21)
Fe2	1	4*a*	0.59432(17)	0.59432(17)	0.59432(17)	1.39(4)	1.935(17)
S1	1	12*b*	0.2210(3)	0.3760(5)	0.0174(4)	1.41(6)	6.417(84)
O1	1	12*b*	0.3108(8)	0.2798(8)	0.9597(7)	2.59(9)	2.180(40)
O2	1	12*b*	0.0845(8)	0.3244(9)	0.0066(7)	2.59(9)	2.065(38)
O3	1	12*b*	0.2353(7)	0.4970(10)	0.9388(11)	2.59(9)	2.146(50)
O4	1	12*b*	0.2540(6)	0.4088(7)	0.1541(9)	2.59(9)	2.120(43)

Electrochemical tests were conducted in Swagelok-type cells assembled in an argon-filled glovebox and cycled in a galvanostatic operating mode. Lithium metal was used as the negative electrode and the working electrode consisted of a composite of the active material and Carbon SP (Csp) (80:20 wt %), prepared by ball-milling for 15 min in a Spex 8000 miller. If not otherwise

specified, cells were cycled at C/20 (1C equals the uptake or removal of 1 Li^+ in 1h) with LP30 as electrolyte. K^+ was extracted from $K_2Fe_2(SO_4)_3$ on the first charge, while Li^+ was inserted/extracted in the following cycles. A typical composition-voltage trace is shown in Figure IV.3. On charge, we observe a pseudo-plateau at around 3.9 V vs. Li^+/Li^0 and a flat plateau at ~4.1 V *vs.* Li^+/Li^0, each accounting for approximately 0.2 K^+. On discharge, however, only ~0.2 Li^+ can be reinserted leading to a large irreversible capacity during the first cycle. Moreover, we observe a large polarization indicating slow diffusion kinetics in the langbeinite structure. Optimization trials of the cathode material (*e.g.* longer ball-milling, higher Csp content) did not improve the electrochemical performance.

We further conducted a chemical oxidation of $K_2Fe_2(SO_4)_3$ using NO_2BF_4 as oxidizing agent in acetonitrile. However, the negligible shift of the XRD pattern of $K_{2-x}Fe_2(SO_4)_3$ as well as the tiny amount of KBF_4 (peak marked with asterisk), which usually forms upon oxidation of a K-based compound with NO_2BF_4, confirm the difficulties of K^+ extraction encountered during the electrochemical cycling. The same result was obtained by additionally performed *ex situ* experiments on charge (Figure IV.4, purple pattern) and discharge (Figure IV.4, maroon pattern).

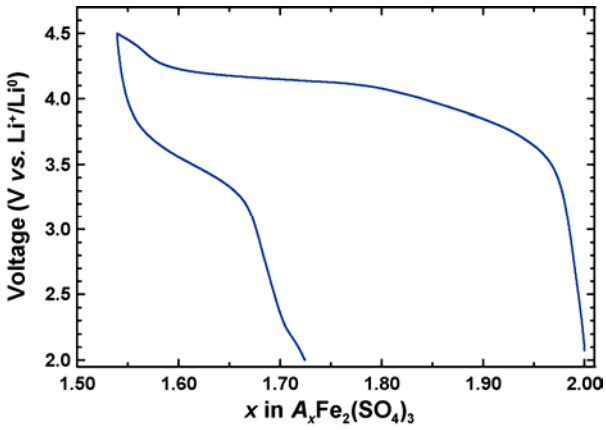

Figure IV.3: Voltage-composition trace of langbeinite $K_2Fe_2(SO_4)_3$ cycled at C/20 with a weight ratio of active material to Csp of 80:20.

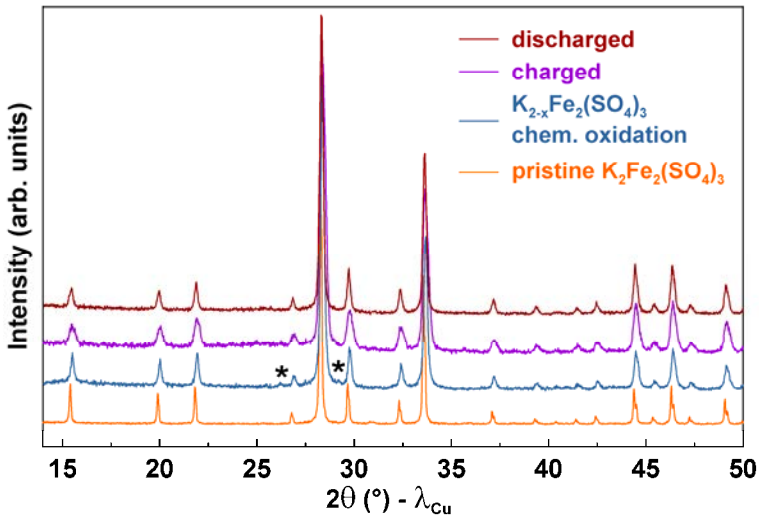

Figure IV.4: XRD patterns of pristine $K_2Fe_2(SO_4)_3$ (orange) and chemically oxidized $K_2Fe_2(SO_4)_3$ using NO_2BF_4 (blue pattern). The purple and red XRD patterns were recorded ex situ on charge and discharge of $K_2Fe_2(SO_4)_3$. The peaks marked with * correspond to KBF_4.

The low amounts of extracted K^+ as well as the large polarization in the electrochemical curve suggest a hampered ion diffusion in the langbeinite structure. This prompted us to examine the diffusion pathways in $K_2Fe_2(SO_4)_3$ via Bond Valence Energy Landscape (BVEL) calculations. Indeed, we obtain a threshold energy of 7.8 eV for an infinitely connected network in at least one direction. This value exceeds by far the usually observed energies of sulfate-based materials obtained by BVEL (~0.5-3 eV)[152,165,211] and emphasizes the low K^+ diffusion. BVEL maps calculated for Li insertion in an hypothetical langbeinite "$Fe_2(SO_4)_3$" framework, on the other side, reveal an activation energy of 0.9 eV, *i.e.* a value suitable for Li insertion. However, previous reports indicated that cubic langbeinite does not accommodate smaller cations such as Li^+ and Na^+ since they cannot stabilize the langbeinite $[M_2(SO_4)_3]^{2-}$ framework.[244] This might explain the low electrochemical activity as well as our unsuccessful trials to prepare langbeinite $A_2Fe_2(SO_4)_3$ with A = Li or Na either from scratch or via ionic substitution of $K_2Fe_2(SO_4)_3$ with $LiNO_3$ and $NaNO_3$.

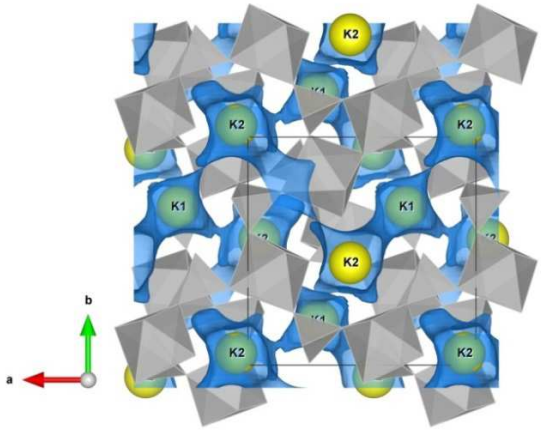

Figure IV.5: Potassium diffusion pathways in $K_2Fe_2(SO_4)_3$ as obtained by BVEL calculations plotted with an activation energy of 7.8 eV.

The above-described results show that $K_2Fe_2(SO_4)_3$ is not a suitable electrode material. However, on the quest for further potentially interesting $A_2M_2(SO_4)_3$ compounds, we noticed that Gattow *et al.* predicted that the Cu-based compound might present a different crystal structure due to the preferential square-planar coordination of Cu^{2+}, without however giving any details about the possible structure.[244] Since this Cu-based material has never been reported, we were intrigued to explore the possibility of stabilizing $K_2Cu_2(SO_4)_3$ and study its properties.

IV.3. Synthesis of a novel $K_2Cu_2(SO_4)_3$ compound

Phase-pure $K_2Cu_2(SO_4)_3$ was successfully prepared by a two-step solid-state route. First, stoichiometric amounts of K_2SO_4 and anhydrous $CuSO_4$, which has been previously dried under vacuum at 260 °C for 24 h, were ball milled for 4 hours in an Ar-filled ball-mill jar with a Spex 8000 vibratory miller and a ball-to-powder weight ratio of 25. The obtained mixture was then pressed to a pellet and heated at 300 °C for 20 h under a constant argon flow. $K_2Cu_2(SO_4)_3$ consists of particles in the sub-micrometer range (Figure IV.6). Note that a thermal treatment above 300 °C leads to the formation of fedotovite $K_2Cu_3O(SO_4)_3$ as a secondary phase. Furthermore, ball-milling times shorter than 4h lead to impurities in the final product. The composition of $K_2Cu_2(SO_4)_3$ was confirmed via EDX measurements and its structure was solved via combined synchrotron X-ray diffraction and electron diffraction measurements as described in the following.

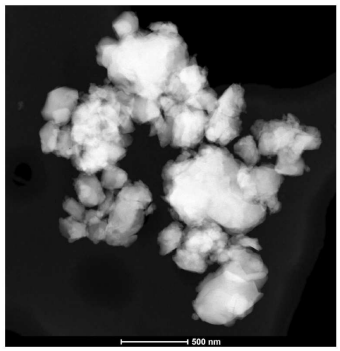

Figure IV.6: STEM image showing a typical agglomerate of $K_2Cu_2(SO_4)_3$ (image taken by D. Batuk, EMAT).

IV.4. Characterization of $K_2Cu_2(SO_4)_3$

IV.4.1. Structure determination of $K_2Cu_2(SO_4)_3$

Synchrotron X-ray diffraction (SXRD) patterns of $K_2Cu_2(SO_4)_3$ were recorded at 300 K in transmission mode (λ=0.4141 Å) at the 11BM beam line at Argonne National Lab. With help of the Dicvol[254,255] program, the Bragg peaks could be indexed in an orthorhombic unit cell with the lattice parameters *a*=4.81065(1) Å, *b*=11.91795(3) Å and *c*=18.67516(4) Å and a volume of V=1070.704(4) $Å^3$ that can therefore accommodate 4 formulae units of $K_2Cu_2(SO_4)_3$. We obtained in total 17 possible space groups. Since no structural model was known for this compound, we performed *ab initio* structural determination methods for all possible space groups using the Fox[256,257] program and compared the obtained structural models to the experimental SXRD data. During this process, the SO_4 tetrahedra were treated as rigid groups. Besides the many possible space groups, the large number of atoms (19 in total) further complicated the search for the correct structural model. The only space group, which indexed all the Bragg peaks obtained by SXRD and which resulted in a meaningful structure was $P2_12_12_1$. Furthermore, electron diffraction (see Annexe for details) indicated the reflection conditions *h*00: *h*=2n; 0*k*0: *k*=2n; 00*l*: *l*=2n and thus supported the orthorhombic space group $P2_12_12_1$ (Figure IV.7a). The final refinement of $K_2Cu_2(SO_4)_3$ with all atoms freely refined using the Rietveld method as implemented in the FullProf[203,214] program is shown in Figure IV.7b. The structural details deduced from the Rietveld refinement are summarized in Table IV.2. Moreover, for a more accurate refinement of the O positions, we performed neutron powder diffraction (NPD) on the D1B powder diffractometer, with a wavelength of 2.529 Å. The Rietveld

refinement conducted on the NPD pattern is shown in Figure IV.7b and fully validates the structural model.

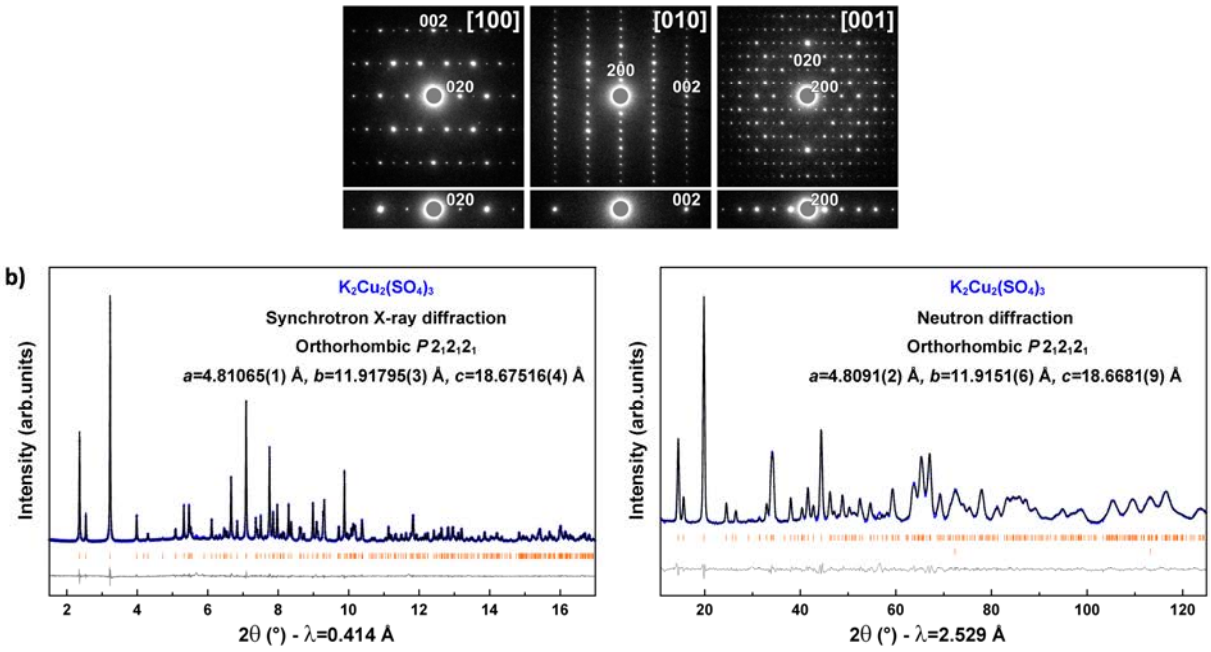

Figure IV.7: a) Electron diffraction image of $K_2Cu_2(SO_4)_3$. b) Rietveld refinement of the synchrotron XRD pattern (left) and neutron pattern (right) of $K_2Cu_2(SO_4)_3$. Blue, black and grey lines represent the experimental, calculated and difference pattern, respectively. Bragg positions are shown as orange bars.

The structure of $K_2Cu_2(SO_4)_3$ is based on distinct infinite "$Cu_2(SO_4)_3$" chains running along [100] (Figure IV.8a). They are stacked in parallel along the *b*-axis but are shifted in a ~90° with respect to each other forming a zig-zag motive in *c*-direction. Each of these chains consists of square-planar CuO_4 and five-fold coordinated square-pyramidal CuO_5 groups (Figure IV.8b). Note that the CuO_4 groups are isolated from each other as are also the CuO_5 units. Figure IV.9 shows the local environment of the Cu1 and Cu2 sites. Cu1 sits in the center of a perfectly regular square-planar and is connected through an O2 atom with Cu2, which forms the center of a square-pyramid. CuO_4 and CuO_5 are connected via SO_4 tetrahedra through their oxygen vertices. In the empty space between the chains, the K1 and K2 atoms, which are nine- and eight-fold coordinated (Figure IV.9), respectively, are located. The oxidation states of the atoms calculated by BVS (Table IV.2) are consistent with what is expected for this composition.

Table IV.2: Crystallographic data and atomic positions of $K_2Cu_2(SO_4)_3$ determined from the Rietveld refinement of its synchrotron XRD pattern. The B_{iso} as well as the BVS values are also indicated.

Orthorhombic $K_2Cu_2(SO_4)_3$

$P2_12_12_1$			R_{Bragg} = 4.84 %			χ^2 = 1.05	
a=4.81065(1)Å		b=11.91795(3) Å	c=18.67516(4) Å			V = 1070.704(4) Å^3	
Atom	Wyckoff position	Occupancy	x/a	y/b	z/c	B_{iso} (Å^2)	BVS
K1	4*a*	1	0.18250(3)	0.13076(11)	0.40811(7)	1.914(4)	1.050(4)
K2	4*a*	1	0.69591(4)	0.32848(11)	0.18436(7)	1.519(4)	1.301(6)
Cu1	4*a*	1	0.24424(3)	0.48396(5)	0.34274(4)	1.330(17)	1.874(10)
Cu2	4*a*	1	0.24010(2)	0.11442(7)	0.05180(3)	1.085(15)	1.937(9)
S1	4*a*	1	0.24667(5)	0.11663(12)	0.21865(7)	0.797(3)	5.820(32)
O1	4*a*	1	0.16573(9)	0.03348(3)	0.27297(2)	1.520(12)	1.930(17)
O2	4*a*	1	0.07946(7)	0.08287(3)	0.15149(2)	0.498(10)	2.083(15)
O3	4*a*	1	0.20298(11)	0.23147(3)	0.23780(17)	1.765(10)	1.976(18)
O4	4*a*	1	0.54695(7)	0.11448(4)	0.19594(19)	0.592(10)	2.052(16)
S2	4*a*	1	0.20980(4)	0.38040(14)	0.04783(8)	1.027(3)	5.956(33)
O5	4*a*	1	0.19490(10)	0.60269(3)	0.47395(17)	1.552(10)	1.804(16)
O6	4*a*	1	0.31752(8)	0.27285(3)	0.07609(16)	0.582(9)	2.086(17)
O7	4*a*	1	0.89854(8)	0.37610(4)	0.04664(2)	1.073(10)	2.052(17)
O8	4*a*	1	0.29464(11)	0.46651(3)	0.09906(19)	1.109(10)	1.798(18)
S3	4*a*	1	0.23111(5)	0.14077(12)	0.59875(8)	0.864(3)	5.938(34)
O9	4*a*	1	0.06258(7)	0.11974(4)	0.66422(19)	0.544(9)	2.001(16)
O10	4*a*	1	0.18384(10)	0.05074(3)	0.54712(2)	1.538(12)	2.150(17)
O11	4*a*	1	0.16777(8)	0.24878(4)	0.56824(17)	0.844(9)	1.986(21)
O12	4*a*	1	0.03586(7)	0.35793(3)	0.37840(2)	0.509(9)	1.957(15)

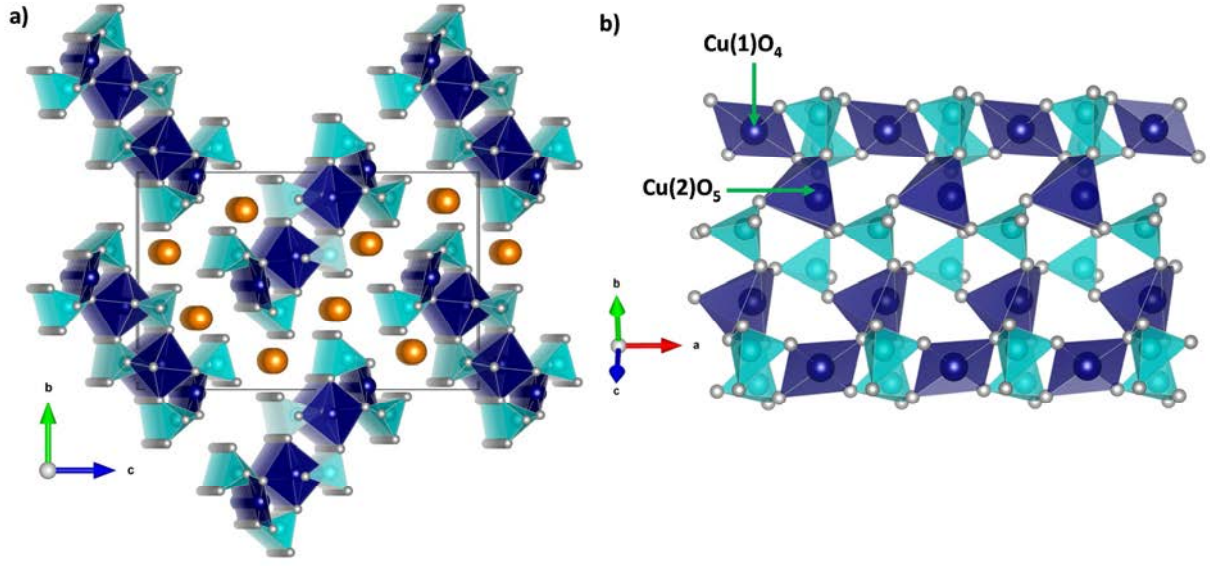

Figure IV.8: a) a) Structure of $K_2Cu_2(SO_4)_3$ shown along [100] consisting of infinite "$Cu_2(SO_4)_3$" chains. The Cu-based polyhedra and SO_4 tetrahedra are shown in blue and turquois, respectively. Oxygen and potassium atoms are represented as grey and orange spheres. b) View of a "$Cu_2(SO_4)_3$" chain running along [100].

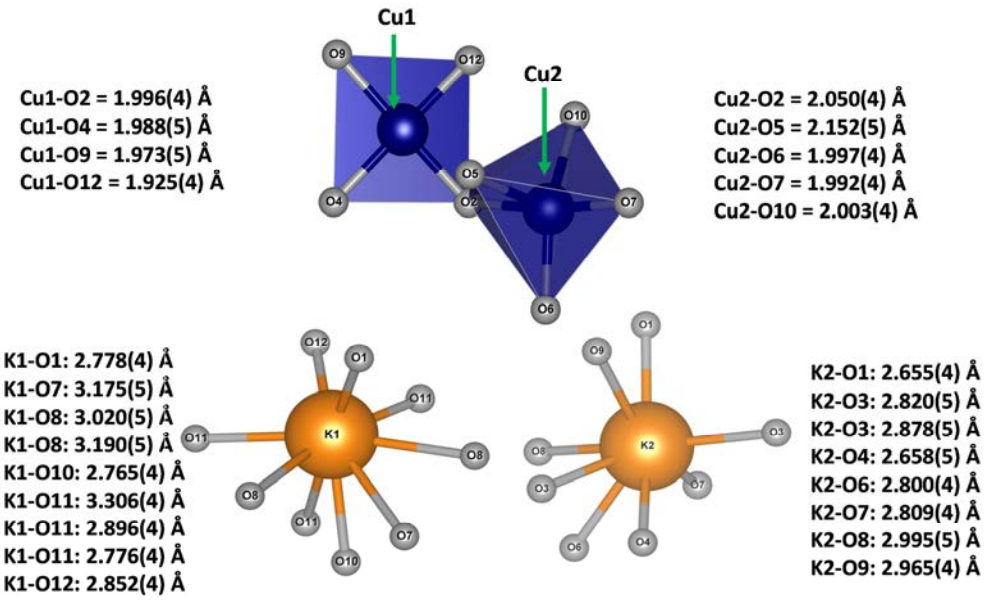

Figure IV.9: Top: Local coordination of square-planar CuO_4 and square-pyramidal CuO_5. The Cu-O bond lengths for Cu1 and Cu2 are indicated. Bottom: Local coordination of K1 and K2.

IV.4.2. Electrochemistry and cation diffusion of $K_2Cu_2(SO_4)_3$

Electrochemical tests against lithium were performed in Swagelok-type cells using LP30 as electrolyte and C/50 cycling rates. The electrode material was prepared via ball-milling $K_2Cu_2(SO_4)_3$ for 15 min with Csp (weight ratio 80:20). During the cycling, K^+ was extracted on the first charge and Li^+ was inserted/extracted in the following cycles. The composition-voltage trace of $K_2Cu_2(SO_4)_3$ cycled between 2-4 V *vs.* Li^+/Li^0 (Figure IV.10a) presents a limited electrochemical response. We observe one major plateau at 3.4 V *vs.* Li^+/Li^0 and two minor sloping contributions at 3.75 V *vs.* Li^+/Li^0 on charge and between 2.5-2.8 V *vs.* Li^+/Li^0 on discharge (Figure IV.10b). After disassembling the cycled cell, traces of elemental copper on the separator were observed indicating a conversion reaction. Charging $K_2Cu_2(SO_4)_3$ up to higher potentials such as 5 V *vs.* Li^+/Li^0 leads to a decomposition of $K_2Cu_2(SO_4)_3$, which might be linked to its highly hygroscopic behaviour.

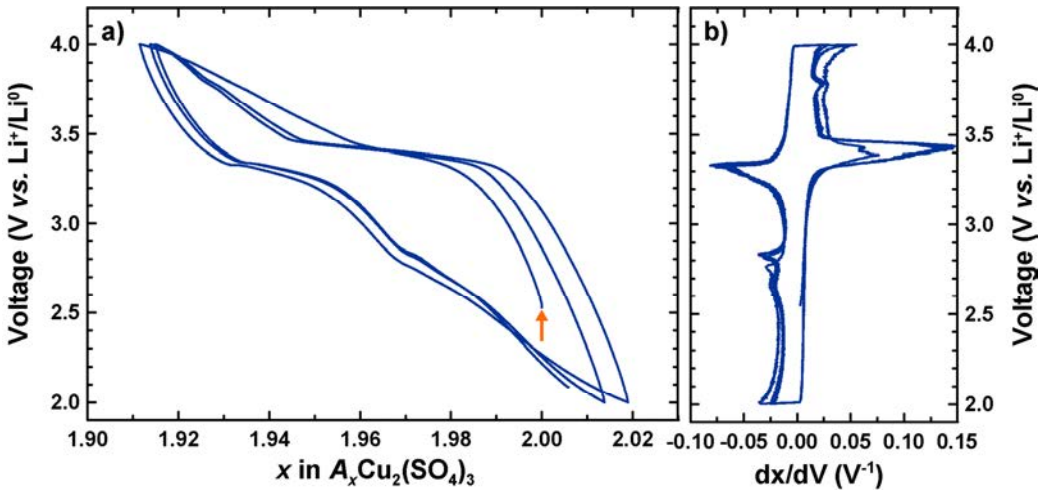

Figure IV.10: Voltage-composition trace of $K_2Cu_2(SO_4)_3$ cycled at C/50 started in oxidation (orange arrow) (a) and its derivative curve (b).

The limited K^+ extraction is further confirmed by *ex situ* experiments after charge and discharge of $K_2Cu_2(SO_4)_3$. We observe no shift of the Bragg peaks in the recorded XRD patterns of the charged (Figure IV.11, purple pattern) and discharged (maroon pattern) samples as compared to the pristine one (orange pattern). Additionally, a chemical oxidation of $K_2Cu_2(SO_4)_3$ was performed with an excess of NO_2BF_4 as oxidizing agent in acetonitrile at room temperature. It is crucial for this experiment to use extensively dry NO_2BF_4 since traces of water decompose highly hygroscopic $K_2Cu_2(SO_4)_3$ and lead to side reactions. Therefore, NO_2BF_4 was heated beforehand under vacuum at 170 °C for several hours. The XRD pattern (blue pattern) resulting from the chemical oxidation does not show any significant shift of the Bragg peaks or the growing of a second oxidized phase. However, we notice the formation of KBF_4 (peaks marked with asterisk). From Rietveld refinements we could estimate the amount of KBF_4 to be 10 %, hence implying that ~10 % of K^+ was extracted.

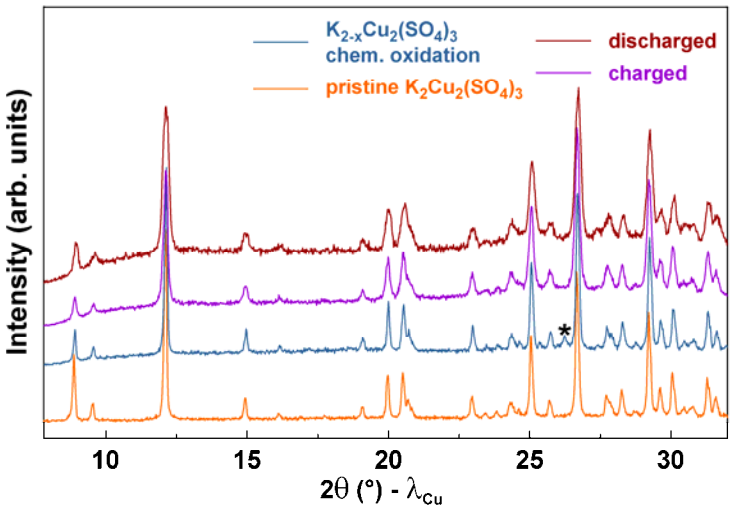

Figure IV.11: XRD patterns of pristine $K_2Cu_2(SO_4)_3$ (orange) and chemically oxidized $K_2Cu_2(SO_4)_3$ using NO_2BF_4 (blue pattern). The purple and red XRD patterns were recorded *ex situ* after charge and discharge of $K_2Cu_2(SO_4)_3$. The peak marked with * corresponds to KBF_4.

To rationalize these results, we calculated the K^+ diffusion pathways via the Bond Valence Energy Landscape (BVEL) approach (Figure IV.12a). We obtained a percolation energy of 1.59 eV necessary to obtain an infinitely connected network in at least one dimension. The preferred diffusion direction is along [100], whereas the diffusion along [010] and [001] is associated with significantly higher activation energies (2.78 eV and 6.38 eV).

In the light of these findings, we performed a.c. impedance spectroscopy on $K_2Cu_2(SO_4)_3$ using a BioLogic MTZ-35 setup with platinum electrodes equipped with an HTF-1100 furnace. The measurement was conducted on a sintered pellet (10 mm diameter, sputtered with gold) in a frequency range from 30 MHz to 0.1 Hz and at temperatures ranging from 200 °C to 450 °C under argon flow. Figure IV.12b shows the temperature-dependent evolution of the a.c. conductivity including the impedance spectrum measured at 363 °C, which was fitted with two RC circuits connected in series as shown in the inset of Figure IV.12b. The first half-circle represents the bulk contribution and the second one the grain boundary of the material. The experimental data points were fitted using the Arrhenius equation $\sigma(T) = \sigma_0 \cdot \exp(-E_a/k_B T)$, where σ is the conductivity at the temperature T, σ_0 is a pre-exponential factor, E_a the apparent activation energy for K^+ migration, and k_B the Boltzmann constant. The activation energy of $K_2Cu_2(SO_4)_3$ accounts for E_a = 1.49 eV with an extrapolated conductivity at room temperature of $\sigma_{RT} = 10^{-13}$ S/cm.

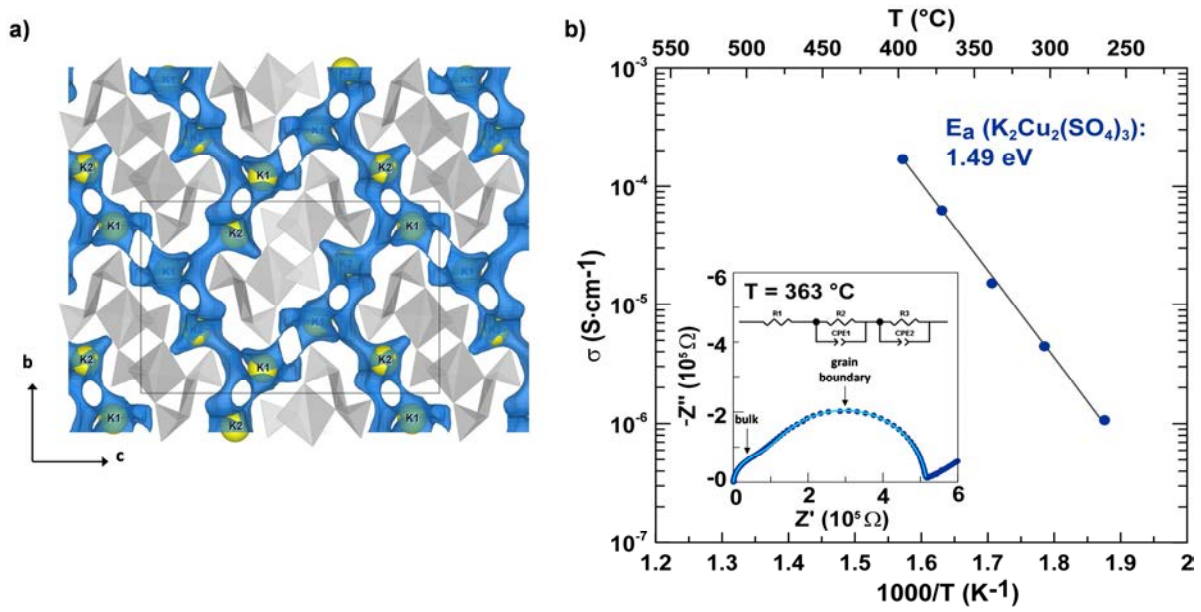

Figure IV.12: a) K1 and K2 diffusion pathways in $K_2Cu_2(SO_4)_3$ as obtained by BVEL calculations. For better visualization, we plotted the BVEL with an energy of 4.6 eV above the minimum threshold energy (1.59 eV). b) Temperature dependence of the a.c. conductivity of $K_2Cu_2(SO_4)_3$ and its activation energy E_a deduced from the Arrhenius equation. The inset shows the measured impedance spectrum at 363 °C and the circuit used for the fit.

IV.5. Stability of $K_2Cu_2(SO_4)_3$

Since sulfate-based compounds are known to be highly water-sensitive, we decided to test $K_2Cu_2(SO_4)_3$ for its stability towards humidity. As shown in Figure IV.13, only after a few hours of air exposure, the pristine XRD pattern (blue pattern) starts to evolve and after one day, the formation of the hydrated phases $K_2Cu(SO_4)_2{\cdot}6H_2O$ and $CuSO_4{\cdot}5H_2O$ at the expense of $K_2Cu_2(SO_4)_3$ can be clearly observed (Equation 2). Finally, after four days pristine $K_2Cu_2(SO_4)_3$ has almost completely decomposed.

$$K_2Cu_2(SO_4)_3 + 11H_2O \rightarrow K_2Cu(SO_4)_2 \cdot 6H_2O + CuSO_4 \cdot 5H_2O \quad \textbf{(2)}$$

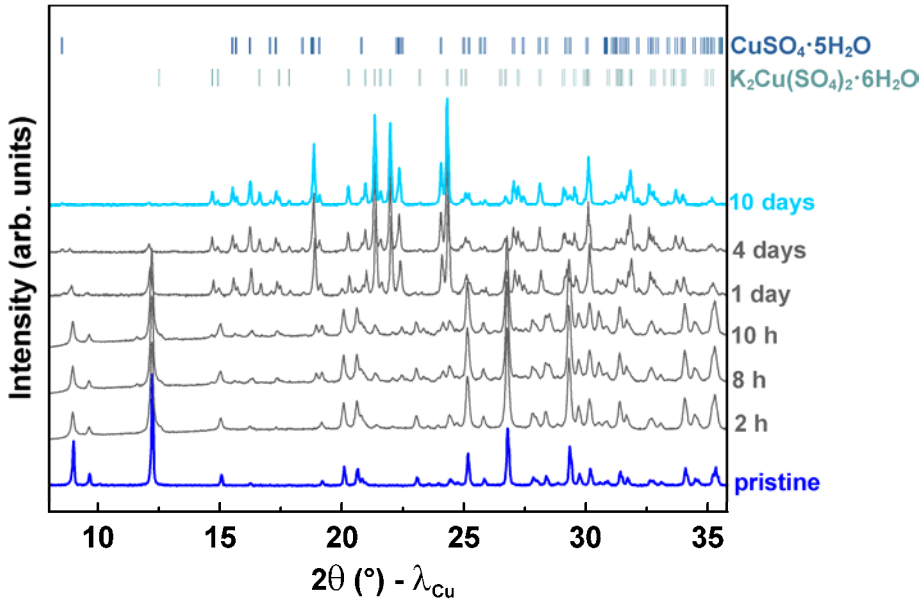

Figure IV.13: XRD patterns recorded of $K_2Cu_2(SO_4)_3$ left at ambient atmosphere. Pristine $K_2Cu_2(SO_4)_3$ (blue) transforms into $K_2Cu(SO_4)_2{\cdot}6H_2O$ and $CuSO_4{\cdot}5H_2O$ (light blue pattern). The Bragg positions of $K_2Cu(SO_4)_2{\cdot}6H_2O$ and $CuSO_4{\cdot}5H_2O$ are indicated as vertical barres.

The strong hygroscopic behaviour of sulfates has been previously reported for materials such as $LiFeSO_4F$ and $Li_2Fe(SO_4)_2$. Such moisture sensitivity is one of the major drawbacks of these compounds since it demands a handling of the cathode material under air-tight condictions during battery manufacturing or a pre-treatment of the compound with special coatings such as a conductive polymer coating (*e.g.* PEDOT) for instance or a carbon coating.[153,258–260]

During the synthesis optimization of $K_2Cu_2(SO_4)_3$ we noticed the formation of fedotovite $K_2Cu_3O(SO_4)_3$ at reaction temperatures above 300 °C. Furthermore, upon heating of $K_2Cu_2(SO_4)_3$ during impedance experiments, we observed a sudden drop of conductivity at around 380 °C (Figure IV.14a) suggesting a possible phase transition. To get more insight into the structural evolution of $K_2Cu_2(SO_4)_3$ with temperature, we performed high-temperature *in situ* XRD measurements (Figure IV.14b), where $K_2Cu_2(SO_4)_3$ was heated under a steady nitrogen flow from 50 °C to 620 °C in 20 °C steps and with a ramp of 5 °C/min and cooled down to 100 °C again. The temperature was held constant at each step during the recording of the XRD pattern (1h). Pristine $K_2Cu_2(SO_4)_3$ is stable until 400 °C and presents only a thermal expansion of the structure as can be seen from a shift of the peaks towards smaller angles. From 420 °C onwards a new peak appears at ~12°, which can be indeed assigned to the mineral fedotovite $K_2Cu_3O(SO_4)_3$. The phase decomposition from $K_2Cu_2(SO_4)_3$ to pure $K_2Cu_3O(SO_4)_3$ is completed at

500 °C. $K_2Cu_3O(SO_4)_3$ remains then stable up to 560 °C before completely decomposing irreversibly. The phase change can be further observed through the colour change upon heating with $K_2Cu_2(SO_4)_3$ being light blue and $K_2Cu_3O(SO_4)_3$ dark green (Figure IV.15).

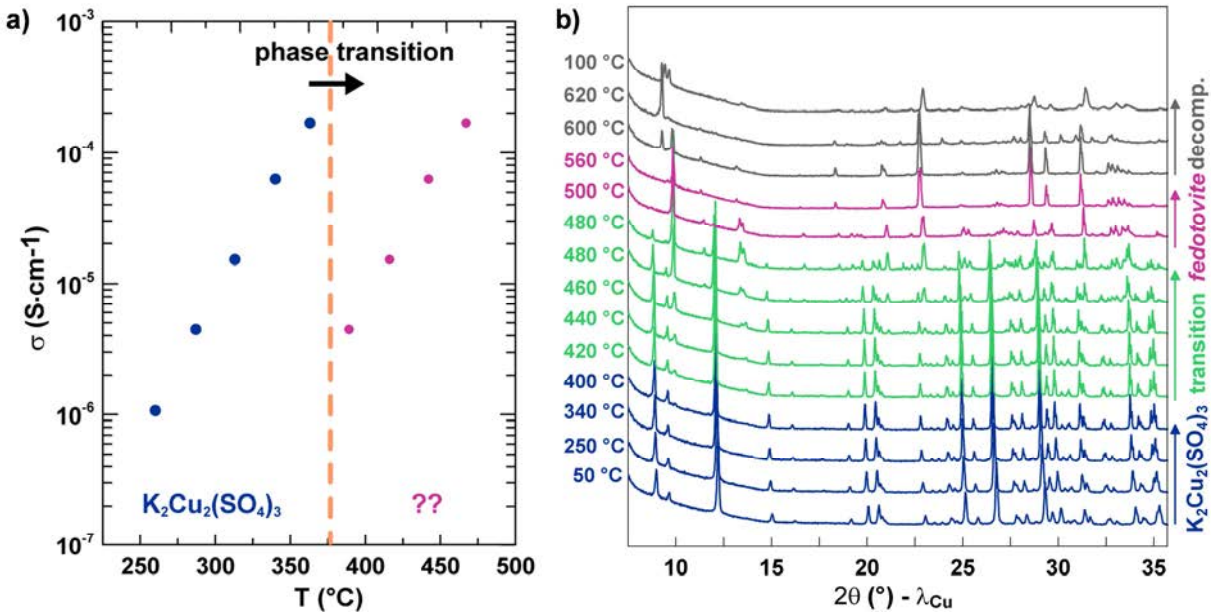

Figure IV.14: a) Temperature dependence of the a.c. conductivity of $K_2Cu_2(SO_4)_3$ heated up to 500 °C. The drop of conductivity around 380 °C suggests a phase transformation. b) High-temperature *in situ* XRD experiment on $K_2Cu_2(SO_4)_3$, which was heated from 50 °C to 620 °C and cooled down to 100 °C under nitrogen flow. The blue, green and purple pattern correspond to the pristine $K_2Cu_2(SO_4)_3$, the transition range (biphasic domain) and to fedotovite $K_2Cu_3O(SO_4)_3$ respectively. The grey patterns correspond to decomposition products.

Figure IV.15: Powder samples of turquois $K_2Cu_2(SO_4)_3$ and dark green fedotovite $K_2Cu_3O(SO_4)_3$.

The thermal evolution of $K_2Cu_2(SO_4)_3$ was further explored through differential scanning calorimetry (DSC; blue line) coupled with thermogravimetric analysis (TGA; green line) from 25 °C to 600 °C with a ramp of 5 °C/min under argon atmosphere (see Annexe for details) (Figure IV.16). The DSC curve shows three endothermic peaks starting from 498 °C, which suggest that the phase change from $K_2Cu_2(SO_4)_3$ to fedotovite is not straight-forward, but might occur via

several intermediate steps. We were however not able to identify possible intermediate phases from the high-temperature XRD experiment. We hypothesize that the last two peaks at 524 °C and 567 °C are related to the phase transition and fedotovite decomposition, respectively.

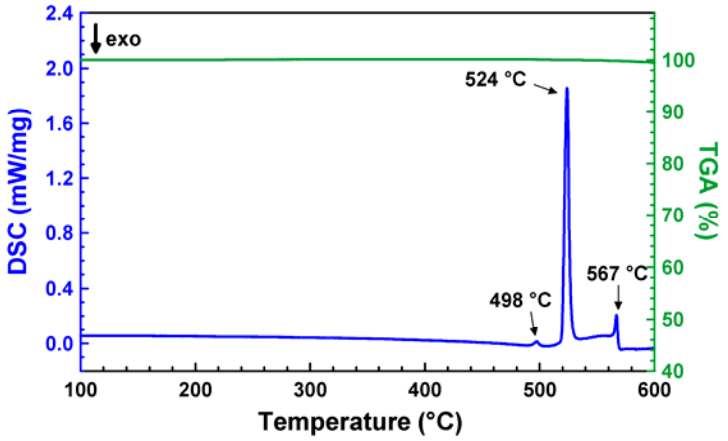

Figure IV.16: DSC (blue line) coupled with TGA (green line) of $K_2Cu_2(SO_4)_3$ showing three endothermic peaks.

IV.6. Synthesis of $K_2Cu_3O(SO_4)_3$

Fedotovite $K_2Cu_3O(SO_4)_3$ is a volcanic mineral, which was first discovered in Kamchatka, Russia, after a volcano eruption in 1975-1976.[261] Its structure has been previously reported by Starova *et al.* and it crystallizes in the monoclinic space group *C*2/*c*.[261] $K_2Cu_3O(SO_4)_3$ shows a layered-like structure along [100] with the potassium cations located between the layers (Figure IV.17a). Each "$Cu_3O(SO_4)_3$" layer is built of units of corner-sharing CuO_5 (more precisely [4+1]) entities connected via an oxygen atom to two distorted square-planar CuO_4 (Figure IV.17b,c). The CuO_4 groups share one edge with each other as well as two oxygen atoms with two SO_4 tetrahedra that are further linked to the CuO_5 square-pyramids. These units are connected via one SO_4 tetrahedra. Note that both $K_2Cu_2(SO_4)_3$ as well as $K_2Cu_3O(SO_4)_3$ present square-planar as well as square-pyramidal Cu^{2+} coordinations coexisting in the same structure.

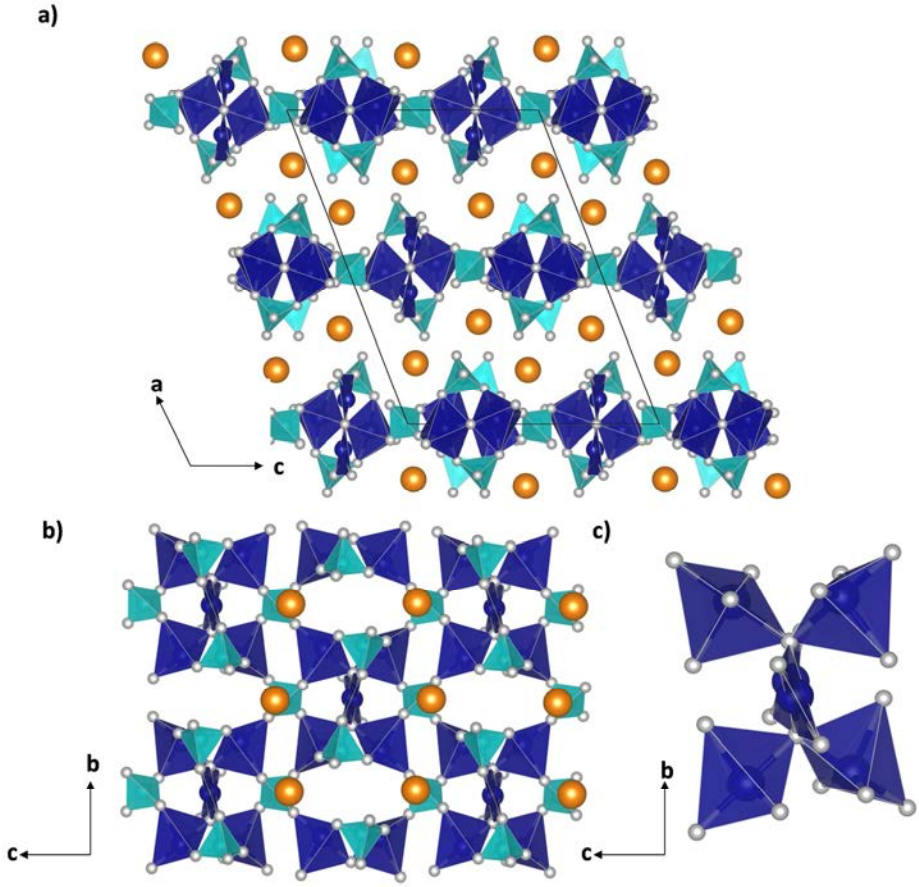

Figure IV.17: Representation of $K_2Cu_3O(SO_4)_3$, which adopts a layered-like structure as shown along the b-axis (a). b) The structure of a single layer shown along the a-axis. The Cu-based polyhedra and SO_4 tetrahedra are shown in blue and turquois, respectively. Oxygen and potassium atoms are illustrated as grey and orange spheres. c) Connectivity of one unit that forms the Cu-based framework of $K_2Cu_3O(SO_4)_3$. Four square-pyramidal CuO_5 are connected to two distorted square-planar CuO_4 via their oxygen vertices.

Fedotovite has only been characterized as a natural mineral, but, to the best of our knowledge, has never been prepared synthetically. For the synthesis of $K_2Cu_3O(SO_4)_3$, we started from as-prepared $K_2Cu_2(SO_4)_3$, which was ball milled for 30 min with an excess of CuO (10 %) (Equation 3). The mixture was then heated at 500 °C for 30-48 h under argon atmosphere.

$$K_2Cu_2(SO_4)_3 + CuO \rightarrow K_2Cu_3O(SO_4)_3 \quad \textbf{(3)}$$

XRD experiments confirmed the purity of the sample. The Rietveld refinement of the synchrotron XRD pattern of as-prepared $K_2Cu_3O(SO_4)_3$ in the monoclinic *C2/c* space group is shown in Figure IV.18 together with the neutron pattern. The structural data summarized in

C 2/*c* RBragg = 2.45 % χ2 = 6.14

a=19.09059(5)Å *b*=9.52853(2) Å *c*=14.18650(3) Å β=110.63109(19)° *V* = 2415.100(9) Å3

Atom	Wyckoff position	Occupancy	*x*/*a*	*y*/*b*	*z*/*c*	Biso (Å2)
K1	8f	1	0.32450(11)	0.7499(3)	0.43781(15)	2.56(4)
K2	8f	1	0.19534(12)	0.7348(3)	0.12292(15)	2.56(4)
Cu1	8f	1	0.48124(6)	0.01768(14)	0.34270(8)	0.681(13)
Cu2	8f	1	0.48655(6)	0.47906(14)	0.14051(8)	0.681(13)
Cu3	8f	1	0.42128(6)	0.74630(16)	0.20640(8)	0.681(13)
S1	8f	1	0.50556(13)	0.7495(3)	0.49027(17)	0.70(3)
S2	8f	1	0.64718(12)	0.0260(3)	0.36632(18)	0.70(3)
S3	8f	1	0.35189(13)	0.4676(3)	0.21723(17)	0.70(3)
O1	4e	1	0.5	0.8869(9)	0.25	0.81(4)
O2	8f	1	0.4511(3)	0.8272(5)	0.4080(4)	0.81(4)
O3	8f	1	0.5611(3)	0.6769(5)	0.4581(4)	0.81(4)
O4	8f	1	0.4635(3)	0.6458(5)	0.5274(4)	0.81(4)
O5	8f	1	0.5892(3)	0.0595(6)	0.4100(4)	0.81(4)
O6	8f	1	0.4042(3)	0.4419(5)	0.3152(4)	0.81(4)
O7	8f	1	0.3389(3)	0.6224(6)	0.2028(4)	0.81(4)
O8	8f	1	0.2808(3)	0.3954(5)	0.2008(4)	0.81(4)
O9	8f	1	0.5479(3)	0.8486(5)	0.5736(4)	0.81(4)
O10	8f	1	0.6200(3)	0.0691(5)	0.2584(4)	0.81(4)
O11	8f	1	0.3894(3)	0.4208(5)	0.1415(4)	0.81(4)
O12	4e	1	0.5	0.6045(9)	0.25	0.81(4)
O13	8f	1	0.6611(3)	0.8718(6)	0.3713(4)	0.81(4)
O14	8f	1	0.7160(3)	0.0942(5)	0.4226(4)	0.81(4)

Table IV.3. Freely refining the S and O positions led to strong deviations in the SO_4 tetrahedra. This can be explained by the large number of atoms and the low crystallinity of the powder. We therefore kept their positions fixed, while Cu and K were freely refined.

Note that the cell parameters obtained by our refinement (*a*=19.09059(5) Å, *b*=9.52853(2) Å *c*=14.18650(3) Å, β= 110.63109(19)°) vary from the ones reported by Starova *et al.* (*a*=19.037(6) Å, *b*=9.479(2) Å, *c*=14.231(5) Å and β=111.04(3)°).[261] This might be related to the fact that their structure was resolved on the natural mineral, which might contain impurities that influence the lattice size.

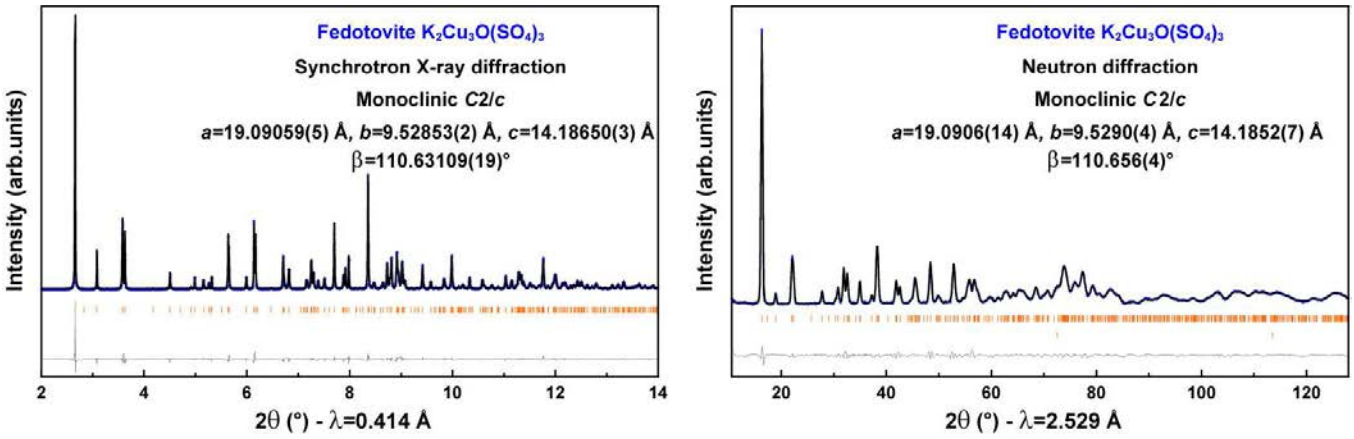

Figure IV.18: Rietveld refinement of the synchrotron X-ray powder diffraction pattern (left) and neutron diffraction pattern (right) of fedotovite $K_2Cu_3O(SO_4)_3$. Blue, black and grey lines represent the experimental, calculated and difference pattern, respectively. Bragg positions are shown as orange bars

Table IV.3: Crystallographic data and atomic positions of fedotovite $K_2Cu_3O(SO_4)_3$ determined from Rietveld refinements of its synchrotron X-ray powder diffraction pattern. The isotropic temperature values (B_{iso}) is listed in the last column.

Monoclinic fedotovite $K_2Cu_3O(SO_4)_3$

C 2/*c*		R_{Bragg} = 2.45 %			χ^2 = 6.14	
a=19.09059(5)Å	*b*=9.52853(2) Å	*c*=14.18650(3) Å	β=110.63109(19)°		*V* = 2415.100(9) Å^3	
Atom	Wyckoff position	Occupancy	*x/a*	*y/b*	*z/c*	B_{iso} (Å^2)
K1	8*f*	1	0.32450(11)	0.7499(3)	0.43781(15)	2.56(4)
K2	8*f*	1	0.19534(12)	0.7348(3)	0.12292(15)	2.56(4)
Cu1	8*f*	1	0.48124(6)	0.01768(14)	0.34270(8)	0.681(13)
Cu2	8*f*	1	0.48655(6)	0.47906(14)	0.14051(8)	0.681(13)
Cu3	8*f*	1	0.42128(6)	0.74630(16)	0.20640(8)	0.681(13)
S1	8*f*	1	0.50556(13)	0.7495(3)	0.49027(17)	0.70(3)
S2	8*f*	1	0.64718(12)	0.0260(3)	0.36632(18)	0.70(3)
S3	8*f*	1	0.35189(13)	0.4676(3)	0.21723(17)	0.70(3)
O1	4*e*	1	0.5	0.8869(9)	0.25	0.81(4)
O2	8*f*	1	0.4511(3)	0.8272(5)	0.4080(4)	0.81(4)
O3	8*f*	1	0.5611(3)	0.6769(5)	0.4581(4)	0.81(4)
O4	8*f*	1	0.4635(3)	0.6458(5)	0.5274(4)	0.81(4)
O5	8*f*	1	0.5892(3)	0.0595(6)	0.4100(4)	0.81(4)
O6	8*f*	1	0.4042(3)	0.4419(5)	0.3152(4)	0.81(4)
O7	8*f*	1	0.3389(3)	0.6224(6)	0.2028(4)	0.81(4)
O8	8*f*	1	0.2808(3)	0.3954(5)	0.2008(4)	0.81(4)
O9	8*f*	1	0.5479(3)	0.8486(5)	0.5736(4)	0.81(4)
O10	8*f*	1	0.6200(3)	0.0691(5)	0.2584(4)	0.81(4)
O11	8*f*	1	0.3894(3)	0.4208(5)	0.1415(4)	0.81(4)
O12	4*e*	1	0.5	0.6045(9)	0.25	0.81(4)
O13	8*f*	1	0.6611(3)	0.8718(6)	0.3713(4)	0.81(4)
O14	8*f*	1	0.7160(3)	0.0942(5)	0.4226(4)	0.81(4)

IV.7. Conclusion

In previous reports, new polyanionic host structures for Li^+ and Na^+ insertion have been stabilized through K^+ extraction from their mother phase. With this in mind, we aimed for a new polymorphic "$Fe_2(SO_4)_3$" framework based on the langbeinite $K_2Fe_2(SO_4)_3$ phase. Electrochemical tests combined with BVEL calculations revealed poor K^+ diffusion features, which might be related to structural instabilities of the langbeinite $K_2Fe_2(SO_4)_3$ structure upon K^+ extraction.

Nevertheless, during the course of the exploration of other langbeinite phases, we synthesized a novel $K_2Cu_2(SO_4)_3$ compound from $CuSO_4$ and K_2SO_4 heated at 300 °C. This new compound crystallizes in an orthorhombic unit cell (space group $P2_12_12_1$) different from the one of the langbeinite phases. Galvanostatic cycling revealed only moderate electrochemical properties, which was further confirmed by *ex situ* experiments as well as chemical oxidation. Upon heating $K_2Cu_2(SO_4)_3$, we identified a phase transformation from $K_2Cu_2(SO_4)_3$ to fedotovite $K_2Cu_3O(SO_4)_3$. Even though the structure of this natural occurring mineral $K_2Cu_3O(SO_4)_3$ has been previously reported, it has never been synthetically prepared. We were able to establish a synthesis protocol via a solid state approach, where $K_2Cu_2(SO_4)_3$ was heated with CuO at 500 °C.

We can conclude that not every material presents the necessary structural features to cope with the extraction of the rather large K^+ cation to form new insertion compounds for lithium. Even though the here described Cu-based compounds are not suitable as electrode materials, the Cu^{2+} (d^9 electronic configuration) presents a spin S=1/2, which might be interesting for other fields such as magnetic applications. Furthermore, this work emphasizes the large variety of existing phases that need to be revisited as potential cathode materials as well as the myriad of compounds that still waits to be discovered.

General conclusions

The aim of this thesis was the preparation of novel high performance electrode materials based on polyanionic frameworks, which combine appealing properties in terms of sustainability, low-cost and electrochemical performances. We focused especially on novel sulfate- and fluorosulfate-based phases, which according to the inductive effect would present elevated redox potentials. Indeed, the logic of the inductive effect has been successfully applied to tavorite/triplite $LiFeSO_4F$, where the strong inductive effect of the SO_4^{2-} group is reinforced by the electronegativity of the fluorine atom.

During the course of this work, we successfully stabilized three new compounds: orthorhombic $Li_2Fe(SO_4)_2$ and the potassium-based phases $KFeSO_4F$ and $K_2Cu_2(SO_4)_3$. The two former are in fact new polymorphs of previously reported phases (monoclinic $Li_2Fe(SO_4)_2$ and KTP-like orthorhombic $KFeSO_4F$), while the latter is a new chemical composition. All phases were studied for their synthesis, structure as well as electrochemical and physical properties.

- Monoclinic $KFeSO_4F$ crystallizes in the *C*2/*c* space group and presents a layered-like structure based on edge- and corner-sharing FeO_6 octahedra and SO_4 tetrahedra. Monoclinic $KFeSO_4F$ is synthesized via a classic ceramic route at 310 °C and transforms into its high-temperature KTP-like counterpart upon heating at ~380 °C. We can electrochemically extract K^+ on charge and reinsert Li^+ at an average potential of 3.7 *vs.* Li^+/Li^0. We obtain a reversible capacity of 78 $mAh{\cdot}g^{-1}$. Besides its electrochemical properties, magnetic studies reveal a long-range antiferromagnetic spin ordering.

- Even though fluorosulfates present interesting properties, the use of fluorine might be the source of safety issues. Therefore we turned towards sulfate-based materials and prepared a polymorphic configuration of $Li_2Fe(SO_4)_2$, which crystallizes in the orthorhombic *Pbca* space group. It presents two plateaus at 3.73 and 3.85 V *vs.* Li^+/Li^0 with stable cycling properties. Neutron diffraction experiments combined with BVEL and DFT calculations revealed a two-step delithiation mechanism with the formation of the intermediate phase $Li_{1.5}Fe(SO_4)_2$, whereas monoclinic $Li_2Fe(SO_4)_2$ presents a one-step delithiation process. The orthorhombic phases present further interesting magnetic properties related to their particular arrangement of the MO_6 octahedra, which allows

solely super-super-exchange interactions with an antiferromagnetic character. Moreover, these compounds may be possible linear magnetoelectrics.

- We further delved into sulfate-based frameworks that could potentially serve as Li^+/Na^+ insertion compounds and focused on $Fe_2(SO_4)_3$ host structures. An electrochemical-wise so far unexplored $Fe_2(SO_4)_3$-based phase is the mineral langbeinite $K_2Fe_2(SO_4)_3$. We tested the feasibility of electrochemically and chemically extract K^+ with however little success. Nevertheless, during our studies of the $K_2M_2(SO_4)_3$ phases, we were able to stabilize a novel $K_2Cu_2(SO_4)_3$ compound, which crystallizes in a complex orthorhombic structure that we solved from X-ray powder diffraction. Upon electrochemical cycling, we observed a hampered K^+ diffusion, which might be related to structural instabilities upon the extraction of the rather large K^+ cation.

Overall, we showed that there is still a myriad of unexplored sulfate- and fluorosulfate-based materials with a large variety of crystal structures and interesting properties. However, for a targeted synthesis approach, a better understanding of the synthesis-structure relation is of importance. In this context, polymorphic phases present a good starting point to correlate structural differences, thermodynamics and synthesis methods. However, it turned out to be complex task to establish a universal "recipe". If we compare for example the ball-milling synthesis approach for the $Li_2Fe(SO_4)_2$ and $KFeSO_4F$ phases, ball-milling led to the stabilization of the denser phase for $Li_2Fe(SO_4)_2$, while for $KFeSO_4F$ it led to the less dense polymorph. The different outcome can be explained by different key parameters: For $Li_2Fe(SO_4)_2$ indeed the density of the structure is the critical factor, whereas for $KFeSO_4F$ the rapid local heating during ball-milling dictates the stabilized polymorph. A consistent result, however, was obtained with the ceramic route, where high temperatures systematically led to the polymorph with the larger volume. The results of our study show that the discovery of a new compound remains a lengthy endeavor. It is therefore of importance to master various synthesis methods and to understand their possible impacts on structural characteristics to get faster to the goal.

If finally a new material has been stabilized, rationalizing its electrochemical properties is equally challenging since a large variety of structural parameters have an impact on the electrochemical performances. The ionicity of the M-O bond described by the inductive effect is only one aspect, but also structural parameters such as the connectivity of the polyhedra and

the density of a material need to be taken into account. For a better understanding of these parameters and their influence on the electrochemistry, we again focused on polymorphic structures. When we compare, for example, the density, we observe better cation diffusion properties (better rate capability and capacity retention, lower polarization, higher a.c. conductivity) for the high-density orthorhombic $Li_2Fe(SO_4)_2$ phase as compared to its monoclinic counterpart. For the $KFeSO_4F$ phases, however, a lower density (orthorhombic polymorph) is accompanied by a better cyclability. Comparing further the connectivity of the MO_6 polyhedra, the higher potential of triplite $LiFeSO_4F$ compared to its tavorite counterpart is explained by the edge-sharing FeO_6 polyhedra in the former. For $KFeSO_4F$, on the other side, the partially edge-sharing FeO_6 octahedra in the monoclinic phase do not increase the Fe^{3+}/Fe^{2+} redox potential compared to orthorhombic $KFeSO_4F$ with only corner-sharing FeO_6 octahedra.

As mentioned in the beginning of this thesis, an ideal cathode material presents high voltage and capacity, stability upon cycling and high electronic/ionic conductivity. Sulfate-based materials do present high voltages, however they show some deficiencies in terms of conductivity and stability. Especially their strong hygroscopic behaviour, which in some cases leads to a complete decomposition of the material after only a few days, is a major drawback being detrimental to their commercialization. Following recent research activities, it seems that the development of new polyanionic materials for lithium ion batteries lost its initial excitation since they still cannot compete with the stellar $LiFePO_4$ in terms of long-cycling performances. However, their eco-friendly and cost-efficient preparation at low temperatures (300-500 °C) with rather short reaction times (*e.g.* only 1 hour for $KFeSO_4F$ and $LiFeSO_4F$) renders these compounds interesting for industrial scale productions. Furthermore, they have been successfully implemented in the development of sodium ion batteries, where they show rather promising performances (*e.g.* $Na_2Fe_2(SO_4)_3$).

In the end, the knowledge accumulated during the studies of polyanionic compounds in general and sulfate-based materials specifically have not only affected the battery community, but also other research fields owing to their large variety of compounds, rich crystal chemistry and physical properties (*e.g.* non-linear optics, magnetoelectric effect *etc.*). Therefore, we believe that this family of compounds is of interest to a broad audience of solid-state and materials

scientists and we hope to have encouraged them to further delve into the exploration of new sulfate-based materials with potentially interesting properties.

Annexe

1. Sample preparation

1.1. Spark Plasma Sintering (SPS)

Spark Plasma Sintering, also known as Flash Sintering, drives the reaction by applying pressure and an electric current on the sample at the same time. This increases the atom diffusion and leads to a high heating ramp and short reaction times.[262]

For the synthesis, the sample is placed between two carbon disks (Papyex®) and fixed in a carbon matrix (10 mm diameter; Mersen 2333®). The reaction is conducted with a HPD 10 FCT SPS apparatus (located in the LRCS, Amiens), which is located inside an argon-filled glovebox (Figure 0.1a). The temperature is controlled via a thermocouple introduced into the carbon matrix (Figure 0.1b). The machine was handled by Fabien Lalère and Vincent Seznec from LRCS, Amiens.

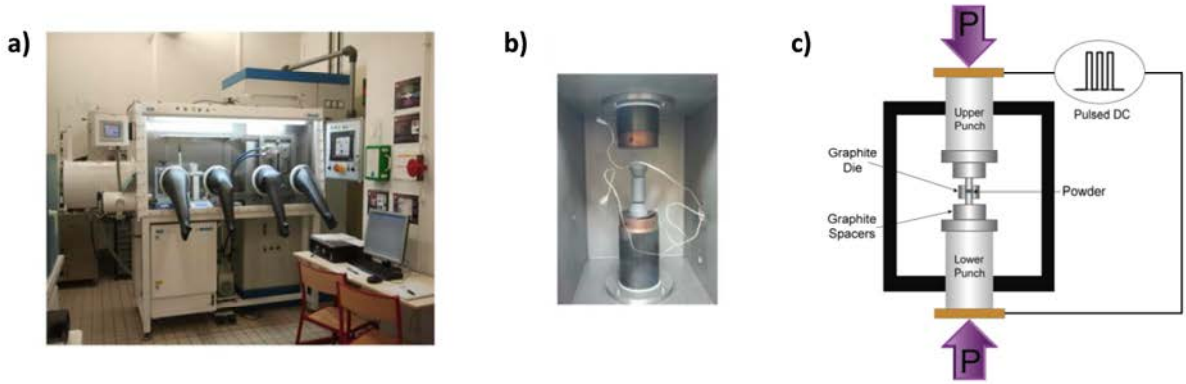

Figure 0.1: a) SPS machine inside an Ar glovebox. b) Carbon matrix between the two punches and the thermocouple. c) Schematic representation of the SPS functioning.[262]

1.2. Ball-milling

Ball-milling (or mechanical milling) is an energetic milling process, which allows the formation of an intimate mixture of compounds. We used it for mixing of our reaction precursors for instance $FeSO_4$ and LiF before the annealing step or for the preparation of the cathode material, where the active material was ball milled with Carbon Super P.

For the ball-milling procedure, we used a Spex 8000® miller (Figure 0.2a), which applies a rotation speed of up to 1400 rpm. The ball-milling container is made out of stainless steel as are also the used balls (7 g). The container presents an inner volume of either 40 cm^3 (Figure 0.2b, left) or 10 cm^3 (Figure 0.2b, right), where the latter is used especially for the preparation of the cathode material. We alternatively also used a Retsch PM100® planetary miller.

The ball-milling approach was also used as an independent synthesis method for the preparation of the orthorhombic $Li_2M(SO_4)_2$ phases. Furthermore we could show that the ball-milling conditions have a major influence on the phase purity of the final product as in the case of $K_2Cu_2(SO_4)_3$ and monoclinic $KFeSO_4F$ and demand therefore careful optimization and control.

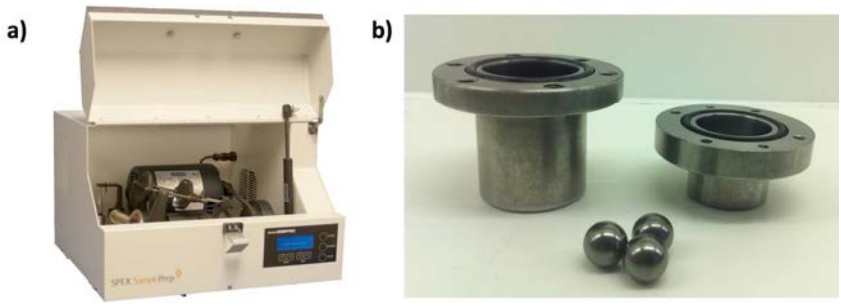

Figure 0.2: a) Spex 8000 miller with b) the used ball mill containers.

2. Structural characterization

2.1. Laboratory X-ray diffraction (XRD)

The following X-ray diffractometers were used during the course of this thesis:

a) Bruker D8 diffractometer (at LRCS, Amiens), equipped with a copper source ($\lambda_{Cu\text{-}K\alpha1}$ = 1.54056 Å, $\lambda_{Cu\text{-}K\alpha2}$ = 1.54439 Å) and a Vantec detector, operating at 40 kV and 40 mA.

b) Panalytical X'Pert Pro MPD diffractometer supplied with a cobalt source ($\lambda_{Co\text{-}K\alpha1}$ = 1.78897 Å, $\lambda_{Co\text{-}K\alpha2}$ = 1.79285 Å) and an X'Celerator detector, operating at 40 kV and 40 mA, at IMPMC, UPMC, Paris.

c) Bruker D8 Advance diffractometer (Collège de France, Paris) equipped with a copper source ($\lambda_{Cu\text{-}K\alpha1}$ = 1.54056 Å, $\lambda_{Cu\text{-}K\alpha2}$ = 1.54439 Å) and a LynxEye detector, operating at 40 kV and 40 mA

Air-sensitive samples were measured in an especially designed airtight sample holder, where the sample was measured through a kapton tape (Figure 0.3).

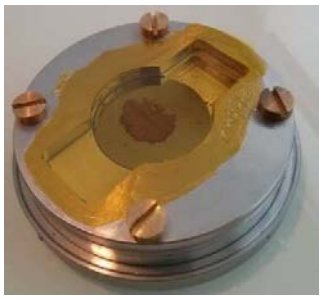

Figure 0.3: Home-made airtight XRD sample holder with a silicium plaque and a kapton tape.

High-temperature in situ XRD experiments were conducted with a Bruker D8 Advance diffractometer equipped with a copper source equipped with an Anton Paar HTK1200N furnace chamber. The sample was placed on an alumina sample holder. The experiments were performed either under air or inert gas (*e.g.* nitrogen).

2.2. Synchrotron XRD

Synchrotron XRD experiments were conducted in order to obtain high-resolution data for structure determinations for instance. The measurements were performed in transmission geometry (Debye-Sherrer) with λ ~ 0.41 Å through the 11BM mail-in service of the Advanced Photon Source (APS) at the Argonne National Laboratory (Argonne, USA). The powdered samples were sealed under argon in quartz capillaries (0.7 mm diameter) and introduced in the kapton tube provided by the APS team (Figure 0.4).

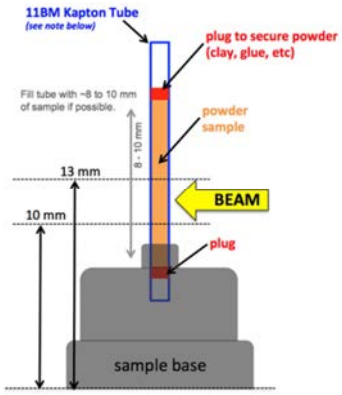

Figure 0.4: Schematic representation of the 11-BM sample holder.[263]

2.3. Neutron diffraction

High intensity neutron powder diffraction (NPD) was applied either for nuclear structure or magnetic structure determinations. For the former, NPD is interesting since it allows the determination of the lithium positions in the structure, which is less accessible from X-ray diffraction. NPD experiments were performed on the D20 diffractometer at the Institute Laue Langevin (ILL, Grenoble, France). The sample was placed in a vanadium cylindrical can, which is transparent to the neutrons, and measured in a high-resolution mode (Take-off angle of 90°) with a wavelength of λ = 1.544 Å for the nuclear structure or with a wavelength of λ = 2.416 Å for the magnetic structure determinations. For the latter, the sample was cooled down below the Néel temperature via an orange cryostat. We thank Thomas Hansen for his assistance during the measurements. Neutron diffraction experiments for $KFeSO_4F$ were performed with a HRPT high resolution powder diffractometer at SINQ-PSI (Villingen, Switzerland) with λ = 1.495 Å in a high intensity mode at 300 K.

2.4. Structure determination

The crystal structures of unknown phases were determined in several steps. First, the Bragg peaks were indexed using the Dicvol[254,255] program provided by the FullProf suite software[203,214]. The proposed space groups and lattice parameters were then tested against the recorded XRD pattern using the Le Bail[264] method (profile matching). The structure was then determined using direct methods (EXPO program[265,266]) and *ab initio* or global optimization methods (FOX program[256,257]). The structures were then refined with the Rietveld[267] method as implemented in the FullProf program.

2.5. Bond Valence Energy Landscape calculations

The Bond Valence Energy Landscape (BVEL) method allows the calculation and visualization of ion diffusion pathways of a mobile species in a 3D framework and is often applied for identifying potentially interesting ionic conductors. The BVEL method, developed by S. Adams and co-workers[215], is based on the Bond Valence Sum (BVS) approach, which calculates the oxidation state of an atom as a function of the distances to its neighboring atoms and their oxidation state, and is an extension of the Bond Valence Sum Maps (BVSM).

To determine the possible ion transport pathways in a structure, the theoretical oxidation state of the mobile ion is calculated as a function of a position in the structure, where positions with a low valence mismatch (low deviation from the ideal oxidation state) are regarded as part of the diffusion pathway. In contrast to the BVS approach, the BVEL calculations transform the valence units (v.u.) given for the BVS into energy units (e.u.). Furthermore, soft bond valence (softBV) parameters are used, which allow to take into account the polarizability of the mobile species as well as the influence of the counterions on the ion mobility. Further included in the BVEL calculations is the cut-off length to the surrounding coordination spheres, which in our case is set to 8 Å.

BVEL calculations are performed with the BondStr software as implemented in the FullProf suite[203], which uses the .cif file as input file. The program calculates the iso-energy surfaces in the structure, which are accessible for the mobile ion and which must be infinitely connected in at least one direction to permit diffusion through the structure. The difference between the minimum energy to get an infinitely connected path in at least one direction and the absolute minimum energy, gives the "activation energy" necessary for the ion diffusion in this structure. The isosurface can be visualized with the VESTA program. Detailed information and theory background can be found in Ref [13-15]. [215,268,269]

3. Electrochemical characterization

3.1. Electrochemical cells

Firstly, the cathode was prepared via ball-milling the active material with carbon Super P (ratio 80:20 wt% except otherwise specified) for 15-20 min under argon atmosphere using a Spex 8000 miller. The as-prepared cathode material was then loaded in Swagelok®-type half-cells for the electrochemical testing against a lithium metal anode (Figure 0.5a). The negative and the positive electrodes were separated by a Whatman® GF/D borosilicate glass fiber sheet saturated with 1 M $LiPF_6$ in EC:DMC (1:1 weight ratio) (LP30) or with 1M $LiClO_4$ in PC. Usual cathode loading was 8-12 $mg{\cdot}cm^{-2}$ per cell. All cells were assembled under argon atmosphere.

For *in situ* measurements, where XRD patterns are recorded during electrochemical cycling, a home-made cell (from LRCS, Amiens) adapted to the Bruker D8 diffractometer was used (Figure

0.5b). The set-up resembles the one of a normal Swagelok®-type cell except that on the cathode side, the current collector is a conducting beryllium window, which can be traversed by X-rays. To avoid oxidation of the beryllium window at high voltages, a thin aluminum foil was placed between the cathode material and the window.

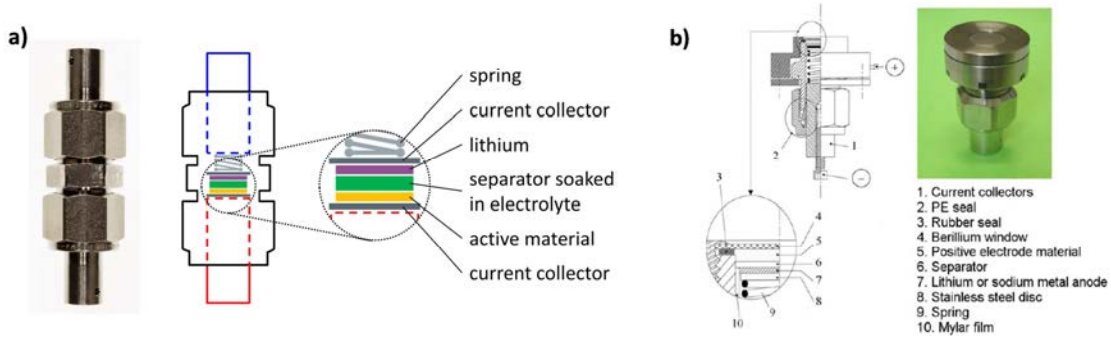

Figure 0.5: Schematic representation of a) a Swagelok®-type half-cell (with courtesy of F. Lepoivre) and of b) the home-made *in situ* electrochemical cell.

3.2. Electrochemical cycling

Galvanostatic cycling: First electrochemical tests were performed in a galvanostatic mode, where a constant current density was applied and the evolution of the cell voltage was recorded. The cells were usually cycled at rates of C/20 or C/50, i.e. 1 Li^+ is exchanged in 20 or 50 hours, respectively. The obtained voltage-composition traces V = f(x) are presented throughout the thesis. An S-shaped curve usually corresponds to a single-phased solid-solution process, while a flat plateau likely indicates a two-phase mechanism.

Galvanostatic Intermittent Titration technique (GITT): This cycling mode combines a galvanostatic cycling with longer periods of open circuit voltage phases (zero applied current) to allow the system to relax to its thermodynamic equilibrium and to determine its redox potential at equilibrium.

Potentiostatic Intermittent Titration technique (PITT): In contrast to the galvanostatic experiments, in the PITT mode, the voltage is slowly increased and the evolution of the current is recorded. This technique gives insights into the redox mechanism of the cathode material and allows in the case of single-phased mechanism the calculation of the diffusion coefficient D.

All electrochemical tests were performed with a VMP3 potientiostat/galvanostat (Biologic S.A., Claix, France) at room temperature.

4. Magnetic properties

4.1. Magnetic measurements

The magnetic spins can lead to paramagnetic, ferromagnetic or antiferromagnetic behaviours (Figure 0.6a). To determine these interactions, magnetic measurements are performed where the magnetization is recorded as a function of the applied magnetic field (Figure 0.6b) as well as the magnetic susceptibility as function of the temperature (Figure 0.6c). The obtained curves indicate the nature of the spin interaction and the ordering temperature (critical temperature T_c for a ferromagnetic compounds; Néel temperature T_N for an antiferromagnetic compound). In the latter case, the high-temperature part of the susceptibility can be fitted with the Curie-Weiss law:

$$\chi_{CW} = \frac{C}{T - \theta}$$

where χ is the susceptibility, C the Curie constant and θ the Curie-Weiss temperature. The latter is correlated to the nature (antiferromagnetic (θ<0) or ferromagnetic (θ>0)) and strength of the interaction. Deviations from the ideal Curie-Weiss law can be related to impurities in the sample for instance.

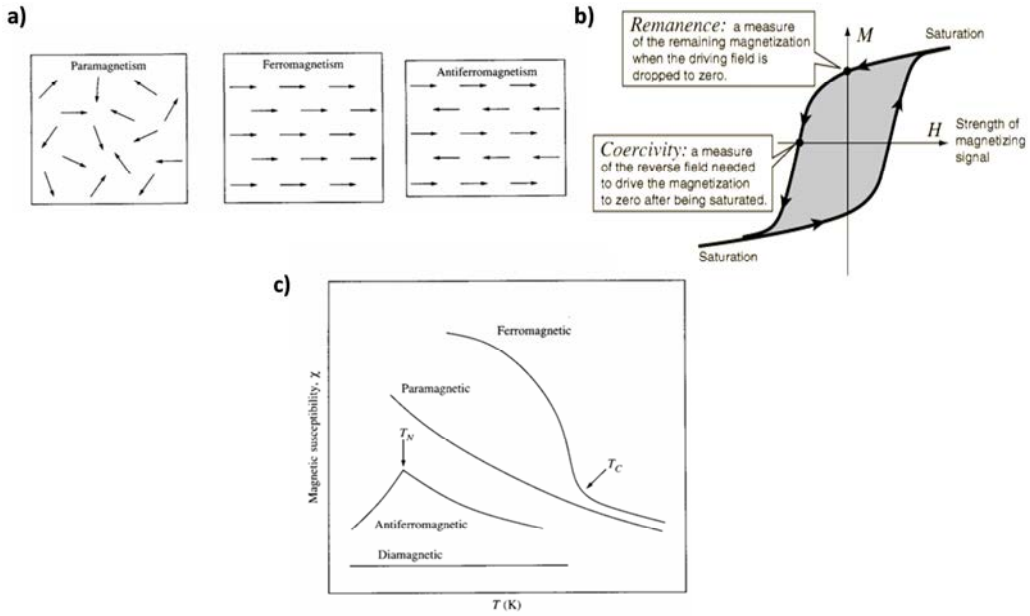

Figure 0.6: a) Paramagnetic, ferromagnetic and antiferromagnetic spin interactions. b) Field dependent magnetization curve of a ferromagnetic material. c) Temperature dependent magnetic susceptibility curves.[270,271]

To measure the susceptibility and magnetization curves, powder samples of roughly 20-30 mg were placed into gel caps for the measurements in such a way as to avoid any motion of the sample during the measurements. Susceptibility measurements were carried out using a SQUID (Superconductivity Quantum Interference Device) XL magnetometer (Quantum design), in zero field cooled (ZFC) and field cooled (FC) modes, under applied magnetic fields of 1 kOe and 10 kOe between 2 K and 400 K. Isothermal magnetization curves M = f(H) were recorded at 2 K in function of a changing field.

4.2. Magnetic structure determination

For the magnetic structure determination, neutron diffraction experiments are conducted between temperatures from 2 K to above the Néel temperature, as described in section 2.3. Contrary to a ferromagnetic ordering, where the Bragg peaks of the magnetic structure superimpose with the Bragg peaks of the nuclear structure, an antiferromagnetic ordering results in the appearance of new Bragg peaks. To solve the magnetic structure, the propagation vector is determined and Bertaut's symmetry analysis[272] via the BasIreps program of the FullProf software is applied, which gives the basis vectors of the irreproducible representations allowed by the symmetry of the structure. In a final step, each irreproducible representation of the magnetic structure is tested against the neutron diffraction pattern.

5. Additional characterization techniques

5.1. Electron microscopy and Energy-dispersive X-ray spectroscopy (EDX)

Scanning electron microscopy (SEM) images were recorded on a Hitachi S-3400N electron microscope. Elemental analyses (EDX) were performed on the same microscope to obtain the sulfur to transition metal ratio.

Transmission electron microscopy (TEM) experiments were performed on a Tecnai G2 electron microscope operated at 200 kV by Dr. Artem Abakumov (EMAT, Antwerp, Belgium). To do so, the sample was prepared in an Ar-filled glove box by crushing the grainy powder in a mortar in anhydrous hexane and depositing drops of suspension onto holey carbon grids. The sample was transported to the microscope column completely excluding contact with air.

5.2. Mössbauer spectroscopy

^{57}Fe Mössbauer spectroscopy records the intensity of gamma rays transmitted through a solid compound, which implies a transition between the ground state and an excited state of a nucleus. The peaks shown in the spectrum are the result of absorbed gamma rays that are resonant with the nuclear transition energies in the sample. The recorded spectrum of a ^{57}Fe nucleus for instance displays usually a doublet, where the characteristics of the peaks contain important information about the oxidation state of the Fe-atom and its environment (Figure 0.7). The quadrupole splitting ΔEq refers to difference between the maxima of two peaks and depends on the interaction of the nucleus with its environment, which leads to a splitting of the excited state energy level. The isomer shift value δ is related to the electron density of the s-orbitals and is deduced from the gravimetric center of the spectra with respect to the zero-value of the velocity.

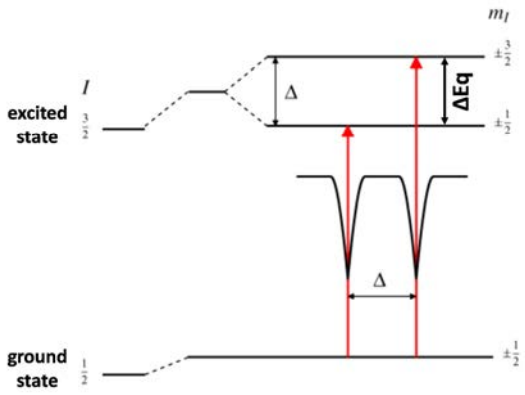

Figure 0.7: Scheme of a Mössbauer spectrum indicating the quadrupole splitting ΔEq.[273]

^{57}Fe Mössbauer spectra were recorded in transmission geometry in constant acceleration mode and with a ^{57}Co(Rh) source with nominal activity of 925 MBq. The velocity scale (± 4 mm/s) was calibrated at room temperature with a α-Fe foil. The absorbers were typically prepared from 20 to 50 mg of powder sample, which was in some cases mixed with boron nitride binder. The hyperfine parameters IS (isomer shift, giving with respect to that of α-Fe) and QS (quadrupole splitting) were fitted lorentzian lines. We are very thankful to Moulay-Tahar Sougrati (Institut Charles Gerhardt, Montpellier, France), who performed the Mössbauer experiments.

5.3. ^{7}Li solid-state nuclear magnetic resonance (NMR)

Solid-state NMR spectra were acquired on a Bruker AVANCE II 300 NMR spectrometer with a 7.05 T wide-bore superconducting magnet operating at 116.6 MHz for ^{7}Li nuclei, which are 92.4% naturally abundant. A Bruker ^{1}H/X double-resonance magic-angle-spinning (MAS) probe head was used with 1.3-mm diameter zirconia rotors, where samples were rotated at 62.5 kHz MAS with pure N_2 gas under ambient conditions. All experiments were conducted with a ^{7}Li radio frequency field strength of 140 kHz (90° pulse of 1.8 µs). 1D ^{7}Li spin-echo MAS spectra were acquired with half-echo delays (τ/2) of one rotor period (16 µs), using a recycle delay of 100 s (calibrated such that all paramagnetic and diamagnetic ^{7}Li species have fully relaxed). Quantitative deconvolutions of the NMR spectra were performed using a custom Maple® program to fit multiple spectra simultaneously subject to global constraints, where initial guesses were fits obtained with the Dmfit[274] program. ^{7}Li shifts were referenced to a 1 M aqueous solution of LiCl. The experiments were conducted by Dr. R. Messinger (CEMHTI, Orléans, France). His contribution to the study of $Li_2M(SO_4)_2$ is much appreciated.

5.4. Thermal analyses

Thermogravimetric Analyses (TGA), which detect mass variations upon heating, were carried out with a STA-449C Jupiter unit (Netzsch) coupled to a quadrupole mass spectrometer QMS 403 Aëlos equipped with a stainless-steel capillary and a secondary-electron multiplier detector (Channeltron). Experiments were performed on around 20 mg of the powder samples placed in alumina crucibles, in the temperature range of 20-800°C (heating rate: 2-10°C/min) under argon flow (50 cm^3/min). Differential Scanning Calorimetry (DSC) measurements indicating phase transformations and chemical reactions were done under the same conditions using a 204F1 Netzsch unit, with the samples sealed in aluminum crucibles. The measurements were performed by M. Courty (LRCS, Amiens).

5.5. Impedance spectroscopy

For temperature-dependent a.c. conductivity measurements, the samples were pressed at 7 tons into pellets of about 10-13 mm diameter and 1-2 mm thickness by means of using a uniaxial press, and were then sintered at 200-300 °C for one night. $KFeSO_4F$ and $K_2Cu_2(SO_4)_3$ were then sputtered with gold. The pellets were mounted in a sample holder where an applied

with low pressure (spring system) ensured good contact. Impedance spectroscopy was performed using a Solartron Analytical Modulab unit (gold wires) for the $Li_2M(SO_4)_2$ phases and a BioLogic MTZ-35 setup with platinum electrodes (ionically blocking electrodes) equipped with an HTF-1100 furnace for $KFeSO_4F$ and $K_2Cu_2(SO_4)_3$. At each temperature step, impedance spectra were recorded from 30 MHz to 0.01 Hz applying a voltage amplitude from 10 to 200 mV and the current response was followed. The measurements were performed in close collaboration with Prof. Christel Laberty and Dr. Daniel Alves Dalla Corte.

Electrochemical impedance spectroscopy (EIS) is a widely used method, able to determine a variety of different phenomena ranging from electrochemical reactions, ionic diffusion etc. However, within the context of this thesis this technique is exclusively used for the determination of transport properties of solids (ionic/ electronic). In general a sinusoidal voltage is applied over a wide frequency range, and the current response is followed. The measured impedance usually contains resistive (R) and capacitive (C)/ inductive components and the data is drawn in the form of imaginary Z" (capacitive) versus real Z' (resistive) impedance, the so called Nyquist plot. Each parallel R/C element results in a perfect semicircle from which both values (R and C) can be extracted (Figure 0.8), where R values are obtained from the intercept of the semicircle with the Z'-axis.[275]

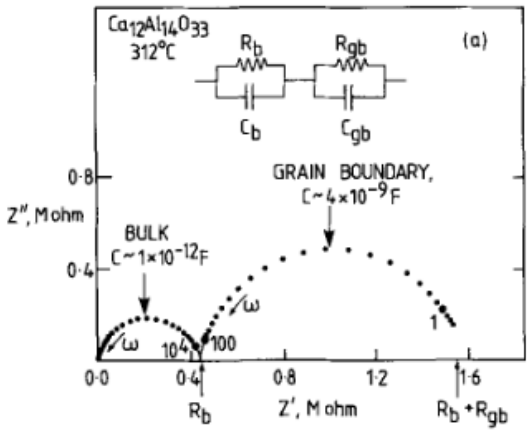

Figure 0.8: Representative Nyquist plot for $Ca_{12}Al_{14}O_{33}$ measured at 312°C. The equivalent circuit to interpret the data is shown as inset.[275]

The semi-circles derived from the complex AC impedance spectra were fitted with a corresponding equivalent circuit, where R_0 represents an initial shift of impedance arc from zero, R_1 is the bulk- and R_2 grain boundary resistance (Figure 0.8). The conductivity σ was

calculated from the resistance R, the pellet's thickness l, and area A according to the following equation:

$$\sigma = \frac{l}{A \cdot R}$$

The activation energy E_a (eV) for Li^+ migration and electron conduction was calculated from fitting the experimentally derived values using the Arrhenius equation,

$$\sigma T = \sigma_0 \cdot e^{-\left(\frac{E_a}{k_B T}\right)}$$

where σT (S·cm^{-1}·K) is the temperature dependent conductivity, σ_0 (S·cm^{-1}) is a pre-exponential factor, and k_B is the Boltzmann constant. Note that the conductivity values are not corrected by the pellet porosities, thus the values are underestimated.

5.6. Raman measurements

The Raman experiments were carried out at 300 K in the back scattering configuration using a Jobin-Yvon HR-460 spectrometer equipped with a monochromator with 1500 grooves/mm and an Andor CCD camera. Raman signal was excited using the 514.5 nm wavelength of an Ar laser, focused into a 2 µm spot by a long-working distance Mitutoyo x20 objective and collected in backscattering geometry. The power of the laser was always kept below 2 mW in order to avoid any photo-induced transformation of the $Li_2M(SO_4)_2$ samples. The experiments were performed in close collaboration with Christophe Bellin and Alain Polian (UPMC, IMPMC, Paris) and we are very thankful for their efforts and fruitful discussions.

5.7. High-pressure experiments

Tiny amounts of $Li_2M(SO_4)_2$ were loaded in a membrane diamond anvil cell (DAC)[276] with a 400 µm culet diameter (Figure 0.9). We used a stainless steel gasket pre-indented to 45 µm, with a 200 µm hole and neon as a pressure transmitting medium.[277] Neon is the best suited pressure transmitting medium in our case since it ensures quasi hydrostatic conditions on the sample in the whole explored pressure range, it is chemically inert and has no Raman activity. The *R*1-line emission of a tiny ruby sphere was used as a pressure gauge.[278,279] The initial loading pressure accounts for 0.15 GPa and the pressure was gradually increased up to 12.3 GPa. These experiments were performed by Christophe Bellin and Alain Polian (UPMC).

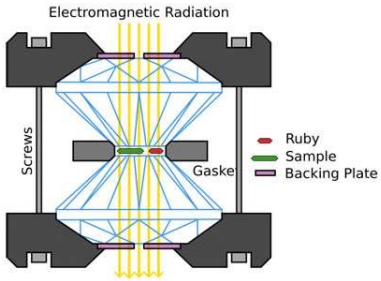

Figure 0.9: Schematic representation of a diamond anvil cell (DAC).

6. Tanabe-Sugano diagrams

Tanabe-Sugano diagrams[216] are often used to analyze UV/Vis spectra and to assign the measured absorption peaks to d-d transitions. In the $Li_2M(SO_4)_2$ series, Mn^{2+} corresponds to a d^5, Fe^{2+} to a d^6, Co^{2+} to a d^7, Ni^{2+} to a d^8 and Zn^{2+} to a d^{10} system. The Tanabe-Sugano diagrams for the respective M^{2+} d-electron configurations are shown in Figure 0.10. The d^9 system does not need a Tanabe-Sugano diagram since the only transition is $^2T_{2g}$ to ^2E_g. The vertical line separates the high-spin states (left side of vertical line) from the low-spin states (right side of vertical line) depending on the strength of the ligand field splitting. In our case, we assume a weak ligand field splitting and a high-spin state of the d-electrons. The high-spin state was further demonstrated by magnetic susceptibility measurements.

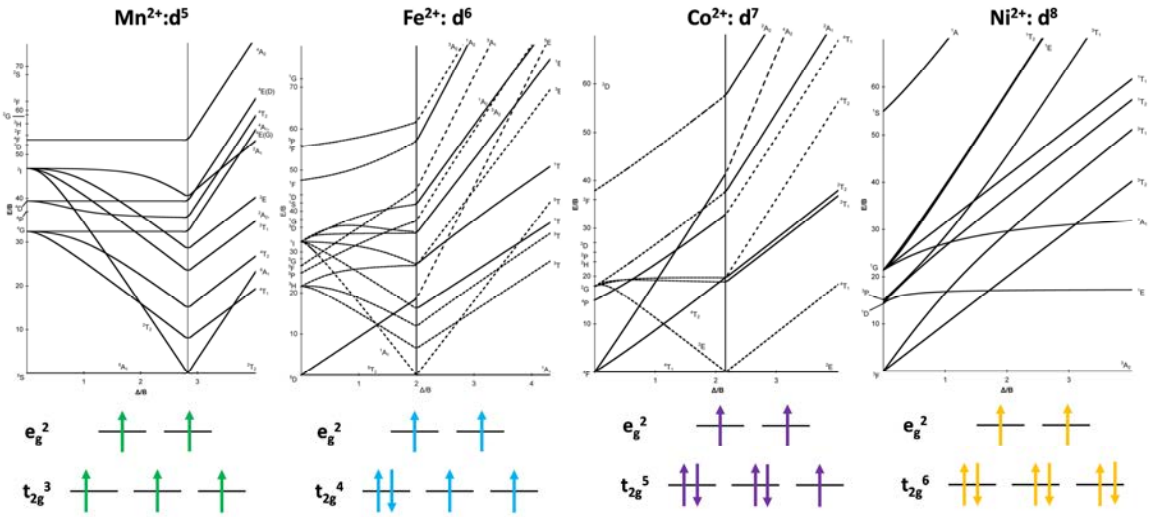

Figure 0.10: Tanabe-Sugano diagrams for d^5, d^6, d^7 and d^8 systems. In the $Li_2M(SO_4)_2$ series we assume a high-spin electron configuration.

7. Density Functional Theory calculations for $Li_2M(SO_4)_2$

Density Functional Theory (DFT) calculations were performed by J. Carrasco and N.A. Katcho from Energigune, Spain. Spin-polarized DFT calculations were performed using a supercell approach and the semi-local Perdew-Burke-Ernzerhof (PBE)[280] functional as implemented in the Vienna *ab initio* Simulation Package (VASP, version 5.3.3)[281,282]. We replaced the inner electrons by PBE-based projector augmented wave potentials[283], whereas Li (2*s*), Fe (3*p*, 3*d*, 4*s*), S (3*s*, 3*p*) and O (2*s*, 2*p*) valence electrons were expanded in plane-waves with a cut-off energy of 700 eV. We employed the DFT+U scheme of Dudarev *et al.*[284], in which the Hubbard U-like term (the difference between the Coulomb U and exchange J parameters, hereinafter referred to as simply U) was added to the exchange-correlation functional. This pragmatic approach is necessary to describe the localized Fe 3*d* states in $Li_xFe(SO_4)_2$ phases. Here, the chosen value of U is 4.0 eV, which is consistent with the value derived for a range of Fe-based cathode materials[285] and with the one used by Clark *et al*. to calculate open cell voltages for monoclinic $Li_2Fe(SO_4)_2$[286].

We used unit cells containing 8 formula units ($Li_xFe_8S_{16}O_{64}$). Equilibrium lattice parameters of bulk $Li_xFe(SO_4)_2$ were computed allowing the atomic positions, lattice constants and cell shape to relax with a residual force threshold of 0.02 eV/Å. We confirmed that the cut-off of 700 eV was sufficiently large to avoid the problems of Pulay stress and changes in basis set that accompany volume changes in plane wave calculations. We considered a 4×4×2 Monkhorst-Pack k-point mesh. These computational settings guarantee a tight convergence in total energies (better than 5 meV per formula unit) and equilibrium distances (better than 0.01 Å). We found that an antiferromagnetic ordering of the moments on all Fe atoms in $Li_2Fe(SO_4)_2$ is only 4 meV per formula unit lower in energy than a ferromagnetic ordering (high-spin states). We considered an antiferromagnetic structure similar to that proposed for orthorhombic $Li_2Ni(SO_4)_2$, where magnetic moments alternate orientations spin up and spin down along the *c*-axis, whereas the same spin orientation is maintained along *a*- and *b*-axis.[287] However, given the small energy difference between the two magnetic orderings, we restricted our calculations on all $Li_xFe(SO_4)_2$ phases to ferromagnetic ordering for the sake of simplicity.

We generated all the possible Li-vacancy arrangements within $Li_1Fe(SO_4)_2$ and $Li_{1.5}Fe(SO_4)_2$ cells using the cluster assisted statistical mechanics (CASM) code[288], which takes into account the

symmetry of the lattice. We took the structure with the lowest energy as the ground-state structure. However, given the large number of possible Li-vacancy configurations, we applied a screening procedure by first computing the electrostatic energy using formal charges and the Ewald summation[289]. The 50 lowest electrostatic energy structures were then optimized using DFT.

8. Calorimetric studies

The calorimetric studies on monoclinic and orthorhombic $Li_2M(SO_4)_2$ and monoclinic and orthorhombic $KMSO_4F$ were conducted by Prof. A. Navrotsky's group at the Peter A. Rock Thermochemistry Laboratory at U.C. Davis.

***Acid solution calorimetry*:** Both CSC 4400 isothermal (with IMC data acquisition software) and Hart Scientific (with Labview software) microcalorimeters with mechanical stirring were used to measure the enthalpies of dissolution of the $Li_2M(SO_4)_2$ and $KMSO_4F$ samples at 25 °C. Calorimeters were calibrated with KCl (NIST standard reference material) by dissolving 15 mg pellets in 25 g of water at 25 °C. The solution enthalpy of this reference concentration (0.008 mol/kg) deduced from the literature and enthalpy of dilution measurements were used to arrive at the calorimeter calibration factor. In a typical calorimetric run, 4-7 mg of sample was pressed into a pellet inside a nitrogen glove box and then dropped into 25 g of 5M HCl placed in the sample chamber of the calorimeter with minimum exposure to air ($\leq$ 1 min). The sample dissolution causes the heat flow due to temperature difference and is recorded as a calorimetric signal. The integrated area under the recorded microwatt signal from a linear baseline corresponds to total heat effects, which on conversion into joules with KCl calibration corresponds to the enthalpy of sample dissolution (ΔH_{solun}). An appropriate thermochemical cycle based on Hess' law was used to calculate the enthalpy of formation.

High temperature oxide melt calorimetry: This method was performed on the $KFeSO_4F$ polymorphs using a custom built isoperibol Tian-Calvet microcalorimeter.[25-27] The calorimeter was calibrated using the heat content of high purity α-Al_2O_3. Molten sodium molybdate was used as a solvent at 700 °C and air was flushed through the glassware at 60 mL/min to maintain constant atmosphere and bubbled through the solvent at 30 mL/min using a bubbling tube to aid dissolution, and prevent local saturation of the solvent. In a typical experiment ~5 mg of

loosely pelletized sample was dropped into the solvent. The resulting heat effect (heat of drop solution, ΔH_{ds}) includes the heat content of the sample, and the heat of dissolution of the sample in the sodium molybdate melt. The total heat effect associated with dropping the sample from room temperature to 700 °C was obtained by integrating the calorimetry signal, which was then converted to joules using the α-Al_2O_3 calibration factor.

References

1. U.S. Energy Information Administration (EIA) - Pub. Available at: https://www.eia.gov/forecasts/aeo/section_energyconsump.cfm.

2. Riebeek, H. Global Warming : Feature Articles. (2010). Available at: http://earthobservatory.nasa.gov/Features/GlobalWarming/page5.php.

3. Whittingham, M. S. Lithium Batteries and Cathode Materials. *Chem. Rev.* **104,** 4271–4302 (2004).

4. Tarascon, J.-M. & Armand, M. Issues and challenges facing rechargeable lithium batteries. *Nature* **414,** 359–367 (2001).

5. Dunn, B., Kamath, H. & Tarascon, J.-M. Electrical Energy Storage for the Grid: A Battery of Choices. *Science* **334,** 928–935 (2011).

6. Landi, B. J., Ganter, M. J., Cress, C. D., DiLeo, R. A. & Raffaelle, R. P. Carbon nanotubes for lithium ion batteries. *Energy Environ. Sci.* **2,** 638 (2009).

7. Goodenough, J. B. Evolution of Strategies for Modern Rechargeable Batteries. *Acc. Chem. Res.* **46,** 1053–1061 (2013).

8. Roy, P. & Srivastava, S. K. Nanostructured anode materials for lithium ion batteries. *J Mater Chem A* **3,** 2454–2484 (2015).

9. Volta, A. On the Electricity Excited by the Mere Contact of Conducting Substances of Different Kinds. *Philos. Trans. R. Soc. Lond.* **90,** 403–431 (1800).

10. Planté, G. Nouvelle pile secondaire d'une grande puissance. *Comptes Rendus Hebd. Séances Académie Sci.* **50,** 640–642 (1860).

11. Whittingham, M. S. Electrical Energy Storage and Intercalation Chemistry. *Science* **192,** 1126–1127 (1976).

12. Rao, B. M. L., Francis, R. W. & Christopher, H. A. Lithium-aluminum electrode. *J. Electrochem. Soc.* **124,** 1490–1492 (1977).

13. Wang, J., Raistrick, I. D. & Huggins, R. A. Behavior of Some Binary Lithium Alloys as Negative Electrodes in Organic Solvent-Based Electrolytes. *J. Electrochem. Soc.* **133,** 457–460 (1986).

14. Dey, A. N. Electrochemical Alloying of Lithium in Organic Electrolytes. *J. Electrochem. Soc.* **118,** 1547–1549 (1971).

15. Armand, M. & Touzain, P. Proceedings of the Franco American Conference on Intercalation Compounds of Graphite Graphite intercalation compounds as cathode materials. *Mater. Sci. Eng.* **31,** 319–329 (1977).

16. Hunger, H. F. & Heymach, G. J. Cathodic Discharge of Graphite Intercalation Compounds in Organic Electrolytes. *J. Electrochem. Soc.* **120,** 1161–1168 (1973).

17. Chung, D. D. L. Review Graphite. *J. Mater. Sci.* **37,** 1475–1489 (2002).

18. Ozawa, K. Lithium-ion rechargeable batteries with $LiCoO_2$ and carbon electrodes: the $LiCoO_2$/C system. *Solid State Ion.* **69,** 212–221 (1994).

19. Nishi, Y. The development of lithium ion secondary batteries. *Chem. Rec.* **1,** 406–413 (2001).

20. Armand, M. The history of polymer electrolytes. *Solid State Ion.* **69,** 309–319 (1994).

21. Osaka, T. & Momma, T. Lithium metal/polymer battery. *J. Power Sources* **97–98,** 765–767 (2001).

22. Kelly, I. E., Owen, J. R. & Steele, B. C. H. Poly (ethylene oxide) electrolytes for operation at near room temperature. *J. Power Sources* **14,** 13–21 (1985).

23. Tarascon, J.-M., Gozdz, A. S., Schmutz, C., Shokoohi, F. & Warren, P. C. Performance of Bellcore's plastic rechargeable Li-ion batteries. *Solid State Ion.* **86,** 49–54 (1996).

24. Mizushima, K., Jones, P. C., Wiseman, P. J. & Goodenough, J. B. Li_xCoO_2 (0< x<-1): A new cathode material for batteries of high energy density. *Mater. Res. Bull.* **15,** 783–789 (1980).

25. Mizushima, K., Jones, P. C., Wiseman, P. J. & Goodenough, J. B. Li_xCoO_2 (0< x<-1): A new cathode material for batteries of high energy density. *Solid State Ion.* **3/4,** 171–174 (1981).

26. Orman, H. J. & Wiseman, P. J. Cobalt(III) Lithium Dioxide, $CoLiO_2$: Structure Refinement by Powder Neutron Diffraction. *Acta Crystallogr.* **C40,** 12–14 (1984).

27. Johnston, W. D., Heikes, R. R. & Sestrich, D. The preparation, crystallography, and magnetic properties of the $Li_xCo_{1-x}O$ system. *J. Phys. Chem. Solids* **7,** 1–13 (1958).

28. Choi, J. W. & Aurbach, D. Promise and reality of post-lithium-ion batteries with high energy densities. *Nat. Rev. Mater.* **1,** 16013 (2016).

29. Reimers, J. N. Electrochemical and In Situ X-Ray Diffraction Studies of Lithium Intercalation in Li_xCoO_2. *J. Electrochem. Soc.* **139,** 2091 (1992).

30. Amatucci, G. G., Tarascon, J. M. & Klein, L. C. CoO_2, the end member of the Li_x CoO_2 solid solution. *J. Electrochem. Soc.* **143,** 1114–1123 (1996).

31. Thomas, M. G. S. R., Bruce, P. G. & Goodenough, J. B. Lithium mobility in the layered oxide $Li_{1-x}CoO_2$. *Solid State Ion.* **17,** 13–19 (1985).

32. Rozier, P. & Tarascon, J. M. Review—Li-Rich Layered Oxide Cathodes for Next-Generation Li-Ion Batteries: Chances and Challenges. *J. Electrochem. Soc.* **162,** A2490–A2499 (2015).

33. Nohma, T. *et al.* Electrochemical characteristics of $LiNiO_2$ and $LiCoO_2$ as a positive material for lithium secondary batteries. *J. Power Sources* **54,** 522–524 (1995).

34. Arai, H., Okada, S., Sakurai, Y. & Yamaki, J. Reversibility of $LiNiO_2$ cathode. *Solid State Ion.* **95,** 275–282 (1997).

35. Dahn, J. R., Von Sacken, U., Juzkow, M. W. & Al-Janaby, H. Rechargeable $LiNiO_2$/carbon cells. *J. Electrochem. Soc.* **138,** 2207–2211 (1991).

36. Ohzuku, T., Ueda, A. & Nagayama, M. Electrochemistry and structural chemistry of $LiNiO_2$ (R3m) for 4 volt secondary lithium cells. *J. Electrochem. Soc.* **140,** 1862–1870 (1993).

37. Ohzuku, Tsutomu, Ueda, A., Nagayama, M., Iwakoshi, Y. & Komori, H. Comparative study of $LiCoO_2$, $LiNi_{1/2}Co_{1/2}O_2$ and $LiNiO_2$ for 4 volt secondary lithium cells. *Electrochimica Acta* **38,** 1159–1167 (1993).

38. Rougier, A., Gravereau, P. & Delmas, C. Optimization of the Composition of the $Li_{1-z}Ni_{1+z}O_2$ Electrode Materials: Structural, Magnetic, and Electrochemical Studies. *J. Electrochem. Soc.* **143,** 1168–1175 (1996).

39. Koetschau, I., Richard, M. N., Dahn, J. R., Soupart, J. B. & Rousche, J. C. Orthorhombic $LiMnO_2$ as a High Capacity Cathode for Li-Ion Cells. *J. Electrochem. Soc.* **142,** 2906–2910 (1995).

40. Johnson, C. S., Li, N., Lefief, C., Vaughey, J. T. & Thackeray, M. M. Synthesis, Characterization and Electrochemistry of Lithium Battery Electrodes: $xLi_2MnO_3 \cdot (1-x)LiMn_{0.333}Ni_{0.333}Co_{0.333}O_2$ ($0 \leq x \leq 0.7$). *Chem. Mater.* **20,** 6095–6106 (2008).

41. Capitaine, F., Gravereau, P. & Delmas, C. A new variety of $LiMnO_2$ with a layered structure. *Solid State Ion.* **89,** 197–202 (1996).

42. Amriou, T., Khelifa, B., Aourag, H., Aouadi, S. M. & Mathieu, C. Ab initio investigation of the Jahn–Teller distortion effect on the stabilizing lithium intercalated compounds. *Mater. Chem. Phys.* **92,** 499–504 (2005).

43. Davidson, I. J., McMillan, R. S., Murray, J. J. & Greedan, J. E. Lithium-ion cell based on orthorhombic $LiMnO_2$. *J. Power Sources* **54,** 232–235 (1995).

44. Reimers, J. N. Synthesis and Electrochemical Studies of $LiMnO_2$ Prepared at Low Temperatures. *J. Electrochem. Soc.* **140,** 3396 (1993).

45. Liu, Z., Yu, A. & Lee, J. Y. Synthesis and characterization of $LiNi_{1-x-y}Co_xMn_yO_2$ as the cathode materials of secondary lithium batteries. *J. Power Sources* **81–82,** 416–419 (1999).

46. Yoshio, M., Noguchi, H., Itoh, J., Okada, M. & Mouri, T. Preparation and properties of $LiCo_yMn_xNi_{1-x-y}O_2$ as a cathode for lithium ion batteries. *J. Power Sources* **90,** 176–181 (2000).

47. Bruce, P. G., Robert Armstrong, A. & Gitzendanner, R. New intercalation compounds for lithium batteries: layered $LiMnO_2$. *J. Mater. Chem.* **9,** 193–198 (1999).

48. Schougaard, S. B., Bréger, J., Jiang, M., Grey, C. P. & Goodenough, J. B. $LiNi_{0.5+\delta}Mn_{0.5-\delta}O_2$—A High-Rate, High-Capacity Cathode for Lithium Rechargeable Batteries. *Adv. Mater.* **18,** 905–909 (2006).

49. Ohzuku, T., Ueda, A. & Kouguchi, M. Synthesis and Characterization of $LiAl_{1/4}Ni_{3/4}O_2$ (R3m) for Lithium-Ion (Shuttlecock) Batteries. *J. Electrochem. Soc.* **142,** 4033–4039 (1995).

50. Lu, Z., MacNeil, D. D. & Dahn, J. R. Layered Cathode Materials $Li[Ni_xLi_{2(1/3-2x/3)}Mn_{(2/3-x/3)}O_2$ for Lithium-Ion Batteries. *Electrochem. Solid-State Lett.* **4,** A191 (2001).

51. Gao, Y., Yakovleva, M. V. & Ebner, W. B. Novel $LiNi_{1-x}Ti_{x/2}Mg_{x/2}O_2$ Compounds as Cathode Materials for Safer Lithium-Ion Batteries. *Electrochem. Solid-State Lett.* **1,** 117–119 (1998).

52. Pouillerie, C. *et al.* Effect of magnesium substitution on the cycling behavior of lithium nickel cobalt oxide. *J. Power Sources* **96,** 293–302 (2001).

53. Yabuuchi, N. & Ohzuku, T. Novel lithium insertion material of $LiCo_{1/3}Ni_{1/3}Mn_{1/3}O_2$ for advanced lithium-ion batteries. *J. Power Sources* **119–121,** 171–174 (2003).

54. Wu, S.-L. *et al.* High Rate Capability of $Li(Ni_{1/3}Mn_{1/3}Co_{1/3})O_2$ Electrode for Li-Ion Batteries. *J. Electrochem. Soc.* **159,** A438 (2012).

55. Dou, S. Review and prospect of layered lithium nickel manganese oxide as cathode materials for Li-ion batteries. *J. Solid State Electrochem.* **17,** 911–926 (2013).

56. Ohzuku, T. & Makimura, Y. Layered lithium insertion material of $LiNi_{1/2}Mn_{1/2}O_2$: A possible alternative to $LiCoO_2$ for advanced lithium-ion batteries. *Chem. Lett.* 744–745 (2001).

57. Sun, Y.-K. *et al.* High-energy cathode material for long-life and safe lithium batteries. *Nat. Mater.* **8,** 320–324 (2009).

58. Thackeray, M. M. *et al.* Li_2MnO_2-stabilized $LiMO_2$ (M = Mn, Ni, Co) electrodes for lithium-ion batteries. *J. Mater. Chem.* **17,** 3112–3125 (2007).

59. Lee, E.-S. & Manthiram, A. Smart design of lithium-rich layered oxide cathode compositions with suppressed voltage decay. *J. Mater. Chem. A* **2,** 3932–3939 (2014).

60. Sathiya, M. *et al.* Reversible anionic redox chemistry in high-capacity layered-oxide electrodes. *Nat. Mater.* **12,** 827–835 (2013).

61. Koga, H. *et al.* Reversible Oxygen Participation to the Redox Processes Revealed for $Li_{1.20}Mn_{0.54}Co_{0.13}Ni_{0.13}O_2$. *J. Electrochem. Soc.* **160,** A786–A792 (2013).

62. McCalla, E. *et al.* Visualization of O-O peroxo-like dimers in high capacity layered oxides for Li-ion batteries. *Science* **350,** 1516–1521 (2015).

63. Sathiya, M. *et al.* High Performance $Li_2Ru_{1-y}Mn_yO_3$ ($0.2 \leq y \leq 0.8$) Cathode Materials for Rechargeable Lithium-Ion Batteries: Their Understanding. *Chem. Mater.* **25,** 1121–1131 (2013).

64. Xiao, R., Li, H. & Chen, L. Density Functional Investigation on Li_2MnO_3. *Chem. Mater.* **24,** 4242–4251 (2012).

65. Croguennec, L. & Palacin, M. R. Recent Achievements on Inorganic Electrode Materials for Lithium-Ion Batteries. *J. Am. Chem. Soc.* **137,** 3140–3156 (2015).

66. Koga, H. *et al.* Different oxygen redox participation for bulk and surface: A possible global explanation for the cycling mechanism of $Li_{1.20}Mn_{0.54}Co_{0.13}Ni_{0.13}O_2$. *J. Power Sources* **236,** 250–258 (2013).

67. Sathiya, M. *et al.* Origin of voltage decay in high-capacity layered oxide electrodes. *Nat. Mater.* **14,** 230–238 (2015).

68. Delmas, C., Braconnier, J.-J., Fouassier, C. & Hagenmuller, P. Electrochemical intercalation of sodium in Na_xCoO_2 bronzes. *Solid State Ion.* **3,** 165–169 (1981).

69. Yabuuchi, N., Kubota, K., Dahbi, M. & Komaba, S. Research Development on Sodium-Ion Batteries. *Chem. Rev.* **114,** 11636–11682 (2014).

70. Han, M. H., Gonzalo, E., Singh, G. & Rojo, T. A comprehensive review of sodium layered oxides: powerful cathodes for Na-ion batteries. *Energy Env. Sci* **8,** 81–102 (2015).

71. Sathiya, M., Hemalatha, K., Ramesha, K., Tarascon, J.-M. & Prakash, A. S. Synthesis, Structure, and Electrochemical Properties of the Layered Sodium Insertion Cathode Material: $NaNi_{1/3}Mn_{1/3}Co_{1/3}O_2$. *Chem. Mater.* **24,** 1846–1853 (2012).

72. Kim, S.-W., Seo, D.-H., Ma, X., Ceder, G. & Kang, K. Electrode Materials for Rechargeable Sodium-Ion Batteries: Potential Alternatives to Current Lithium-Ion Batteries. *Adv. Energy Mater.* **2,** 710–721 (2012).

73. Yabuuchi, N. *et al.* P2-type Nax[Fe1/2Mn1/2]O2 made from earth-abundant elements for rechargeable Na batteries. *Nat. Mater.* **11,** 512–517 (2012).

74. Komaba, S. *et al.* Study on the Reversible Electrode Reaction of Na_{1-x} $Ni_{0.5}Mn_{0.5}O_2$ for a Rechargeable Sodium-Ion Battery. *Inorg. Chem.* **51,** 6211–6220 (2012).

75. Kataoka, R., Mukai, T., Yoshizawa, A. & Sakai, T. Development of High Capacity Cathode Material for Sodium Ion Batteries $Na_{0.95}Li_{0.15}(Ni_{0.15}Mn_{0.55}Co_{0.1})O_2$. *J. Electrochem. Soc.* **160,** A933–A939 (2013).

76. Thackeray, M. M., David, W. I. F., Bruce, P. G. & Goodenough, J. B. Lithium insertion into manganese spinels. *Mater. Res. Bull.* **18,** 461–472 (1983).

77. Feng, Q., Miyai, Y., Kanoh, H. & Ooi, K. Lithium(1+) extraction/insertion with spinel-type lithium manganese oxides. Characterization of redox-type and ion-exchange-type sites. *Langmuir* **8,** 1861–1867 (1992).

78. Thackeray, M. M., Johnson, P. J., De Picciotto, L. A., Bruce, P. G. & Goodenough, J. B. Electrochemical extraction of lithium from $LiMn_2O_4$. *Mater. Res. Bull.* **19,** 179–187 (1984).

79. Eriksson, T. *$LiMn_2O_4$ as a Li-Ion battery cathode: from bulk to electrolyte interface*. (Acta Universitatis Upsaliensis, 2001).

80. Gummow, R. & Thackeray, M. M. An Investigation of Spinel-Related and Orthorhombic $LiMnO_2$ Cathodes for Rechargeable Lithium Batteries. *J. Electrochem. Soc.* **141,** 1178–1182 (1994).

81. Tarascon, J. M. The Spinel Phase of $LiMn_2O_4$ as a Cathode in Secondary Lithium Cells. *J. Electrochem. Soc.* **138,** 2859 (1991).

82. Amine, K. *et al.* Improved lithium manganese oxide spinel/graphite Li-ion cells for high-power applications. *J. Power Sources* **129,** 14–19 (2004).

83. Huang, H., Vincent, C. A. & Bruce, P. G. Capacity Loss of Lithium Manganese Oxide Spinel in $LiPF_6$/Ethylene Carbonate-Dimethyl Carbonate Electrolytes. *J. Electrochem. Soc.* **146,** 481–485 (1999).

84. Guyomard, D. & Tarascon, J. M. The carbon/$Li_{1-x}Mn_2O_4$ system. *Solid State Ion.* **69,** 222–237 (1994).

85. Huang, H., Vincent, C. A. & Bruce, P. G. Correlating capacity loss of stoichiometric and nonstoichiometric lithium manganese oxide spinel electrodes with their structural integrity. *J. Electrochem. Soc.* **146,** 3649–3654 (1999).

86. Amatucci, G. G., Pereira, N., Zheng, T. & Tarascon, J.-M. Failure Mechanism and Improvement of the Elevated Temperature Cycling of $LiMn_2O_4$ Compounds Through the Use of the $LiAl_xMn_{2-x}O_{4-z}F_z$ Solid Solution. *J. Electrochem. Soc.* **148,** A171 (2001).

87. Hu, M., Pang, X. & Zhou, Z. Recent progress in high-voltage lithium ion batteries. *J. Power Sources* **237,** 229–242 (2013).

88. Ohzuku, T., Takeda, S. & Iwanaga, M. Solid-state redox potentials for $Li[Me_{1/2}Mn_{3/2}]O_4$ (Me: 3d-transition metal) having spinel-framework structures: a series of 5 volt materials for advanced lithium-ion batteries. *J. Power Sources* **81–82,** 90–94 (1999).

89. Wang, J. *et al.* Superconcentrated electrolytes for a high-voltage lithium-ion battery. *Nat. Commun.* **7,** 12032 (2016).

90. Padhi, A. K., Nanjundaswamy, K. S. & Goodenough, J. B. Phospho-olivines as positive-electrode materials for rechargeable lithium batteries. *J. Electrochem. Soc.* **144,** 1188–1194 (1997).

91. Masquelier, C. & Croguennec, L. Polyanionic (Phosphates, Silicates, Sulfates) Frameworks as Electrode Materials for Rechargeable Li (or Na) Batteries. *Chem. Rev.* **113,** 6552–6591 (2013).

92. Padhi, A. K., Nanjundaswamy, K. S., Masquelier, C. & Goodenough, J. B. Mapping of transition metal redox energies in phosphates with NASICON structure by lithium intercalation. *J. Electrochem. Soc.* **144,** 2581–2586 (1997).

93. Nanjundaswamy, K. S. *et al.* Synthesis, redox potential evaluation and electrochemical characteristics of NASICON-related-3D framework compounds. *Solid State Ion.* **92,** 1–10 (1996).

94. Manthiram, A. & Goodenough, J. B. Lithium insertion into $Fe_2(SO_4)_3$ frameworks. *J. Power Sources* **26,** 403–408 (1989).

95. Manthiram, A. & Goodenough, J. B. Lithium insertion into $Fe_2(MO_4)_3$ frameworks: Comparison of M = W with M = Mo. *J. Solid State Chem.* **71,** 349–360 (1987).

96. Wu, Q., Xu, Y. & Ju, H. New-type low-cost cathode materials for Li-ion batteries: Mikasaite-type $Fe_2(SO_4)_3$. *Ionics* **19,** 471–475 (2012).

97. Wang, J. & Sun, X. Understanding and recent development of carbon coating on $LiFePO_4$ cathode materials for lithium-ion batteries. *Energy Env. Sci* **5,** 5163–5185 (2012).

98. Ravet, N. *et al.* Electroactivity of natural and synthetic triphylite. *J. Power Sources* **97–98,** 503–507 (2001).

99. Chen, R., Zhao, T., Zhang, X., Li, L. & Wu, F. Advanced cathode materials for lithium-ion batteries using nanoarchitectonics. *Nanoscale Horiz* (2016). doi:10.1039/C6NH00016A

100. Wagemaker, M. & Mulder, F. M. Properties and Promises of Nanosized Insertion Materials for Li-Ion Batteries. *Acc. Chem. Res.* **46,** 1206–1215 (2013).

101. Malik, R., Abdellahi, A. & Ceder, G. A Critical Review of the Li Insertion Mechanisms in $LiFePO_4$ Electrodes. in (Electrochemical Society, 2013).

102. Gong, Z. & Yang, Y. Recent advances in the research of polyanion-type cathode materials for Li-ion batteries. *Energy Environ. Sci.* **4,** 3223 (2011).

103. Julien, C., Mauger, A., Vijh, A. & Zaghib, K. in *Lithium Batteries* 201–268 (Springer International Publishing, 2016).

104. Amine, K. Olivine $LiCoPO_4$ as 4.8 V Electrode Material for Lithium Batteries. *Electrochem. Solid-State Lett.* **3,** 178 (1999).

105. Moreau, P., Guyomard, D., Gaubicher, J. & Boucher, F. Structure and Stability of Sodium Intercalated Phases in Olivine $FePO_4$. *Chem. Mater.* **22,** 4126–4128 (2010).

106. Zhu, Y., Xu, Y., Liu, Y., Luo, C. & Wang, C. Comparison of electrochemical performances of olivine $NaFePO_4$ in sodium-ion batteries and olivine $LiFePO_4$ in lithium-ion batteries. *Nanoscale* **5,** 780–787 (2013).

107. Zaghib, K. *et al.* Characterization of Na-based phosphate as electrode materials for electrochemical cells. *J. Power Sources* **196,** 9612–9617 (2011).

108. Nishimura, S., Nakamura, M., Natsui, R. & Yamada, A. New Lithium Iron Pyrophosphate as 3.5 V Class Cathode Material for Lithium Ion Battery. *J. Am. Chem. Soc.* **132,** 13596–13597 (2010).

109. Blidberg, A. *et al.* Structural and Electronic Changes in $Li_2FeP_2O_7$ during Electrochemical Cycling. *Chem. Mater.* **27,** 3801–3804 (2015).

110. Shimizu, D., Nishimura, S., Barpanda, P. & Yamada, A. Electrochemical Redox Mechanism in 3.5 V $Li_{2-x}FeP_2O_7$ ($0 \leq x \leq 1$) Pyrophosphate Cathode. *Chem. Mater.* **24,** 2598–2603 (2012).

111. Furuta, N., Nishimura, S., Barpanda, P. & Yamada, A. Fe^{3+}/Fe^{2+} Redox Couple Approaching 4 V in $Li_{2-x}(Fe_{1-y}Mn_y)P_2O_7$ Pyrophosphate Cathodes. *Chem. Mater.* **24,** 1055–1061 (2012).

112. Ye, T. *et al.* General Observation of Fe3+/Fe2+ Redox Couple Close to 4 V in Partially Substituted Li2FeP2O7 Pyrophosphate Solid-Solution Cathodes. *Chem. Mater.* **25,** 3623–3629 (2013).

113. Adam, L., Guesdon, A. & Raveau, B. A new lithium manganese phosphate with an original tunnel structure in the $A_2MP_2O_7$ family. *J. Solid State Chem.* **181,** 3110–3115 (2008).

114. Kim, H. *et al.* Neutron and X-ray Diffraction Study of Pyrophosphate-Based $Li_{2-x}MP_2O_7$ (M = Fe, Co) for Lithium Rechargeable Battery Electrodes. *Chem. Mater.* **23,** 3930–3937 (2011).

115. Tamaru, M., Barpanda, P., Yamada, Y., Nishimura, S. & Yamada, A. Observation of the highest Mn^{3+}/Mn^{2+} redox potential of 4.45 V in a $Li_2MnP_2O_7$ pyrophosphate cathode. *J. Mater. Chem.* **22,** 24526 (2012).

116. Padhi, A. K., Nanjundaswamy, K. S., Masquelier, C., Okada, S. & Goodenough, J. B. Effect of Structure on the Fe^{3+}/Fe^{2+} Redox Couple in Iron Phosphates. *J. Electrochem. Soc.* **144,** 1609–1613 (1997).

117. Marx, N. *et al.* The structure of tavorite $LiFePO_4(OH)$ from diffraction and GGA + U studies and its preliminary electrochemical characterization. *Dalton Trans.* **39,** 5108 (2010).

118. Ramesh, T. N., Lee, K. T., Ellis, B. L. & Nazar, L. F. Tavorite Lithium Iron Fluorophosphate Cathode Materials: Phase Transition and Electrochemistry of $LiFePO_4F$–Li_2FePO_4F. *Electrochem. Solid-State Lett.* **13,** A43 (2010).

119. Mba, J.-M. A., Croguennec, L., Basir, N. I., Barker, J. & Masquelier, C. Lithium insertion or extraction from/into tavorite-type $LiVPO_4F$: an in situ X-ray diffraction study. *J. Electrochem. Soc.* **159,** A1171–A1175 (2012).

120. Ateba Mba, J.-M., Masquelier, C., Suard, E. & Croguennec, L. Synthesis and Crystallographic Study of Homeotypic $LiVPO_4F$ and $LiVPO_4O$. *Chem. Mater.* **24,** 1223–1234 (2012).

121. Barker, J., Saidi, M. Y. & Swoyer, J. L. Electrochemical Insertion Properties of the Novel Lithium Vanadium Fluorophosphate, LiVPO[sub 4]F. *J. Electrochem. Soc.* **150,** A1394 (2003).

122. Masquelier, C., Padhi, A. K., Nanjundaswamy, K. S. & Goodenough, J. B. New Cathode Materials for Rechargeable Lithium Batteries: The 3-D Framework Structures $Li_3Fe_2(XO_4)_3$ (X=P, As). *J. Solid State Chem.* **135,** 228–234 (1998).

123. Bianchini, M. *et al.* Comprehensive Investigation of the $Na_3V_2(PO_4)_2F_3$ –$NaV_2(PO_4)_2F_3$ System by Operando High Resolution Synchrotron X-ray Diffraction. *Chem. Mater.* **27,** 3009–3020 (2015).

124. Chihara, K., Kitajou, A., Gocheva, I. D., Okada, S. & Yamaki, J. Cathode properties of $Na_3M_2(PO_4)_2F_3$ [M = Ti, Fe, V] for sodium-ion batteries. *J. Power Sources* **227,** 80–85 (2013).

125. Shakoor, R. A. *et al.* A combined first principles and experimental study on $Na_3V_2(PO_4)_2F_3$ for rechargeable Na batteries. *J. Mater. Chem.* **22,** 20535–20541 (2012).

126. Zhang, B. *et al.* Insertion compounds and composites made by ball milling for advanced sodium-ion batteries. *Nat. Commun.* **7,** 10308 (2016).

127. Dugas, R., Zhang, B., Rozier, P. & Tarascon, J. M. Optimization of Na-Ion Battery Systems Based on Polyanionic or Layered Positive Electrodes and Carbon Anodes. *J. Electrochem. Soc.* **163,** A867–A874 (2016).

128. Islam, M. S. *et al.* Silicate cathodes for lithium batteries: alternatives to phosphates? *J. Mater. Chem.* **21,** 9811–9818 (2011).

129. Nishimura, S. *et al.* Structure of Li_2FeSiO_4. *J. Am. Chem. Soc.* **130,** 13212–13213 (2008).

130. Nytén, A., Abouimrane, A., Armand, M., Gustafsson, T. & Thomas, J. O. Electrochemical performance of Li_2FeSiO_4 as a new Li-battery cathode material. *Electrochem. Commun.* **7,** 156–160 (2005).

131. Sirisopanaporn, C., Masquelier, C., Bruce, P. G., Armstrong, A. R. & Dominko, R. Dependence of Li_2FeSiO_4 Electrochemistry on Structure. *J. Am. Chem. Soc.* **133,** 1263–1265 (2011).

132. Dominko, R., Conte, D. E., Hanzel, D., Gaberscek, M. & Jamnik, J. Impact of synthesis conditions on the structure and performance of Li_2FeSiO_4. *J. Power Sources* **178,** 842–847 (2008).

133. Nytén, A., Kamali, S., Häggström, L., Gustafsson, T. & Thomas, J. O. The lithium extraction/insertion mechanism in Li_2FeSiO_4. *J Mater Chem* **16,** 2266–2272 (2006).

134. Muraliganth, T., Stroukoff, K. R. & Manthiram, A. Microwave-Solvothermal Synthesis of Nanostructured Li_2MSiO_4/C (M = Mn and Fe) Cathodes for Lithium-Ion Batteries. *Chem. Mater.* **22,** 5754–5761 (2010).

135. He, G. & Manthiram, A. Nanostructured Li_2MnSiO_4/C Cathodes with Hierarchical Macro-/Mesoporosity for Lithium-Ion Batteries. *Adv. Funct. Mater.* **24,** 5277–5283 (2014).

136. Gummow, R. J. & He, Y. Recent progress in the development of Li2MnSiO4 cathode materials. *J. Power Sources* **253,** 315–331 (2014).

137. Legagneur, V. *et al.* $LiMBO_3$ (M=Mn, Fe, Co): synthesis, crystal structure and lithium deinsertion/insertion properties. *Solid State Ion.* **139,** 37–46 (2001).

138. Bo, S.-H. *et al.* Degradation and (de)lithiation processes in the high capacity battery material $LiFeBO_3$. *J. Mater. Chem.* **22,** 8799–8809 (2012).

139. Yamada, A. *et al.* Lithium Iron Borates as High-Capacity Battery Electrodes. *Adv. Mater.* **22,** 3583–3587 (2010).

140. Kim, J. C. *et al.* Synthesis and Electrochemical Properties of Monoclinic $LiMnBO_3$ as a Li Intercalation Material. *J. Electrochem. Soc.* **158,** A309 (2011).

141. Strauss, F. *et al.* Electrochemical activity and high ionic conductivity of lithium copper pyroborate $Li_6CuB_4O_{10}$. *Phys Chem Chem Phys* (2016). doi:10.1039/C6CP01581F

142. Rousse, G. & Tarascon, J. M. Sulfate-Based Polyanionic Compounds for Li-Ion Batteries: Synthesis, Crystal Chemistry, and Electrochemistry Aspects. *Chem. Mater.* **26,** 394–406 (2014).

143. Reynaud, M. *et al.* $Li_2Fe(SO_4)_2$ as a 3.83 V positive electrode material. *Electrochem. Commun.* **21,** 77–80 (2012).

144. Reynaud, M. Design of new sulfate-based positive electrode materials for Li- and Na-ion batteries / Elaboration de nouveaux matériaux à base de sulfates pour l'électrode positive des batteries à ions Li et Na. (Université de Picardie Jules Verne, 2013).

145. Reynaud, M. *et al.* Design of new electrode materials for Li-ion and Na-ion batteries from the bloedite mineral $Na_2Mg(SO_4)_2{\cdot}4H_2O$. *J. Mater. Chem. A* **2,** 2671–2680 (2014).

146. Barpanda, P., Oyama, G., Ling, C. D. & Yamada, A. Kröhnkite-Type $Na_2Fe(SO_4)_2{\cdot}2H_2O$ as a Novel 3.25 V Insertion Compound for Na-Ion Batteries. *Chem. Mater.* **26,** 1297–1299 (2014).

147. Lander, L. *et al.* Synthesis and Electrochemical Performance of the Orthorhombic $Li_2Fe(SO_4)_2$ Polymorph for Li-Ion Batteries. *Chem. Mater.* **26,** 4178–4189 (2014).

148. Barpanda, P., Oyama, G., Nishimura, S., Chung, S.-C. & Yamada, A. A 3.8-V earth-abundant sodium battery electrode. *Nat. Commun.* **5,** (2014).

149. Subban, C. V. *et al.* Preparation, Structure, and Electrochemistry of Layered Polyanionic Hydroxysulfates: $LiMSO_4OH$ (M = Fe, Co, Mn) Electrodes for Li-Ion Batteries. *J. Am. Chem. Soc.* **135,** 3653–3661 (2013).

150. Anji Reddy, M., Pralong, V., Caignaert, V., Varadaraju, U. V. & Raveau, B. Monoclinic iron hydroxy sulphate: A new route to electrode materials. *Electrochem. Commun.* **11,** 1807–1810 (2009).

151. Sun, M. *et al.* An Oxysulfate $Fe_2O(SO_4)_2$Electrode for Sustainable Li-Based Batteries. *J. Am. Chem. Soc.* **136,** 12658–12666 (2014).

152. Sun, M. *et al.* $Li_2Cu_2O(SO_4)_2$: a Possible Electrode for Sustainable Li-Based Batteries Showing a 4.7 V Redox Activity vs Li^+/Li^0. *Chem. Mater.* **27,** 3077–3087 (2015).

153. Zhang, L., Tarascon, J.-M., Sougrati, M. T., Rousse, G. & Chen, G. Influence of relative humidity on the structure and electrochemical performance of sustainable $LiFeSO_4F$ electrodes for Li-ion batteries. *J. Mater. Chem. A* **3,** 16988–16997 (2015).

154. Recham, N. *et al.* A 3.6 V lithium-based fluorosulphate insertion positive electrode for lithium-ion batteries. *Nat. Mater.* **9,** 68–74 (2009).

155. Barpanda, P. *et al.* A 3.90 V iron-based fluorosulphate material for lithium-ion batteries crystallizing in the triplite structure. *Nat. Mater.* **10,** 772–779 (2011).

156. Ati, M. *et al.* Synthesis and electrochemical properties of pure $LiFeSO_4F$ in the triplite structure. *Electrochem. Commun.* **13,** 1280–1283 (2011).

157. Barpanda, P. *et al.* $LiZnSO_4F$ Made in an Ionic Liquid: A Ceramic Electrolyte Composite for Solid-State Lithium Batteries. *Angew. Chem. Int. Ed.* **50,** 2526–2531 (2011).

158. Ati, M. *et al.* Understanding and Promoting the Rapid Preparation of the *Triplite* -Phase of $LiFeSO_4$ F for Use as a Large-Potential Fe Cathode. *J. Am. Chem. Soc.* **134,** 18380–18387 (2012).

159. Kim, M., Jung, Y. & Kang, B. High electrochemical performance of 3.9 V $LiFeSO_4F$ directly synthesized by a scalable solid- state reaction within 1 h. *J Mater Chem A* **3,** 7583–7590 (2015).

160. Barpanda, P. *et al.* Structural, Transport, and Electrochemical Investigation of Novel $AMSO_4F$ (A = Na, Li; M = Fe, Co, Ni, Mn) Metal Fluorosulphates Prepared Using Low Temperature Synthesis Routes. *Inorg. Chem.* **49,** 7401–7413 (2010).

161. Reynaud, M. *et al.* Synthesis and crystal chemistry of the $NaMSO_4F$ family (M = Mg, Fe, Co, Cu, Zn). *Solid State Sci.* **14,** 15–20 (2012).

162. Ati, M. *et al.* Synthesis, Structural, and Transport Properties of Novel Bihydrated Fluorosulphates $NaMSO_4F{\cdot}2H_2O$ (M = Fe, Co, and Ni). *Chem. Mater.* **22,** 4062–4068 (2010).

163. Melot, B. C. *et al.* Synthesis, Structure, and Magnetic Properties of the $NaCoXO_4F{\cdot}2H_2O$ Phases Where *X* = S and Se. *Inorg. Chem.* **50,** 7662–7668 (2011).

164. Recham, N. *et al.* Preparation and Characterization of a Stable $FeSO_4F$-Based Framework for Alkali Ion Insertion Electrodes. *Chem. Mater.* **24,** 4363–4370 (2012).

165. Lander, L. *et al.* Structural, electrochemical and magnetic properties of a novel $KFeSO_4F$ polymorph. *J. Mater. Chem. A* **3,** 19754–19764 (2015).

166. Muldoon, J., Bucur, C. B. & Gregory, T. Quest for Nonaqueous Multivalent Secondary Batteries: Magnesium and Beyond. *Chem. Rev.* **114,** 11683–11720 (2014).

167. Aurbach, D. *et al.* A short review on the comparison between Li battery systems and rechargeable magnesium battery technology. *J. Power Sources* **97,** 28–32 (2001).

168. Aurbach, D., Weissman, I., Gofer, Y. & Levi, E. Nonaqueous magnesium electrochemistry and its application in secondary batteries. *Chem. Rec.* **3,** 61–73 (2003).

169. Yoo, H. D. *et al.* Mg rechargeable batteries: an on-going challenge. *Energy Environ. Sci.* **6,** 2265 (2013).

170. Ponrouch, A., Frontera, C., Bardé, F. & Palacín, M. R. Towards a calcium-based rechargeable battery. *Nat. Mater.* **15,** 169–172 (2015).

171. Luntz, A. C. & McCloskey, B. D. Nonaqueous Li–Air Batteries: A Status Report. *Chem. Rev.* **114,** 11721–11750 (2014).

172. Wild, M. *et al.* Lithium sulfur batteries, a mechanistic review. *Energy Environ. Sci.* **8,** 3477–3494 (2015).

173. Manthiram, A., Fu, Y., Chung, S.-H., Zu, C. & Su, Y.-S. Rechargeable Lithium–Sulfur Batteries. *Chem. Rev.* **114,** 11751–11787 (2014).

174. Palomares, V. *et al.* Na-ion batteries, recent advances and present challenges to become low cost energy storage systems. *Energy Environ. Sci.* **5,** 5884–5901 (2012).

175. Radha, A. V. *et al.* Understanding the stability of fluorosulfate Li-ion battery cathode materials: a thermochemical study of $LiFe_{1-x}Mn_xSO_4F$ ($0 \leq x \leq 1$) polymorphs. *J. Mater. Chem.* **22,** 24446 (2012).

176. Radha, A. V., Subban, C. V., Sun, M. L., Tarascon, J.-M. & Navrotsky, A. Possible correlation between enthalpies of formation and redox potentials in $LiMSO_4OH$ (M = Co, Fe, Mn), Li-ion polyanionic battery cathode materials. *J. Mater. Chem. A* **2,** 6887–6894 (2014).

177. Masquelier, C. & Croguennec, L. Polyanionic (Phosphates, Silicates, Sulfates) Frameworks as Electrode Materials for Rechargeable Li (or Na) Batteries. *Chem. Rev.* **113,** 6552–6591 (2013).

178. Manthiram, A. & Goodenough, J. B. Lithium insertion into $Fe_2(SO_4)_3$ frameworks. *J. Power Sources* **26,** 403–408 (1989).

179. Sebastian, L., Gopalakrishnan, J. & Piffard, Y. Synthesis, crystal structure and lithium ion conductivity of $LiMgFSO_4$. *J. Mater. Chem.* **12,** 374–377 (2002).

180. Recham, N. *et al.* A 3.6 V lithium-based fluorosulphate insertion positive electrode for lithium-ion batteries. *Nat. Mater.* **9,** 68–74 (2010).

181. Barpanda, P. *et al.* Structure and electrochemical properties of novel mixed $Li(Fe_{1-x}M_x)SO_4F$ (M = Co, Ni, Mn) phases fabricated by low temperature ionothermal synthesis. *J. Mater. Chem.* **20,** 1659–1668 (2010).

182. Barpanda, P. *et al.* A 3.90 V iron-based fluorosulphate material for lithium-ion batteries crystallizing in the triplite structure. *Nat. Mater.* **10,** 772–779 (2011).

183. Waldrop, L. The crystal structure of triplite, $(Mn,Fe)_2FPO_4$.

184. Rea, J. R. & Kostiner, E. The crystal structure of manganese fluorophosphate, $Mn_2(PO_4)F$. *Acta Crystallogr. B* **28,** 2525–2529 (1972).

185. Ati, M. *et al.* Understanding and Promoting the Rapid Preparation of the triplite-phase of $LiFeSO_4F$ for Use as a Large-Potential Fe Cathode. *J. Am. Chem. Soc.* **134,** 18380–18387 (2012).

186. Ati, M. *et al.* Synthesis and electrochemical properties of pure $LiFeSO_4F$ in the triplite structure. *Electrochem. Commun.* **13,** 1280–1283 (2011).

187. Tripathi, R., Popov, G., Ellis, B. L., Huq, A. & Nazar, L. F. Lithium metal fluorosulfate polymorphs as positive electrodes for Li-ion batteries: synthetic strategies and effect of cation ordering. *Energy Environ. Sci.* **5,** 6238 (2012).

188. Lee, S. & Park, S. S. Comparative Study of Tavorite and Triplite $LiFeSO_4F$ as Cathode Materials for Lithium Ion Batteries: Structure, Defect Chemistry, and Lithium Conduction Properties from Atomistic Simulation. *J. Phys. Chem. C* **118,** 12642–12648 (2014).

189. Rousse, G. & Tarascon, J.-M. Sulfate-based Polyanionic Compounds for Li-ion Batteries: Synthesis, Crystal Chemistry and Electrochemistry Aspects. *Chem. Mater.* **26,** 394–406 (2014).

190. Tripathi, R., Popov, G., Sun, X., Ryan, D. H. & Nazar, L. F. Ultra-rapid microwave synthesis of triplite $LiFeSO_4F$. *J. Mater. Chem. A* **1,** 2990 (2013).

191. Sobkowiak, A. $LiFeSO_4F$ as a Cathode Material for Lithium-Ion Batteries: Synthesis, Structure, and Function. (Acta Universitatis Upsaliensis, 2015).

192. Liu, L., Zhang, B. & Huang, X. A 3.9 V polyanion-type cathode material for Li-ion batteries. *Prog. Nat. Sci. Mater. Int.* **21,** 211–215 (2011).

193. Chung, S. C., Barpanda, P., Nishimura, S., Yamada, Y. & Yamada, A. Polymorphs of $LiFeSO_4F$ as cathode materials for lithium ion batteries – a first principle computational study. *Phys. Chem. Chem. Phys.* **14,** 8678 (2012).

194. Radha, A. V. *et al.* Understanding the Stability of Fluorosulfate Li-ion Battery Cathode Materials: A Thermochemical Study of $LiFe_{1-x}Mn_xSO_4F$ ($0 \leq x \leq 1$) Polymorphs. *J. Mater. Chem.* **22,** 24446–24452 (2012).

195. Yahia, M. B. *et al.* Origin of the 3.6 V to 3.9 V voltage increase in the $LiFeSO_4F$ cathodes for Li-ion batteries. *Energy Environ. Sci.* **5,** 9584–9594 (2012).

196. Sun, M. *et al.* A Fully Ordered Triplite, $LiCuSO_4F$. *Chem. Mater.* **28,** 1607–1610 (2016).

197. Melot, B. C. *et al.* Magnetic Structure and Properties of the Li-Ion Battery Materials $FeSO_4F$ and $LiFeSO_4F$. *Chem. Mater.* **23,** 2922–2930 (2011).

198. Tordjman, I., Masse, R. & Guitel, J. C. Structure cristalline du monophosphate $KTiPO_5$. *Z. Für Krist.* **139,** 103–115 (1974).

199. Ati, M. *et al.* Fluorosulfate Positive Electrodes for Li-Ion Batteries Made via a Solid-State Dry Process. *J. Electrochem. Soc.* **157,** A1007–A1015 (2010).

200. Ling, C. & Mizuno, F. Mechanistic study of the electrochemical extraction of K^+ from $KFeSO_4F$. *J. Mater. Chem. A* **1,** 8000–8006 (2013).

201. Radha, A. V., Lander, L., Rousse, G., Tarascon, J. M. & Navrotsky, A. Thermodynamic stability and correlation with synthesis conditions, structure and phase transformations in orthorhombic and monoclinic $Li_2M(SO_4)_2$ (M = Mn, Fe, Co, Ni) polymorphs. *J Mater Chem A* **3,** 2601–2608 (2015).

202. Bertaut, E. F. Magnetic structure analysis and group theory. *J. Phys. Colloq.* **32,** C1-462-C1-470 (1971).

203. Rodríguez-Carvajal, J. *FullProf Suite*. (www.ill.eu/sites/fullprof/).

204. Fedotov, S. S. *et al.* $AVPO_4F$ (A = Li, K): A 4 V Cathode Material for High-Power Rechargeable Batteries. *Chem. Mater.* **28,** 411–415 (2016).

205. Hammami, A., Raymond, N. & Armand, M. Lithium-ion batteries: Runaway risk of forming toxic compounds. *Nature* **424,** 635–636 (2003).

206. Reynaud, M. *et al.* Design of new electrode materials for Li-ion and Na-ion batteries from the Bloedite mineral Na2Mg(SO4)2•4H2O. *J. Mater. Chem. A* **2,** 2671–2680 (2013).

207. Reynaud, M. *et al.* $Li_2Fe(SO_4)_2$ as a 3.83 V positive electrode material. *Electrochem. Commun.* **21,** 77–80 (2012).

208. Isasi, J., Jaulmes, S., Elfakir, A. & Quarton, M. Crystal structure of dilithium nickel disulfate, $Li_2Ni(SO_4)_2$. *Z. Für Krist. - New Cryst. Struct.* **216,** 331–332 (2001).

209. Recham, N. *et al.* Preparation and Characterization of a Stable $FeSO_4F$-based Framework for Alkali Ion Insertion Electrodes. *Chem. Mater.* (2012). doi:10.1021/cm302428w

210. Subban, C. V. *et al.* Preparation, Structure, and Electrochemistry of Layered Polyanionic Hydroxysulfates: $LiMSO_4OH$ (M=Fe, Co, Mn) Electrodes for Li-ion Batteries. *J. Am. Chem. Soc.* **135,** 3653–3661 (2013).

211. Lander, L. *et al.* Unveiling the electrochemical mechanisms of $Li_2Fe(SO_4)_2$ polymorphs by neutron diffraction and density functional theory calculations. *Phys Chem Chem Phys* **18,** 14509–14519 (2016).

212. Lander, L. *et al.* Synthesis and electrochemical performance of the orthorhombic Li2Fe(SO4)2 polymorph for Li-ion batteries. *Chem. Mater.* (2014). doi:10.1021/cm5012845

213. Touboul, M., Quarton, M., Lokaj, J. & Kettmann, V. Structure of dilithium dimagnesium trisulfate. *Acta Crystallogr. C* **44,** 1887–1889 (1988).

214. Rodriguez-Carvajal, J. Recent advances in magnetic structure determination by neutron powder diffraction. *Phys. B Condens. Matter* **192,** 55 (1993).

215. Adams, S. From bond valence maps to energy landscapes for mobile ions in ion-conducting solids. *Solid State Ion.* **177,** 1625–1630 (2006).

216. Tanabe, Y. & Sugano, S. tanabe1954.pdf. *J. Phys. Soc. Jpn.* **9,** 766–779 (1954).

217. KUBELKA, P. New Contributions to the Optics of Intensely Light-Scattering Materials. Part I. *J. Opt. Soc. Am.* **38,** 448–448 (1948).

218. López, R. & Gómez, R. Band-gap energy estimation from diffuse reflectance measurements on sol–gel and commercial TiO2: a comparative study. *J. Sol-Gel Sci. Technol.* **61,** 1–7 (2012).

219. Zhou, F., Kang, K., Maxisch, T., Ceder, G. & Morgan, D. The electronic structure and band gap of LiFePO4 and LiMnPO4. *Solid State Commun.* **132,** 181–186 (2004).

220. Zhang, L.-L. *et al.* Study on electrochemical performance and mechanism of V-doped Li2FeSiO4 cathode material for Li-ion batteries. *Electrochimica Acta* **152,** 496–504 (2015).

221. Xie, Y. *et al.* Thermodynamic stability and transport properties of tavorite LiFeSO4F as a cathode material for lithium-ion batteries. *J. Mater. Chem. A* **3,** 19728–19737 (2015).

222. Liu, Z. & Huang, X. Structural, electronic and Li diffusion properties of LiFeSO4F. *Solid State Ion.* **181,** 1209–1213 (2010).

223. Frayret, C. *et al.* LiMSO4F (M = Fe, Co and Ni): promising new positive electrode materials through the DFT microscope. *Phys. Chem. Chem. Phys.* **12,** 15512–15522 (2010).

224. Chung, S. C., Barpanda, P., Nishimura, S., Yamada, Y. & Yamada, A. Polymorphs of LiFeSO4F as cathode materials for lithium ion batteries – a first principle computational study. *Phys. Chem. Chem. Phys.* **14,** 8678–8682 (2012).

225. Lundén, A. Evidence for and against the paddle-wheel mechanism of ion transport in superionic sulphate phases. *Solid State Commun.* **65,** 1237–1240 (1988).

226. Tao, L. *et al.* Magnetic Structures of $LiMBO_3$ (M = Mn, Fe, Co) Lithiated Transition Metal Borates. *Inorg. Chem.* **52,** 11966–11974 (2013).

227. Melot, B. C. *et al.* Magnetic structure and properties of $NaFeSO_4F$ and $NaCoSO_4F$. *Phys. Rev. B* **85,** 094415 (2012).

228. Rousse, G., Rodríguez-Carvajal, J., Patoux, S. & Masquelier, C. Magnetic Structures of the Triphylite $LiFePO_4$ and of Its Delithiated Form $FePO_4$. *Chem. Mater.* **15,** 4082–4090 (2003).

229. Rousse, G., Rodríguez-Carvajal, J., Wurm, C. & Masquelier, C. A neutron diffraction study of the antiferromagnetic diphosphate $LiFeP_2O_7$. *Solid State Sci.* **4,** 973–978 (2002).

230. Rousse, G., Rodríguez-Carvajal, J., Wurm, C. & Masquelier, C. Magnetic structure of two lithium iron phosphates: A- and B-$Li_3Fe_2(PO_4)_3$. *Appl. Phys. A* **74,** s704–s706 (2002).

231. Reynaud, M., Rousse, G., Chotard, J.-N., Rodríguez-Carvajal, J. & Tarascon, J.-M. Marinite $Li_2M(SO_4)_2$ (M = Co, Fe, Mn) and $Li_1Fe(SO_4)_2$: model compounds for super−super exchange magnetic interactions. *Inorg. Chem.* **52,** 10456–10466 (2013).

232. Reynaud, M., Rodríguez-Carvajal, J., Chotard, J.-N., Tarascon, J.-M. & Rousse, G. Magnetic structure and properties of orthorhombic $Li_2Ni(SO_4)_2$: A possible magnetoelectric material. *Phys. Rev. B* **89,** 104419 (2014).

233. Rousse, G., Radtke, G., Klein, Y. & Ahouari, H. Long-range antiferromagnetic order in malonate-based compounds $Na_2M(H_2C_3O_4)_2 \cdot 2H_2O$ (M = Mn, Fe, Co, Ni). *Dalton Trans* **45,** 2536–2548 (2016).

234. Borovik-Romanov, A. S., Karasik, V. R. & Kreines, N. M. The Antiferromagnetism of anhydrous sulfates of Ni^{2+}, Fe^{2+}, Co^{2+} and Cu^{2+}. *J Exptl Theor. Phys* **4,** 18–24

235. Moron, M. C., Palacio, F. & Rodriguez-Carvajal, J. Crystal and magnetic structures of $RbMnF_4$ and $KMnF_4$ investigated by neutron powder diffraction: the relationship between structure and magnetic properties in the Mn^{3+} layered perovskites $AMnF_4$ (A=Na, K, Rb, Cs). *J. Phys. Condens. Matter* **5,** 4909 (1993).

236. Fiebig, M. Revival of the magnetoelectric effect. *J. Phys. Appl. Phys.* **38,** R123–R152 (2005).

237. Folen, V. J., Rado, G. T. & Stalder, E. W. Anisotropy of the Magnetoelectric Effect in Cr_ ${$2$}$ O_ ${$3$}$. *Phys. Rev. Lett.* **6,** 607 (1961).

238. Shtrikman, S. & Treves, D. Observation of the Magnetoelectric Effect in Cr2O3 Powders. *Phys. Rev.* **130,** 986–988 (1963).

239. Krichevtsov, B. B., Pavlov, V. V. & Pisarev, R. V. Giant linear magnetoelectric effect in garnet ferrite films. *JETP Lett.* **49,** 535 (1989).

240. Recham, N. *et al.* Preparation and Characterization of a Stable $FeSO_4F$-Based Framework for Alkali Ion Insertion Electrodes. *Chem. Mater.* **24,** 4363–4370 (2012).

241. Meng, Y., Yu, T., Zhang, S. & Deng, C. Top-down synthesis of muscle-inspired alluaudite $Na_{2+2x}Fe_{2-x}(SO_4)_3$/SWNT spindle as a high-rate and high-potential cathode for sodium-ion batteries. *J. Mater. Chem. A* **4,** 1624–1631 (2016).

242. Oyama, G., Nishimura, S., Suzuki, Y., Okubo, M. & Yamada, A. Off-Stoichiometry in Alluaudite-Type Sodium Iron Sulfate Na2+2xFe2−x(SO4)3 as an Advanced Sodium Battery Cathode Material. *ChemElectroChem* **2,** 1019–1023 (2015).

243. Windhaus, M., Mosel, B. D. & Muller-Warmuth, W. Moessbauer Studies of Fe^{2+} in Iron Langbeinites and other Crystals with Langbeinite Structure. *Z. Naturforschung -J. Phys. Sci.* **53,** 27–37 (1998).

244. Gattow, G. & Zemann, J. Über Doppelsulfate vom Langbeinit-Typ $A_2B_2(SO_4)_3$. *Z Anorg Allg Chem* **293,** 233–240 (1958).

245. Oelkrug, H., Brückel, T., Hohlwein, D., Hoser, A. & Prandl, W. The magnetic structure of the langbeinite $K_2Mn_2(SO_4)_3$. *Phys. Chem. Miner.* **16,** 246–249 (1988).

246. Emmenegger, F. Crystal Growth and Electro-optic Effect of Some Double Sulfates with the Langbeinite Structure. *J. Appl. Phys.* **39,** 3039 (1968).

247. Hernández-Rodríguez, C., Geday, M. A., Kreisel, J., Glazer, A. M. & Hidalgo-López, A. Optical birefringence imaging of the phase transition of $K_2Mn_2(SO_4)_3$. *J. Appl. Crystallogr.* **36,** 914–919 (2003).

248. Speer, D. & Salje, E. Phase transitions in langbeinites I: Crystal chemistry and structures of K-double sulfates of the langbeinite type $M_2^{2+}K_2(SO_4)_3$, M^{2+}= Mg, Ni, Co, Zn, Ca. *Phys. Chem. Miner.* **13,** 17–24 (1986).

249. Abrahams, S. C. & Bernstein, J. L. Piezoelectric langbeinite-type $K_2Cd_2(SO_4)_3$: Room temperature crystal structure and ferroelastic transformation. *J. Chem. Phys.* **67,** 2146 (1977).

250. Abrahams, S. C., Lissalde, F. & Bernstein, J. L. Piezoelectric langbeinite-type $K_2Cd_2(SO_4)_3$ structure at four temperatures below and one above the 432°K ferroelastic–paraelastic transition. *J. Chem. Phys.* **68,** 1926 (1978).

251. Ramsdell, L. S. An X-ray study of the system K_2SO_4-$MgSO_4$-$CaSO_4$. *Am. Mineral.* **20,** 596–574 (1935).

252. Yamada, N., Maeda, M. & Adachi, H. Structures of Langbeinite-Type $K_2Mn_2(SO_4)_3$ in Cubic and Orthorhombic Phases. *J. Phys. Soc. Jpn.* **50,** 907–913 (1981).

253. Hikita, T., Kitabatake, M. & Ikeda, T. Effect of Hydrostatic Pressure on the Phase Transitions of Langbeinite-Type Crystals. *J. Phys. Soc. Jpn.* **49,** 1421–1428 (1980).

254. Boultif, A. History of the dichotomy method for powder pattern indexing. *Powder Diffr.* **20,** 284–287 (2005).

255. Boultif, A. & Louër, D. Indexing of powder diffraction patterns for low-symmetry lattices by the successive dichotomy method. *J. Appl. Crystallogr.* **24,** 987–993 (1991).

256. Favre-Nicolin, V. & Cerny, R. FOX, `free objects for crystallography': a modular approach to ab initio structure determination from powder diffraction. *J. Appl. Crystallogr.* **35,** 734–743 (2002).

257. FoxWiki - FOX, Free Objects for Crystallography Wiki. Available at: http://fox.vincefn.net/.

258. Sobkowiak, A. *et al.* Understanding and Controlling the Surface Chemistry of $LiFeSO_4F$ for an Enhanced Cathode Functionality. *Chem. Mater.* **25,** 3020–3029 (2013).

259. Ponrouch, A. *et al.* A new room temperature and solvent free carbon coating procedure for battery electrode materials. *Energy Environ. Sci.* **6,** 3363–3371 (2013).

260. Meng, Y., Zhang, S. & Deng, C. Superior sodium–lithium intercalation and depressed moisture sensitivity of a hierarchical sandwich-type nanostructure for a graphene–sulfate composite: a case study on $Na_2Fe(SO_4)_2{\cdot}2H_2O$. *J. Mater. Chem. A* **3,** 4484–4492 (2015).

261. Starova, G. L., Filatov, S. K., Fundamensky, V. S. & Vergasova, L. P. The crystal structure of fedotovite, $K_2Cu_3O(SO_4)_3$. *Mineral. Mag.* **55,** 613–616 (1991).

262. Munir, Z. A., Quach, D. V. & Ohyanagi, M. Electric Current Activation of Sintering: A Review of the Pulsed Electric Current Sintering Process. *J. Am. Ceram. Soc.* **94,** 1–19 (2011).

263. 11bm-sample. Available at: https://wiki-ext.aps.anl.gov/ug11bm/index.php/File:SampleBase_Diagram.png.

264. Le Bail, A. Whole powder pattern decomposition methods and applications: A retrospection. *Powder Diffr.* **20,** 316–326 (2005).

265. Altomare, A. *et al. EXPO2013* : a kit of tools for phasing crystal structures from powder data. *J. Appl. Crystallogr.* **46,** 1231–1235 (2013).

266. Altomare, A. *et al. EXPO* : a program for full powder pattern decomposition and crystal structure solution. *J. Appl. Crystallogr.* **32,** 339–340 (1999).

267. Rietveld, H. M. A profile refinement method for nuclear and magnetic structures. *J. Appl. Crystallogr.* **2,** 65–71 (1969).

268. Brown, I. D. Recent Developments in the Methods and Applications of the Bond Valence Model. *Chem. Rev.* **109,** 6858–6919 (2009).

269. Sale, M. Large throughput analysis of crystal structures for identification of promising Li-ion battery materials. (University of Wollongong, Australia, 2014).

270. Permanent Magnets. Available at: http://hyperphysics.phy-astr.gsu.edu/hbase/solids/magperm.html.

271. Magnetic interactions. Available at: http://www.ch.ntu.edu.tw/~jtchen/course/inorganic/magnetism.html.

272. Bertaut, E. F. Magnetic structure analysis and group theory. *J. Phys. Colloq.* **32,** C1–462 (1971).

273. Introduction to Mössbauer Spectroscopy: Part 2. Available at: http://www.rsc.org/Membership/Networking/InterestGroups/MossbauerSpect/part2.asp.

274. Massiot, D. *et al.* Modelling one- and two-dimensional solid-state NMR spectra. *Magn. Reson. Chem.* **40,** 70–76 (2002).

275. Irvine, J. T. S., Sinclair, D. C. & West, A. R. Electroceramics: Characterization by Impedance Spectroscopy. *Adv. Mater.* **2,** 132–138 (1990).

276. Chervin, J. C., Canny, B., Besson, J. M. & Pruzan, P. A diamond anvil cell for IR microspectroscopy. *Rev. Sci. Instrum.* **66,** 2595–2598 (1995).

277. Couzinet, B., Dahan, N., Hamel, G. & Chervin, J.-C. Optically monitored high-pressure gas loading apparatus for diamond anvil cells. *High Press. Res.* **23,** 409–415 (2003).

278. Chervin, J. C., Canny, B. & Mancinelli, M. Ruby-spheres as pressure gauge for optically transparent high pressure cells. *High Press. Res.* **21,** 305–314 (2001).

279. Barnett, J. D., Block, S. & Piermarini, G. J. An Optical Fluorescence System for Quantitative Pressure Measurement in the Diamond-Anvil Cell. *Rev. Sci. Instrum.* **44,** 1–9 (1973).

280. Perdew, J. P. *et al.* Restoring the Density-Gradient Expansion for Exchange in Solids and Surfaces. *Phys. Rev. Lett.* **100,** 136406 (2008).

281. Kresse, G. & Furthmüller, J. Efficient iterative schemes for ab initio total-energy calculations using a plane-wave basis set. *Phys. Rev. B* **54,** 11169–11186 (1996).

282. Kresse, G., Marsman, M. & Furthmüller, J. *VASP (Vienna Ab-initio Simulation Package)*.

283. Kresse, G. & Joubert, D. From ultrasoft pseudopotentials to the projector augmented-wave method. *Phys. Rev. B* **59,** 1758–1775 (1999).

284. Dudarev, S. L., Botton, G. A., Savrasov, S. Y., Humphreys, C. J. & Sutton, A. P. Electron-energy-loss spectra and the structural stability of nickel oxide: An LSDA+U study. *Phys. Rev. B* **57,** 1505–1509 (1998).

285. Hautier, G. *et al.* Designing Multielectron Lithium-Ion Phosphate Cathodes by Mixing Transition Metals. *Chem. Mater.* **25,** 2064–2074 (2013).

286. Clark, J. *et al.* High-Voltage Sulphate Cathodes $Li_2M(SO_4)_2$ (M = Fe, Mn, Co): Atomic-Scale Studies of Structures, Lithium Diffusion and Voltage Trends. *J. Mater. Chem. A* **2,** 7446–7453 (2014).

287. Reynaud, M., Rodríguez-Carvajal, J., Chotard, J.-N., Tarascon, J.-M. & Rousse, G. Magnetic structure and properties of orthorhombic $Li_2Ni(SO_4)_2$: a possible magnetoelectric material. *Phys. Rev. B* **89,** 104419 (2014).

288. Van der Ven, A., Thomas, J. C., Xu, Q., Swoboda, B. & Morgan, D. Nondilute diffusion from first principles: Li diffusion in Li_xTiS_2. *Phys. Rev. B* **78,** 104306 (2008).

289. Ewald, P. P. Die Berechnung optischer und elektrostatischer Gitterpotentiale. *Ann. Phys.* **369,** 253–287 (1921).